



ISSN 1605-2730

MATERIALS PHYSICS AND MECHANICS

Vol. 44, No. 1, 2020

MATERIALS PHYSICS AND MECHANICS

Principal Editors:

Dmitrii Indeitsev

*Institute of Problems of Mechanical Engineering
of the Russian Academy of Science (RAS), Russia*

Andrei Rudskoi

Peter the Great St.Petersburg Polytechnic University, Russia

Founder and Honorary Editor: Ilya Ovid'ko (1961-2017)

*Institute of Problems of Mechanical Engineering
of the Russian Academy of Sciences (RAS), Russia*

Associate Editors:

Anna Kolesnikova

*Institute of Problems of Mechanical Engineering
of the Russian Academy of Sciences (RAS), Russia*

Alexander Nemov

Peter the Great St.Petersburg Polytechnic University, Russia

Editorial Board:

E.C. Aifantis

Aristotle University of Thessaloniki, Greece

K.E. Aifantis

University of Florida, USA

U. Balachandran

Argonne National Laboratory, USA

A. Bellosi

Research Institute for Ceramics Technology, Italy

A.K. Belyaev

Institute of Problems of Mechanical Engineering (RAS), Russia

S.V. Bobylev

Institute of Problems of Mechanical Engineering (RAS), Russia

A.I. Borovkov

Peter the Great St.Petersburg Polytechnic University, Russia

G.-M. Chow

National University of Singapore, Singapore

Yu. Estrin

Monash University, Australia

A.B. Freidin

Institute of Problems of Mechanical Engineering (RAS), Russia

Y. Gogotsi

Drexel University, USA

I.G. Goryacheva

Institute of Problems of Mechanics (RAS), Russia

D. Hui

University of New Orleans, USA

G. Kiriakidis

IESL/FORTH, Greece

D.M. Klimov

Institute of Problems of Mechanics (RAS), Russia

G.E. Kodzhaspirov

Peter the Great St.Petersburg Polytechnic University, Russia

S.A. Kukushkin

Institute of Problems of Mechanical Engineering (RAS), Russia

T.G. Langdon

University of Southampton, U.K.

V.P. Matveenko

Institute of Continuous Media Mechanics (RAS), Russia

A.I. Melker

Peter the Great St.Petersburg Polytechnic University, Russia

Yu.I. Meshcheryakov

Institute of Problems of Mechanical Engineering (RAS), Russia

N.F. Morozov

St.Petersburg State University, Russia

R.R. Mulyukov

Institute for Metals Superplasticity Problems (RAS), Russia

Yu.V. Petrov

St.Petersburg State University, Russia

N.M. Pugno

Politecnico di Torino, Italy

B.B. Rath

Naval Research Laboratory, USA

A.E. Romanov

Ioffe Physico-Technical Institute (RAS), Russia

A.M. Sastry

University of Michigan, Ann Arbor, USA

B.A. Schrefler

University of Padua, Italy

N.V. Skiba

Institute of Problems of Mechanics (RAS), Russia

A.G. Sheinerman

Institute of Problems of Mechanics (RAS), Russia

R.Z. Valiev

Ufa State Aviation Technical University, Russia

K. Zhou

Nanyang Technological University, Singapore

"Materials Physics and Mechanics" Editorial Office:

Phone: +7(812)552 77 78, ext. 224 **E-mail:** mpmjournal@spbstu.ru **Web-site:** <http://www.mpm.spbstu.ru>

International scientific journal "Materials Physics and Mechanics" is published by Peter the Great St.Petersburg Polytechnic University in collaboration with Institute of Problems of Mechanical Engineering of the Russian Academy of Sciences in both hard copy and electronic versions.

The journal provides an international medium for the publication of reviews and original research papers written in English and focused on the following topics:

- Mechanics of composite and nanostructured materials.
- Physics of strength and plasticity of composite and nanostructured materials.
- Mechanics of deformation and fracture processes in conventional materials (solids).
- Physics of strength and plasticity of conventional materials (solids).
- Physics and mechanics of defects in composite, nanostructured, and conventional materials.
- Mechanics and physics of materials in coupled fields.

Owner organizations: Peter the Great St. Petersburg Polytechnic University; Institute of Problems of Mechanical Engineering RAS.

Materials Physics and Mechanics is indexed in Chemical Abstracts, Cambridge Scientific Abstracts, Web of Science Emerging Sources Citation Index (ESCI) and Elsevier Bibliographic Databases (in particular, SCOPUS).



МЕХАНИКА И ФИЗИКА МАТЕРИАЛОВ

Materials Physics and Mechanics

Том 44, номер 1, 2020 год

Учредители:

ФГАОУ ВО «Санкт-Петербургский политехнический университет Петра Великого»
ФГБУН «Институт проблем машиноведения Российской Академии Наук»

Редакционная коллегия журнала

Главные редакторы:

д.ф.-м.н., чл.-корр. РАН **Д.А. Индейцев**
Институт проблем машиноведения Российской Академии Наук
(РАН)

д.т.н., академик РАН **А.И. Рудской**
Санкт-Петербургский политехнический университет
Петра Великого

Основатель и почетный редактор: д.ф.-м.н. **И.А. Овидько (1961-2017)**

Институт проблем машиноведения Российской Академии Наук (РАН)

Ответственные редакторы

д.ф.-м.н. **А.Л. Колесникова**
Институт проблем машиноведения Российской Академии Наук
(РАН)

к.т.н. **А.С. Немов**
Санкт-Петербургский политехнический университет Петра
Великого

Международная редакционная коллегия:

д.ф.-м.н., проф. **А.К. Беляев**
Институт проблем машиноведения РАН, Россия
д.ф.-м.н. **С.В. Бобылев**
Институт проблем машиноведения РАН, Россия
к.т.н., проф. **А.И. Боровков**
Санкт-Петербургский политехнический у-т Петра Великого, Россия
д.ф.-м.н., проф. **Р.З. Валнев**
Уфимский государственный технический университет, Россия
д.ф.-м.н., академик РАН **И.Г. Горячева**
Институт проблем механики РАН, Россия
д.ф.-м.н., академик РАН **Д.М. Климов**
Институт проблем механики РАН, Россия
д.т.н., проф. **Г.Е. Коджаспиров**
Санкт-Петербургский политехнический у-т Петра Великого, Россия
д.ф.-м.н., проф. **С.А. Кукушкин**
Институт проблем машиноведения РАН, Россия
д.ф.-м.н., академик РАН **В.П. Матвеев**
Институт механики сплошных сред РАН, Россия
д.ф.-м.н., проф. **А.И. Мелькер**
Санкт-Петербургский политехнический у-т Петра Великого, Россия
д.ф.-м.н., проф. **Ю.И. Мещеряков**
Институт проблем машиноведения РАН, Россия
д.ф.-м.н., академик РАН **Н.Ф. Морозов**
Санкт-Петербургский государственный университет, Россия
д.ф.-м.н., чл.-корр. РАН **Р.Р. Мулюков**
Институт проблем сверхпластичности металлов РАН, Россия
д.ф.-м.н., чл.-корр. РАН **Ю.В. Петров**
Санкт-Петербургский государственный университет, Россия
д.ф.-м.н., проф. **А.Е. Романов**
Физико-технический институт им. А.Ф. Иоффе РАН, Россия
д.ф.-м.н. **Н.В. Скиба**
Институт проблем машиноведения РАН, Россия
д.ф.-м.н., проф. **А.Б. Фрейдлин**
Институт проблем машиноведения РАН, Россия
д.ф.-м.н. **А.Г. Шейнман**
Институт проблем машиноведения РАН, Россия

Prof., Dr. **E.C. Aifantis**
Aristotle University of Thessaloniki, Greece
Dr. **K.E. Aifantis**
University of Florida, USA
Dr. **U. Balachandran**
Argonne National Laboratory, USA
Dr. **A. Bellosi**
Research Institute for Ceramics Technology, Italy
Prof., Dr. **G.-M. Chow**
National University of Singapore, Singapore
Prof., Dr. **Yu. Estrin**
Monash University, Australia
Prof., Dr. **Y. Gogotsi**
Drexel University, USA
Prof., Dr. **D. Hui**
University of New Orleans, USA
Prof., Dr. **G. Kiriakidis**
IESL/FORTH, Greece
Prof., Dr. **T.G. Langdon**
University of Southampton, UK
Prof., Dr. **N.M. Pugno**
Politecnico di Torino, Italy
Dr. **B.B. Rath**
Naval Research Laboratory, USA
Prof., Dr. **A.M. Sastry**
University of Michigan, Ann Arbor, USA
Prof., Dr. **B.A. Schrefler**
University of Padua, Italy
Prof. Dr. **K. Zhou**
Nanyang Technological University, Singapore

Тел.: +7(812)552 77 78, доб. 224 E-mail: mpmjournal@spbstu.ru Web-site: <http://www.mpm.spbstu.ru>

Тематика журнала

Международный научный журнал "Materials Physics and Mechanics" издается Санкт-Петербургским политехническим университетом Петра Великого в сотрудничестве с Институтом проблем машиноведения Российской Академии Наук в печатном виде и электронной форме. Журнал публикует обзорные и оригинальные научные статьи на английском языке по следующим тематикам:

- Механика композиционных и наноструктурированных материалов.
- Физика прочности и пластичности композиционных и наноструктурированных материалов.
- Механика процессов деформации и разрушения в традиционных материалах (твердых телах).
- Физика прочности и пластичности традиционных материалов (твердых тел).
- Физика и механика дефектов в композиционных, наноструктурированных и традиционных материалах.
- Механика и физика материалов в связанных полях.

Редколлегия принимает статьи, которые нигде ранее не опубликованы и не направлены для опубликования в другие научные издания. Все представляемые в редакцию журнала "Механика и физика материалов" статьи рецензируются. Статьи могут отправляться авторам на доработку. Не принятые к опубликованию статьи авторам не возвращаются.

Журнал "Механика и физика материалов" ("Materials Physics and Mechanics") включен в систему цитирования Web of Science Emerging Sources Citation Index (ESCI), SCOPUS и PИИЦ.

© 2020, Санкт-Петербургский политехнический университет Петра Великого

© 2020, Институт проблем машиноведения Российской Академии Наук

Содержание

On cracking in thick GaN layers grown on sapphire substrates	1-7
M.G. Mynbaeva, A.A. Sitnikova, A.N. Smirnov, K.D. Mynbaev, H. Lipsanen, A.V. Kremleva, D.A. Bauman, V.E. Bougrov, A.E. Romanov	
Two scale homogenization in ternary locally resonant metamaterials.....	8-18
C. Comi, M. Moscatelli, J-J. Marigo	
Probing of polycrystalline magnesium at ultrasonic frequencies by mechanical spectroscopy.....	19-25
V.V. Kaminskii, Y.V. Lyubimova, A.E. Romanov	
Interaction of impurity atoms of light elements with vacancies and vacancy clusters in fcc metals.....	26-33
G.M. Poletaev, I.V. Zorya, R.Y. Rakitin, M.A. Iliina, M.D. Starostenkov	
Deposition kinetics and boundary layer theory in the chemical vapor deposition of β-SiC on the surface of C/C composite	34-47
H. Aghajani, N. Hosseini, B. Mirzakhani	
Strain-hardening effect on critical strain assessment of pipe plastic bending at buckling	48-60
M. Zheng, Z.M. Li	
Homogeneous horizontal and vertical seismic barriers: mathematical foundations and dimensional analysis	61-65
V.A. Bratov, A.V. Ilyashenko, S.V. Kuznetsov, T.-K. Lin, N.F. Morozov	
Hyperbolic two temperature fractional order one dimensional thermoelastic model heated by a pulse of laser.....	66-76
E. Bassiouny	
Hybrid acoustic panel: the effect of fiber volume fraction and panel thickness.....	77-82
NPG. Suardana, IKG. Sugita, IGN. Wardana	
Structural transformation of HCP metallic nanowire using cleri-rosato potential	83-93
M.M. Aish	
Numerical optimization of the cantilever piezoelectric generatorl.....	94-102
A.N. Soloviev, V.A. Chebanenko, I.V. Zhilyaev, A.V. Cherpakov, I.A. Parinov	
Single-walled carbon nanotube as a nanoscale quantum system.....	103-109
M.V. Krasinkova	
Structure and properties of nanoporous oxide dielectrics modified by carbon	110-115
Yu.V. Sakharov	
Pair interaction of coaxial circular prismatic dislocation loops in elastic solids with spherical surfaces.....	116-124
S.A. Krasnitckii, A.M. Smirnov, M.Yu. Gutkin	
Crystallographic orientation, delay time and mechanical constants influence on thermal fatigue strength of single - crystal nickel superalloys	125-136
A.V. Savikovskii, A.S. Semenov, L.B. Getsov	

Упругие свойства, поверхность нагружения и критерий течения нанопорошковых компактов.....	137-158
Г.Ш. Болтачев, Е.А. Чингина, Н.Б. Волков, К.Е. Лукьяшин	

Contents

On cracking in thick GaN layers grown on sapphire substrates	1-7
M.G. Mynbaeva, A.A. Sitnikova, A.N. Smirnov, K.D. Mynbaev, H. Lipsanen, A.V. Kremleva, D.A. Bauman, V.E. Bougrov, A.E. Romanov	
Two scale homogenization in ternary locally resonant metamaterials.....	8-18
C. Comi, M. Moscatelli, J-J. Marigo	
Probing of polycrystalline magnesium at ultrasonic frequencies by mechanical spectroscopy.....	19-25
V.V. Kaminskii, Y.V. Lyubimova, A.E. Romanov	
Interaction of impurity atoms of light elements with vacancies and vacancy clusters in fcc metals.....	26-33
G.M. Poletaev, I.V. Zorya, R.Y. Rakitin, M.A. Iliina, M.D. Starostenkov	
Deposition kinetics and boundary layer theory in the chemical vapor deposition of β-SiC on the surface of C/C composite	34-47
H. Aghajani, N. Hosseini, B. Mirzakhani	
Strain-hardening effect on critical strain assessment of pipe plastic bending at buckling	48-60
M. Zheng, Z.M. Li	
Homogeneous horizontal and vertical seismic barriers: mathematical foundations and dimensional analysis	61-65
V.A. Bratov, A.V. Ilyashenko, S.V. Kuznetsov, T.-K. Lin, N.F. Morozov	
Hyperbolic two temperature fractional order one dimensional thermoelastic model heated by a pulse of laser.....	66-76
E. Bassiouny	
Hybrid acoustic panel: the effect of fiber volume fraction and panel thickness.....	77-82
NPG. Suardana, IKG. Sugita, IGN. Wardana	
Structural transformation of HCP metallic nanowire using cleri-rosato potential	83-93
M.M. Aish	
Numerical optimization of the cantilever piezoelectric generatorl.....	94-102
A.N. Soloviev, V.A. Chebanenko, I.V. Zhilyaev, A.V. Cherpakov, I.A. Parinov	
Single-walled carbon nanotube as a nanoscale quantum system.....	103-109
M.V. Krasinkova	
Structure and properties of nanoporous oxide dielectrics modified by carbon	110-115
Yu.V. Sakharov	
Pair interaction of coaxial circular prismatic dislocation loops in elastic solids with spherical surfaces.....	116-124
S.A. Krasnitckii, A.M. Smirnov, M.Yu. Gutkin	
Crystallographic orientation, delay time and mechanical constants influence on thermal fatigue strength of single - crystal nickel superalloys	125-136
A.V. Savikovskii, A.S. Semenov, L.B. Getsov	

Elastic properties, yield surface and flow rule of nanopowder compacts 137-158
G.Sh. Boltachev, E.A. Chingina, N.B. Volkov, K.E. Lukyashin

ON CRACKING IN THICK GAN LAYERS GROWN ON SAPPHIRE SUBSTRATES

M.G. Mynbaeva^{1,2*}, A.A. Sitnikova¹, A.N. Smirnov¹, K.D. Mynbaev^{1,2}, H. Lipsanen^{2,3},
A.V. Kremleva², D.A. Bauman², V.E. Bougrov², A.E. Romanov^{1,2}

¹Ioffe Institute, Polytechnicheskaya 26, Saint-Petersburg 194021, Russia

²ITMO University, Kronverkskiy 49, Saint-Petersburg 197101, Russia

³Aalto University, Tietotie 3, Espoo 13500, Finland

*e-mail: mgm@mail.ioffe.ru

Abstract. Self-organization mechanisms promoting elimination of cracks in thick GaN layers grown on sapphire substrates are considered on the basis of the experimental results on the fabrication of the layers by Hydride Vapor-Phase Epitaxy on MOCVD-grown GaN/Al₂O₃ templates. The obtained data support the supposition on the closure of tensile stress-related cracks via diffusion processes and demonstrate the strong contribution of bulk diffusion in addition to surface diffusion discussed earlier.

Keywords: GaN, defects, cracking, Hydride vapor phase epitaxy

1. Introduction

Currently, development of III-nitride epitaxial technology is aimed at the achievement of the best possible quality of the material. Despite numerous efforts to commercialize III-nitride homoepitaxy, most of the epitaxial structures for GaN-based devices are still grown on foreign substrates, mainly on sapphire [1]. Sapphire (0001)Al₂O₃ substrates are known to be highly mismatched to GaN layers in respect to both lattice parameter (14%) and thermal expansion coefficient (30%). It is known that the increase in thickness of heteroepitaxially grown GaN layers provides the decrease in threading dislocation (TD) density, and this improves crystalline perfection [2]. At the same time, growth of thick layers often leads to cracking in both the substrate and the layer due to thermally-induced stress caused by aforementioned mismatches. When relaxation mechanisms are not taken into account, calculations predict that the compressive stress in GaN is reduced by over two orders of magnitude under cooling if the film thickness is increased to 1 mm. Thus, the tensile stress in sapphire substrate is increased by over two orders of magnitude [3]. Stress calculations for GaN/Al₂O₃ with consideration of relaxation mechanisms were performed in Ref. [4]. Three mechanisms of relaxation accompanied with the formation of structural defects were proposed for different film thicknesses: (i) pure lattice deformation for films with thicknesses <4 μm, (ii) enhancement of the density of interface defects such as "microcracks" and/or dislocations (4-20 μm), and (iii) generation of "macrocracks" in sapphire (>20 μm). Macrocracks that develop in GaN/(0001)Al₂O₃ structures are the cause of the mechanical failure of the entire wafer during post-growth cool-down (an example is shown in Fig. 1(a)).

Yet the failure does not necessarily occur in all cases. For instance, as was shown for Metal-Organic Chemical-Vapor Deposition (MOCVD) of GaN, cracking could be observed for 13 μm-thick layers, but did not necessarily appear in the layers with the thickness of 30 μm [5]. This phenomenon was treated in detail by Etzkorn and Clarke [6]. They have

http://dx.doi.org/10.18720/MPM.4412020_1

© 2020, Peter the Great St. Petersburg Polytechnic University

© 2020, Institute of Problems of Mechanical Engineering RAS

shown that in sufficiently thick GaN layers grown on sapphire substrates, a particular net of buried cracks, which do not extend to either bottom or top of the film, is formed. Etzkorn and Clarke argued that this cracking pattern could not be produced under compression. Their general conclusion was that cracking resulted from tensile stress, which was generated during the growth when a certain critical thickness of the film was reached. This supposition was supported by the results of some experimental and theoretical studies (see, e.g., [7-9]). For the explanation of crack elimination phenomenon, Etzkorn and Clarke considered several possible scenarios involving diffusion-type processes or non-diffusion crack retraction [6]. Later, Liu et al. [7], who demonstrated formation and healing of buried cracks in thick GaN layers grown by Hydride Vapor-Phase Epitaxy (HVPE), suggested that the lateral overgrowth was the predominating process. In this paper, we will discuss our experimental results on fabrication of thick GaN layers with HVPE using MOCVD-grown templates. Our results are indicative of the dominance of diffusion (both bulk and surface) mechanism of the crack closure during the growth.

2. Experimental technique

The initial substrates were 2" (0001)Al₂O₃ wafers with 3.2 to 4.6 μm-thick GaN layers grown by MOCVD on low-temperature GaN buffer layers. Thick (100-1500 μm) epitaxial layers were grown in a home-made horizontal HVPE reactor at the atmospheric pressure. The growth temperature was 1050 °C. Argon with 99.997% purity was used as a carrier gas, while metallic Ga (99.9999%) and gaseous NH₃ (99.999%) were used as Ga and N sources, respectively. Gallium was chlorinated with gaseous HCl with 99.999% purity. It appeared that HVPE-grown layers with thicknesses exceeding 400 μm were not necessarily destructed during the cool-down from the growth temperature to the room temperature. An example of the appearance of a 1000 μm-thick HVPE layer is shown in Fig. 1(b), where it is seen that the whole structure is undamaged and retains its integrity.

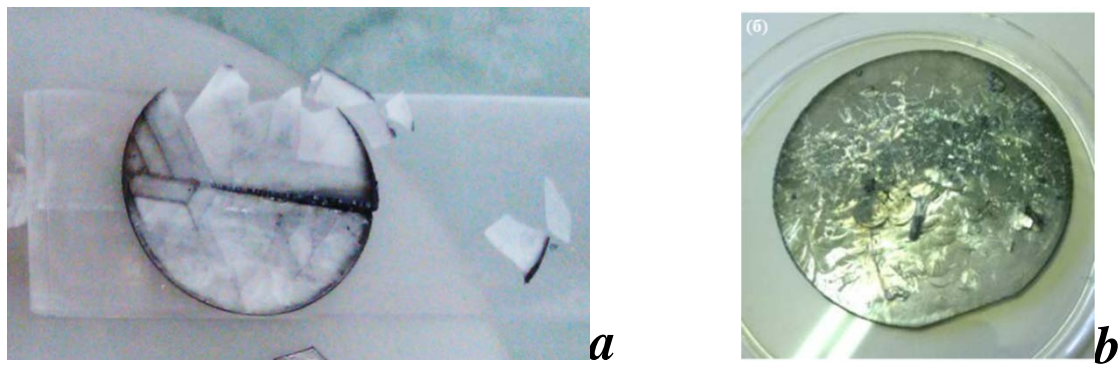


Fig. 1. Optical photographs of thick GaN layers grown by HVPE on templates prepared with MOCVD: *a*, a layer with thickness <100 μm, this sample experienced destruction right on the growth pedestal after cooling down to the room temperature; *b*, a layer with thickness of 1000 μm, which retained its integrity. The diameter of both wafers is 50.8 mm

3. Experimental results

Optical microscopy study was performed with various focus depths from the surface to the bulk of the material (down to approx. 200 μm). The studies revealed the presence of a set of crack nets located at a considerable distance from the HVPE layer/substrate interface. The nets were arranged one above another in the bulk of the layer with crack density decreasing towards the surface. Figures 2 and 3 show the specifics of crack propagation. Figure 2(a) shows an image obtained with the maximum focus depth. The observed area does not contain

any cracks. Figure 2(b) shows the image obtained with the minimum focus depth, which allowed for observing a buried crack (indicated by arrow) that did not intersect the surface.

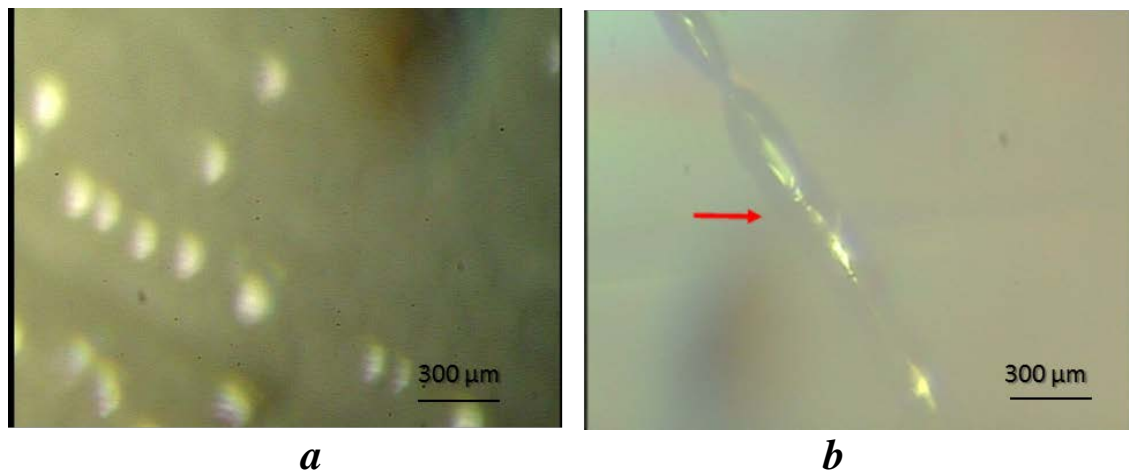


Fig. 2. Optical photographs of a thick HVPE-grown GaN layer taken with various focus depths of the microscope: *a*, maximum focus depth; *b*, minimum focus depth. An arrow in image (*b*) points to a buried crack

Images presented in Fig. 3 show the evolution of the microstructure of buried cracks within the bulk of the material. Moving the focus from the layer/substrate interface along the growth direction, a heavily cracked region was detected. This can be seen in Fig. 3(a), where a net of cracks with irregular shape is seen with weaker contrast (marked with white arrows). Also, cracks with good contrast with lower density are seen above them (marked with a red arrow). Important features of the defect pattern here are spheroid-like voids formed along the crack trajectory as well as spherical micropores located in the immediate vicinity of the cracks (Fig. 3(b,c)). The upper portion of the GaN bulk is shown in Fig. 3(d). This image demonstrates that all the underlying cracks are completely closed and only micropores exist above them (as seen in the lower left side of the image).

Transmission Electron Microscopy (TEM) studies were performed with the use of Philips EM-420 (accelerating voltage 80 kV, resolution 5 Å) and Jeol JEM-2100F (accelerating voltage 200 kV, resolution 2 Å) microscopes. Specimens for TEM studies were prepared using standard procedures of mechanical thinning and subsequent etching with Ar⁺ ions with energy 3 to 4 keV. According to TEM data, the crack-free surface layer in the investigated sample had a thickness of 10 to 15 μm with TD density as low as $4 \times 10^7 \text{ cm}^{-2}$. TEM results also confirmed the existence of both voids (Fig. 4(a)) and micropores (Fig. 4(b)) in the bulk of the studied layer. The TEM study also showed that the process of evolution of the shape of buried cracks via formation of voids was accompanied by changes in the trajectories of TDs, so dislocations got deviated from their typical path along the direction of the growth. Figure 4(a) shows a TEM image of a cross-section of the layer, where one can see a buried void and a dislocation that changed its direction near the surface of the void. The change of the direction of dislocation propagation can be indicative of the existence of diffusion processes leading to dislocation motion [10].

For accessing the quality of the GaN material, we used Raman and PL techniques. Horiba Jobin-Yvon T64000 Raman spectrometer (France) was used in these studies. Raman signal was excited with YAG:Nd laser (excitation wavelength $\lambda=532 \text{ nm}$). The results of Raman spectroscopy performed in backscattering geometry at 300 K revealed low residual strain value in the studied sample. In Raman spectra (not shown), three allowed lines related to phonons of E₂(low), E₂(high) and A₁(LO) symmetry were observed. The Raman shift and full-width at half-maximum (FWHM) of the E₂(high) line equaled 567.5 cm^{-1} and 2.1 cm^{-1} ,

respectively, and these values were close to those typical of non-deformed GaN (567.8 cm^{-1} and 1.9 cm^{-1} , respectively [11,12]). According to the Raman shift of $A_1(\text{LO})$ phonon line (733.7 cm^{-1}), free electron concentration in the sample equaled $(5-6)\times 10^{16}\text{ cm}^{-3}$.

Low-temperature ($T=10\text{ K}$) PL spectrum of the layer (not shown) was dominated by excitonic lines (bound exciton, BE, peaks) and their LO phonon replicas. The high quality of the material was confirmed by the absence of strong "yellow" PL line (with peak at $\sim 2.2\text{ eV}$), which can be often observed in GaN luminescence spectra [13]. This was indicative of low concentration of point defects that are responsible for the appearance of this line. There was no indication of the presence of other 'defect' lines, such as 'green' (with peak at $\sim 2.4\text{ eV}$) and blue (with peak at $\sim 2.9\text{ eV}$) lines that are typical of HVPE-grown GaN even with relatively high purity [14] either. High-resolution PL spectrum revealed a number of narrow excitonic bands, which were also indicative of the high quality of the material [15].

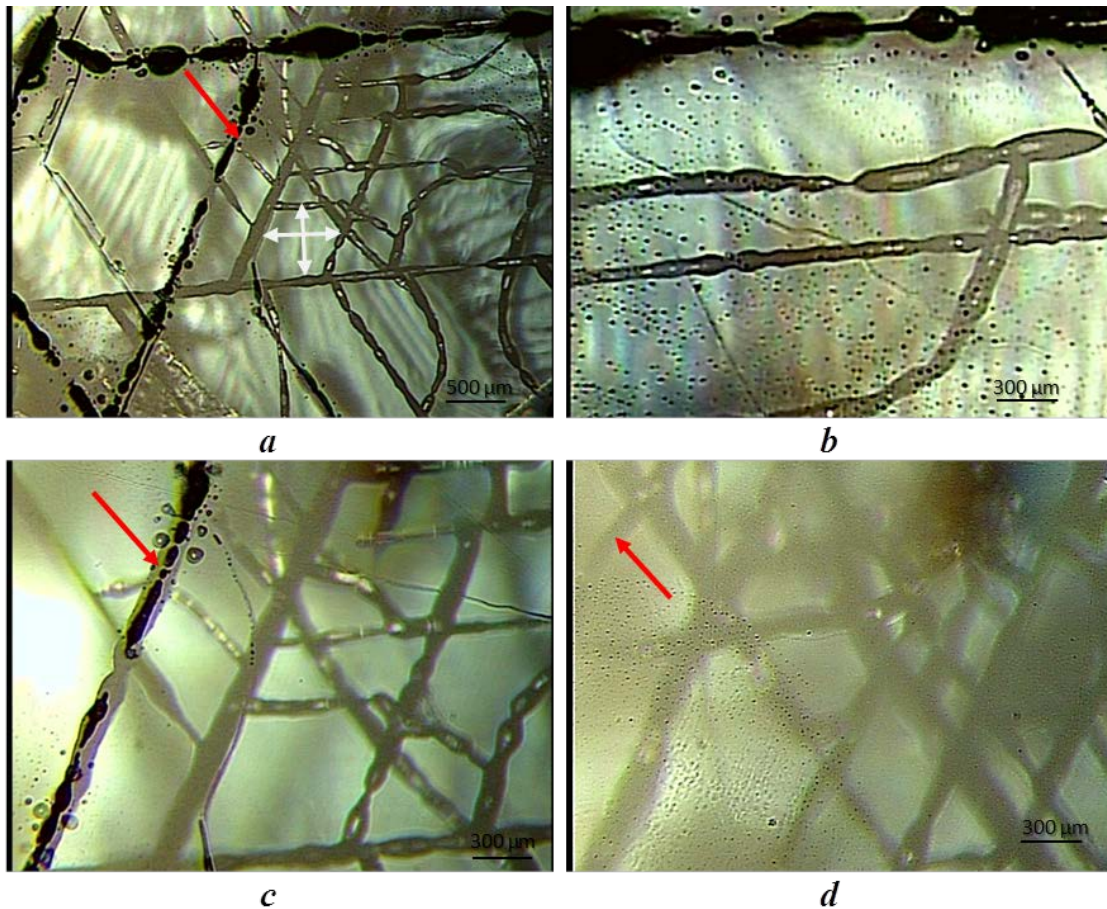


Fig. 3. Optical microscopy images illustrating reduction of crack density during HVPE of the $650\text{ }\mu\text{m}$ -thick GaN layer: *a*, deeply buried cracks; *b*, spherical micropores located in the vicinity of the cracks; *c*, partly closed crack propagated in the overlying section; *d*, the third (upper) section that does not contain cracks. Red arrows in images (*a*), (*c*), and (*d*) show the same crack, which allows for following its propagation, changes in its shape and its complete closure

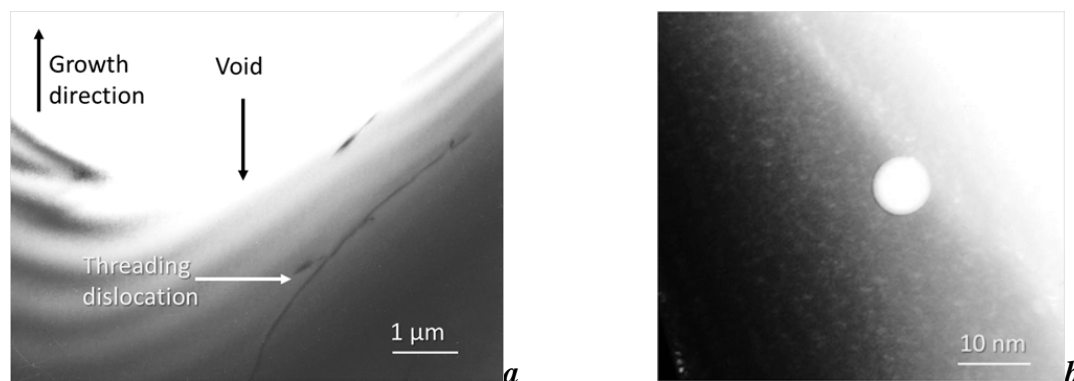


Fig. 4. TEM image of a cross-section of the thick GaN layer with buried cracks, which illustrates the interaction between an inner void and a threading dislocation (*a*), and a spherical micropore located in the immediate vicinity of the void (*b*)

4. Discussion

We shall start the discussion with the established fact that cracks in thick GaN layers originate from the increase of tensile strain during the growth when material reaches a certain critical thickness and that they remain buried in the bulk of the material [6]. Etzkorn and Clarke offered some possible scenarios of the formation of buried cracks. One of them was a diffusion-type process of crack closure. The driving force for this process obviously was the 'desire' of the system to lower the overall stored energy, which resulted in the decrease of the surface area of cracks [6]. We believe that the dominating role of the diffusion mechanism is now supported by our experimental results. On the basis of our data it can be suggested that the observed formation of multi-layered nets of cracks in the bulk of thick GaN layers proceeds according to the following scenario. After the layer reaches the critical thickness, cracks of the first level are formed. Under high temperatures (those of GaN HVPE growth), surface diffusion occurs at the walls of the cracks while bulk diffusion occurs in their vicinity. This leads to the evolution of the shape of the cracks, which proceeds till their continuity is interrupted as a result of the formation of voids along the crack trajectory. Then the cracks break up into a series of voids via a series of pinch-off events [16,17]. It can be suggested that the formation of micropores in the vicinity of the voids results from the subsequent process of void spheroidisation, which completes crack closure. These processes of the formation of cracks and their diffusion-mediated closure at the first level partly relax the strain that was generated during the growth. Thus, newly formed net of second-level cracks have lower density. These cracks undergo similar changes and additionally serve as internal sinks for micropores that had resulted from the first-level crack closure. As a result of this, the cracks of the lower level become fully closed, and the voids of the next level have larger mean diameter as compared to that of the channels of the lower level. With growth strain gradually relaxing, the density of cracks decreases and they all become closed. The remaining micropores, which now have no internal sinks, are absorbed by the free surface, which serve as an external sink, and thus, disappear. This scenario of buried crack evolution is also supported by TEM observation of the dislocation motion. The change in the direction of dislocation propagation could be considered as an extra proof of the existence of intensive diffusion processes, namely, a mass transfer by two counter-fluxes, where vacancies are moving towards the cracks or voids, which serve as powerful internal sinks for them, while atoms are moving towards the dislocation. The first flux defines the changes in the shape of both the crack and voids, while the second flux leads to non-conservative dislocation motion. As growth of the material proceeds further, the crack/void-containing region gets buried in

the bulk of GaN and strain-free portion of the material with low TD density is formed above it, as was confirmed by the results of Raman, PL, and TEM studies presented above.

Conclusion

In conclusion, the results of the study of crack elimination in thick GaN layers grown by HVPE on GaN/Al₂O₃ templates prepared with MOCVD showed that non-catastrophic (those not leading to sample destruction) cracks that form during long growth runs appeared to be an important structural element, which encouraged additional relaxation processes in the bulk of thick GaN layers grown on foreign substrates. The suggestion by Etzkorn and Clarke [6], who postulated that changes in the shape of initial buried cracks result from surface diffusion, were complemented with our experimental data that were indicative of the existence of simultaneous processes of bulk diffusion. This provides extra arguments in favor of diffusion mechanisms of crack closure. The diffusion processes obviously reduce free energy and help strain relaxation in the growing thick GaN layers.

Acknowledgment. Authors acknowledge support from the Ministry of Science and Higher Education of the Russian Federation, goszadanie No. 3.1421.2017/4.6.

References

- [1] Li G, Wang W, Yang W, Lin Y, Wang H, Lin Z, Zhou S. GaN-based light-emitting diodes on various substrates: a critical review. *Reports on Progress in Physics*. 2016;79(5): 056501.
- [2] Mathis SK, Romanov AE, Chen LF, Beltz GE, Pompe W, Speck JS. Modeling of threading dislocation reduction in growing GaN layers. *Journal of Crystal Growth*. 2001;231: 371-390.
- [3] Williams AD, Moustakas TD. Formation of large-area freestanding gallium nitride substrates by natural stress-induced separation of GaN and sapphire. *Journal of Crystal Growth*. 2007;300: 37-41.
- [4] Hiramatsu K, Detchprohm T, Akasaki I. Relaxation Mechanism of Thermal Stresses in the Heterostructure of GaN Grown on Sapphire by Vapor Phase Epitaxy. *Japanese Journal of Applied Physics 1*. 1993;32(4): 1528-1533.
- [5] Itoh N, Rhee JC, Kawabata T, Koike S. Study of cracking mechanism in GaN/ α -Al₂O₃ structure. *Journal of Applied Physics*. 1985;58(5): 1828-1837.
- [6] Etzkorn EV, Clarke DR. Cracking of GaN films. *Journal of Applied Physics*. 2001;89(2): 1025-1034.
- [7] Liu J, Liu X, Li C, Wei H, Guo Y, Jiao C, Li Z, Xu X, Song H, Yang S, Zhu Q, Wang Z, Yang A, Yang T, Wang H. Investigation of cracks in GaN films grown by combined hydride and metal organic vapor-phase epitaxial method. *Nanoscale Research Letters*. 2011;6(1): 69.
- [8] Romanov AE, Beltz GE, Speck JS. Crack formation in surface layers with strain gradients. *International Journal of Material Research*. 2007;98(8): 723-728.
- [9] Soman R, Mohan N, Chandrasekar H, Bhat N, Raghavan S. Dislocation bending and stress evolution in Mg-doped GaN films on Si substrates. *Journal of Applied Physics*. 2018;124(24): 245104.
- [10] Geguzin IaE. *The Diffusion Zone*. Moscow: Nauka; 1979. (In Russian)
- [11] Röder C, Lipski F, Habel F, Leibiger G, Abendroth M, Himcinschi C, Kortus J. Raman spectroscopic characterization of epitaxially grown GaN on sapphire. *Journal of Physics D: Applied Physics*. 2013;46(28): 285302.
- [12] Davydov VY, Averkiev NS, Goncharuk IN, Nelson DK, Nikitina IP, Polkovnikov AS, Smirnov AN, Jacobson MA, Semchinova OK. Raman and photoluminescence studies of biaxial strain in GaN epitaxial layers grown on 6H-SiC. *Journal of Applied Physics*. 1997;82(10): 5097-5102.

- [13] Reshchikov MA, Morkoc H. Luminescence properties of defects in GaN. *Journal of Applied Physics*. 2005;97(6): 061301.
- [14] Reshchikov M, Usikov A, Helava H, Makarov Y. Defect-related luminescence in undoped GaN grown by HVPE. *Journal of Electronic Materials*. 2015;44(5): 1281-1286.
- [15] Mynbaeva MG, Pechnikov AI, Smirnov AN, Kirilenko DA, Raufov SC, Sitnikova AA, Odnoblyudov MA, Bougrov VE, Mynbaev KD, Nikolaev VI, Romanov AE. Optical properties of thick GaN layers grown with hydride vapor-phase epitaxy on structured substrates. *Materials Physics and Mechanics*. 2016;29(1): 24-31.
- [16] Glaeser AM. Model studies of Rayleigh instabilities via microdesigned interfaces. *Interface Science*. 2001;9(1-2): 65-82.
- [17] Joshi C, Abinandanan TA, Choudhury A. Phase field modelling of rayleigh instabilities in the solid-state. *Acta Materialia*. 2016;109: 286-291.

TWO SCALE HOMOGENIZATION IN TERNARY LOCALLY RESONANT METAMATERIALS

C. Comi^{1*}, M. Moscatelli^{1,2}, J.-J. Marigo²

¹Dept. of Civil and Environmental Eng. - Politecnico di Milano, P.za L. da Vinci 32, 20133 Milano, Italy

²Laboratoire de Mécanique des Solides, Ecole polytechnique, Palaiseau, France

*e-mail: claudia.comi@polimi.it

Abstract. In this work, we exploit the two-scale homogenization approach to compute explicitly the band gaps for out-of-plane wave propagation in ternary locally resonant metamaterials (LRM) with two-dimensional periodicity. The homogenization approach, recently developed by the authors for binary LRM, leads to the definition of the dynamic effective mass density, depending on the frequency, that becomes negative near the resonant frequencies of the inclusions. The intervals of negative effective mass give the band gaps. These explicit solutions put in evidence the dependence of the spectral gaps on the geometric parameters of the unit cell and on the mechanical properties of the three constituent materials. The range of frequency where the asymptotic homogenization approach is equivalent to the Bloch-Floquet theory is also established and confirmed by numerical simulations.

Keywords: metamaterials, homogenization, effective mass, band gaps, wave propagation

1. Introduction

Sonic and phononic crystals based on the localized resonant principle have been proposed and studied in the last twenty years. In particular, periodic materials with heavy, stiff inclusions with a soft coating embedded in a stiff matrix have been demonstrated to have broad spectral gaps at low frequency, see e.g. [1] with pioneering experimental results on a composite with lead spheres coated by silicone rubber in epoxy matrix. The intervals of frequency inside which no waves with real wavenumber can propagate, can have different applications especially in vibration isolation [2,3] or impact absorption [4,5].

The physical mechanism of local resonance with the corresponding spectral gaps can be associated with the concept of negative effective mass. This can be well understood with help of simple discrete mass-spring structures and many works have been performed in this direction, see e.g. [6,7]. Also in actual continuum composites one can, by different approaches, define an equivalent, effective mass density. In particular in [8] and [9] quite complex expressions of the effective mass were derived for ternary composites considering a single cell with rigid cylindrical or spherical inclusions coated by a soft materials and the possibility of negative effective mass were demonstrated. However, the limit of validity of these solutions was not explicitly settled.

The two-scale homogenization approach, first proposed in [10] for high-contrast binary elastic composite materials in the long wavelength regime, provides a powerful tool to define equivalent material properties. In [11] the approach was developed for a row of locally resonant inclusions and recently the authors studied the spectral properties and the band gaps of binary LRM through homogenization, [12].

In the same line, in the present work, we address the problem of out-of-plane wave propagation in ternary LRM by the two-scale homogenization approach. The material has two-dimensional periodicity, with cylindrical inclusions, modelled as rigid, coated by a very compliant material. In the low frequency regime, under the hypothesis of high contrast between the stiffness of the coating and of the matrix, homogenization leads to the definition of the dynamic effective mass density, depending on the frequency, that becomes negative near the resonant frequencies of the inclusions. The intervals of negative effective mass give the band gaps. The influence of geometric parameters of the unit cell, such as the filling fraction or the coating thickness, on the spectral gaps can thus be simply studied. This can be useful for the design of the metamaterial.

The paper is organized as follows. Section 2 sets the problem and the basic assumptions. The homogenization approach is developed in Section 3, where a closed form expression for the effective mass is derived. Results in terms of band gaps for different LRM are shown in Section 4. Section 5 provides a comparison of the analytical results with the numerical results obtained on a single cell with Bloch-Floquet boundary conditions; the range of frequency where the asymptotic homogenization approach is equivalent to the Bloch-Floquet theory is also established and confirmed by the simulations. Some conclusions are given in Section 6.

2. Problem formulation

We consider out-of-plane wave propagation in a ternary material endowed with two dimensional periodicity. The heterogeneous body Ω has a cross section S in the plane x_1 - x_2 and has a length in the direction x_3 very large with respect to the heterogeneities, see Fig. 1a. The unit cell that periodically repeats in the plane x_1 - x_2 is composed by a stiff matrix m containing a cylindrical heavy inclusion (also referred to as fibers, f) coated by a very compliant material c , as shown in Fig. 1b. The matrix and the coating are isotropic with linear elastic behavior, while the fiber is considered as rigid. The two dimensional Bravais lattice has primitive vectors \mathbf{a}_1 and \mathbf{a}_2 , which can have different moduli and can be non-orthogonal.

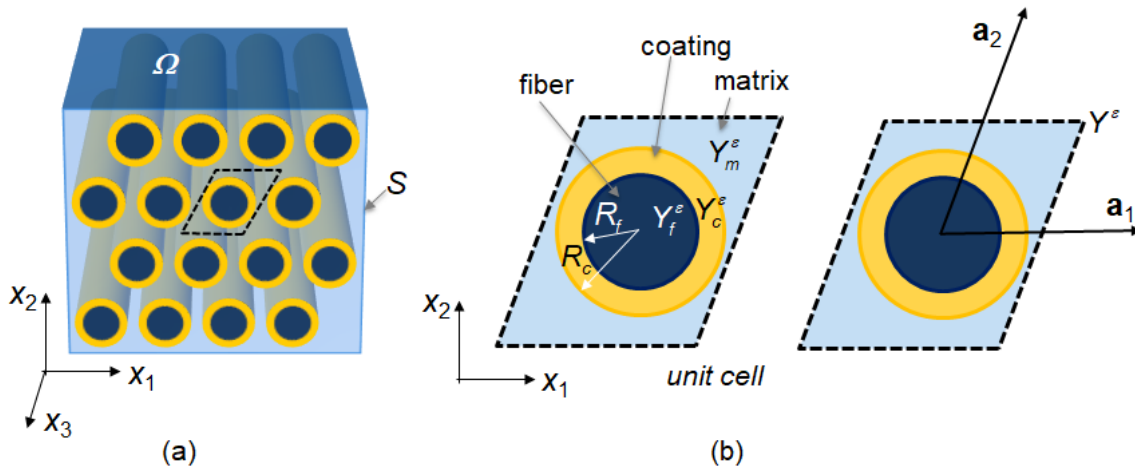


Fig. 1. Metamaterial with periodically distributed coated cylindrical inclusions: (a) geometry, (b) unit cell with primitive vectors \mathbf{a}_i

In this work, we assume that the size $a = \|\mathbf{a}_1 \wedge \mathbf{a}_2\|$ of the in-plane area Y^ϵ of the unit cell is small with respect to the considered wavelengths in the matrix material L_m

$$a = \epsilon L_m = \frac{\epsilon}{\omega} \sqrt{\frac{\mu_m}{\rho_m}}, \quad (1)$$

with ϵ a dimensionless small parameter, ω the angular frequency of the wave, μ_m the elastic shear modulus and ρ_m the mass density of the matrix. The coated inclusion has radius $R_c^\epsilon = \epsilon R_c$ and the heavy stiff core has radius $R_f^\epsilon = \epsilon R_f$. The area of the coating and of the fiber inside the unit cell are Y_c^ϵ and Y_f^ϵ , respectively. The filling fraction ϕ is defined as the ratio between the area of the coated inclusion and the total area

$$\phi = \frac{|Y_f^\epsilon| + |Y_c^\epsilon|}{|Y^\epsilon|}. \quad (2)$$

We further assume that there is high contrast between the stiffness of the matrix and that of the coating, namely the ratio between the elastic shear modulus of the coating and of the matrix is of the order of ϵ^2 . We denote by $\epsilon^2 \mu_c$ the coating shear modulus, with μ_c of the order of μ_m , and by ρ_c its mass density.

The motion, for a wave of angular frequency ω with out-of-plane polarization, is described by a displacement field, which has only one component $u^\epsilon = u_3^\epsilon$ in the direction x_3 that depends only on the in-plane coordinates x_1 and x_2 . The non-vanishing stress components σ_{31}^ϵ and σ_{32}^ϵ are collected in vector $\boldsymbol{\sigma}^\epsilon$ that reads:

$$\boldsymbol{\sigma}^\epsilon = \mu^\epsilon \text{grad} u^\epsilon \text{ in } \Omega, \quad (3)$$

with μ^ϵ equal to $\epsilon^2 \mu_c$ in Y_c^ϵ and μ_m in Y_m^ϵ . In view of the simplifying assumption of rigid inclusion, the stress in Y_f^ϵ is only fixed by equilibrium.

The equation of motion is expressed by:

$$\text{div} \boldsymbol{\sigma}^\epsilon + \rho^\epsilon \omega^2 u^\epsilon = 0 \text{ in } \Omega. \quad (4)$$

The two scale asymptotic method [13], [11] allows to construct the homogenized equation of motion for the composite material and to derive analytical conditions for wave propagation and band gaps prediction.

3. Homogenization approach

Let us introduce first the rescaled unit cell $Y = Y^\epsilon/\epsilon$ and a microscopic coordinate $\mathbf{y} = \mathbf{x}/\epsilon$ within it. The displacement and the stress are expanded in the form:

$$u^\epsilon(\mathbf{x}) = u^0(\mathbf{x}, \mathbf{x}/\epsilon) + \epsilon u^1(\mathbf{x}, \mathbf{x}/\epsilon) + \epsilon^2 u^2(\mathbf{x}, \mathbf{x}/\epsilon) + \dots \quad (5)$$

$$\boldsymbol{\sigma}^\epsilon(\mathbf{x}) = \boldsymbol{\sigma}^0(\mathbf{x}, \mathbf{x}/\epsilon) + \epsilon \boldsymbol{\sigma}^1(\mathbf{x}, \mathbf{x}/\epsilon) + \epsilon^2 \boldsymbol{\sigma}^2(\mathbf{x}, \mathbf{x}/\epsilon) + \dots \quad (6)$$

The fields $u^\alpha = u^\alpha(\mathbf{x}, \mathbf{y})$ and $\boldsymbol{\sigma}^\alpha = \boldsymbol{\sigma}^\alpha(\mathbf{x}, \mathbf{y})$, $\alpha = 0, 1, 2, \dots$, depend on both the macroscopic \mathbf{x} and microscopic \mathbf{y} coordinates and are Y -periodic with respect to \mathbf{y} . Accordingly, their spatial partial derivatives are denoted by an index \mathbf{x} or \mathbf{y} . From (5) and (6) one obtains:

$$\text{grad} u^\epsilon(\mathbf{x}) = \epsilon^{-1} \text{grad}_{\mathbf{y}} u^0 + \text{grad}_{\mathbf{y}} u^1 + \text{grad}_{\mathbf{x}} u^0 + \epsilon (\text{grad}_{\mathbf{y}} u^2 + \text{grad}_{\mathbf{x}} u^1) + \dots \quad (7)$$

$$\text{div} \boldsymbol{\sigma}^\epsilon(\mathbf{x}) = \epsilon^{-1} \text{div}_{\mathbf{y}} \boldsymbol{\sigma}^0 + \text{div}_{\mathbf{y}} \boldsymbol{\sigma}^1 + \text{div}_{\mathbf{x}} \boldsymbol{\sigma}^0 + \epsilon (\text{div}_{\mathbf{y}} \boldsymbol{\sigma}^2 + \text{div}_{\mathbf{x}} \boldsymbol{\sigma}^1) + \dots \quad (8)$$

The expansions (5-8) are substituted in the governing equations (3-4) and the terms of the same order in ϵ are then considered.

At order -1 from (3) we get $\text{grad}_{\mathbf{y}} u^0 = 0$ in Y_m and Y_f , while from (4) we get $\text{div}_{\mathbf{y}} \boldsymbol{\sigma}^0 = \mathbf{0}$ in Y . Hence:

$$u^0(\mathbf{x}, \mathbf{y}) = U_m^0(\mathbf{x}) \text{ in } S \times Y_m; \quad u^0(\mathbf{x}, \mathbf{y}) = U_f^0(\mathbf{x}) \text{ in } S \times Y_f \quad (9)$$

and

$$\boldsymbol{\sigma}^0 = \mu_m (\text{grad}_x U_m^0 + \text{grad}_y u^1) \text{ in } S \times Y_m; \quad \boldsymbol{\sigma}^0 = \mathbf{0} \text{ in } S \times Y_c . \quad (10)$$

The term $\text{grad}_x U_m^0$ in eq. (10) can be interpreted as a constant eigenstrain in the cell. For any value of $\text{grad}_x U_m^0$, one can solve a linear elastic static problem in the matrix only, with periodic boundary conditions, subject to the additional condition of zero stress at the boundary with the coating ∂Y_c . The out-of-plane displacement u^1 in the matrix can be expressed as

$$u^1(\mathbf{x}, \mathbf{y}) = \sum_{i=1}^2 \frac{\partial U_m^0}{\partial x_i}(\mathbf{x}) \chi^i(\mathbf{y}) + U^1(\mathbf{x}) \text{ in } S \times Y_m , \quad (11)$$

with χ^i solution of the problem

$$\begin{cases} \text{div grad}_y \chi^i = 0 & \text{in } Y_m \\ \mu_m (\text{grad}_y \chi^i + \mathbf{e}_i) \cdot \mathbf{n} = 0 & \text{on } \partial Y_c \\ \chi^i \text{ periodic, } \mu_m \text{grad}_y \chi^i \cdot \mathbf{n} \text{ anti-periodic} & \text{on } \partial Y \end{cases} \quad (12)$$

\mathbf{e}_i being the unit vector of the axis x_i .

The stress in the matrix reads

$$\boldsymbol{\sigma}^0(\mathbf{x}, \mathbf{y}) = \sum_{i=1}^2 \mu_m (\text{grad}_y \chi^i + \mathbf{e}_i) \frac{\partial U_m^0}{\partial x_i}(\mathbf{x}) \text{ in } S \times Y_m . \quad (13)$$

The homogenized displacement u^0 in the coating is the solution of the following problem, obtained by considering the terms of order 0 in ϵ in equilibrium equation (4) and those of order 1 in ϵ in the constitutive equation (3):

$$\begin{cases} \mu_c \text{div grad}_y u^0 + \rho_c \omega^2 u^0 = 0 & \text{in } S \times Y_c \\ u^0 = U_m^0 & \text{on } S \times \partial Y_c . \\ u^0 = U_f^0 & \text{on } S \times \partial Y_f \end{cases} \quad (14)$$

For a given U_m^0 and a given ω , different from the eigen-frequencies of the coated inclusion fixed at its boundary ∂Y_c , problem (14) admits a unique solution that can be expressed as:

$$u^0(\mathbf{x}, \mathbf{y}) = U_m^0(\mathbf{x}) \eta(\mathbf{y}) \text{ in } S \times Y_c , \quad (15)$$

where $\eta(\mathbf{y})$ is the solution of

$$\begin{cases} \text{div grad}_y \eta + k^2 \eta = 0 & \text{in } Y_c \\ \eta = 1 & \text{on } \partial Y_c \\ \eta = U_f^0 / U_m^0 & \text{on } \partial Y_f \end{cases} \quad (16)$$

with: $k = \omega \sqrt{\frac{\rho_c}{\mu_c}}$.

The displacement of the rigid fiber U_f^0 is obtained from the global dynamic equilibrium of the fiber subject to inertia forces and surface tractions transmitted by the coating

$$\rho_f |Y_f| \omega^2 U_f^0 + \int_{\partial Y_f} \mu_c \text{grad}_y \eta(\mathbf{y}) \cdot \mathbf{n} dy U_m^0 = 0 . \quad (17)$$

For the coated circular inclusion, problem (16)-(17) can be solved in close form and the solution in polar coordinates ($r = \|\mathbf{y}\|$) for $R_f \leq r \leq R_c$ reads:

$$\eta(\mathbf{y}) = \frac{k R_f \rho_f (J_0(kr) Y_0(k R_f) - Y_0(kr) J_0(k R_f)) + 2 \rho_c (Y_0(kr) J_1(k R_f) - J_0(kr) Y_1(k R_f))}{den} \quad (18)$$

with

$$den = kR_f \rho_f \left(J_0(kR_c)Y_0(kR_f) - Y_0(kR_c)J_0(kR_f) \right) + 2\rho_c \left(Y_0(kR_c)J_1(kR_f) - J_0(kR_c)Y_1(kR_f) \right), \quad (19)$$

where J_0 and J_1 are Bessel function of the first kind and Y_0 and Y_1 are Bessel function of the second kind.

The ratio between the displacement in the fiber and in the matrix reads

$$\frac{U_f^0}{U_m^0} = \eta(R_f) = \frac{2\rho_c \left(Y_0(kR_f)J_1(kR_f) - J_0(kR_f)Y_1(kR_f) \right)}{den}. \quad (20)$$

The discussion for ω equal to an eigenfrequency of the coated inclusion follows the same lines of the case of binary metamaterials developed in [12] and is not reported here for brevity.

Having obtained the above solutions for u^0 and σ^0 in the three constituent materials one can finally obtain an effective equation of motion for the propagation of out-of-plane waves in the metamaterial. To this purpose, let us consider the expansion of the equation of motion at order 0:

$$\operatorname{div}_y \sigma^1 + \operatorname{div}_x \sigma^0 + \rho \omega^2 u^0 = 0 \quad \text{in } S \times Y, \quad (21)$$

and let us integrate it over Y . The integral of the first term equals the integral on the cell boundary of the traction forces which vanishes by virtue of the periodic boundary conditions. The other two terms give

$$\operatorname{div}_x (\mathbf{M}^* \operatorname{grad}_x U_m^0) + \rho^*(\omega) \omega^2 U_m^0 = 0 \quad \text{in } S, \quad (22)$$

where \mathbf{M}^* is the second order effective stiffness tensor, whose components are given by

$$M_{ij}^* = \frac{1}{|Y|} \int_{Y_m} \mu_m (\operatorname{grad}_y \chi^i + \mathbf{e}_i) \cdot (\operatorname{grad}_y \chi^j + \mathbf{e}_j) dy, \quad (23)$$

and $\rho^*(\omega)$ is the effective mass density. This latter reads

$$\rho^*(\omega) = \rho_m \frac{|Y_m|}{|Y|} + \rho_f \frac{|Y_f|}{|Y|} \frac{U_f^0}{U_m^0} + \frac{\rho_c}{|Y|} \int_{Y_c} \eta(\mathbf{y}) dy. \quad (24)$$

Using the expression (18) of η one has

$$\int_{Y_c} \eta(\mathbf{y}) dy = 2\pi(h(R_c) - h(R_f)) \quad (25)$$

with

$$h(r) = \frac{r}{k} \frac{kR_f \rho_f \left(J_1(kr)Y_0(kR_f) - Y_1(kr)J_0(kR_f) \right) + 2\rho_c \left(Y_1(kr)J_1(kR_f) - J_1(kr)Y_1(kR_f) \right)}{den} \quad (26)$$

which, inserted into (24) together with (20), gives the explicit form of the effective mass. For $\omega=0$ the integral in (25) is $|Y_c|$, and $U_f^0 = U_m^0$, hence the effective mass coincides with the static mass density of the composite material ρ_{st} :

$$\rho_{st} = \rho_m \frac{|Y_m|}{|Y|} + \rho_f \frac{|Y_f|}{|Y|} + \rho_c \frac{|Y_c|}{|Y|}. \quad (27)$$

The effective mass is not defined for the frequencies ω_n which are roots of $den=0$ (eq. 19), it tends to $-\infty$ and $+\infty$ when ω tends to ω_n from above and from below, respectively. Therefore, the effective mass density is negative in a countable set of intervals. The values of ω_n , which fix the position of these intervals, depend only on the geometry and material properties of the coating through the non-dimensional groups kR_f and kR_c defined for the rescaled problem in Y . The corresponding real physical quantities in Y^c are defined as

$$k^\epsilon = \omega \sqrt{\frac{\rho_c}{\epsilon^2 \mu_c}}, \quad R_f^\epsilon = \epsilon R_f, \quad R_c^\epsilon = \epsilon R_c, \quad (28)$$

hence $k^\epsilon R_f^\epsilon = k R_f$ and $k^\epsilon R_c^\epsilon = k R_c$ and the frequencies intervals determined with the above analysis remain valid for the physical problem.

In view of eq. (22), waves with frequency ω such that the effective mass density becomes negative cannot propagate inside the composite material; the interval of negative effective mass identify then the band gaps. One should remark however that the homogenization approach applies only to waves with low frequency, as specified by hypothesis (1). This condition involves the properties of the matrix material and should be checked for the particular cases considered.

4. Results

Figure 2a shows the variation of the effective mass density, normalized with the static one, with the frequency $\omega/2\pi$ for the ternary metamaterial constituted by lead inclusions coated with rubber and embedded in epoxy matrix. The ratio between the external radius and internal radius of the coating is 0.2, the filling fraction is $\phi = \pi R_c^2 / |Y| = 0.4$ and the materials parameters are listed in Table 1. The effective mass becomes negative in several intervals of frequency (shaded in the figure) that correspond to band gaps.

Table 1. Materials properties

Constituents	E [MPa]	ν [-]	ρ [Kg/m ³]
matrix – epoxy	3600.	0.370	1180.
coating – rubber	0.118	0.469	1300.
inclusion – lead	14000.	0.420	11340.

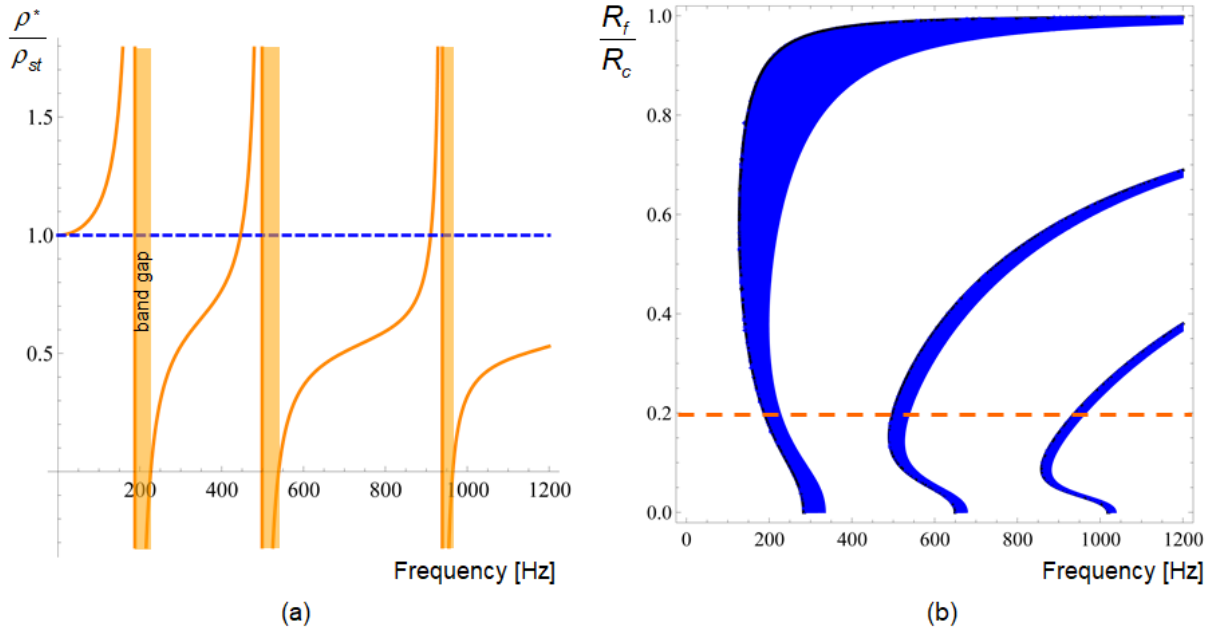


Fig. 2. Ternary metamaterial with filling fraction 0.4: (a) normalized effective mass vs. frequency for $R_f/R_c = 0.2$, intervals of negative effective mass give the first three band gaps; (b) intervals of negative effective mass in the plane frequency- R_f/R_c , the dashed line corresponds to the case shown on the left

The influence of the thickness of the coating is highlighted in Fig. 2b, where the regions of negative effective mass are shown at varying R_f/R_c . The dashed line corresponds to the effective mass evolution shown in Fig. 2a. The amplitude of the first band gap increases as the thickness of the coating decreases since, at fixed filling ratio, this corresponds to an increase of the resonating fiber mass.

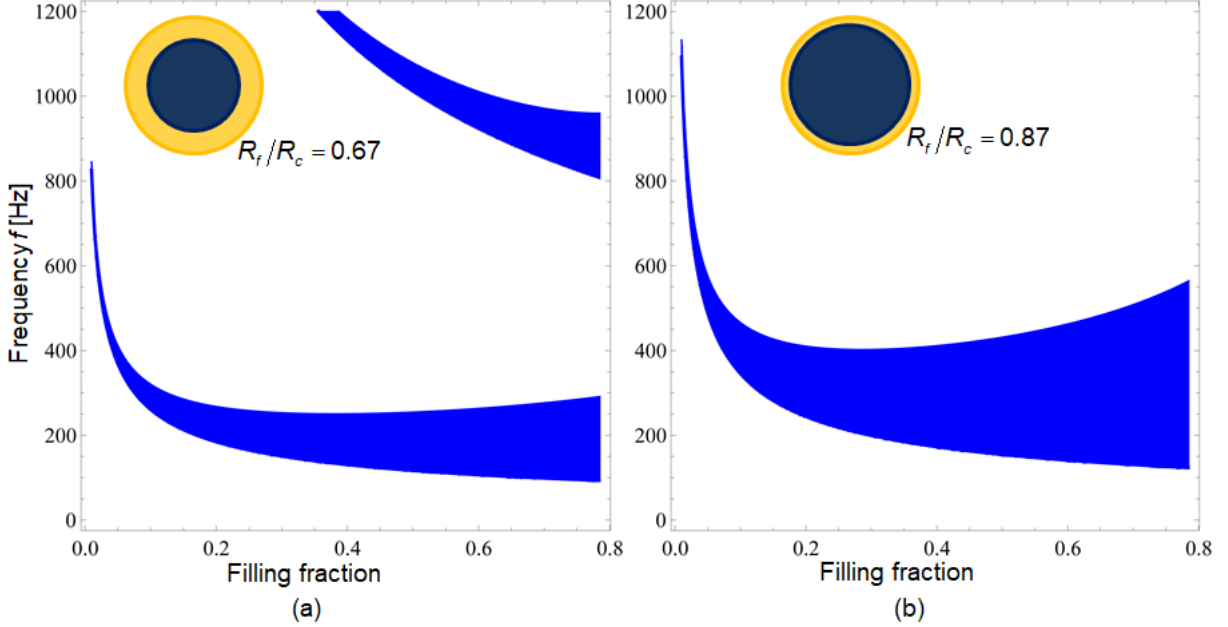


Fig. 3. Frequency intervals of negative effective mass for varying filling fraction: (a) thick coating $R_f/R_c = 0.67$, (b) thin coating $R_f/R_c = 0.87$

Since a closed form solution is obtained, one can easily perform parametric studies to evidence the influence of different geometries on the wave propagation properties.

As an example, Fig. 3 displays the frequency intervals of negative effective mass at varying fillings fractions for the case of a thick coating (Fig. 3a) and that of a thin coating (Fig. 3b).

In the first case, two strips are visible since two band gaps are inside the considered interval of frequency, while for the thin coating only the first band gap is inside the considered interval. In both cases, as the filling fraction increases, the opening frequency of the first band gap decreases and the amplitude of the bandgap increases.

5. Discussion and comparison with Bloch-Floquet analysis

The propagation of waves in periodic materials is often studied making use of the Bloch-Floquet theory solving an eigen-problem for the elementary cell subject to peculiar boundary conditions. These latter, also called Bloch-Floquet boundary conditions, relate the displacements of opposite sides of the unit cell and depend on the wave vector \mathbf{k} considered. The dispersion surfaces, $\omega = \omega(\mathbf{k})$ can be numerically evaluated, e.g. by finite elements [14,15].

Due to the periodicity and to the symmetries of the unit cell (if any), the description of the dynamic behavior of the metamaterial for all the possible wave vectors can be obtained by considering only the first Irreducible Brillouin Zone (IBZ) of the reciprocal lattice. Furthermore, often only the wave vectors along the boundary of the IBZ are considered, see [16,17] for details. The frequency of each mode is then plotted as a function of the arc length

along the boundary of the IBZ. The diagrams thus obtained are called dispersion diagrams and characterize the transmission properties of the periodic material. The intervals of frequencies where no real solutions exist define the band-gaps.

In a recent work [12], the authors proved that the asymptotic analysis of the Bloch-Floquet problem leads to the same effective equation of motion (20) obtained through the two scale homogenization methods described in Section 3. The two approaches therefore, in the low frequency range, give the same prediction of the band structure. In the following we illustrate these results for the ternary material with two dimensional periodicity.

We refer to the material shown in Fig. 1. To perform the numerical analysis, we consider that the inclusions are distributed on S following a square lattice, characterized by orthogonal base vectors \mathbf{a}_1 and \mathbf{a}_2 with the same modulus, so that the unit cell is a square of side a .

Note that the results of the homogenization theory are general, independent from the actual shape of the unit cell, while of course the numerical analysis of the Bloch-Floquet problem requires to fix the shape of the unit cell.

Assuming a square primary lattice, the reciprocal lattice of wave vectors is also square and the Brillouin Zone is a square with side $2\pi/a$. Exploiting symmetries, the IBZ is the triangle Γ -X-M, shown in the inset of Fig. 4a. The properties of the constituent materials are reported in Table 1.

Figure 4a shows the dispersion plot for the metamaterial with $a = 21\text{mm}$, $R_c = 7.5\text{ mm}$, (corresponding to filling fraction of 0.4) and $R_f = 5\text{ mm}$. The band gaps are shaded and the relative amplitude, defined as the bandwidth divided by the central band-gap frequency, is also reported. Figure 4b shows the evolution of the normalized effective mass density with frequency obtained through homogenization (note that this diagram is rotated of $\pi/2$ to facilitate the comparison). The shaded regions correspond to negative effective mass density and hence give the homogenization-based predictions of band gaps. One can observe an extremely good agreement of the two approaches for the determination of the first band gap.

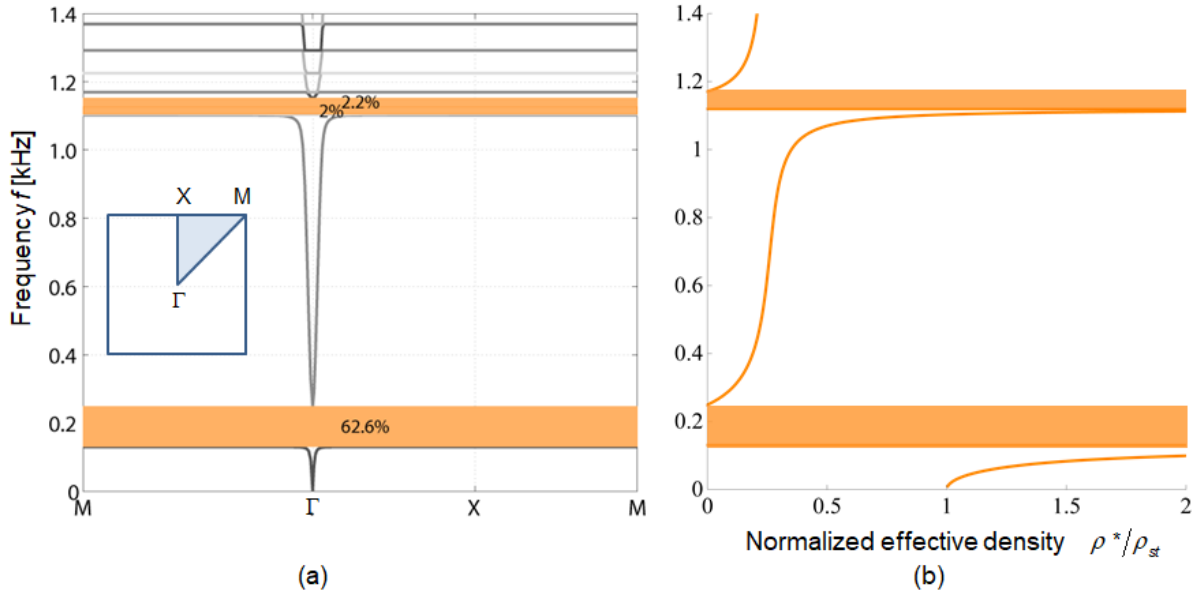


Fig. 4. Three components metamaterial, filling fraction 0.4, $R_f/R_c = 0.67$: (a) dispersion plot with dashed bandgaps, (b) normalized effective mass density vs frequency, shaded areas correspond to negative effective mass

The opening and the closing modes of the first band gap are shown in Fig. 5a-b, they are axial symmetric and correspond to different symmetry points of the IBZ, as common for

band-gaps generated by a local resonant mechanism. The second band gap in the dispersion plot is actually separated into two smaller bandgaps by the flat modes shown in Fig. 5d, and Fig. 5e corresponding to local resonances inside the coating characterized by displacement depending on both the radial and the angular coordinates.

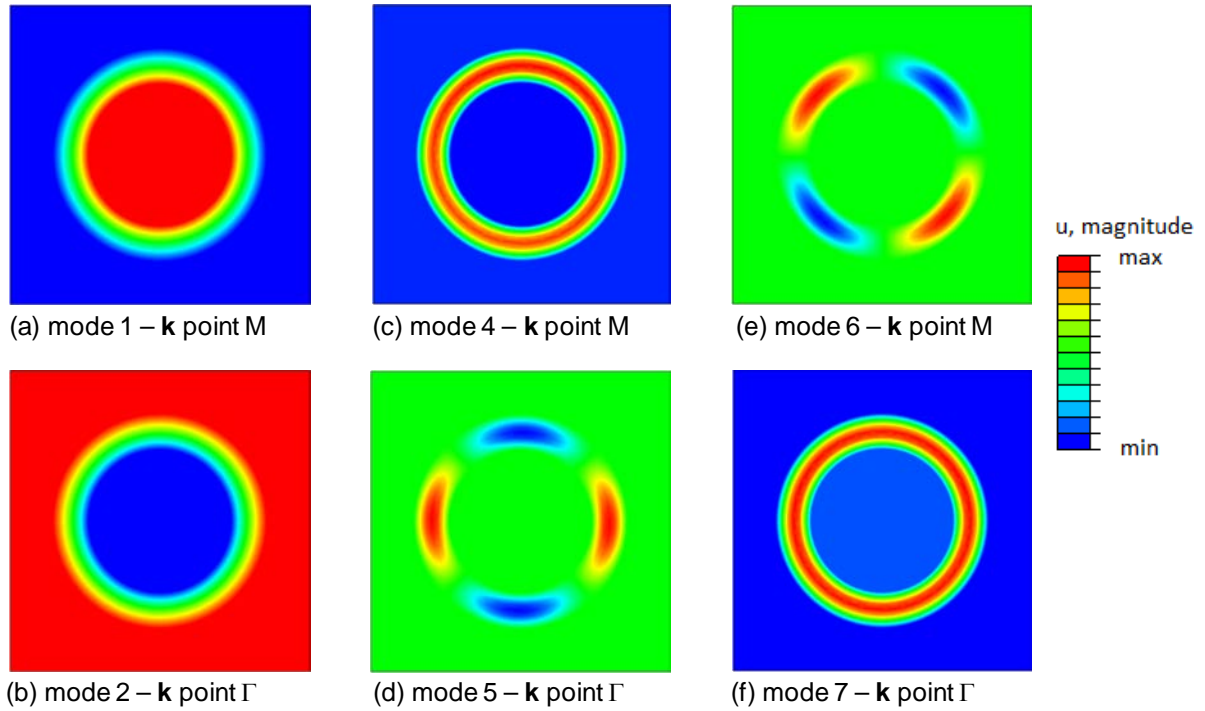


Fig. 5. Three components metamaterial, filling fraction 0.4, $R_f/R_c = 0.67$: (a) opening mode of first band gap, (b) closing mode of first band gap, (c) opening mode of second band gap, (d-e) flat modes inside second band gap, (f) closing mode of second band gap

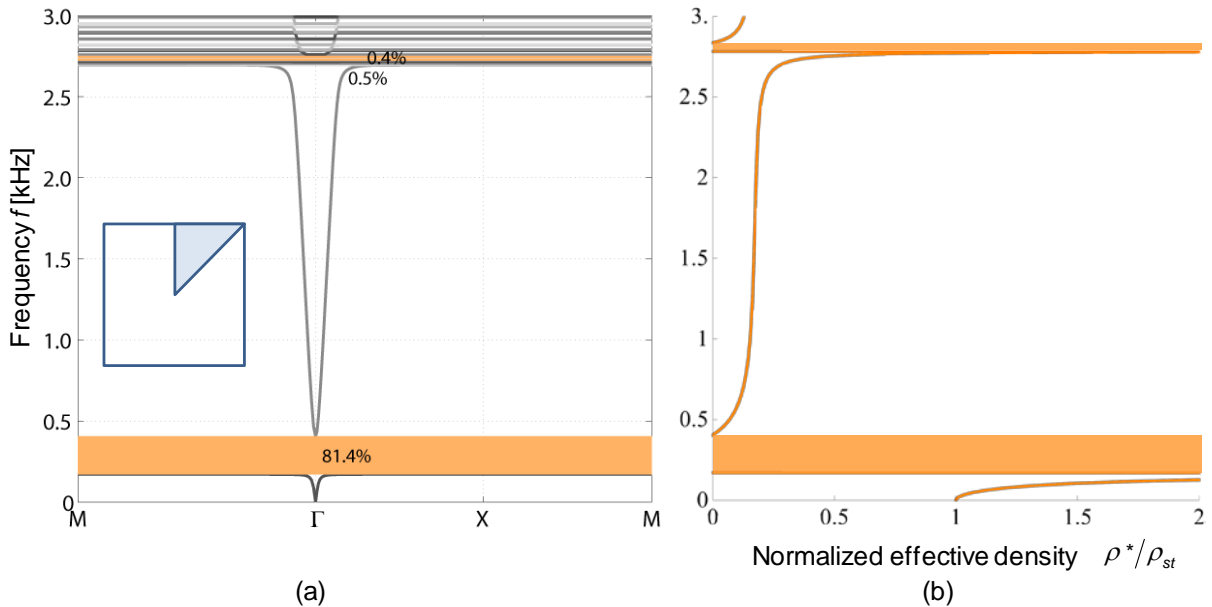


Fig. 6. Three components metamaterial, filling fraction 0.4, $R_f/R_c = 0.87$: (a) dispersion plot with dashed bandgaps, (b) normalized effective mass density vs frequency, shaded areas correspond to negative effective mass

The prediction of these flat modes through the homogenization approach would require to consider more general, not axial-symmetric, solutions. This part is not developed in this paper. The opening mode of the first part of this second band gap, shown in Fig. 5c, and the closing mode of the second part of this second band gap, Fig. 5f, are again axial-symmetric. From Fig. 5 one can also observe that the displacement is uniform in the internal lead inclusion, the hypothesis of rigid inclusion is therefore justified.

Another comparison between the two approaches is presented in Fig. 6 for the metamaterial with inclusions with a thin coating ($R_c = 7.5$ mm and $R_f = 6.5$ mm). The agreement is very good also in this case, especially as far as the first band gap is concerned.

One should remark that, in both cases considered in Figs. 4 and 6, the first band gaps fall inside the domain of validity of the homogenization approach, which is based on hypothesis (1). In fact, using the properties of the epoxy matrix and the cell dimension a , from (1) one obtains the following limit of validity of the asymptotic analysis:

$f \ll f_{\max} = \frac{1}{2\pi a} \sqrt{\frac{\mu_m}{\rho_m}} = 8 \text{ kHz}$; the frequency of the actual first band gaps are one order of magnitude lower than f_{\max} .

6. Conclusions

Based on the two-scale homogenization approach, we present an analytical expression for the dynamic effective mass density of a ternary LRM with cylindrical inclusions. The results, which provide an estimate of the band gaps in the low frequency regime, are independent from the shape of the unit cell and from the matrix stiffness. On the contrary, the gaps in the spectral properties strongly depend on the filling fraction and on the thickness and stiffness of the coating. This dependence is explicitly given in this work.

The range of validity of the homogenization approach is given and the results are also validated by comparison with those numerically obtained from the Bloch-Floquet theory.

The findings may be useful in designing LRM for specific applications where the required band gap frequencies are fixed. The extensions to in-plane wave propagation and spherical inclusions do not bring conceptual difficulties and are currently under development.

Acknowledgements. *Financial support of the Italian MIUR (PRIN project nr.2015LYYXA8 on Multi-scale mechanical models for the design and optimization of micro-structured smart materials and metamaterials) and of the Laboratoire de Mécanique des Solides are gratefully acknowledged.*

References

- [1] Liu Z, Zhang X, Mao Y, Zhu YY, Yang Z, Chan CT, Sheng P. Locally Resonant Sonic Materials. *Science*. 2000;289(5485): 1734-1736.
- [2] Tan KT, Huang HH, Sun CT. Blast-wave impact mitigation using negative effective mass density concept of elastic metamaterials. *Int. J. Impact Eng.* 2014;64: 20-29.
- [3] D'Alessandro L, Belloni E, D'Alo G, Daniel L., Ardito R, Corigliano A, Braghin F. Modelling and experimental verification of a single phase three-dimensional lightweight locally resonant elastic metamaterial with complete low frequency bandgap. In: *11th International Congress on Engineered Material Platforms for Novel Wave Phenomena, Metamaterials 2017*. IEEE: 2017. p.70-77.
- [4] Briccola D, Ortiz M, Pandolfi A. Experimental Validation of Metaconcrete Blast Mitigation Properties. *J. Appl. Mech.* 2016;84(3): 031001.
- [5] Comi C, Driemeier L. Metamaterials for crashworthiness of small cars. In: Ascione L, Berardi V, Feo L, Fraternali F, Tralli AM. (eds.) *AIMETA 2017 - Proceedings of the 23rd*

- Conference of the Italian Association of Theoretical and Applied Mechanics*. 2017. p.2119-2129.
- [6] Huang HH, Sun CT, Huang GL. On the negative effective mass density in acoustic metamaterials. *Int. J. Eng. Sci.* 2009; 47(4): 610-617.
- [7] Li X, Chen Y, Barnhart MV, Xu X, Huang G. Tailoring vibration suppression bands with hierarchical metamaterials containing local resonators. *J. Sound Vib.* 2018;442: 237-248.
- [8] Liu Z, Chan CT, Sheng P. Analytic model of phononic crystals with local resonances. *Phys. Rev. B - Condens. Matter Mater. Phys.* 2005;71(1): 1-8.
- [9] Zhou X, Hu G. Analytic model of elastic metamaterials with local resonances. *Phys. Rev. B - Condens. Matter Mater. Phys.* 2009;79(19): 1-9.
- [10] Auriault JL, Bonnet G. Dynamique des composites élastiques périodiques. *Arch.Mech.* 1985; 37: 269-284.
- [11] Pham K, Maurel A, Marigo JJ. Two scale homogenization of a row of locally resonant inclusions - the case of anti-plane shear waves. *J. Mech. Phys. Solids.* 2017;106: 80-94.
- [12] Comi C, Marigo JJ. Homogenization approach and Bloch-Floquet theory for band-gap prediction in 2D locally resonant metamaterials. To be published in *Journal of elasticity*. [Preprint] 2019. Available from: doi.org/10.1007/s10659-019-09743-x.
- [13] Allaire G. Homogenization and two-scale convergence. *Siam J. Math. Anal.* 1992;23(6): 1482-1518.
- [14] Åberg M, Gudmundson P. The usage of standard finite element codes for computation of dispersion relations in materials with periodic microstructure. *J. Acoust. Soc. Am.* 1997;102(4): 2007-2013.
- [15] Comi C, Driemeier L. Wave propagation in cellular locally resonant metamaterials. *Lat. Am. J. Solids Struct.* 2018;15(4): 1-15.
- [16] Kittel C. *Elementary solid state physics: a short course*. New York: Wiley; 1962.
- [17] Phani AS, Woodhouse J, Fleck NA. Wave propagation in two-dimensional periodic lattices. *J. Acoust. Soc. Am.* 2006;119(4): 1995-2005.

PROBING OF POLYCRYSTALLINE MAGNESIUM AT ULTRASONIC FREQUENCIES BY MECHANICAL SPECTROSCOPY

V.V. Kaminskii*, Y.V. Lyubimova, A.E. Romanov

ITMO University, Kronverkskiy pr. 49, St. Petersburg, 197101, Russia

*e-mail: vvkaminskii@itmo.ru

Abstract. In the present work, using the method of a composite piezoelectric oscillator at a frequency of 99-102 kHz, polycrystalline magnesium was studied under two types of treatment: deformation and subsequent annealing. The influence of these types of treatments on changes in the dislocation density and such an important structurally sensitive parameter as the dynamic Young's modulus has been established. The values of micro-yield stress are determined. With a longitudinal deformation of 1.7%, at the strain amplitude of 5×10^{-6} , its value decreased from 2.9 MPa to 1.7 MPa; after annealing at 400 °C, it increased to 5.8 MPa.

Keywords: Magnesium, mechanical spectroscopy, dislocation density, Young's modulus, internal friction, microplastic deformation

1. Introduction

Magnesium (Mg) and alloys based on it are widely used in the aerospace industry, shipbuilding and mechanical engineering due to its low weight, specific strength and environmental friendliness [1,2]. The low density of magnesium alloys has motivated the development of structural Mg alloys for automobiles and aerial vehicle, where weight reduction is needed to achieve high fuel efficiency [3]. In recent years, there has been a surge of interest in magnesium and its alloys as revolutionary materials for biomedical applications [4]. However, the poor plastic properties of Mg-based materials limit their applications [5]. At present, the development of new and improvement of existing Mg-based alloys does not stop [6,7,8]. For example, in 2001, rapidly solidified Mg–Zn–Y alloys were found to have excellent mechanical properties, including maximum tensile yield strength of ~600 MPa and elongation of ~5% at room temperature [7,8].

One of significant aspects of the properties of structural alloys is the study of the influence of microdeformations. Multiple microdeformations during the operation of the material lead to fatigue, wear, the formation of microcracks, and finally the fracture of samples or constructions [9]. The formation of new dislocations in the structure of the material lead to increase of internal stresses, which are the main reason for the degradation of materials strength properties. Knowledge of changes in the density of dislocations can be very useful in the practical applications due to the direct connection of this change with the fracture and wear of materials [10]. In this paper, we present the results of investigation of elastic and anelastic properties of pure polycrystalline magnesium using mechanical spectroscopy. The aim of our work is to study the changes in such a structurally sensitive parameter as the dynamic Young's modulus (YM) and mechanical damping or internal friction (IF) under deformation and annealing of magnesium.

2. Method and samples

Polycrystalline magnesium samples with purity 99.99% in the shape of rectangular bars with characteristic dimensions of 2.5x2.5x24.5 mm were fabricated by casting. To study the microplastic behavior, the samples were passed through three processing steps: i) 1.7% longitudinal deformation carried out using a press ii) annealing at 200°C in vacuum iii) annealing at 400°C in vacuum. The measurements were taken before these processing steps and after each of them. The grain size in the experimental samples remained in the range from 10 to 100 μm .

All measurements were conducted using the composite piezoelectric oscillator technique at a oscillatory frequency about 100 kHz [11]. The size of the samples was specially selected to ensure resonance of longitudinal oscillation. The temperature range used in the experiments was from 80 to 300 K. The low temperature range is optimal for studying dislocation motions since the contribution of thermal vibrations of the lattice decreases. In this range, the temperature dependencies of oscillation frequency and the IF were measured in the sample at a fixed oscillatory strain amplitude 10^{-5} . Along with this, the amplitude dependence of IF was recorded at different temperatures and oscillation frequencies at constant temperature. Young's modulus was determined using the resonant frequency of the sample:

$$E = 4\rho l^2 f^2, \quad (1)$$

where f is oscillatory frequency, ρ is density of magnesium, l is length of the sample.

The frequency change in these experiments was approximately in 99-102 kHz range. Internal friction was determined by the change in voltage on the quartz transducer [11].

3. Results

Figure 1 shows the temperature dependencies of YM and IF as a result of heating; in general, there is a tendency for YM and IF to decrease with increasing temperature. The dependencies of internal friction at low temperatures after deformation and after annealing at 200°C show the formation of a Bordoni relaxation peak close to 80 K [10], Fig. 1b. The value of Young's modulus over the entire range decreases by about 1.5%, as it is shown in Fig. 1a. To verify the adequacy of the obtained Young's modulus values, we used the traditional method of estimation of the elastic constants for polycrystals by Voigt – Reuss – Hill averaging [13]. Room temperature Young's modulus found with such averaging for magnesium is 43.2 GPa, which is close to our values determined before deformation and after annealing. Therefore, this indicates on the isotropy of the investigated Mg polycrystalline samples, which also means that the effects of texturing can be neglected [13].

Figure 2 demonstrates temperature spectra of IF on cooling and subsequent heating before deformation. The amplitude dependencies were measured during cooling at fixed temperatures, Fig. 3, and during heating the continuous temperature spectra were obtained (Fig. 1b). Places where the data for amplitude dependencies were taken can be seen from the curve discontinuities during the cooling processes, see Fig. 2. It also important to note, that after each event of measuring amplitude dependence (Fig. 3) the level of IF sharply increases (Fig. 2), which may be associated with an increase in the density of dislocations after each act of loading. The heating process does not lead to stress relaxation, and the heating curve goes higher than spectrum for cooling.

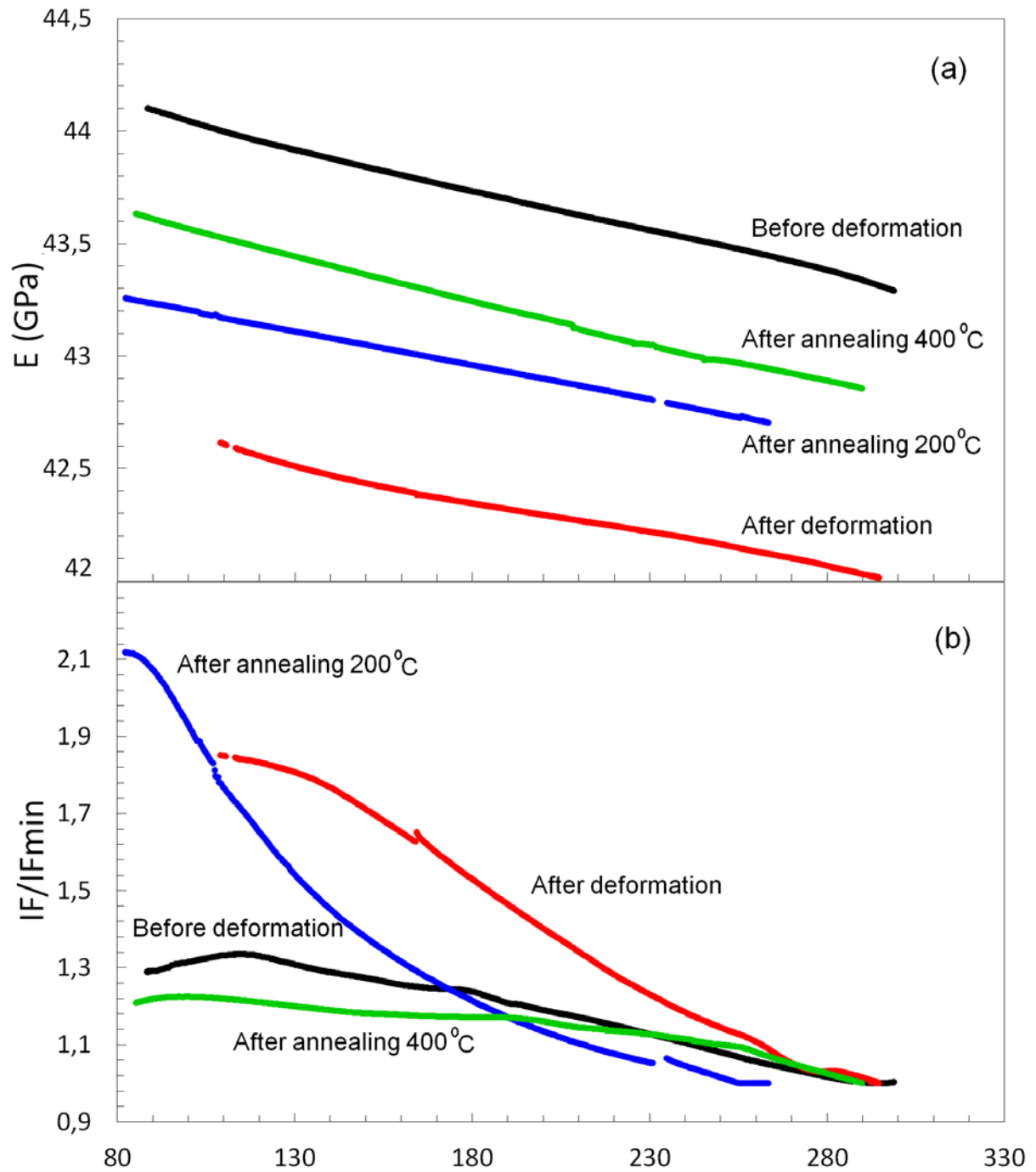


Fig. 1. Temperature dependencies of the dynamic Young's modulus (a) and normalized internal friction (b) for differently treated samples: — before deformation, — after deformation, — after annealing 200°C, — after annealing 400°C; oscillatory strain amplitude is 10^{-5}

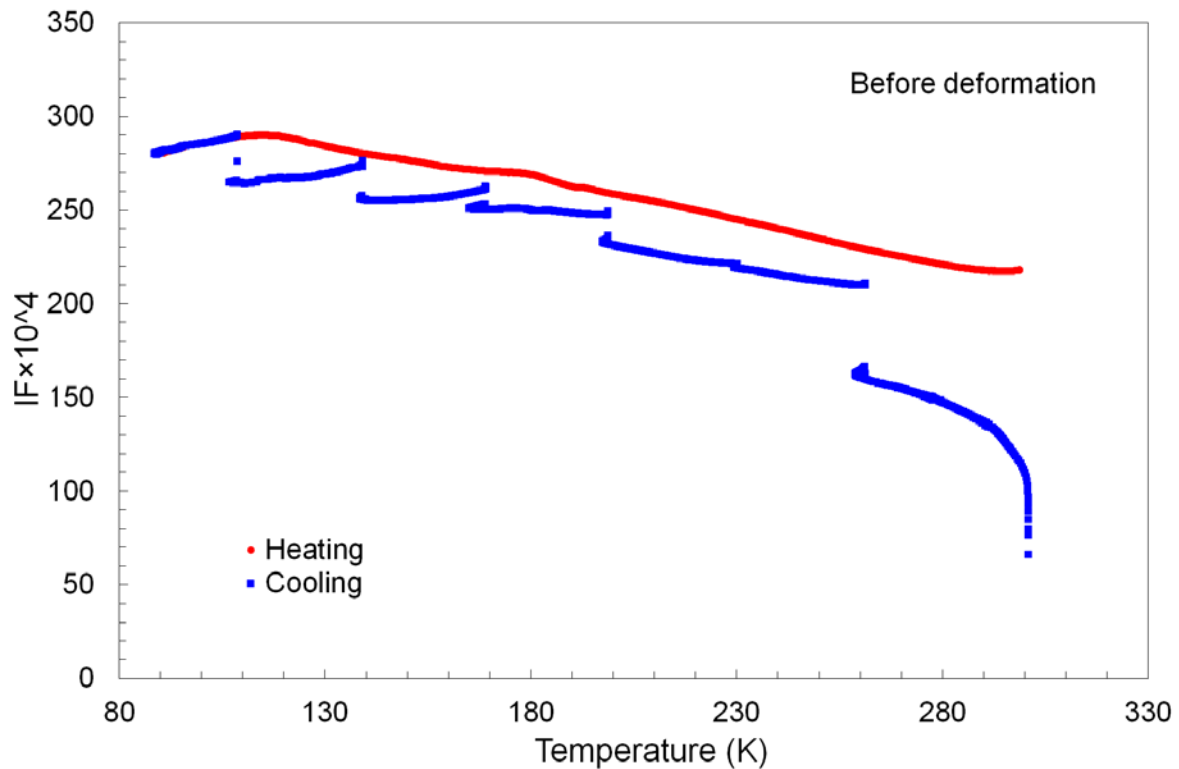


Fig. 2. Temperature dependence of internal friction in the cooling-heating cycle before deformation: — heating; — cooling; oscillatory strain amplitude is 10^{-5}

Figure 3 shows the amplitude dependences of the internal friction at various temperatures divided into 3 groups. For the first group the measurements were conducted before deformation of the sample, for the second – after deformation, and for the third – after deformation and deep annealing. Each individual curve consists of two parts: amplitude-independent internal friction (AIIF), where a change of the oscillatory strain amplitude is not accompanied by a change in the IF, (up to about 10^{-7}) and amplitude-dependent internal friction (ADIF), where a change in the strain amplitude is accompanied by a sharp change in internal friction (after about 10^{-7}) [14]. The amplitude dependences before deformation and after deep annealing are characterized by a pronounced increase in ADIF. At the same time, one can notice an increase in the hysteresis value (the difference between the forward and backward running) for these curves.

Our measurements also allowed us to evaluate the mechanical (or microplastic) properties of magnesium using stress – strain diagram. We explored the algorithm to calculate microplastic deformation as it was proposed in [15]. To estimate the contribution of microplastic deformation, we plotted the dependence of microplastic deformation versus anelastic strain amplitude for three cases: before deformation; after deformation and after deep annealing, Fig. 4.

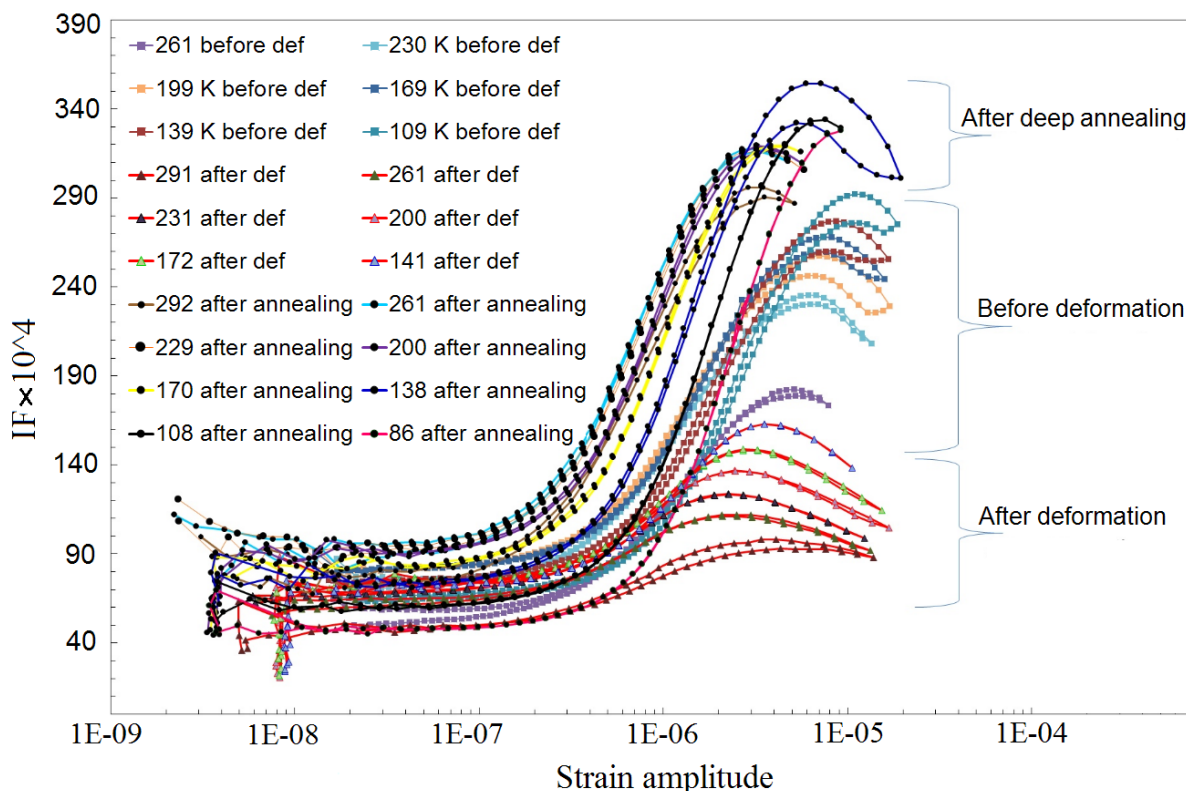


Fig. 3. Internal friction as function of the oscillatory strain amplitude at different fixed temperatures under different treatments of polycrystalline magnesium: before deformation; after deformation; after deep annealing

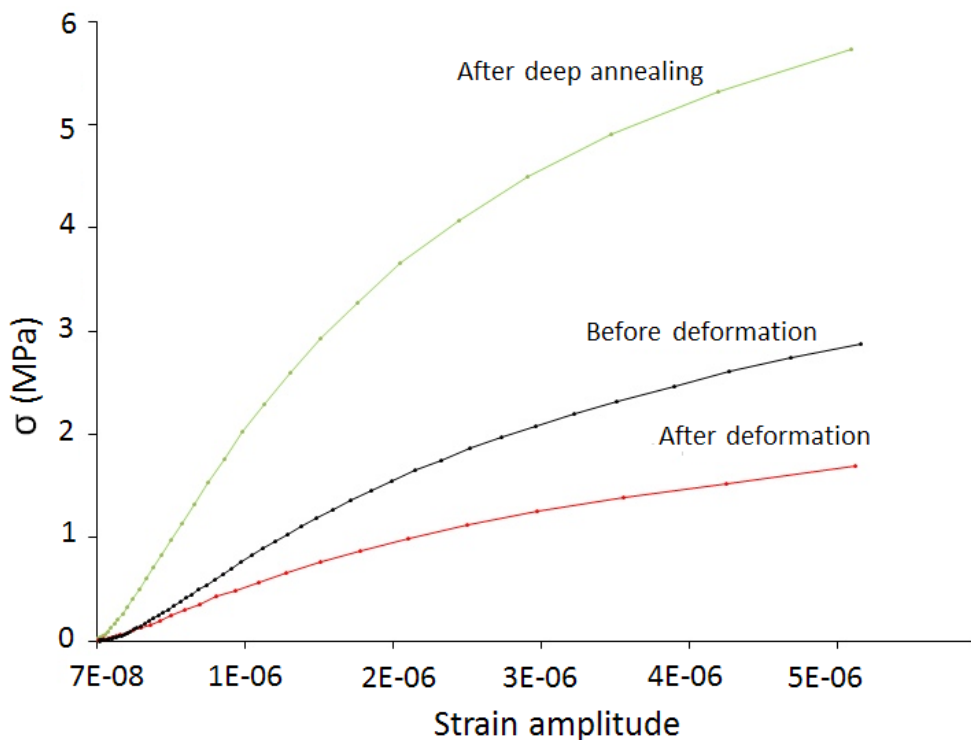


Fig. 4. Microplastic deformation diagram for different treatments of magnesium polycrystal: — before deformation; — after deformation; — after deep annealing

4. Discussion

A change in the dislocation density of the material directly affects such important structurally sensitive parameters as the dynamic Young's modulus and mechanical damping: plastic deformation produces additional (fresh) dislocations and results in YM decreasing and the increasing of IF. This effect was previously observed on numerous crystalline materials [12,13,16]. In this paper we show that the reduction of Young's modulus after deformation of 1.7% is accompanied by a thermally activated Bordoni peak, as it follows from Fig. 1. The basis of this relaxation process is the formation and movement of thermal or geometric kinks at edge, screw and mixed dislocations [17]. The changes in the elastic modulus under different treatment are clearly seen in Fig. 1a. A drop in YM during deformation is caused by a raise of the dislocation density in the material. After annealing the structure relaxes and this process is accompanied by a decrease in the dislocation density and in the height of the Bordoni peak until its complete disappearance, and at the same time in a raise in the Young's modulus, see Fig. 1. The dynamic elastic modulus clearly raises with the annealing temperature increase; this can be explained by the diffusion of point defects to dislocations hindering their movement and annealing of the dislocations themselves [18,19]. It is also worth noting the recovery of the curvature of the elastic modulus graph, Fig. 1a, after annealing at 400°C; this indirectly reflects the state of equilibrium of the structure [11]. Investigation of amplitude dependences of IF after different treatments of magnesium is a clear evidence of a change in the dislocation structure, Fig. 3. These ADIF dependences relate on the formation of the microplastic regions, in which the damping raises as a consequence of dislocation multiplication [13]. The motion of dislocations in some cases is controlled by point defects [18,19]. Figure 3 shows that the deformation of the sample is accompanied by a sharp drop of the amplitude-dependent part of IF and appearance of strain hysteresis, which is connected with partial blocking of the dislocation movement. The magnitude of microplastic deformation at various amplitudes can be seen from Fig. 4. An increase in the dislocation density leads to blocking the propagation of dislocations, thereby reducing the magnitude of microplastic deformation. With a strain amplitude about 5×10^{-6} the values of micro-yield stress drop from 2.9 MPa to 1.7 MPa, and after annealing it increases by more than 3 times reaching the level of 5.8 MPa.

5. Conclusions

We studied the evolution of dislocation density of a polycrystalline magnesium under plastic deformation and annealing by mechanical spectroscopy at a frequency about 100 kHz. It was found that micro-yield stress caused by the movement of dislocations is reduced by 1.2 MPa at a strain amplitude of 5×10^{-6} after longitudinal sample deformation of 1.7% due to the increased dislocation density inside the polycrystal. After annealing the value of micro-yield stress increased by more than 3 times, which indicates a decrease in stresses inside the structure due to both the diffusion of point defects to dislocations and the annealing of the dislocations themselves. At the same time these processes are confirmed by a pronounced changes in the dynamic elastic modulus.

Acknowledgments. This work was supported by the Ministry of Science and Higher Education of the Russian Federation, goszadanie No. 3.1421.2017/4.6.

References

- [1] Pollock TM. Weight loss with magnesium alloys. *Science*. 2010;328(5981): 986-987.
- [2] Kramar V, Dushko V, Rodkina A, Zaiets A. Influence of stress-corrosion fractures on potential of ship-building. *Metals in the Sea Water Engineering*. 2015;100: 1068-1074.

- [3] Das S. Magnesium for automotive applications: Primary production cost assessment. *JOM*. 2003;55(11): 22.
- [4] Vinogradov A, Vasilev E, Kopylov V, Linderov M, Brilevesky A, Merson D. High performance fine-grained biodegradable Mg-Zn-Ca alloys processed by severe plastic deformation *Metals*. 2019;9(2): 186.
- [5] Agnew SR, Duygulu O. Plastic anisotropy and the role of non-basal slip in magnesium alloy AZ31B. *Intern. J. Plasticity*. 2005;21(6): 1161-1193.
- [6] Suzuki A, Saddock ND, Jones JW, Pollock TM. Solidification paths and eutectic intermetallic phases in Mg–Al–Ca ternary alloys. *Acta Mater*. 2005;53(9): 2823-2834.
- [7] Kawamura Y, Hayashi K, Inoue A, Masumoto T. Rapidly solidified powder metallurgy Mg₉₇Zn₁Y₂ alloys with excellent tensile yield strength above 600 MPa. *Mater. Trans*. 2001;42(7): 1172-1176.
- [8] Inoue A, Kawamura Y, Matsushita M, Hayashi K, Koike J. Novel hexagonal structure and ultrahigh strength of magnesium solid solution in the Mg–Zn–Y system. *Mater. Res*. 2001;16(7): 894-1900.
- [9] Zerbst U, Klinger C. Material defects as cause for the fatigue failure of metallic components. *International Journal of Fatigue*. 2019;127: 312-323.
- [10] Zhang S, Tian S, Yu H, Tian N. Deformation and damage behaviors of as-cast TiAl-Nb alloy during creep. *Progress in Natural Science: Materials International*. 2018;28(5): 618-625.
- [11] Kustov S, Golyabdin S, Ichino A, Gremaud G. A new design of automated piezoelectric composite oscillator technique. *Materials Science and Engineering A*. 2006;442(1): 532-537.
- [12] Tsui RTC, Sack HS. Internal friction and transmission electron microscopy studies of magnesium. *Acta Metallurgica*. 1967;15(11): 1715-1722.
- [13] Pal-Val PP, Loginov YN, Demakov SL. Unusual Young's modulus behavior in ultrafine-grained and microcrystalline copper wires caused by texture changes during processing and annealing. *Materials Science & Engineering A*. 2014;618: 9-15.
- [14] Sapozhnikov KV, Golyandin SN, Kustov SV. Temperature dependence of the internal friction of polycrystalline indium. *Physics of the Solid State*. 2010;52(12): 2501-2509.
- [15] Moskalenko VA, Betekhtin VI, Kardashev BK, Kadomtsev AG, Smirnov AR, Smolyanets RV, Narykova MV. Mechanical properties and structural features of nanocrystalline titanium produced by cryorolling. *Physics of the Solid State*. 2014;56(8): 1590-1596.
- [16] Lebedev AB. Internal friction in the process of quasistatic deformation of crystals. *Solid State Physics*. 1993;35(9): 2305-2341.
- [17] Blanter MS, Golovin IS, Neuhäuser H, Sinning HR. *Internal friction in metallic materials*. Springer; 2012.
- [18] Indenbom VL, Chernov VM. Thermally activated glide of a dislocation in a point defect field. In: Indenbom VL, Lothe J. (eds.) *Elastic strain fields and dislocation mobility*. Amsterdam: North-Holland; 1992. p.517-570.
- [19] Gremaud G. Dislocation - point defect interactions. *Mater. Sci. Forum*. 2001;366-368: 178-246.

INTERACTION OF IMPURITY ATOMS OF LIGHT ELEMENTS WITH VACANCIES AND VACANCY CLUSTERS IN FCC METALS

G.M. Poletaev^{1*}, I.V. Zorya², R.Y. Rakitin³, M.A. Iliina⁴, M.D. Starostenkov¹

¹Altai State Technical University, Lenin Str. 46, 656038 Barnaul, Russia

²Siberian State Industrial University, Kirova Str. 42, 654007 Novokuznetsk, Russia

³Altai State University, Lenin Str. 61, 656049 Barnaul, Russia

⁴Financial University under the Government of the Russian Federation, Lenin Str. 54, 656036 Barnaul, Russia

*e-mail: gmpoletaev@mail.ru

Abstract. The interaction of impurity atoms of light elements C, N, O with vacancies and vacancy clusters in fcc metals Ni, Ag and Al was studied by the molecular dynamics method. The binding energies of impurity atoms with vacancies, divacancies and stacking fault tetrahedron (SFT) are calculated. It is shown that the impurity atom in a vacancy is not located at its center, but is displaced relative to it in the direction of the $\langle 100 \rangle$ type. The changes in the activation energy of vacancy migration upon interaction with an impurity atom are calculated. When studying the interaction of impurity atoms with a SFT, it was found that the binding energy of C, N and O atoms for all the considered metals is higher with the SFT edge (i.e. with partial dislocation) than with the top of the SFT.

Keywords: molecular dynamics, metal, vacancy, impurity, binding energy, divacancy, vacancy cluster, stacking fault tetrahedron

1. Introduction

Impurity atoms of light elements (primarily the most common ones: hydrogen, oxygen, nitrogen, carbon) have high chemical activity and already at low concentrations strongly influence on the properties of metals. Being effective stoppers of dislocations and grain boundaries, the impurities of light elements significantly increase the strength, hardness, frictional properties simultaneously, as a rule, with brittleness [1-3]. A high melting temperature and chemical resistance are typical for many interstitial alloys. Despite the importance of understanding the mechanisms and processes underlying the effect of doping light elements on the properties of metals, now there are many questions regarding the behavior of impurities at the atomic level in the metallic matrix. In particular, the questions of interaction at the atomic level of various interstitial impurities with defects in the crystal lattice, especially dislocations and grain boundaries, remain insufficiently studied. In this case, computer simulation is an effective research tool.

This work is devoted to the study using molecular-dynamic modeling of the interaction of impurity atoms of light elements C, N and O with vacancies and vacancy clusters in metals with fcc lattice. As metals, Ni, Ag and Al were chosen. This set of three metals is unique in that two of them have almost the same radii of atoms, while the other two have almost identical electronegativities. The radii of atoms: Al – 1.43 Å, Ag – 1.44 Å, Ni – 1.24 Å [1]. Electronegativity (Pauling scale): Al – 1.61, Ag – 1.93, Ni – 1.91 Å [3]. Thus, when obtaining different dependencies for these three metals, the relationship either with the size of atoms or with electronegativity will be seen.

2. Description of the model

The simulation was performed using the molecular dynamics method. The calculation block of the crystal had the shape of a parallelepiped and contained 8400 atoms. Periodic boundary conditions were used. Interactions of metal atoms with each other were described by the EAM tight-binding Cleri-Rosato potentials [4]. In this case, the energy of the i -th atom is found using expression:

$$U_i = \sum_j A \exp\left(-p\left(\frac{r_{ij}}{r_0} - 1\right)\right) - \sqrt{\sum_j \xi^2 \exp\left(-2q\left(\frac{r_{ij}}{r_0} - 1\right)\right)}. \quad (1)$$

Here A , p , q , ξ , r_0 are the potential parameters; r_{ij} is the distance between the i -th and j -th atoms. The parameters of the Cleri-Rosato potentials were taken from [4].

To describe the interactions of impurity atoms of light elements with metal atoms and impurity atoms with each other the Morse potential was chosen:

$$\varphi(r_{ij}) = D\beta e^{-\alpha r_{ij}} (\beta e^{-\alpha r_{ij}} - 2), \quad (2)$$

where α , β , D are the parameters of the potential. Cleri-Rosato and Morse potentials have proved themselves in numerous calculations performed by the molecular dynamics method [5-8]. Pair potentials are relatively often used by various researchers to describe interatomic interactions in metal-impurity systems. Multi-particle potentials are physically more reasonable, but taking into account the high error of the experimental data on which the potential parameters are selected, as well as the error of the search methods of the parameters themselves, the choice of pair potentials is justified.

The parameters of the potentials for describing the interactions of impurity atoms C, N and O with the metal atoms under consideration were taken from [9], where they were found taking into account empirical dependencies and known characteristics, such as the melting or decomposition temperature of the corresponding chemical compound of a metal with a light element, activation energy of the diffusion of an impurity atom in the crystal lattice of the metal. In [9], to describe the interactions of impurity atoms with each other in metals, the potentials proposed by other authors have been taken as a basis. For the C-C bond, the pair potential from [10] was transformed into Morse potentials. For N-N and O-O bonds, potentials were taken from [11,12].

3. Interaction of impurity atoms with vacancies

The binding energy of an impurity atom with a vacancy E_{bv} was calculated as the difference between the potential energy of a calculation block containing a vacancy and an impurity atom at such a distance from each other, which eliminates their interaction, and the potential energy of a calculation block containing an impurity atom inside a vacancy. In both cases, before the calculation of the energy of the computational block, the structure was relaxed, after which the calculation block was cooled to 0 K.

When conducting structural relaxation of the calculation block containing an impurity atom inside a vacancy, it was observed that the impurity atom in the vacancy is not located at its center, but is displaced relative to it in the direction of the $\langle 100 \rangle$ type. In Table 1, in addition to the binding energy of an impurity with a vacancy, the values of the displacement of the impurity atom δ from the center of the vacancy are shown (Fig. 1).

In the literature there is very little information on the binding energy of light-element atoms with defects of the crystal lattice of metals. For fcc metals, we found only the binding energy of a carbon atom with a vacancy in γ -Fe: 0.67 eV [13] and 0.37–0.41 eV [14]. In [14], this quantity was found experimentally and with the help of ab-initio calculations; in [13] – only by the calculations. Of the metals under consideration, the characteristics of γ -Fe are closest to Ni (atomic radii: 1.29 Å (γ -Fe) and 1.24 Å (Ni); differences of electronegativities

with carbon: 0.72 (Fe) and 0.64 (Ni)). The binding energy of a carbon atom with a vacancy in nickel, found in our model, turned out to be 0.70 eV, which is close to the values in [13].

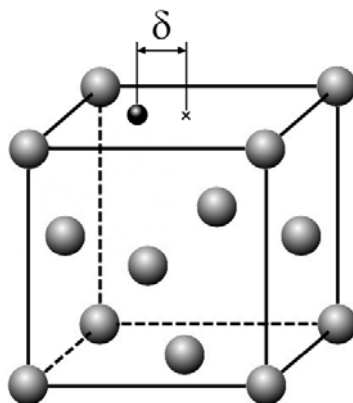


Fig. 1. The displacement of the impurity atom δ from the vacancy center (the vacancy center is marked with a cross)

Table 1. The binding energy of an impurity atom with a vacancy (eV)

	C		N		O	
	E_{bv}	δ (Å)	E_{bv}	δ (Å)	E_{bv}	δ (Å)
Ni	0.70	0.44	0.39	0.68	-0.05	0.80
Ag	0.05	1.03	-0.25	1.24	-0.59	1.97
Al	0.86	0.95	0.14	1.00	-0.58	1.05

According to the data obtained in the work, the binding energy of impurity atoms with a vacancy is not always positive. For example, negative values were obtained for the oxygen atom for all three considered metals. This means that between a vacancy and an impurity oxygen atom there must be a kind of repulsion, their combination is energetically unfavorable. The largest values of the binding energy with a vacancy are obtained for a carbon atom in Ni and Al, which is apparently related to the largest size of carbon atoms among considered impurities. The smallest values of the binding energy and at the same time the largest displacements of impurity atoms from the center of the vacancy δ were obtained for Ag. In this case, impurity atoms are shifted almost to the position of the neighboring octahedral pore.

Thus, vacancies are a "trap" mainly for relatively large impurity atoms, for example, carbon. For atoms of small size, such as, for example, oxygen, combining with vacancies is energetically not beneficial.

In this work, we also investigated the effect of impurity atoms on the diffusion of vacancies in the metals under consideration. The migration energy of a vacancy was determined by the magnitude of the energy barrier in the migration path of the defect. In addition to the migration of a "pure" vacancy, the migration energies of a vacancy in the presence of an impurity atom in it were calculated. To obtain each point on the graph of the change in the energy of the calculation block, the structure was relaxed, during which the displaced atom, adjacent to the vacancy, remained stationary. Figure 2 shows the dependences of the change in the energy of the calculation block ΔU on the displacement Δr of an atom adjacent to a vacancy in the case of the vacancy without impurity (graph 1) and with an impurity carbon atom (graph 2).

The graphs obtained for a vacancy with an impurity carbon atom, as can be seen from Fig. 2, asymmetric, in contrast to the graphs for vacancies without impurities. Nevertheless, the extremum is distinct and it is possible to estimate the activation energy of vacancy

migration with its separation from the impurity atom. It should be noted that the peak at the 2nd dependence in Fig. 2 is located to the right of the peak for the "pure" vacancy in the case of Ni and to the left in the case of Al.

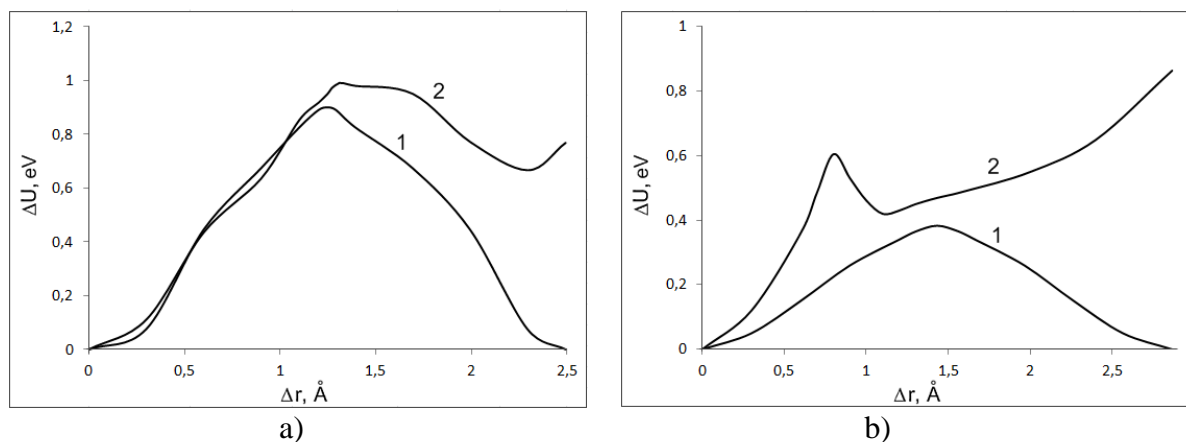


Fig. 2. The change in the energy of the calculation block when an atom adjacent to a vacancy moves to its place: a) in Ni, b) in Al. 1 – in pure metal. 2 – in the case of the presence of an impurity carbon atom in the vacancy

Table 2 shows the values obtained in the present work for the migration energy of a vacancy with and without impurities. These values are obtained for the "separation" of vacancies from impurities, not for the case of joint movement of vacancies and impurities. For joint migration of vacancy and impurity, it is necessary to implement an additional mechanism consisting in the exchange of places of the metal atom and impurity atom adjacent to the vacancy.

Table 2. The migration energy of a vacancy with and without an impurity atom (eV)

	without impurity	C	N	O
Ni	0.90	0.99	0.78	0.52
Ag	0.91	0.81	0.74	0.87
Al	0.38	0.60	0.61	0.26

The obtained values of the migration energy of a vacancy in a pure metal are in satisfactory agreement with the data of other authors. For example, for Ni, values in the range of 0.9–1.1 eV are given in [15,16] and 0.4–0.6 eV for Al.

The effect of impurities on the diffusion mobility of a vacancy is consistent with the previously mentioned binding energies of impurity atoms with a vacancy (Table 1). As can be seen from the Table 2, carbon atoms, having a positive binding energy, inhibit the diffusion of vacancies in Ni and especially in Al. In this case, due to the much higher mobility of vacancies compared to the mobility of impurity atoms [1,9], it seems more correct to say that impurity atoms are a "trap" for vacancies, and not vice versa. Oxygen atoms, on the contrary, "accelerate" the migration of vacancies, reducing their activation energy due to the negative binding energy of oxygen atoms with a vacancy. Nitrogen for different metals has a different effect on the migration of vacancies: it reduces the energy of migration in the case of Ni and Ag and increases it in the case of Al.

4. Interaction of impurity atoms with divacancies and stacking fault tetrahedron

Along with the vacancy mechanism, the contribution to diffusion in crystals is made by the migration of divacancies (bivacancies) – doubled vacancies [15,17]. Even in equilibrium

conditions in crystals there is a small concentration of them (as a rule, approximately two orders of magnitude lower than the concentration of monovacancies). Divacancies are unique in that they are the most mobile among vacancy clusters. In [17], using the molecular dynamics method, the activation energies of divacancy migration were found: 0.23 eV in Ni, 0.18 eV in Ag, and 0.09 eV in Al. As can be seen, these values are several times lower than the energies of monovacancy migration (Table 2). With an increase in the number of vacancies in a cluster, its mobility sharply reduced. The next cluster, trivacancy, has a much lower mobility than mono- and, especially, divacancy [15].

Table 3 shows the binding energy of impurity atoms with divacancies in the metals under consideration. It should be noted that they are close to the values for monovacancies, differing, as a rule, only by the second decimal place. In accordance with these values, as for monovacancies, the influence of impurity atoms on the diffusion mobility of divacancies should be expected.

Table 3. The binding energy of an impurity atom with a divacancy (eV)

	C	N	O
Ni	0.76	0.50	0.02
Ag	0.06	-0.23	-0.57
Al	0.89	0.22	-0.28

The role of point defects is not limited to diffusion. With their high concentration in materials, they have a significant impact on the strength properties. Nonequilibrium high concentrations of point defects are formed as a result of rapid cooling from high temperatures, plastic deformation and radiation damage [15,18].

In addition to the defects mentioned above, of interest are unique vacancy clusters in fcc crystals – stacking fault tetrahedrons (SFT). At present, it is reliably established that small vacancy clusters in fcc metals are mainly stacking fault tetrahedrons [19,20]. The faces of the stacking fault tetrahedron (Fig. 3) are oriented along the (111) planes and are stacking faults, and the edges are oriented along the $\langle 110 \rangle$ directions and are partial dislocations with the $1/6\langle 110 \rangle$ Burgers vector [19]. SFTs are formed in all fcc metals, but their critical size, at which the vacancy disks become energetically more advantageous, depends to a large extent on the formation energy of the stacking fault in a given metal [21]. SFTs are formed as a result of radiation damage, rapid cooling from high temperatures, plastic deformation.

In the molecular dynamics model, SFTs were created by introducing "triangular vacancy disks" (Fig. 3a). To do this, atoms were removed from the region having the shape of an equilateral triangle in the close-packed atomic (111) plane. For the formation of a SFT from such a "vacancy disk", additional thermal activation was not required. The mechanism of the "triangular vacancy disks" in the (111) plane to the SFT consisted in successively displacing (settling) of groups of atoms in the form of equilateral triangles from the planes parallel to the "vacancy disk" plane toward it (Fig. 3a). Because of the peculiarities of the fcc lattice, the sizes of the shifting groups of atoms of a triangular shape were successively decreased, as a result of which the free volume of the initial "vacancy disk" propagated into the tetrahedral region of the crystal and evenly distributed over the edges of the SFT (Fig. 3b). In Figure 3b it was used the visualizator of excess free volume, i.e. free volume over that which is characteristic of a pure crystal. It can be seen, for example, that inside the SFT itself, the structure corresponds to the structure of an ideal crystal, and all the excess free volume is concentrated on the edges of the SFT, which, as already mentioned, are partial dislocations. The faces of a SFT are stacking faults and contain almost as much free volume as an ideal crystal.

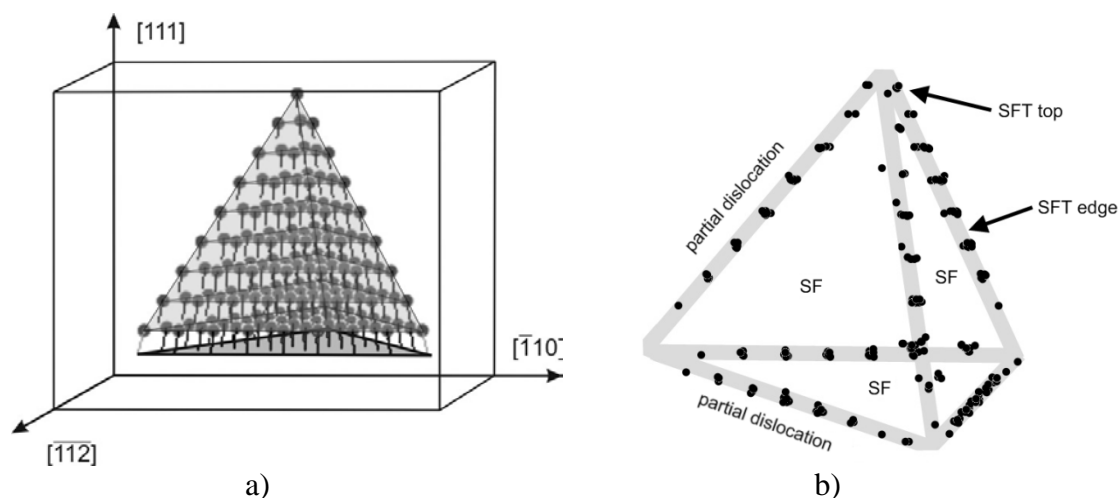


Fig. 3. Stacking fault tetrahedron in the molecular dynamic model: a) creation of a SFT from a "triangular vacancy disk" (displacements of atoms in the process of structural relaxation are shown by segments); b) the distribution of excess free volume in the SFT

Impurity atoms were introduced in two positions: at the top and edge of the SFT. The values obtained are shown in Table 4. As can be seen from the table, the binding energy of C, N and O atoms for all metals turned out to be higher with the edge of the SFT (i.e. with $1/6\langle 110 \rangle$ partial dislocation) than with the top. In addition, in all cases the binding energies are positive, which indicates the attraction of impurities by such dislocations. The highest binding energy is obtained for a carbon atom with a SFT edge in Al – 1.40 eV. Such a high value of the binding energy speaks in favor of a relatively strong bond of carbon atoms with dislocations of this type. The lowest binding energies are obtained for Ag, which is apparently due to two factors simultaneously: a relatively large lattice parameter and not deep interaction potentials of impurity atoms with metal atoms. As in the cases of vacancies and divacancies, the lowest values of the binding energy are obtained for oxygen.

Table 4. The binding energy of an impurity atom with a top and edge of SFT (eV)

	C		N		O	
	top	edge	top	edge	top	edge
Ni	0.64	0.77	0.49	0.72	0.27	0.62
Ag	0.10	0.30	-0.03	0.15	-0.34	0.01
Al	0.80	1.40	0.24	0.88	-0.11	0.44

5. Conclusion

The interaction of impurity atoms of light elements C, N, O with vacancies and vacancy clusters in fcc metals Ni, Ag and Al was studied by the molecular dynamics method. The binding energies of impurity atoms with vacancies, divacancies and stacking fault tetrahedron (SFT) are calculated. It is shown that the impurity atom in a vacancy is not located at its center, but is displaced relative to it in the direction of the $\langle 100 \rangle$ type. According to data obtained, vacancies are a "trap" mainly for relatively large impurity atoms, for example, carbon. For atoms of small size, such as, for example, oxygen, combining with vacancies is energetically not beneficial. The changes in the activation energy of vacancy migration upon interaction with an impurity atom are calculated. It is shown that at the positive binding energy of an impurity atom and a vacancy, they inhibit the migration of each other during the interaction. When studying the interaction of impurity atoms with a SFT, it was found that the binding energy of C, N and O atoms for all the considered metals is higher with the SFT edge (i.e. with partial dislocation) than with the top of the SFT.

Acknowledgements. No external funding was received for this study.

References

- [1] Goldschmidt HJ. *Interstitial Alloys*. London: Butterworths; 1967.
- [2] Toth LE. *Transition metal carbides and nitrides*. New York: Academic Press; 1971.
- [3] Pauling L. *The Nature of the Chemical Bond. Third Edition*. Ithaca: Cornell University Press; 1960.
- [4] Cleri F, Rosato V. Tight-binding potentials for transition metals and alloys. *Physical Review B*. 1993;48(1): 22-33.
- [5] Poletaev GM, Zorya IV, Starostenkov MD, Rakitin RYu, Tabakov PYa. Molecular dynamics simulation of the migration of tilt grain boundaries in Ni and Ni₃Al. *Journal of Experimental and Theoretical Physics*. 2019;128(1): 88-93.
- [6] Poletaev G, Zorya I, Rakitin R. Molecular dynamics study of migration mechanism of triple junctions of tilt boundaries in fcc metals. *Computational Materials Science*. 2018;148: 184-189.
- [7] Poletaev GM, Zorya IV, Novoselova DV, Starostenkov MD. Molecular dynamics simulation of hydrogen atom diffusion in crystal lattice of fcc metals. *International Journal of Materials Research*. 2017;108(10): 785-790.
- [8] Poletaev GM, Zorya IV, Medvedeva ES, Novoselova DV, Starostenkov MD. The study of the interaction of hydrogen impurity with point and linear defects in palladium and nickel. *Materials Physics and Mechanics*. 2017;32(2): 117-122.
- [9] Zorya IV, Poletaev GM, Starostenkov MD. Impurity atoms of light elements in metal crystals: a molecular dynamics simulation. *Fundamentalnye problemy sovremennogo materialovedeniya*. 2018;15(4): 526-532. (In Russian)
- [10] Ruda M, Farkas D, Garcia G. Atomistic simulations in the Fe–C system. *Computational Materials Science*. 2009;45: 550-560.
- [11] Vashishta P, Kalia RK, Nakano A, Rino JP. Interaction potentials for alumina and molecular dynamics simulations of amorphous and liquid alumina. *Journal of Applied Physics*. 2008;103(8): 083504.
- [12] San Miguel MA, Sanz JF. Molecular-dynamics simulations of liquid aluminum oxide. *Physical Review B*. 1998;58(5): 2369-2371.
- [13] Lee BJ. A modified embedded-atom method interatomic potential for the Fe–C system. *Acta Materialia*. 2006;54(3): 701-711.
- [14] Slane JA, Wolverton C, Gibala R. Experimental and theoretical evidence for carbon-vacancy binding in austenite. *Metallurgical and Materials Transactions A*. 2004;35(8): 2239-2245.
- [15] Wollenberger HJ. Point defects. In: Cahn RW. (ed.) *Physical Metallurgy. Vol. 3: Physicomechanical Properties of Metals and Alloys*. Moscow: Mir; 1987. p.5-74. (In Russian)
- [16] Orlov AN, Trushin YV. *Energies of point defects in metals*. Moscow: Energoatomizdat; 1983. (In Russian)
- [17] Poletaev GM, Starostenkov MD. Contributions of different mechanisms of self-diffusion in face-centered cubic metals under equilibrium conditions. *Physics of the Solid State*. 2010;52(6): 1146-1154.
- [18] Zolnikov KP, Korchuganov AV, Kryzhevich DS. Anisotropy of plasticity and structural transformations under uniaxial tension of iron crystallites. *Computational Materials Science*. 2018;155: 312-319.
- [19] Matsukawa Y, Zinkle SJ. Dynamic observation of the collapse process of a stacking fault tetrahedron by moving dislocations. *Journal of Nuclear Materials*. 2004;329-333: 919-923.

- [20] Rodney D, Martin G, Brechet Y. Irradiation hardening by interstitial loops: atomistic study and micromechanical model. *Materials Science and Engineering*. 2001;309-310: 198-202.
- [21] Kiritani M, Satoh Y, Kizuka Y, Arakawa K, Ogasawara Y, Arai S, Shimomura Y. Anomalous production of vacancy clusters and the possibility of plastic deformation of crystalline metals without dislocations. *Philosophical Magazine Letters*. 1999;79(10): 797-804.

DEPOSITION KINETICS AND BOUNDARY LAYER THEORY IN THE CHEMICAL VAPOR DEPOSITION OF β -SiC ON THE SURFACE OF C/C COMPOSITE

H. Aghajani^{1*}, N. Hosseini¹, B. Mirzakhani²

¹Department of Materials Engineering, University of Tabriz, Tabriz, Iran

²Faculty of Engineering, Arak University, Arak, Iran

*e-mail: h_aghajani@tabrizu.ac.ir

Abstract. In this study, SiC was deposited on carbon/carbon (C/C) composite substrate using chemical vapor deposition (CVD) method to investigate the kinetics of the deposition process. Therefore, the time, temperature, precursor composition ($\text{SiCl}_4\text{:N}_2\text{:CH}_4$) and substrate position in the reactor were varied to evaluate the deposition rate. X-ray diffraction (XRD) method was used to characterize the phase composition and calculate the grain size and the texture coefficient of the coatings. Field emission scanning electron microscopy (FESEM) was utilized to observe the coating morphology, microstructure and thickness. As observed β -SiC was the dominant phase of the coating with varied preferred growth crystalline planes of (111), (220) or (311). The coating thickness was 2 μm and 5 μm for the samples treated at 1000 and 1100°C, respectively.

Keywords: chemical vapor deposition, boundary layer, deposition rate, SiC coating, C/C composite

1. Introduction

Carbon/carbon (C/C) composites have recently attracted much interest due to their unique physical, mechanical and chemical properties. Some advantageous properties such as low weight, good high-temperature strength, high thermal conductivity, resistance to thermal shock and resistance to high-temperature erosion make C/C composites more useful [1-6]. The most important defect of these composites is oxidation at temperatures higher than 500°C, which could be prevented by applying an appropriate coating on them. Silicon carbide (SiC) is the most applicable coating for C/C composites due to the low thermal expansion coefficient and high adhesion between coating and the substrate [7-12]. Chemical vapor deposition (CVD) is an attractive and efficient coating method for applying SiC coating on C/C composite. This method is based on the decomposition of a gaseous reactant in an activated environment and the formation of solid products. The thermodynamics and kinetics of CVD process could be used for identification of the process and reactions. Thermodynamic calculations could be employed to investigate the feasibility of the reaction, while kinetics study could be used to determine the controlling factor in deposition procedure. To obtain a uniform coating with a certain morphology and expected properties, an exhaustive investigation should be carried out on the deposition process to determine the controlling factors [13-18]. The aim of this research is to study the relationship between boundary layer theory and deposition kinetics of β -SiC coating on a C/C composite by CVD method. Therefore, the influences of various parameters on the deposition rate were studied.

2. Material and methods

C/C 2D bi-directional structured samples was obtained from Jiao company. The modulus of elasticity, thermal conductivity and density of the composite were about 180 GPa, 100 W/m·K and $1.8 \cdot 10^3 \text{kg/m}^3$, respectively. Cubic specimens with dimensions of 10 mm×10 mm×10 mm were cut from the bulk C/C composite by means of wire-cutting method. The samples were ground with emery silicon carbide papers of 400-1300 grits. Thereafter, the ground specimens were cleaned ultrasonically in acetone and ethanol for 15 min followed by drying in the oven at 200°C for 2 h. Low pressure chemical vapor deposition (LPCVD) process was carried out by means of a setup with horizontal reactor (NSSG, Iran). The deposition was performed using pure SiCl_4 (Merck, Germany) and CH_4 as well as N_2 as dilution and carrier gas. The schematic diagram of the CVD setup is shown in Fig. 1.

To evaluate the deposition rate, deposition parameters varied as follows; temperature: 900, 1000 and 1100°C, time: 1, 2 and 3 h, $\text{SiCl}_4:\text{N}_2:\text{CH}_4$: 2:100:100, 4:100:100 and 6:100:100 (sccm). Furthermore, the samples were deposited at different positions in the reactor to study the effect of sample position.

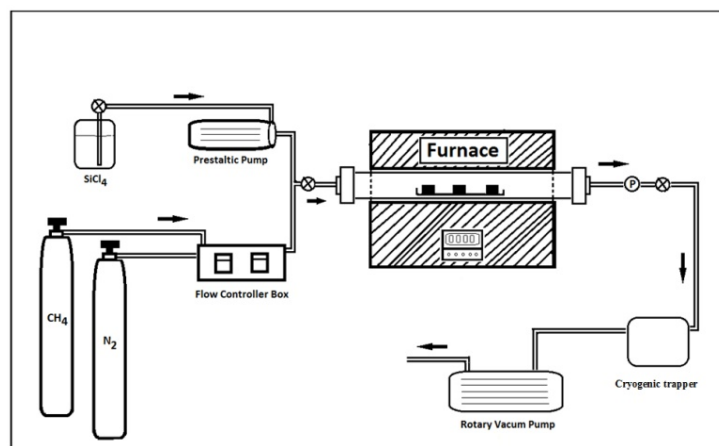


Fig. 1. The schematic diagram of the CVD setup

Deposition rate of the SiC coating were calculated utilizing the following equation:

$$R = \frac{W - W_0}{A \cdot t}, \quad (1)$$

where, W_0 and W are the weight of the sample before and after CVD process, respectively, A is the sample surface area and t is the deposition time.

X-ray diffraction (XRD) (Bruker, Germany, $\text{Cu K}\alpha=1.54 \text{ \AA}$) was used to characterize the phase composition and measure the grain size and texture of the coatings. Field emission scanning electron microscopy (FESEM) (Tescan, Czech Republic) was utilized to measure the thickness and investigate the morphology of the coatings.

3. Results and discussion

X-ray diffraction analysis. Figure 2 illustrates XRD pattern of SiC coating applied on a C/C composite by CVD method. It can be seen that β -SiC is the major phase of the coating and also one carbon peak is observable.

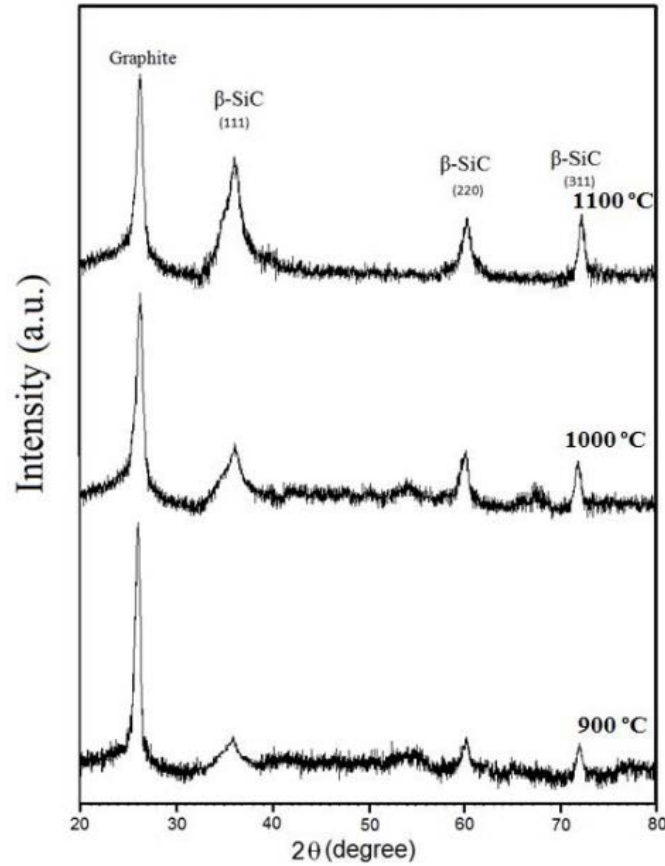


Fig. 2. XRD pattern of β -SiC coating applied on C/C composite by CVD method

The intensity of the carbon peak for the coatings produced at 1100°C is lower than that of the coatings produced at 900 and 1000°C. This carbon peak is related to the C/C substrate as X-ray beam can penetrate through 30 μm thick coatings [19]. As can be seen in FESEM cross-sectional images (Fig. 3), the thickness of the coatings produced at 1000 and 1100°C was about 3 and 5 μm , respectively. Therefore, the carbon peak rises from substrate. Furthermore, with increasing deposition temperature, the intensity of β -SiC diffraction peaks enhanced. From the X-ray diffraction patterns, the texture coefficient (TC) of the coatings could be measured. The TC represents texture and preferred orientation of the crystal surface. The lower the TC value for certain (h k l) plane, the weaker the growth for that plane and vice versa. The TC and preferred growth orientation depend on the deposition conditions and on the deposition kinetics. The TC of (111), (220) and (311) crystal planes in polycrystalline SiC coating can be calculated using Harris method [19-20]:

$$TC = \frac{I_i/I_0}{(1/n) \times \sum_{i=1}^n (I_i/I_0)}, \quad (2)$$

where, I_i is the measured relative intensity of a (h k l) plane and I_0 is the standard intensity of the plane (taken from ASTM standard intensities) and n is the number of reflections. TC values for (111), (200) and (311) crystalline planes are shown in Fig. 4. It can be observed that at 900 and 1000°C, the TC of (200) and (311) is higher than (111) plane. At 1100°C, the TC of (111) direction is higher than that of (220) and (311). Hence, with increasing temperature, preferred orientation changes from (220) and (311) to (111) and at higher temperatures β -SiC tends to grow through densely-packed atomic planes.

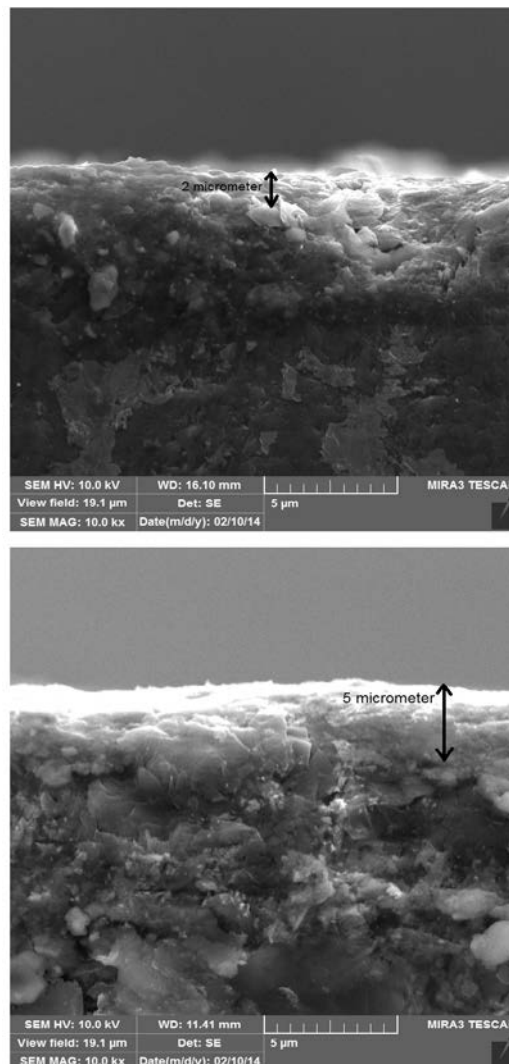


Fig. 3. Cross section of SiC coated C/C at different temperatures of 1000 and 1100°C

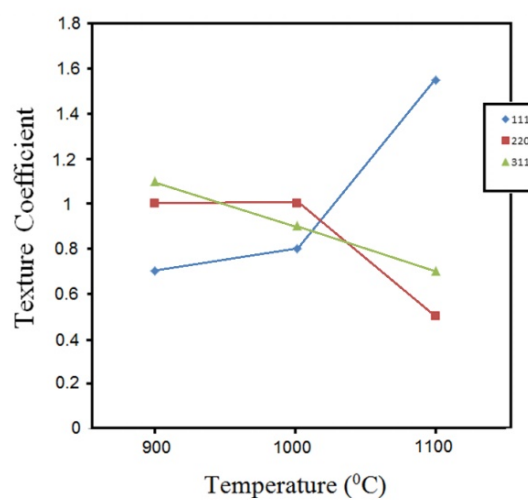


Fig. 4. Texture coefficients of β -SiC coating at different temperatures

The SiC coating grain size was calculated using the Debye-Scherer formula, as given in Equation (3) [21]:

$$D = \frac{0.9\lambda}{\beta \cos \theta}, \quad (3)$$

where, D is the grain size of the crystallite, λ is the wavelength of the incident X-ray, β is the width of peak in the middle of maximum intensity and θ is the related point on the horizontal axis. Table 1 presents the average crystal size of the SiC coating deposited at different temperatures. As it can be seen, the grain size of coating increases from 70 to 350 nm as the deposition temperature increases from 900 to 1100°C.

Table 1. Calculated average grain size of coating at different temperatures

Deposition temperature (°C)	Average grain size (nm)
900	70
1000	145
1100	350

Effects of different parameters on deposition kinetics. In general, the CVD process involves the following seven key steps [22]:

1. Transport of gaseous species in to the reactor.
2. Formation of intermediate species from reactant gaseous species.
3. Diffusion of intermediate species through the boundary layer to the substrate surface.
4. Adsorption of these species on the surface.
5. A single-step or multi-step reactions on the substrate surface.
6. Desorption of by-product species from the substrate.
7. Forced exit of un-reacted gases and by-product species from the reactor.

The schematic illustration of CVD steps during the deposition is shown in Fig. 5. Steps (1) and (7) are mass transport-controlled processes. Rate of step (1) is controlled by experimental conditions and flow rate of the precursors in the reactor. In addition, step (7) is controlled by the gas flow rate in the reactor and the power of vacuum systems. Step (5) is consisting of the intermediate gas reaction in the surface. Steps (3) and (6) show mass transport through the boundary layer. The rate of these steps can be determined by Fick's first law. In general, the steps in this model can be classified into two categories; the mass-transport-controlled steps (1, 3, 6 and 7) and the surface-reaction-controlled steps (2, 4 and 5). Amongst, the slowest step determines either the process is a mass-transport or surface-reaction controlled [18,22]. Thus, various parameters were studied to determine the kinetics of coating process.

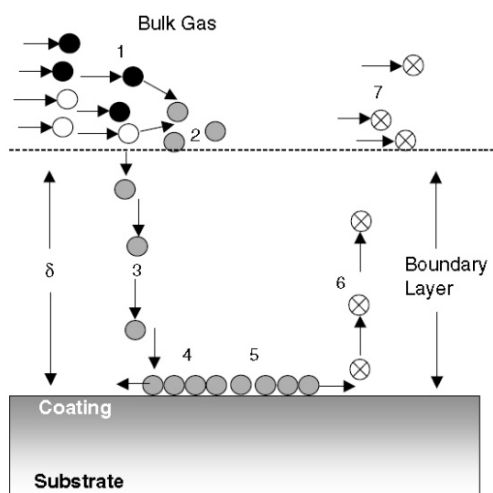


Fig. 5. Schematic diagram of the mechanistic steps of CVD process [20]

Temperature. Figure 6 illustrates the deposition rate of coating as a function of temperature. It can be seen that the deposition rate increases with deposition temperature due to overcoming the thermodynamically-formed barriers. However, at elevated temperatures, the consumption rate of the reactants at the surface of furnace hot wall is high too and it has a destructive effect on the deposition rate which can be clearly seen in Fig. 6. Thus, increasing the deposition temperature can be assumed as a positive and negative factor in SiC deposition.

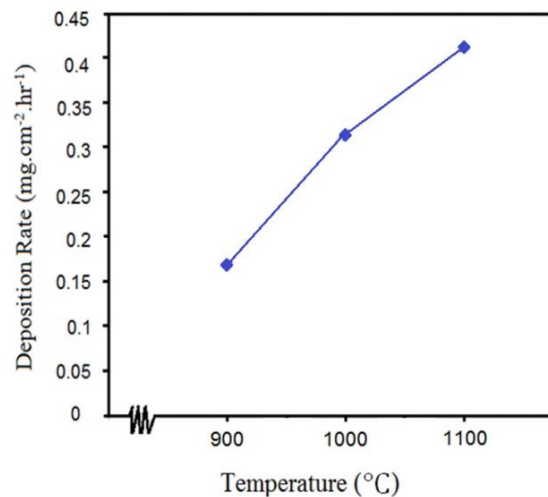


Fig. 6. Deposition rate of coating versus temperature

For determination of deposition kinetics in CVD process, an accurate knowledge of boundary layer is necessary. According to boundary layer theory [11], mass transport through boundary layer could be pursued utilizing Fick's first law [22].

$$J_A = -\frac{D_{AB}}{RT} \frac{dC_A}{dx}, \quad (4)$$

where, J_A is the diffusion flux of specie A , D_{AB} is diffusivity of reactants, C_A is concentration of specie A , R is gas constant, T is temperature and x is the direction perpendicular to the substrate surface. In boundary layer theory of a CVD process, x is the thickness of boundary layer. The average boundary layer thickness as a function of temperature is given as [22]:

$$\delta = \frac{10}{3} \sqrt{\frac{L\mu_{mix}}{\rho u}}, \quad (5)$$

where, L is the length of the substrate, μ_{mix} is the viscosity of the gas mixture, ρ and u are the density of the gas and the linear velocity of the gas in reactor, respectively. The density and velocity of the gas are function of temperature. The density is estimated by ideal gas law and the viscosity is estimated by some models [23]. Calculated results of the average boundary layer are shown in Fig. 7. As it is illustrated, an increase in temperature causes an increase in the thickness of boundary layer. Increasing the temperature causes the viscosity enhancement of the gas in reactor. With increasing gas concentration, the velocity of reactants in the reactor decreases. Thus, according to Eq. 5, the boundary layer will get thicker. With more thickening of the boundary layer, the growth kinetics will be controlled by mass transport. When the deposition rate is controlled by mass transport, the particles pass through the boundary layer thickness and reach to the substrate surface and the coating has enough time to grow. As can be seen in Fig. 4, the preferred orientation for growth of the crystals at high temperatures is (111) crystalline plane. Thus, it can be concluded that at elevated temperatures, the boundary layer thickness increases and the deposition process is controlled

by mass transfer. Due to having enough time for being ordered, crystals grow in high density orientation.

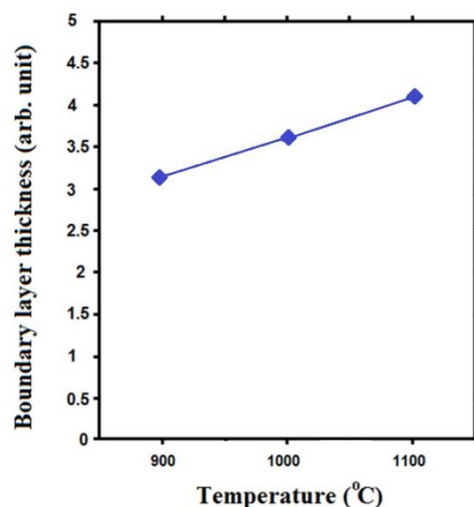


Fig. 7. Calculated boundary layer thickness at different temperatures

Precursor composition. The effect of composition of precursor on deposition rate of coating is shown in Fig. 8. The results indicate that the deposition rate increases with increasing the amount of SiCl_4 in the gas composition. Increasing SiCl_4 as precursor from 2 to 4 sccm has a meaningful effect on deposition rate, but increasing it from 4 to 6 sccm has a lower effect on deposition rate. When SiCl_4 amount is 2 sccm, the concentration of active particles containing Si is very low in comparison to the active particles containing C, thus the deposition rate is very low. With increasing SiCl_4 up to 4 sccm, the concentration of Si-containing particles on the surface increases and the deposition rate increases severely. However, with increasing SiCl_4 content up to 6 sccm, the deposition rate slightly increases. In this case, the excessive concentration is the controlling factor of the deposition process.

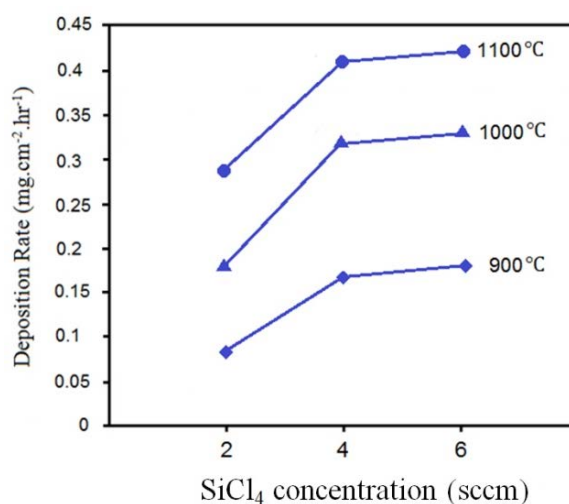


Fig. 8. Deposition rate of SiC coating versus SiCl_4 concentration

Time. The deposition time is one of the most important and controlling parameters in the nucleation and growth of SiC on C/C composite. Figure 9 shows the effect of time on deposition rate of SiC coatings. It can be seen that the deposition rate is low at first hour, followed by a significant increase especially when the deposition time increased to 3 hours. When the deposition time is low, SiC nucleates on the surface of C/C composite.

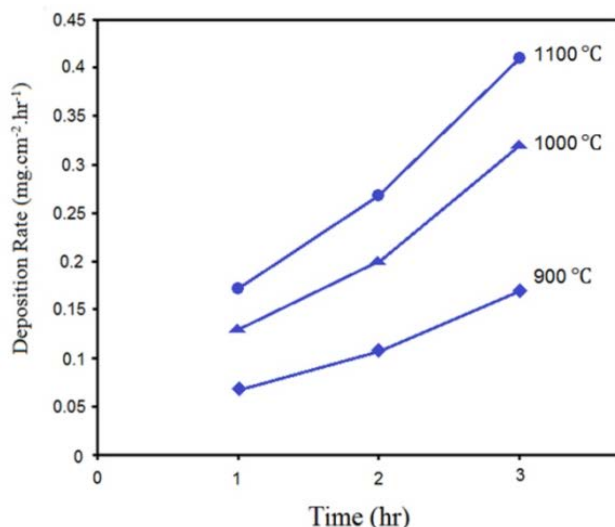


Fig 9. Deposition rate of SiC coating versus deposition time

Position of the samples in the reactor. Position of substrate in the CVD reactor is one of the effective parameters on deposition rate. In different parts of the reactor, temperature, pressure and gas flow input is sometimes different. Figure 10 illustrates substrate positioning in the CVD reactor and its effects on deposition rate. As it is obvious, the deposition rate is higher in position 2 than that in positions 1 and 3. Thermocouples of the CVD reactor furnace are located close to this location and displayed temperature is the temperature of this position. In this position, since the distance from the inlet and outlet of reactor is high, the temperature is higher and mass transfer is easier. Thus, the activated particles suspended in the reactor react readily on the substrate surface. However, around position (1) and (3) due to the closeness to input and output gates, the temperature is lower and the deposition rate is less.

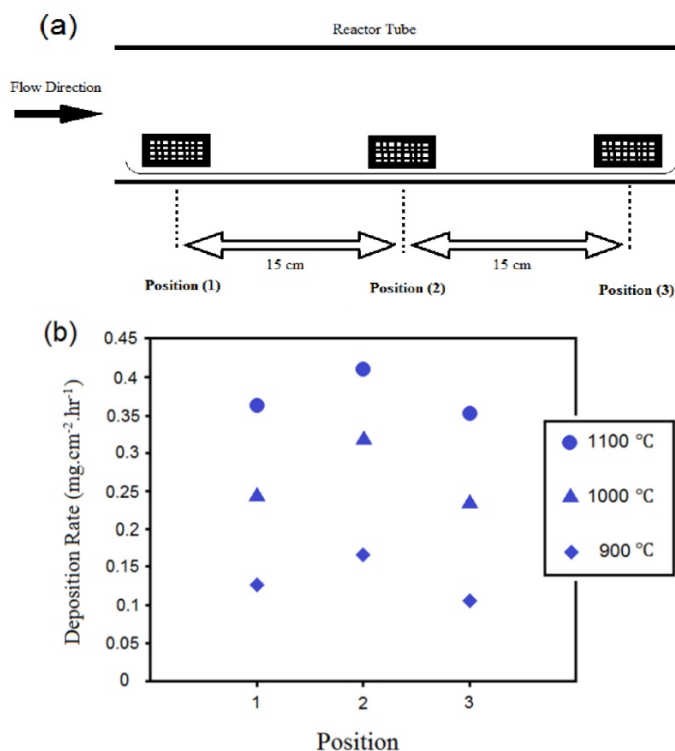


Fig. 10. (a) Schematic illustration of substrate position in reactor, (b) deposition rate of SiC coating versus substrate position

Controlling factors of deposition. To determine the factors controlling the deposition rate, its changes versus temperature is plotted in Fig. 11. The resulted curve can be divided into two regions. Due to the changes in region (a), the slope of the curve is constant, but in region (b), a noticeable decrease of the slope could be clearly seen. From the calculated slope, it could be noted that chemical reactions, mass transfer and surface migration, network integration and byproducts desorption from surface are the controlling factors in region (a). The surface processes strongly depend on deposition temperature and the processes speed up with temperature enhancement. Also, it could be mentioned that deposition could be controlled by mass transport of the activated particles in the boundary layer in region (b). Hence, there is a limitation in mass transport and deposition rate, which are slightly dependent on temperature. In fact, at high temperatures, surface processes are accelerating, thus fewer particles could reach the surface. Therefore, the growth mechanism of the deposit also changes. The change in mechanism of the crystal growth was also observed by calculation of the preferred orientation of crystals. The (111) crystalline plane is more compact than (220) and (311) crystalline planes and Si and C atoms, are arranged in this plane in compressed mode. It can be concluded that, at low temperatures, deposition is controlled by chemical reaction and particles can easily reach the surface at lower speeds. When the surface reaction is carried out at lower speeds, the particles deposit in irregular form and may be stacked with little compression. In this state, the texture coefficient (TC) of (220) and (311) planes are more than that of (111). When the deposition rate is controlled by mass transport, the transfer of activated particle to surface is done slower and atoms have adequate time to be arranged and compressed. The crystals grow in plane (111) with the lowest surface energy. Certainly, there is a little information about the details of the surface process mechanisms, but the relationship between temperature and activation energy can be defined by the following Arrhenius formula [18]:

$$R = A \exp\left(-\frac{E_a}{RT}\right), \quad (6)$$

where E is the activation energy, A is a constant; R and T are the gas constant and temperature, respectively. The activation energy could be obtained from the slope of the Fig. 11. Results of the activation energy calculation showed that the activation energies in regions (a) and (b) are 69 kJ.mol^{-1} and 18 kJ.mol^{-1} , respectively.

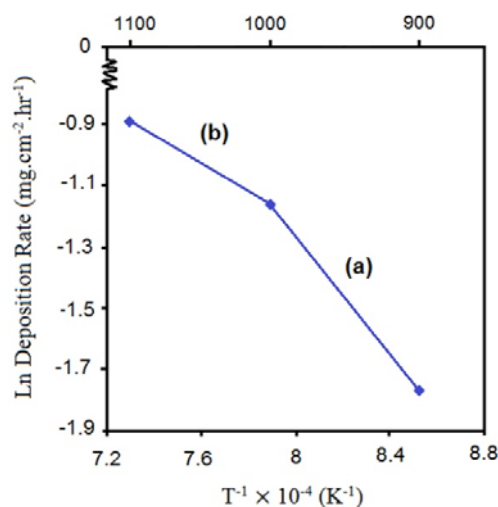


Fig. 11. The deposition rate curve versus inverse temperature

Region (a) represents a region that is controlled by chemical reaction and the activation energy in this area is much greater. The high activation energy indicates that deposition takes

Deposition kinetics and boundary layer theory in the chemical vapor deposition of β -SiC on the surface of C/C composite 43 place with difficulty and barriers ahead of deposition process are high. Therefore, it is expected that the formed coating has a low thickness. In region (b), the activation energy is lower. Deposition has a lower dependence on temperature in this region. Hence, SiC deposits more easily.

FESEM images of coatings. Figure 12 demonstrates surface morphology of C/C composite before and after SiC deposition. As it is observed, C/C has a laminate configuration due to the flake-like structure of C/C, which acts as a template for further SiC growth. As it is seen from the figure, SiC crystals grow according to flakes of the substrate and are not capable of growing on the surface porosities of C/C surface. Therefore, deposition time needs to be extended. On the other hand, since the temperature is an effective parameter, it also needs to be elevated to prepare adequate energy for SiC particles to grow in porosities.

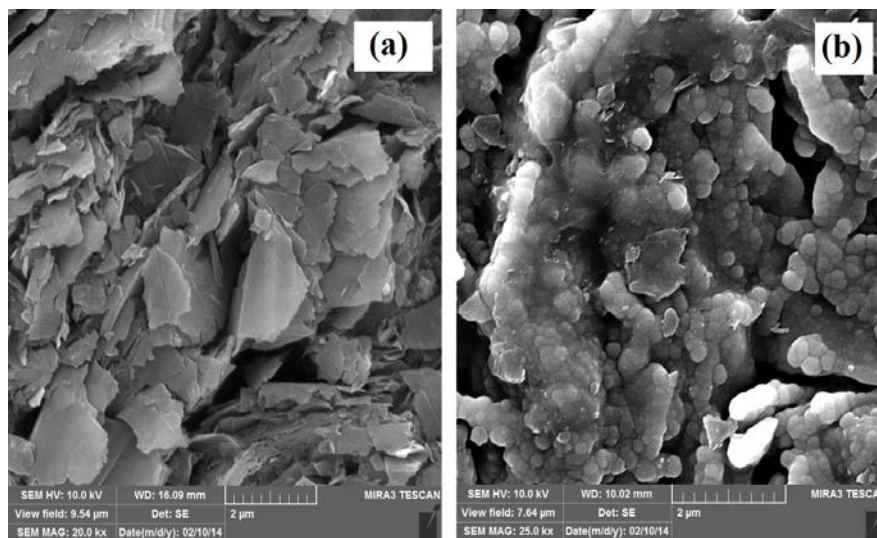


Fig. 12. Surface morphology of C/C composite (a) before and (b) after SiC deposition

Figure 13 presents EDS analysis of SiC coating. As it is seen, the coating is consisted of high percentage of C and Si. Presence of O in composition of coating indicates that some areas of SiC have undergone oxidation. However, as the amount of oxygen is low, oxidation cannot be widespread on the coating.

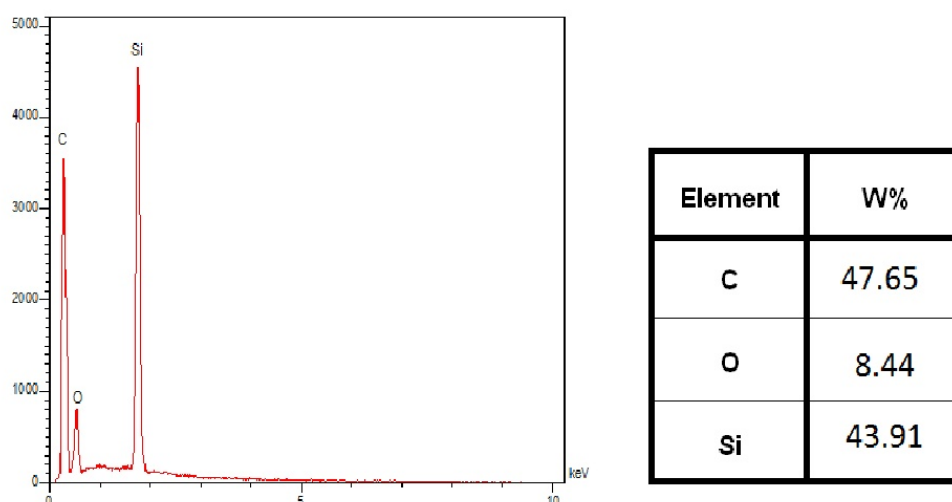


Fig. 13. EDS analysis of SiC coating on C/C substrate

Figure 14 shows FESEM images of SiC-coated C/C with two different magnifications. As it is observed, at 900 and 1000°C, the generated clusters are very small and by increasing temperature, they start to grow and become bigger and bigger. At 1100°C, many crystals could grow and in some cases, crystal size has even reached 300 μm .

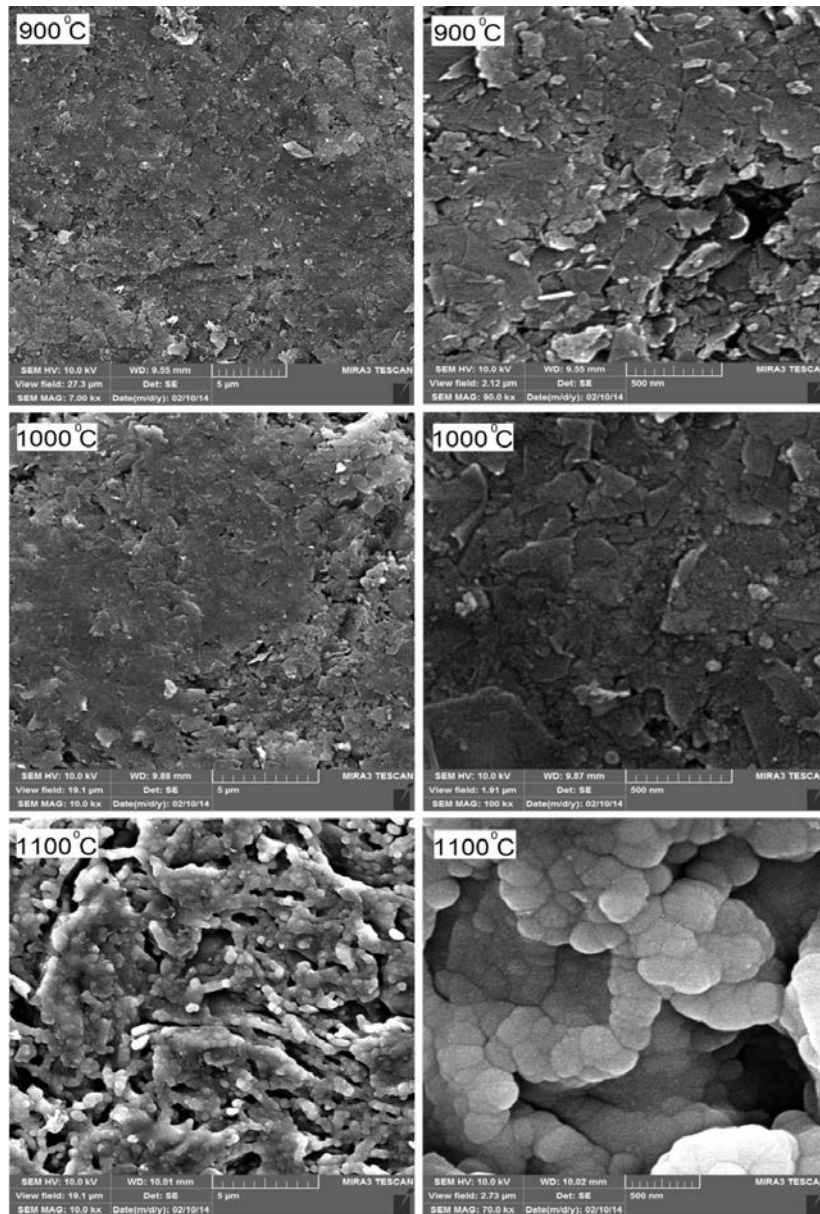


Fig. 14. FESEM images of SiC coated C/C with two different magnifications at 900 and 1000°C

Effect of deposition time on growth morphology of coating. Figure 15 presents FESEM images of the applied SiC coating in different periods of times. As it is observed, by increasing deposition time, the crystallized grains on the surface of C/C have grown and their size have increased. When the deposition time is less, crystals nucleate and if they reach critical radius, begin to grow. As can be observed in the figure, during 1 h, small particles have been generated on the surface of the composite. By increasing deposition time up to 2 h, the same particles exist on the surface. However, they had the sufficient time to absorb more Si and C atoms to be enlarged and reach the diameter of 100 nm. When the time was further

Deposition kinetics and boundary layer theory in the chemical vapor deposition of β -SiC on the surface of C/C composite 45 allocated, initial nucleation and growth both occurred at the first hour of deposition. However, the main growth happened at the last hour of deposition and crystals have been able to reach themselves to the diameter of 200 to 300 nm homogeneously. From above mentioned discussion, it is concluded that SiC crystals grow in an Island-type manner.

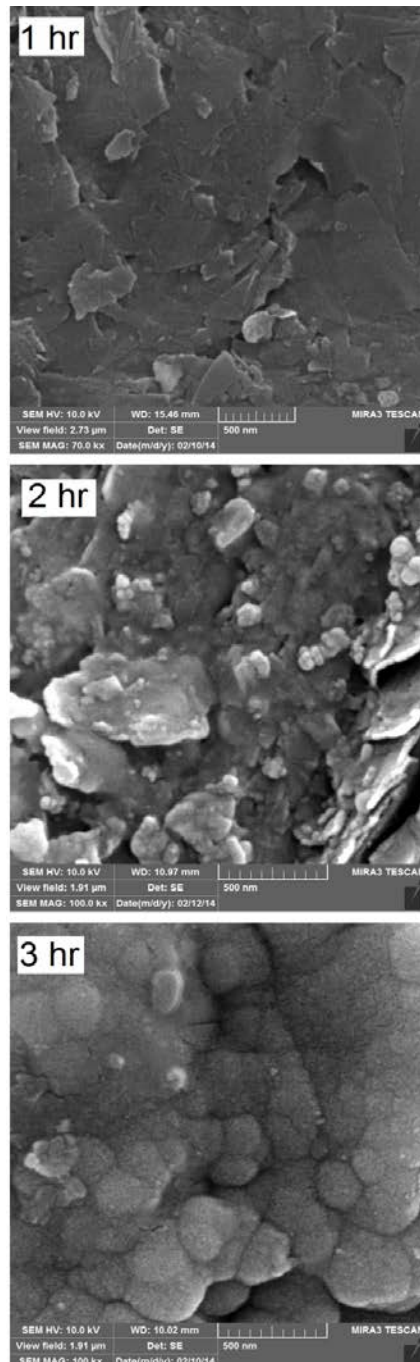


Fig. 15. FESEM images of the applied SiC coatings in different periods of times

4. Conclusions

From the above-mentioned results, the following conclusions could be drawn;

1) Phase characterization of SiC coating applied at different temperatures shows that the β -SiC phase in crystalline planes (111), (200) and (311) grows on the surface of C/C composite and the phase peak intensity increases with increasing temperature.

2) Texture coefficient calculation results using XRD analysis revealed that crystal preferential orientation at 900 and 1000°C were (311) and (200) and at 1100°C, preferred orientation of crystalline plane was (111).

3) Grain size calculation by utilizing XRD analysis revealed that grain size of the coating applied at 900, 1000 and 1100°C were 70, 145 and 350 nm, respectively.

4) With increasing temperature, the amount of SiCl₄ in precursor, and placement of sample in middle position of reactor, deposition rate of SiC on C/C composite increases.

5) Kinetics studies show that at 900 and 1000°C, controlling factor is the chemical reaction and at 1100°C, it is mass transport.

Acknowledgements. No external funding was received for this study.

Reference

- [1] Pierre D. *Fibers and Composites, World of Carbon*. France: Taylor & Francis Routledge; 2003; 2.
- [2] Inagaki M. *New Carbons: Control of structure and Functions*. Japan: Elsevier Science Ltd; 2000.
- [3] Burchell TD. *Carbon materials for advanced Technologies*. USA: Elsevier Science Ltd; 1999.
- [4] Luo R, Liu T, Li J, Zhang H, Chen Zh, Tian G. Thermophysical properties of carbon/carbon composites and physical mechanism of thermal expansion and thermal conductivity. *Carbon*. 2004;42: 2887-2895.
- [5] Liu H, Jin Zh, Haob Zh, Zeng X. Improvement of the mechanical properties of two-dimensional carbon/carbon composites. *Materials Science and Engineering: A*. 2008;483: 316-318.
- [6] Tzeng Sh Sh, Pan JH. Densification of two-dimensional carbon/carbon composites by pitch impregnation. *Materials Science and Engineering: A*. 2001;316: 127-134.
- [7] Bacos MP. Carbon-carbon composites: oxidation behavior and coatings protection. *Journal of Physics*. 1993;3: 1895-1903.
- [8] Strife JR. Protective Coating for Carbon-Carbon Composites. In: ASM Handbook *Surface Engineering*. 1994; 5. p. 2337-2347.
- [9] Don J, Wright MA, He J. *Investigation of Oxidation protection Systems for Carbon-Carbon Composites: formed by chemical vapor deposition and plasma-assisted chemical vapor deposition technique*. Airf. Office of Scientific Research. 1991; 122.
- [10] Kravetskii GA, Firsova TD, Kolesnikov SA. Composite Refractory Protective Coatings for Carbon-Graphite Materials. *Refractories and Industrial Ceramics*. 2008;49: 455-460.
- [11] Zhao J, Wang G, Guob Q, Liu L. Microstructure and Property of Sic Coating for Carbon Materials. *Fusion Engineering and Design*. 2007;82: 363-368.
- [12] Xin Y, Qi-zhong H, Yan-hong Z, Xin C, Zhe-an S, Ming-yu Z, Zhi-yong X. Anti-Oxidation Behavior of Chemical Vapor Reaction SiC Coatings on Different Carbon Materials at High Temperatures. *Transactions of Nonferrous Metals Society of China*. 2009;19: 1044-1050.
- [13] Pierson HO. *Handbook of Chemical Vapor Deposition (CVD): Principles, Technology, and Applications*. New Mexico: Noyes Publications/William Andrew Pub.; 1999.
- [14] Spear KE. Principles and applications of chemical vapor deposition (CVD). *Pure and Applied Chemistry*. 1982;54: 1297-1311.
- [15] Rees WSJr. *CVD of Nonmetals*. New York; VCH; 1996.
- [16] Jones AC, Hitchman ML. *Chemical Vapor Deposition: Precursors, Processes and Applications*. Glasgow: Royal Society of Chemistry; 2008.

- [17] Yan Y, Weigang Zh. Kinetic and microstructure of SiC deposited from SiCl₄-CH₄-H₂. *Chinese Journal of Chemical Engineering*. 2009;17: 419-426.
- [18] Choy KL. Chemical vapour deposition of coatings, *Progress in Materials Science*. 2003;48: 57-170.
- [19] Long Y, Javed A, Chen ZK, Xiong X, Xiao P. Deposition Rate, Texture, and Mechanical Properties of SiC Coatings Produced by Chemical Vapor Deposition at Different Temperatures. *International Journal of Applied Ceramic Technology*. 2013;10: 11-19.
- [20] Liu R, Zhang C, Zhou X, Cao Y. Structural Analysis of Chemical Vapor Deposited β -SiC Coatings from CH₃SiCl₃-H₂ Gas Precursor, *Journal of Crystal Growth*. 2004;270: 124-127.
- [21] Cullity BD, Stock SR. *Elements of X-ray diffraction*. 3rd ed. USA: Prentice Hall; 2001.
- [22] Park JH, Sudarshan TS. *Chemical Vapour Deposition, Surface Engineering Series, Vol. 2*. Ohio: ASM International; 2001.
- [23] Poling BE, Prausnitz JM, Oconnell JP. *The Properties of Gases and Liquids, 5th ed*. New York: McGraw-Hill; 2004.

STRAIN-HARDENING EFFECT ON CRITICAL STRAIN ASSESSMENT OF PIPE PLASTIC BENDING AT BUCKLING

M. Zheng^{*}, Z.M. Li

School of Chemical Engineering, Northwest University, Xi'an, 710069, China

*e-mail: mszheng2@yahoo.com

Abstract. In the current paper, the characteristic factor $\beta = [1 + 0.904(\sigma_b / \sigma_s) \cdot (1 - \sigma_s / \sigma_b)]$ is extracted from the analytical solution of the bending moment for a rectangular strain-hardening beam first. Thereafter, the characteristic factor β is transplanted into the previously proposed assessment of the critical buckling strain for rigid-perfectly plastic bending pipe by analogy method, thus an extended expression of the critical buckling strain for a pipe plastic bending including strain-hardening effect is developed, $\varepsilon_c = 0.19 \frac{t}{r} \cdot (1 + \frac{t}{1.78r}) \cdot [0.096 + 0.904 / (1 - n)^2]$. Moreover, available test data is employed to check the suitability of the extended expression. The results show that the extended expression is reasonable to reveal the effect of Hollomon type strain-hardening behavior on the critical buckling strain of pipe plastic bending.

Keywords: plastic bending, buckling, critical strain, strain-hardening, pipe

List of symbols

M_{BR} : critical bending moment of a pipe

r : cross-sectional radius of a pipe

t : thickness of a pipe

E : Young's modulus of a pipe material

ν : Poisson's ratio of a pipe material

D_0 : cross-sectional diameter of a pipe

M : bending moment of a pipe

κ : bending curvature of a pipe

$$\kappa_1 = t / D_0^2$$

ΔD : change in diameter of a pipe

σ_s : yielding strength of pipe material

P : internal pressure of a pipe

$$P_0 = 2 \sigma_0 t / D_0$$

σ_{ac} : critical buckling stress of classical (elastic) solution for Donnell equation for circular shell

ε_{ac} : critical buckling strain of classical (elastic) solution for Donnell equation for circular shell

p_i : maximum internal design pressure

p_e : minimum external hydrostatic pressure

http://dx.doi.org/10.18720/MPM.4412020_6

© 2020, Peter the Great St. Petersburg Polytechnic University

© 2020, Institute of Problems of Mechanical Engineering RAS

$$E_s = 207\text{GPa}$$

F_y : effective specified minimum yield strength

σ_h : characteristic hoop stress

α_h : maximum yield to tensile ratio;

α_{gw} : girth weld factor

C : longitudinal curvature of the pipe during bending

C_c : critical longitudinal curvature C

γ : dimensionless parameter to reflect the ovalization of the cross section of the bending pipe

γ_c : critical value of γ

k : the intensity factor of metal

n : hardening exponent of metal

σ_b : ultimate strength

$R = \sigma_s / \sigma_b$: ratio of yield strength to ultimate strength

ε_u : uniform elongation

$$M_0 = bh^2\sigma_s / 4$$

b : width of a beam

h : height of the beam

M_p : bending moment of the rectangular strain- hardening beam

$\beta = [1 + 0.904(\sigma_b / \sigma_s) \cdot (1 - \sigma_s / \sigma_b)]$: factor characterizing strain -hardening effect on bending moment of a beam as compared to the ideal plastic one

1. Introduction

Buckling failure is a common phenomenon in pipe production and service conditions involving bending. This kind of failure is fatal due to the loss of load capacity. However, the assessment of critical strain of plastic bending pipe at buckling is still insufficient.

In general, buckling initiation can be used to define the failure of pipeline. During pipe bending, the cross - section shape of pipe changes from a round to an oval one gradually, and the bending load or moment increases at the beginning stage; however, the bending load or moment could no longer increase or even suddenly decreases when the pipe bending exceeds certain degree, which is defined as buckling failure of the bending pipe.

Early in 1927 [1], Brazier proposed an elastic solution to correlate the bending moment and critical state at the limit point. His work showed that when an initial straight pipe is bent uniformly, the tension and compression in longitudinal direction in the pipe resist the applied bending moment, at the same time the cross section of the pipe tends to ovalize or flatten elastically, which in turn reduces the flexural stiffness of the member as the bending curvature increasing. He showed that the flexural stiffness has a maximum value which is defined as the critical instable moment, $M_{BR} = 0.987Et^2r/(1-\nu^2)^{1/2}$, where r and t are the cross-sectional radius and thickness of a pipe, E is its Young's modulus and ν is the Poisson's ratio, respectively.

Similar to Brazier, Chwalla studied the flattening of pipe cross-section due to pipe bending in 1933 [2]. It diminishes the bending resistance of pipes progressively due to the production of a certain curvature, and the bending moment for an oval section is smaller than that of a round one. This nonlinear effect leads to instability [3]. The theoretical flexural limit moment of cylindrical shells in considering section flattening (ovalization) is with a high critical value [4]. Seide and Weingarten studied the bifurcation of bending cylindrical shell, a

linear pre-buckling state and a Ritz-type bifurcation solution were assumed [5]. Their results indicated that the buckling stress of a finite length simply supported cylindrical shell bending is similar to the pure compression shell. Reddy observed the wave - like ripples on the compression side of bending pipes ahead of collapse with steel and aluminum specimens [6]. Kyriakides and Ju studied the instability of cylindrical aluminum shells in pure bending [7,8], the ratio of diameter to thickness of the cylindrical aluminum shells was 19.5 ~ 60.5, and the length to diameter ratio was 18.1 ~ 30.1; the appearance of wave - like ripples was observed on the compression side of the bent pipes once more before collapse. Libai and Bert [9], Tatting et al. [10], Stephens and Starnes [11] also investigated the dependence of bifurcation instability on Brazier's flattening effect.

In these decades, massive work has been done to study the stability of circular pipe bending due to the needs of safety assessment of pipeline and behavior of nano-pipe.

As to the buried pipeline, it might suffer from complex and changeable environmental conditions, which could induce deformation and strain or even lead to pipe failure, the critical value of strain for a bending pipe at buckling might be rationally taken as a parameter in pipeline design in nowadays [12-15]. However, the assessment of critical buckling strain is still on the way, though some formulae have been proposed [13-15]. Till now some formulae are either short of physical meaning or unreasonable. The prediction of classical analytical solution is far from experimental results due to its elastic feature though it is with clear physical meaning [13,14], other regressive or fitted formulae are short of physical meaning or unreasonable [15], see the analysis in next section in detail. This situation indicates that the assessment of the critical strain of plastic bending pipe at buckling is still an important and open problem.

In 2006, Khurram Wadee et al. proposed a variational model to formulate the deformation localization of bending round thin-walled pipes in elastic status [16]. The results are compared to a number of case studies including nano-pipe, but it is in elastic case. Philippe Le Grogneq and Anh Le van studied the theoretical aspects of elasto-plastic buckling of plates and cylinders under uniform compression in 2009 [17]. 3-D plastic bifurcation theory assuming the J_2 plastic flow with von Mises yield criterion and a linear isotropic hardening are involved in the analysis. The critical loads, the buckling modes and the initial slope of the bifurcated branch are obtained for the rectangular plates under uni-axial or biaxial compression (-tension) and cylinders under axial compression. Poonaya et al. analyzed the plastic collapse of thin-walled round pipe bending in 2009 [18]. The oblique hinge lines along the longitudinal pipe within the length of the plastic deformed zone were introduced in the 3-D geometrical collapse mechanism analysis. The internal energy dissipation rates, the inextensional deformation and perfect plastic material behavior were assumed in the derivations. Gianluca Ranzi and Angelo Luongo proposed an approach to illustrate the cross-section change in the context of the generalized beam theory (GBT) in 2011 [19]. The semi-variational method was employed to formulate the problem.

In 2012, Christo Michael et al. studied the effects of ovality and variable wall thickness on collapse loads of pipe bending in-plane by finite element limit analyses with elastic-perfect plastic material model [20]. It showed that ovality affects collapse load more significantly than thinning in the pipe bending process. They proposed a regressive mathematical equation to include the oval effect for their finite element analysis results.

Currently, Gayan Rathnaweera et al. studied the performance of aluminum / Terocore hybrid structures in quasi-static three-point bending by experiment and finite element analysis [21]. They observed two failure modes in their study, i.e., the top surface failure (compression) from structures made of AA7075 T6 and the bottom surface failure (tensile) from structures with higher percentage volume of foam.

Wrinkling is an accompanying phenomenon in pipe bending [22,23]. Guarracino

pointed out that the growth of ripples on the compressed side of the pipe has a softening effect on the overall response of the bent pipe [22]. Lamam et al. studied the inelastic wrinkling and collapse of stainless steel (SS) 321 pipes with a D_0/t about 52 under combined bending and internal pressure experimentally [23], where D_0 and t are the diameter and thickness of the pipe. Their results indicated that the moment (M) – bending curvature (κ) response $M - \kappa$ can be characterized by an initial linear elastic regime during which the pipe underwent a small amount of ovalization. Then the elastic regime eases into a smooth moment knee caused by the onset of inelastic action. The knee is followed an essentially linear "hardening" regime, which continues to a relatively high curvature. The increase of the change rate in diameter ΔD indicates a growth of ovalization accompanied by a net plastic circumferential expansion of the pipe. Meanwhile, pockets of small amplitude wrinkles were observed on the compressed side of the pipe soon after the moment knee. Under zero pressure condition, the wrinkles were short lived, which developed on the compressed side of the pipe and soon thereafter one of them localized, it results in a sharp local inward kink. This is a sudden event that is associated with the sharp loss of rigidity at the end of the $M - \kappa$ response, which corresponds to the appearance of maximum moment. This phenomenon implies that the limit carrying capacity of the pipe could be characterized by $M - \kappa$ response at the buckling though small amplitude wrinkles were observed on the compressed side of the pipe [23].

While, in the presence of internal pressure the moment–curvature response $M - \kappa$ after the knee becomes stiffer and follows an early linear path that is higher than that of the pure bending test [23]. The bulging led to the drop in moment observed at the termination of the $M - \kappa$ response indicating that the structure started collapsing. The collapse point of the pipe is defined at the curvature corresponding to the maximum moment. As the pressure increases the response after the knee maintains approximately the same slope but gradually moves down with pressure. The zero pressure case is seen to have a different post-yield slope than the rest due to the significance of the pipe cross section ovalization [23].

In summary, the limit carrying capacity of a bending pipe could be characterized by $M - \kappa$ response at the buckling regardless of the presence or absence of internal pressure.

In 2015, Ji and Zheng et al developed an analytical approach for assessing critical strain of plastic bending pipeline at buckling with the cross section ovalization and rigid-perfect plastic material models [24]. The available test data from Ref. [13,14] was employed to check the validity of the assessment, good agreement was obtained. However, strain-hardening effect of pipeline material was not included in such approach, which is a shortcoming of the work, see the analysis in next section in detail.

In this paper, an expression including strain-hardening effect on assessment of critical strain for plastic bending pipe at buckling is developed; the cross section ovalization model and the Hollomon type strain-hardening behavior of the pipe material are employed.

2. Typical approaches for assessing critical buckling strain of bending pipe

Elastic solution (classical solution). The classical (elastic) solution for Donnell equation of circular shell is [25,26],

$$\sigma_{cr} = \frac{E}{\sqrt{3(1-\nu^2)}} \frac{t}{r}, \quad (1)$$

in which, r , and t are the radius, and thickness of the circular shell, respectively; E is elastic modulus of the circular shell; σ is the uniform stress on the circular shell along its axial direction.

For common metallic material, such as steel, its Poisson's ratio is $\nu = 0.3$, while for aluminium and copper, their Poisson's ratio is $\nu = 0.34$ [27], Eq. (1) reduces,

$$\sigma_{cr} = 0.605E \frac{t}{r}, \text{ for steel;} \quad (2)$$

$$\sigma_{cr} = 0.614E \frac{t}{r}, \text{ for aluminium and copper.} \quad (2')$$

The corresponding critical strain is

$$\varepsilon_{cr} = 0.605 \frac{t}{r}, \text{ for steel;} \quad (3)$$

$$\varepsilon_{cr} = 0.614 \frac{t}{r}, \text{ for aluminium and copper.} \quad (3')$$

For a bending circular shell, it gives the same results as Eqs. (3) and (3').

The experimental data shows that Eqs. (3) and (3') give more significant overestimations than the test results [24].

In general, the value of radius-thickness ratio r/t for a practical pipeline, is about 30 ~ 50, which results in a higher $\varepsilon_{cr} = 1.21\% \sim 2.02\%$ from Eq. (3), it exceeds the usual elastic limit strain of the pipeline steel so much, says, about 0.2% [24]. This phenomenon indicates that the prediction of Eq. (3) exceeds its actual application scope for a practical pipeline seriously, so it isn't valid for practical pipeline.

Other expressions. Some other empirical approaches have been proposed to predict the critical strain of bending pipe at buckling, such as [24],

$$\text{Sherman (1976): } \varepsilon_c = 16(t/D)^2;$$

$$\text{Stephens (1991): } \varepsilon_c = 2.42(t/D)^{1.59}.$$

However, the comparison of their results with experiments indicates the non-reasonability of these formulae [24].

Available codes in industry.

(1) CSAZ662-07

CSAZ662-07 code C.C6.3.3.3 gives an assessment of local critical buckling strain including primary loads, secondary loads, or both [24],

$$\varepsilon_c = 0.5 \frac{t}{D} - 0.0025 + 3000 \left(\frac{(p_i - p_e)D}{2tE_s} \right), \frac{(p_i - p_e)D}{2tF_y} \leq 0.4, \quad p_i \geq p_e, \quad (4)$$

$$\varepsilon_c = 0.5 \frac{t}{D} - 0.0025 + 3000 \left(\frac{0.4F_y}{E_s} \right)^2, \frac{(p_i - p_e)D}{2tF_y} \geq 0.4, \quad (5)$$

in which, ε_c is the ultimate compressive strain capacity of the pipe; t is the wall thickness of the pipe, mm; D is outside diameter of pipe, mm, p_i is maximum internal design pressure, MPa; p_e is minimum external hydrostatic pressure, MPa; $E_s = 207\text{GPa}$, F_y = effective specified minimum yield strength, MPa.

(2) DNV-OS-F101

DNV-OS-F101 clause 507 supplies the characteristic compressive bending strain capacity, $\varepsilon_{M,c}$ as [24],

$$\varepsilon_{M,c} = 0.78 \left(\frac{t}{D} - 0.01 \right) \left(1 + 5 \frac{\sigma_h}{\sigma_s} \right) R^{-1.5} \alpha_{gw}, \quad (6)$$

$$\sigma_h = P \cdot \left(\frac{D-t}{2t} \right), \quad (7)$$

in which, t and D represent the thickness and diameter of the pipe; σ_h is the characteristic

hoop stress; σ_s is the yield strength of material; R is ratio of yielding strength to ultimate strength; α_{gw} girth weld factor (=1 for specimen with no weld); P is the internal pressure.

However, studies show that the accuracy of predictions of both two codes is also limited [24].

3. Cross section ovalization model for assessing critical buckling strain of pipe plastic bending

Ji and Zheng et al proposed an analytical assessment for critical strain of pipe plastic bending at buckling, which considered the cross section ovalization during bending and rigid-perfect plastic material models [24].

In the derivations, the energy rates of cross section ovalization and the oval pipe bending were established, which were combined to derive the macro bending moment of pipe. Furthermore, the maximum of macro bending moment of the pipe at buckling is yielded, and the assessment for critical buckling strain of the plastic bending pipe is then obtained.

The longitudinal curvature of the pipe during bending is expressed by C , which could be used to characterize the instant status of the bending pipe [24].

For a thin-wall circular pipe [24], $t \ll r$, if a standard ellipse is employed to characterize its ovalized cross-section shape due to bending, a dimensionless parameter γ could be introduced to reflect the ovalization of the cross section, thus the lengths of the longer and shorter half axis of the ellipse could be written as, $a = r(1 + \gamma)$ and $b = r(1 - \gamma)$, respectively. The dimensionless parameter γ depends on the longitudinal curvature C of the bending pipe, which could be seen in [24] for details. Besides, the material of the pipe behaves as a rigid - perfect plastic one.

Instability of the bending pipe occurs when the curve of bending moment M with respect to γ reaches to the peak. Thus the critical value of γ_c is derived, it obtains $\gamma_c = 0.11$ [24].

Furthermore, it derives the critical longitudinal curvature C_c of the bending pipe by completing the complicated integral calculations in [24],

$$C_c = 0.2131 \frac{t}{r^2} = 0.8524 \frac{t}{D^2}. \quad (8)$$

Correspondingly, the apparent strain of the outer-fiber-line for the bending pipe at buckling is derived [24]:

$$\varepsilon_c = \left[r(1 - \gamma) + \frac{t}{2} \right] \cdot C_c = r \left(0.89 + \frac{t}{2r} \right) \cdot 0.2131 \frac{t}{r^2} = 0.19 \frac{t}{r} \cdot \left(1 + \frac{t}{1.78r} \right). \quad (9)$$

Eq. (9) is the expression of apparent strain of the outer-fiber-line of the bending pipe at buckling geometrically. In the derivation, a rigid-perfect plastic material model and cross section ovalization are involved.

The factor 0.19 in Eq. (9) is close to the most experimental results [24].

In Ref. [24], the available test data from Ref. [13,14] was employed to check the validity of the predictions of cross section ovalization model for plastic bending pipe, good agreement was obtained.

Obviously, strain-hardening effect of pipeline material was not included in the above proposed model, which is the main shortcoming of the work.

4. Extension of critical buckling strain assessment to include strain-hardening effect on plastic bending pipe

Function of strain-hardening on critical buckling strain of plastic bending pipe. Strain

hardening or deformation strengthening ability of metallic material is one of the most important properties of metals, and the most commonly used relationship describing this ability is the Hollomon formula [28],

$$\sigma = k\varepsilon^n, \quad (10)$$

in which, σ and ε present the true stress and true strain, respectively; k is the intensity factor; n is the hardening exponent of metal.

Okatsu et al. conducted buckling experiments for small scale linepipes of Hollomon type material with different strain-hardening exponent n [29]. Their results showed that higher strain-hardening exponent n obviously corresponds to higher critical buckling strain ε_c for pipes with different diameter to thickness ratio, D/t , see Fig. 1 [29]. Their results also indicated that high deformability linepipe "JFE - HIPER" is with superior resistance to buckling, which is developed by multiphase micro - structural control from X52 to X100 grades. The stress-strain curves in the longitudinal direction are round-house type for all pipes, and high n - value (low Y/T ratio).

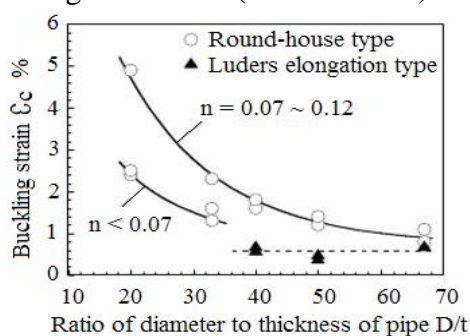


Fig. 1. ε_c vs D/t for small scale linepipes [29]

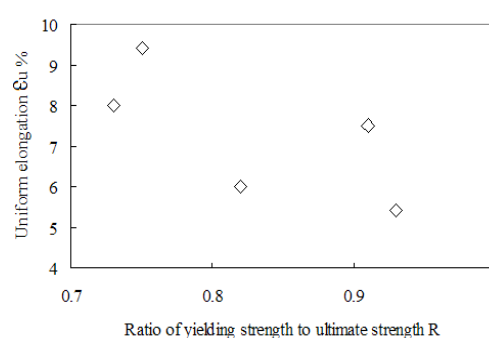


Fig. 2. ε_u vs R for X70, X80, and X90 steels [30]

With the development of pipeline steel from X65 to X100, the ratio of yielding strength to ultimate strength, $R = \sigma_s / \sigma_b$, increases from 0.80 to 0.90 ~ 0.93 or higher. Excessive ratio of yielding strength to ultimate strength leads to a decrease in the strain - hardening property of the steel pipe, which is harmful to the safe service of the pipe structure in a large displacement environment. Meanwhile, the increase of the yielding strength to ultimate strength ratio results in a decrease in the uniform elongation, ε_u .

Ji L.K. et al. studied the tensile behaviors of X70, X80, and X90 steels. Tensile specimens were cut longitudinally [30]. The rectangular tensile specimens with 50 - mm gage length, 38.1 - mm width, and full wall thickness were used to carry out their tensile tests on SHT 4106 machine according to ASTM A370. The tensile performance of the five specimens is shown in Fig. 2. It can be seen from Fig. 2 that the tendency of uniform elongation ε_u for the line pipe steels decreases with the increasing of the yielding strength to ultimate strength ratio, R . This phenomenon has been reported for various structural steels as well [30].

In addition, the deformability of the steel pipe decreases as the structural size D/t increases. Due to the use of high-strength pipeline steel, the wall of the steel pipe is thinned, which further limits the ultimate plastic deformation ability of the pipeline. As to the two-phase structure steel, its features of low yielding strength to ultimate strength ratio, high uniform elongation and strain strengthening exponent ensure the safety of pipeline structures in service, especially under strain-controlled load condition.

In fact, strain-hardening exponent is an important material parameter of pipe, which reflects the strengthening behavior of material during deformation. The value of strain-hardening exponent equals to the maximum uniform strain of material in principle [31],

which represents the ability of the material to perform strain hardening so as to make deformation uniformly before necking. Hu et al proposed a relationship to correlate the strain-hardening exponent n and the ratio of yielding strength to ultimate strength for Hollomon type material [32],

$$n = 1 - (\sigma_s / \sigma_b)^{1/2}. \quad (11)$$

Hu et al. also collected many experimental data to check the reasonability of Eq. (11) [32], which are shown in Fig. 3. It can be seen from Fig. 3 that good agreement is obtained.

These results indicate that the strain-hardening exponent n is the rate of the increase of strength or hardness of Hollomon type material during deformation process. It reveals the internal relationship between strength and plasticity. Higher σ_s / σ_b corresponds to lower n .

Jaske C.E. also studied the correlation of strain - hardening exponent n and σ_s / σ_b , the variation of strain-hardening exponent n vs σ_s / σ_b for typical pipeline steels with Hollomon type is shown in Fig. 4 [33].

From Figure 3 and Figure 4, the result of higher σ_s / σ_b corresponds to lower critical buckling strain ε_c reasonably.

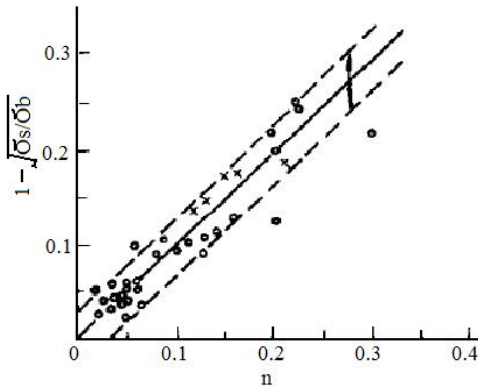


Fig. 3. Variation of σ_s / σ_b with n [32]

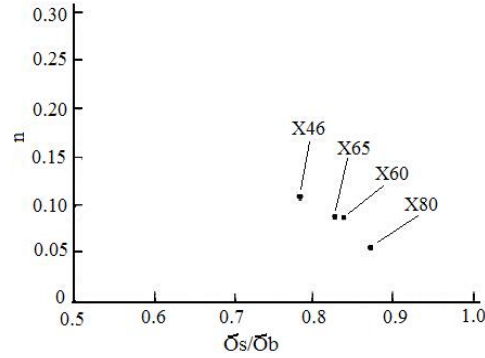


Fig. 4. n vs σ_s / σ_b for typical pipeline steels [33]

Extraction of the characteristic factor β from bending moment of a rectangular strain-hardening beam to specifically characterize the strain-hardening effect on plastic bending beam. The effect of hardening exponent on pipe bending was once studied by Murata et al. with both FEM (Finite Element Method) and experiment [34]. In their FEM, the tube is axial symmetry, and therefore a quarter part of tube was analyzed, the strain-hardening behavior of pipe material is Hollomon type. The hardening exponent changed with $n = 0.1, 0.3, 0.5$ and 1.0 . A commercial finite element code ELFEN was employed to conduct the 3D explicit analysis for the press bending process of circular, and shell element was employed. ELFEN is a widely used code for the analysis of metal forming developed by Rockfield Software Limited, Swansea [34]. The results showed that the increasing of hardening exponent significantly resists the flatness of pipe cross section during bending due to its action for deformation uniformity.

Yang investigated the strain-hardening effect on bending moment of a rectangular strain-hardening beam [35], an analytical expression was developed. The strain-hardening behavior of the material is Hollomon type.

Yang's analytical result showed that the bending moment of the rectangular strain-hardening beam could be written as [35]:

$$M_p \approx bh^2 \sigma_s \cdot [1 + 0.904(\sigma_b / \sigma_s) \cdot (1 - \sigma_s / \sigma_b)] / 4 = M_0 \cdot [1 + 0.904(\sigma_b / \sigma_s) \cdot (1 - \sigma_s / \sigma_b)], \quad (12)$$

in which $M_0 \approx bh^2\sigma_s/4$ represents the bending moment of the beam with ideal plasticity property and yielding strength σ_s ; b and h represent the width and the height of the beam, respectively.

Obviously, Eq. (12) indicates that a specifically characteristic factor β can be extracted from the expression, which reflects the effect of strain-hardening behaviour on bending moment of the beam as compared to the ideal plastic beam, i.e.

$$\beta = [1 + 0.904(\sigma_b / \sigma_s) \cdot (1 - \sigma_s / \sigma_b)]. \quad (13)$$

Extension of critical buckling strain assessment to include strain-hardening effect for plastic bending pipe at buckling. On the other hand, recalling to the two cases of elastic buckling condition, i.e., the 1st one is the classical (elastic) solutions for critical moment and strain of circular shell at bending buckling [36,37],

$$M'_{cc} = \pi Et^2 r / [3(1 - \nu^2)]^{1/2} = 0.577 \pi Et^2 r / (1 - \nu^2)^{1/2}, \quad (14)$$

$$\varepsilon'_{cc} = (r / R) / [3(1 - \nu^2)]^{1/2} = 0.577 (r / R) / (1 - \nu^2)^{1/2}, \quad (15)$$

in which the cross-section shape of the elastic circular shell keeps completely round.

While the 2nd one is the Brazier solution, which involves the cross-section shape of the elastic circular shell changing into an ellipse during bending, in this case the critical moment and strain of circular shell at bending buckling are,

$$M''_{bc} = 0.314 \pi Et^2 r / (1 - \nu^2)^{1/2}, \quad (16)$$

$$\varepsilon''_{bc} = 0.366 (r / R) / (1 - \nu^2)^{1/2}. \quad (17)$$

Compare Eqs. (14) and (15) with Eqs. (16) and (17), it yields two significant conclusions: 1) the numerical factors in the classical (elastic) solutions for critical moment and strain are identically all bigger than those in Brazier solutions, which is due to the consideration of out-round of the pipe cross-section shape in Brazier mode. This phenomenon clearly indicates that pipe with better roundness of cross-section shape will have bigger critical buckling moment and strain at the same time during bending; 2) the numerical factors are almost the same for the critical moment and strain at buckling.

Meanwhile, the previous section states that the action of strain hardening is to make deformation uniformly before necking, and it may retain the roundness of cross-section shape of pipe during bending. Therefore, as to the Hollomon type strain-hardening material and bending moment problem, the specifically characteristic factor β extracted from bending moment of a rectangular strain-hardening beam could be employed and transplanted into the expression for assessing the critical bending moment and strain of bending pipe at buckling to reflect effect of strain-hardening effect due to the similarity of the problem.

On the other hand, recalling to the three cases of elastically bending buckling condition of pipe, i.e., the 1st one that is the classical (elastic) solution of the bending pipe retaining the cross-section shape perfect round, the Brazier's solution which involves the cross-section shape changing into an elliptical one during of pipe bending, and Li's solution considering the cross section ovalization of pipe due to elastic bending [24], the corresponding critical moment and strain of above models for bending buckling are shown in Table 1.

From Table 1, it results in a significant consequence that the numerical factors in the classical (elastic) solutions for critical moment and strain are all greater than those in Brazier solution and Li's solution, which is due to the consideration of out-round of the pipe cross-section shape in Brazier and Li models. This phenomenon obviously reveals that pipe with better roundness of cross-section shape exhibits greater critical buckling moment and strain at the same time during bending, and ratio of the numerical factor ε_c to M_c are all not far from 1.0 in the above three examples.

Table 1. Solutions of critical moments and strains for initially circular pipe bending at buckling corresponding 3 elastic models [24]

Elastic model	Classical (elastic) solution	Brazier solution	Li's solution
M_c	$M_c = 0.577\pi Et^2 r / (1 - \nu^2)^{1/2}$	$M_c = 0.314\pi Et^2 r / (1 - \nu^2)^{1/2}$	$M_c = 0.388\pi Et^2 r / (1 - \nu^2)^{1/2}$
ε_c	$\varepsilon_c = 0.577(r/R) / (1 - \nu^2)^{1/2}$	$\varepsilon_c = 0.366(r/R) / (1 - \nu^2)^{1/2}$	$\varepsilon_c = 0.461(r/R) / (1 - \nu^2)^{1/2}$
Ratio of numerical factor ε_c to M_c	1.000	1.166	1.188
Shape of pipe cross-section during bending	Perfect round	Ellipse	Ovalization

Meanwhile, the previous section indicates that the function of strain hardening is to ensure deformation uniformly before necking, and it may retain the roundness of cross-section shape of pipe during bending. Therefore, as to the Hollomon type strain-hardening material and the bending moment problem, the characteristic factor β separated from bending moment of a rectangular strain-hardening beam could be transplanted into the representation for assessing the critical buckling moment and strain of a bending tube to reveal the effect of strain-hardening effect due to the similarity of the problem.

Referring that Eq. (9) is the estimation of the critical buckling strain of the outer-fiber-line of a rigid-perfectly plastic bending tube due to cross section ovalization, which is a complete geometric one without considering the action of strain-hardening.

Therefore, Eq. (9) could be extended to contain the action of deformation uniformity of strain-hardening effect by the specifically characteristic factor β reasonably, thus it yields

$$\begin{aligned} \varepsilon_c &= 0.19 \frac{t}{r} \cdot \left(1 + \frac{t}{1.78r}\right) \cdot \beta = 0.19 \frac{t}{r} \cdot \left(1 + \frac{t}{1.78r}\right) \cdot [1 + 0.904(\sigma_b / \sigma_s) \cdot (1 - \sigma_s / \sigma_b)] = \\ &= 0.19 \frac{t}{r} \cdot \left(1 + \frac{t}{1.78r}\right) \cdot (0.096 + 0.904\sigma_b / \sigma_s). \end{aligned} \quad (18)$$

In the light of Eq. (10), Eq. (18) becomes,

$$\varepsilon_c = 0.19 \frac{t}{r} \cdot \left(1 + \frac{t}{1.78r}\right) \cdot [0.096 + 0.904 / (1 - n)^2]. \quad (19)$$

Eq. (19) is the extended expression of the critical buckling strain assessment containing the strain-hardening of plastic bending pipe.

Ishikawa N. et al. collected the variation of ε_c with respect to n for some pipes with different $D/t = 40$ to 44 and 62 [38]. These data is redrawn in Fig. 5 to check the validity of Eq. (19), and it takes the average value 42 for the $D/t = 40$ to 44 . Figure 5 represents the reasonability of Eq. (19) obviously.

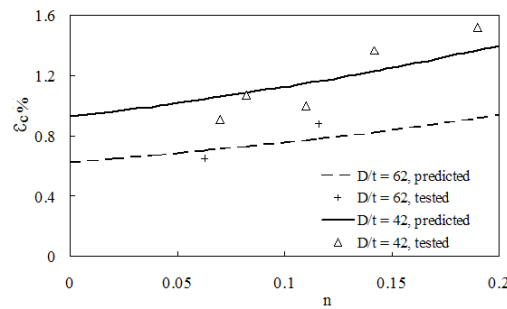


Fig. 5. Variation of ε_c vs n for Hollomon type pipes different D/t

5. Conclusion

By extracting the characteristic factor $\beta = [1 + 0.904 \sigma_b / \sigma_s (1 - \sigma_s / \sigma_b)]$ from the analytical solution of the bending moment for a rectangular strain - hardening beam, the Hollomon type strain - hardening effect on plastic bending moment of beam can be characterized specifically. Furthermore, by analogy method the critical strain assessment for strain - hardening pipeline plastic bending at buckling is developed. The result shows the reasonability of the developed expression for the critical buckling strain assessment of pipe with Hollomon type strain-hardening behavior.

Acknowledgements. No external funding was received for this study.

References

- [1] Brazier LG. On the flexure of thin cylindrical shells and other thin sections. *Proc. Roy. Soc. Series A*. 1927;116(773): 104-114.
- [2] Chwalla E. Reine Biegung schlanker, dünnwandiger Rohre mit gerader Achse. *Zeitschrift für angewandte Mathematik und Mechanik*. 1933;13(1): 48-53.
- [3] Singer J. *Buckling experiments: experimental methode in buckling of thin-walled structures*. New York: Wiley; 2002.
- [4] Imperial FF. *The criterion of elastic instability of thin duralumin tubes subjected to bending*. MS Thesis. University of California; 1932.
- [5] Seide P, Weingarten VI. On the buckling of circular cylindrical shells under pure bending. *J. Appl. Mech. ASME*. 1961;28: 112-116.
- [6] Reddy BD. An experimental study of the plastic buckling of circular cylinders in pure bending. *Int. J. Solids Struct.* 1979;15(9): 669-683.
- [7] Kyriakides S, Ju GT. Bifurcation and localization instabilities in cylindrical shells under bending. I. Experiments. *Int. J. Solids Struct.* 1992;29(9): 1117-1142.
- [8] Ju GT, Kyriakides S. Bifurcation and localization instabilities in cylindrical shells under bending. II. Predictions. *Int. J. Solids Struct.* 1992;29(9): 1143-1171.
- [9] Libai A, Bert CW. A mixed variational principle and its application to the nonlinear bending problem of orthotropic tubes-II: application to nonlinear bending of circular cylindrical tubes. *Int. J. Solids Struct.* 1994;31(7): 1019-1033.
- [10] Tatting BF, Gürdal Z, Vasiliev VV. The Brazier effect for finite length composite cylinders under bending. *Int. J. Solids Struct.* 1997;34(12): 1419-1440.
- [11] Stephens WB, Starnes Jr JH. Collapse of long cylindrical shells under combined bending and pressure loads. *AIAA J.* 1975;13(1): 20-25.
- [12] Li HL. Development and application of strain based design and anti- large- strain pipeline steel. *Petroleum Sci. & Tech. Forum*. 2008;27(2): 19-25. [In Chinese]
- [13] Dorey AB, Murray DW, Cheng JJR. An experimental evaluation of critical buckling strain criteria. *Proceedings of the Biennial International Pipeline Conference, IPC*. 2000;1:

71-80.

- [14] Dorey AB, Murray DW, Cheng JJ. Critical buckling strain equations for energy pipelines – A Parametric Study. *Transaction of the ASME*. 2006;128(3): 248-255.
- [15] Vitali L, Bruschi R, Mork KJ, Verley R. Hotpipe project-capacity of pipes subjected to internal pressure, axial force and bending moment. In: *Proceedings of the 9th International Offshore and Polar Engineering Conference. Brest: The international Society off Offshore and Polar Engineering*. 1999. p.22-33.
- [16] Wadee MK, Wadee MA, Bassom AP, Aigner AA. Longitudinally inhomogeneous deformation patterns in isotropic tubes under pure bending. *Proc. R. Soc.: A*. 2006;462(2067): 817-838.
- [17] Le Grogne P, Le Van A. Some new analytical results for plastic buckling and initial post-buckling of plates and cylinders under uniform compression. *Thin Walled Struct*. 2009;47(8-9): 879-889.
- [18] Poonaya S, Teeboonma U, Thinvongpituk C. Plastic collapse analysis of thin-walled circular tubes subjected to bending. *Thin Walled Struct*. 2009;47(6-7): 637-645.
- [19] Ranzi G, Luongo A. A new approach for thin-walled member analysis in the frame work of GBT. *Thin Walled Struct*. 2011;49(11): 1404-1414.
- [20] Michael TC, Veerappan AR, Shanmugam S. Effect of ovality and variable wall thickness on collapse loads in pipe bends subjected to in-plane bending closing moment. *Eng. Fract. Mech*. 2012;79: 138-148.
- [21] Rathnaweera G, Ruan D, Hajj M, Durandet Y. Performance of aluminium / Terocore hybrid structures in quasi-static three – point bending: experimental and finite element analysis study. *Mater Des*. 2014;54: 880-892.
- [22] Guarracino F. On the analysis of cylindrical tubes under flexure: theoretical formulations, experimental data and finite element analyses. *Thin-Walled Struct*. 2003;41(2-3): 127-147.
- [23] Limam A, Lee LH, Corona E, Kyriakides S. Inelastic wrinkling and collapse of tubes under combined bending and internal pressure. *Inter. J. of Mech. Sci*. 2010;52(5): 637-647.
- [24] Ji LK, Zheng M, Chen HY, Zhao Y, Yu LJ, Hu J, Teng HP. Apparent strain of a pipe at plastic bending buckling state. *J. of the Brazilian Soc. of Mech. Sci. & Eng*. 2015;37(6): 1811-1818.
- [25] Donnell LH. *Stability of thin-walled tubes under torsion*. National Advisory Committee for Aeronautics, NACA. Report number: 479, 1933.
- [26] Hoff NJ. The accuracy of Donnell's equations. *J. Appl. Mech*. 1955;32(3): 329-334.
- [27] Zheng XL. *Mechanical behaviors of engineering materials*. Northwestern Polytechnic University Press; 2004.
- [28] Hollomon JH. Tensile deformation. *Transaction the Metallurgical Society, American Institute of Mining, Metallurgical and Petroleum Engineers*. 1949;16: 268-290.
- [29] Okatsu M, Shinmiya T, Ishikawa N, Kondo J, Endo S. Development of high strength linepipe with excellent deformability. In: *24th Inter. Conf. on offshore Mechanics and Arctic Engineering: OMAE2005-67149, V. 3*. Halkidiki, Greece; 2005. p.63-70.
- [30] Ji LK, Li HL, Wang HT, Zhang JM, Zhao WZ, Chen HY, Li Y, Chi Q. Influence of dual-Phase microstructures on the properties of high strength grade line pipes. *Journal of Materials Engineering and Performance*. 2014;23(11): 3867-3874.
- [31] Toyoda M, Koi M, Hagiwara Y, Seto A. Effects of yield to tensile ratio and uniform elongation on the deformability of welded steel frame structures. *Welding Inter*. 1991;5(2): 95-101.
- [32] Hu Z, Cao S. Relation between strain – hardening exponent and strength. *Journal of Xi'an Jiaotong University*. 1993;27(6): 71-76.
- [33] Jaske CE. Development and evaluation of improved model for engineering critical

- assessment of pipelines. In: *Proceedings of International Pipeline Conference*. New York: ASME; 2002. p. 1459-1466.
- [34] Murata M, Kuboki T, Takahashi K, Goodarzi M, Jin Y. Effect of hardening exponent on tube bending. *Journal of Materials Processing Technology*. 2008;201(1-3): 189-192.
- [35] Yang Z. Plastic limit analysis of beams considering hardening effect. *Journal of Huaqiao University (Natural Science)*. 2006;27(3): 277-279.
- [36] Yudo H, Yoshikawa T. Buckling phenomenon for straight and curved pipe under pure bending. *J Mar Sci. Technol*. 2015;20(1): 94-103.
- [37] Karam GN, Gibson LJ. Elastic buckling of cylindrical shells with elastic cores. I: Analysis. *Int. J. Solids Struct*. 1995;32(8/9): 1259-1283.
- [38] Ishikawa N, Okatsu M, Endo S, Kondo J. Design conception and production of high deformability linepipe. In: *Proceedings of IPC2006 6th International Pipeline Conference*. Canada; 2006. p.215-222

HOMOGENEOUS HORIZONTAL AND VERTICAL SEISMIC BARRIERS: MATHEMATICAL FOUNDATIONS AND DIMENSIONAL ANALYSIS

V.A. Bratov^{1,2*}, A.V. Ilyashenko³, S.V. Kuznetsov⁴, T.-K. Lin⁵, N.F. Morozov²

¹Institute for Problems in Mechanical Engineering RAS, Bolshoj pr. 61, St Petersburg, 199178, Russia

²St Petersburg State University, 13B Universitetskaya Emb, St Petersburg 199034, Russia

³Moscow State University of Civil Engineering, Yaroslavsckoe sh. 26, Moscow, Russia

⁴Ishlinsky Institute for Problems in Mechanics RAS, Prospekt Vernadskogo 101-1, Moscow 119526, Russia

⁵National Chiao Tung University, Hsinchu, Taiwan, 300

*e-mail: vladimir@bratov.com

Abstract. The concept of a vertical barrier embedded in soil to protect from seismic waves of the Rayleigh type is discussed. Horizontal barriers are also analyzed. The principle idea for such a barrier is to reflect and scatter energy of an oncoming wave by the barrier, thus decreasing the amplitude of surface vibrations beyond the barrier. Numerical FE simulations of a plane model are presented and discussed.

Keywords: seismic protection, seismic barrier, Rayleigh waves, Lamb problem

1. Introduction

Ground vibrations generated by the external sources, such as earthquakes, blasts, railroads, etc. can affect structures and cause their damage. During recent few decades, several approaches were suggested to mitigate effects of the ground vibrations inside the protected regions by introducing barriers of different nature; see [1-11].

Most of these works concern with vertical barriers filled by an acoustically softer material than the one of the ambient soil. However, as observed in [8], horizontal barriers filled by acoustically stiffer material than the ambient soil can produce even stronger protective effect against vibrations. The discussed effect relates to Chadwick's theorem [12,13] stating that no Rayleigh waves can propagate over a clamped surface of a halfspace or a halfplane.

Herein, different materials for filling in the vertical barriers are analyzed with respect to their ability to mitigate ground vibrations beyond the barrier. The main attention is paid to Rayleigh waves, as the major factor causing ground surface vibrations at regions sufficiently distant from the buried dynamic sources [14].

2. Basic notations

The starting point for the analysis of interaction of surface acoustic waves (in the considered case of a homogeneous halfplane the surface waves are reduced to Rayleigh waves) with the vertical barrier, is analysis of the equation of motion

$$c_P \nabla \operatorname{div} \mathbf{u} - c_S \operatorname{rot} \operatorname{rot} \mathbf{u} = \frac{\partial^2 \mathbf{u}}{\partial t^2}, \quad (1)$$

where \mathbf{u} is the displacement field, c_P and c_S are velocities of the longitudinal and transverse bulk waves respectively:

$$c_P = \sqrt{\frac{\lambda+2\mu}{\rho}}, \quad c_S = \sqrt{\frac{\mu}{\rho}}. \quad (2)$$

In (2) λ and μ are Lamé constants and ρ is the material density.

Due to Helmholtz decomposition, the displacement field can be represented in terms of scalar (Φ) and vector (Ψ) potentials

$$\mathbf{u} = \nabla\Phi + \text{rot}\Psi. \quad (3)$$

The potentials are assumed harmonic in time

$$\Phi(\mathbf{x}, t) = \Phi'(\mathbf{x})e^{i\omega t}, \quad \Psi(\mathbf{x}, t) = \Psi'(\mathbf{x})e^{i\omega t}. \quad (4)$$

Substituting representation (4) into Eq. (1) yields two independent Helmholtz equations

$$\left(\Delta + \frac{\omega^2}{c_P^2}\right)\Phi' = 0, \quad \left(\Delta + \frac{\omega^2}{c_S^2}\right)\Psi' = 0. \quad (5)$$

To define plane waves and to simplify the analysis, the splitting spatial argument is needed

$$\mathbf{x} = (\mathbf{x} \cdot \mathbf{n})\mathbf{n} + (\mathbf{x} \cdot \mathbf{v})\mathbf{v} + (\mathbf{x} \cdot \mathbf{w})\mathbf{w}, \quad (6)$$

where \mathbf{n} is the unit wave vector, is the unit normal to the median plane of the plate, and $\mathbf{w} = \mathbf{n} \times \mathbf{v}$.

The further assumption relates to the periodicity of the potentials in the direction of propagation

$$\Phi'(\mathbf{x}) = \varphi(x'')e^{x'}, \quad \Psi'(\mathbf{x}) = \psi(x'')e^{x'}, \quad (7)$$

where the dimensionless complex coordinates x' and x'' are

$$x' = ir\mathbf{x} \cdot \mathbf{n}, \quad x'' = ir\mathbf{x} \cdot \mathbf{v}. \quad (8)$$

In (8) $i = \sqrt{-1}$ and r is the wave number related to the wavelength l by

$$r = \frac{2\pi}{l}. \quad (9)$$

Substituting representations (7) into Eq. (5) results in the decoupled system of two ordinary differential equations

$$\frac{d^2\varphi}{dx''^2} + \left(1 - \frac{c^2}{c_P^2}\right)\varphi = 0, \quad \frac{d^2\psi}{dx''^2} + \left(1 - \frac{c^2}{c_S^2}\right)\psi = 0, \quad (10)$$

where the phase speed c relates to the frequency and the wave number by the following relation

$$c = \frac{\omega}{r}. \quad (11)$$

The boundary surface is $\mathbf{x} \cdot \mathbf{v} = 0$ assumed free from the surface tractions:

$$\mathbf{t}_v \equiv \left(\lambda \text{tr}(\nabla\mathbf{u})\mathbf{I} + \mu(\nabla\mathbf{u} + \nabla\mathbf{u}^t)\right) \cdot \mathbf{v} = 0, \quad \mathbf{x} \cdot \mathbf{v} = 0. \quad (12)$$

Substitution representation (3) into boundary conditions (12) yields boundary conditions written in terms of potentials φ'' and ψ''

$$\left(\lambda\Delta\Phi'\mathbf{I} + 2\mu\left(\nabla\nabla\Phi' + \frac{1}{2}\left(\nabla\text{rot}\Psi' + (\nabla\text{rot}\Psi')^t\right)\right)\right) \cdot \mathbf{v} = 0, \quad \mathbf{x} \cdot \mathbf{v} = 0. \quad (13)$$

The equation (13) is one, we are looking for; it describes propagation of Rayleigh waves along free surface of a halfspace/halfplane.

Equation (13) should be supplemented with equation of motion for the barrier, analogous to Eq. (1), and boundary conditions at the interface between barrier and soil. The ideal mechanical contact is imposed at the interface:

$$\left. \begin{aligned} \mathbf{u}_{bar} &= \mathbf{u}_{soil} \\ \mathbf{t}_{v,bar} &= \mathbf{t}_{v,soil} \end{aligned} \right|_{\text{interface}} \quad (14)$$

In the next section the FE approach for solving the considered equations will be developed, allowing us to analyze the interaction of Rayleigh waves with the vertical seismic barrier.

3. FE modeling of a system "soil-vertical barrier"

Herein, some results based on numerical modeling of seismic waves propagation as well as their interaction with vertical seismic barriers are presented. The shown results are received utilizing an explicit FE code.

Basic Remarks. The analysis has shown that similarly to the horizontal barriers [8], vertical barriers should satisfy several important conditions in order to protect the given area from seismic waves effectively: (i) height of the barrier should be comparable with the lengths of the waves which it protects from; (ii) material of the barrier should have larger Young's module and density than the ambient soil has (iii).

2D Model. In connection with the complexity of this problem, 2D model was used in order to simplify the subsequent studies. These are models consisting of a symmetric plate with sizes which were chosen lest the waves reflected from the boundaries of the model should return to the points of observation during the calculation time. The condition of symmetry (3) is applied on the left edge of the plate while, the lower and the right edges were fixed. The source of waves was simulated as a harmonic load (1) applied on the upper edge in the center of the plate (on the top of the axe of symmetry). Vertical barrier (2) was created at a distance from the axe of symmetry so that the wave picture might stabilize. Figure 1 represents the picture of wave propagation in the model.

Comparing the kinetic energy of a piece of the plate beyond the barrier with the energy of the same area without barrier provides us with the information on the efficiency of this barrier. The same comparison may be carried out with the magnitudes of displacement of the observation points behind the barrier.

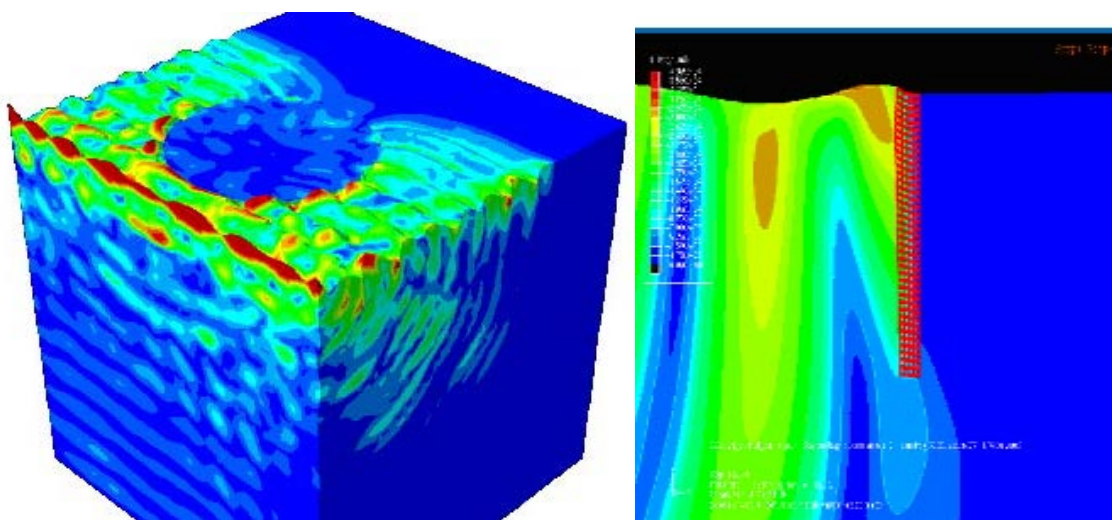


Fig. 1. Finite element model with a vertical round-shaped barrier. 3D model (left) and cross section (right)

Similarly, Figure 2 shows a finite element model of a horizontal barrier. The latter utilizes Chadwick's theorem on non-propagating Rayleigh waves in a clamped halfspace. In view of this theorem, the modeled horizontal barrier had either larger Young's modulus than the halfspace, or larger density, or both. The latter case, as numerical computations reveal, appears the best in terms of reduction vibrations behind the barrier: Rayleigh waves are almost completely eliminated in the protecting zone.

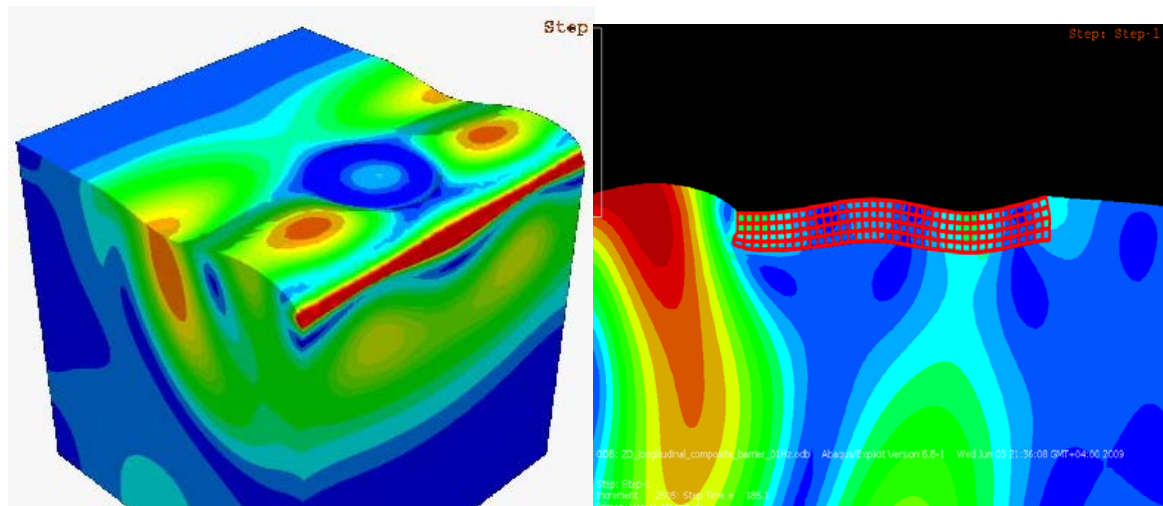


Fig. 2. Finite element model with a horizontal round-shaped barrier. 3D model (left) and cross section (right)

4. Dimensional analysis

In accordance with the π -theorem [15] which states that physical law does not depend on the form of units, the kinetic energy field E_{kin}^{bar} of an area Δ beyond the barrier can be described by the following group of dimensionless parameters:

$$E_{kin}^{bar} \left(\frac{E_{bar}}{E_{soil}}, \frac{\rho_{bar}}{\rho_{soil}}, \frac{d \times h}{\lambda^2}, \frac{d}{h}, \frac{\Delta}{\lambda}, \frac{\omega \lambda_{soil}}{\sqrt{E_{soil} / \rho_{soil}}} \nu_{bar}, \nu_{soil} \right), \quad (15)$$

where index *soil* marks the ambient material of the half-space, while index *bar* corresponds to the parameters of the barrier; λ is the wavelength of the Rayleigh wave in a half-space (this wavelength can be solved from the Bergmann-Victorov's equation); E_{bar}, E_{soil} are the corresponding Young's moduli; ν_{bar}, ν_{soil} are the Poisson's ratios; ρ_{bar}, ρ_{soil} are the densities; d and h are the thickness and the height of the barrier accordingly; ω is the circular frequency of the exciting load (here it is always equal to the wave circular frequency).

According to the analyses performed in [8] as well as this research, both Poisson's ratios almost do not have the influence on the kinetic energy field of the area, therefore, we can eliminate both Poisson's ratios. Apart from that, the frequencies of considered waves remain constant (because the applied harmonic load has a constant frequency). That is why the expression (15) can be simplified to the following:

$$E_{kin}^{bar} \left(\frac{E_{bar}}{E_{soil}}, \frac{\rho_{bar}}{\rho_{soil}}, \frac{d \times h}{\lambda^2}, \frac{d}{h} \right). \quad (16)$$

5. Conclusions

It was demonstrated that seismic barriers can be utilized to successfully protect areas from oncoming seismic waves significantly reducing amplitudes of vibrations and surface

accelerations. Further research is required in order to establish best possible geometry and material for the barriers. The developed approach can be verified experimentally on both the laboratory scale and outdoor experiment.

Acknowledgements. *This work is supported by the Russian Science Foundation under grant nr. 20-49-08002.*

References

- [1] Adam M, Estorff O. Reduction of train-induced building vibrations by using open and filled trenches. *Computers and Structures*. 2005;83(1): 11-24.
- [2] Herle V. Long-term performance of reinforced soil structures. *Proceedings of the 13. Danube-Conference on Geotechnical Engineering*. Ljubljana, Slovenia: Slovenian Geotechnical Society; 2006. p.251-256.
- [3] Jesmani M, Fallahil MA, Kashani HF. Effects of geometrical properties of rectangular trenches intended for passive isolation in sandy soils. *Earth Science Research*. 2012;1(2): 137-151.
- [4] Ketchart K, Wu JTH. *Performance test for geosynthetic reinforced soil including effects of preloading*. U.S. Department of Transportation. Federal Highway Administration. Report number: FHWA-R-01-018, 2001
- [5] Kim SH, Das MP. Artificial seismic shadow zone by acoustic metamaterials. *Modern Physics Letters B*. 2013;27(20):1350140
- [6] Kusakabe O, Takemura J, Takahashi A, Izawa J, Shibayama S. Physical modeling of seismic responses of underground structures. In: *Proceedings of the 12th International Conference of International Association for Computer Methods and Advances in Geomechanics*. Goa, India; 2008. p.1459-1474.
- [7] Kuznetsov SV. A new principle for protection from seismic waves. In: *Performance-Based Design in Earthquake Geotechnical Engineering. International Conference*. Tokyo, Japan; 2009. p.463–468,
- [8] Kuznetsov SV. Seismic waves and seismic barriers. *Acoustical Physics*. 2011;57(3): 420-426.
- [9] Kuznetsov SV, Nafasov AE. Horizontal acoustic barriers for protection from seismic waves. *Advances in Acoustics and Vibration*. 2011;2011: 150310.
- [10] Motamed R, Itoh K, Hirose S, Takahashi A, Kusakabe O. Evaluation of Wave Barriers on Ground Vibration Reduction through Numerical Modeling in ABAQUS. In: *Proceedings of SIMULIA Customer Conference 2009*. London, UK; 2009. p.402-441.
- [11] Takahashi A, Takemura J, Shimodaira T. Seismic performance of reinforced earth wall with geogrid. In: *Proceedings of the 15th International Conference on Soil Mechanics and Geotechnical Engineering*. Istanbul, Turkey; 2001. p.1265-1268.
- [12] Chadwick P, Borejko P. Existence and uniqueness of Stoneley waves. *International Journal of Geophysics*. 1994;118(2): 279-284.
- [13] Chadwick P, Smith GD. Foundations of the theory of surface waves in anisotropic elastic materials. *Advances in Applied Mechanics*. 1977;17: 303-376.
- [14] Kuznetsov SV, Terentjeva EO. Plane inner Lamb problem: waves in the near epi zone by the vertical point source. *Acoustical Physics*. 2014;60(4): 12-18.
- [15] Gibbins JC. *Dimensional Analysis*. London: Springer; 2011.

HYPERBOLIC TWO TEMPERATURE FRACTIONAL ORDER ONE DIMENSIONAL THERMOELASTIC MODEL HEATED BY A PULSE OF LASER

E. Bassiouny*

Department of Mathematics, College of Sciences and Humanitarian Studies, Prince Sattam Bin Abdulaziz
University, Al Kharj 11942, Saudi Arabia

Department of Mathematics, Faculty of Sciences, Fayoum University, Fayoum, Egypt

*e-mail: esambassiouny@yahoo.com

Abstract. The behaviour of an isotropic homogeneous thermoelastic semi-infinite medium is investigated based on the acceleration of conductive and thermodynamic temperatures. A half-space $x \geq 0$, under stress-free boundary condition at the near end, is considered. At this near end, a laser pulse decaying exponentially with time is applied. In the framework of fractional order generalized thermoelasticity theory, a one-dimensional coupled model is reduced using Laplace transform and corresponding thermally-induced temperature, stress and strain distribution functions are determined in the Laplace domain. Different inverse field functions are investigated numerically through a complex inversion formula of Laplace transform. The behavior of the field functions with different parameters are studied and presented graphically. Comparisons with the classical two temperature model are discussed.

Keywords: hyperbolic two temperatures, fractional order strain, fractional order equation of motion, laser short pulse, thermal loading, generalized thermoelasticity

List of symbols

- φ : the conductive temperature in the hyperbolic two-temperature model
- φ^c : the conductive temperature in the classical two temperature model
- σ : principal stress component in the case of hyperbolic two-temperature model
- σ^c : principle stress component in the classical two temperature model
- e : cubic dilatation in the hyperbolic two-temperature model
- e^c : cubic dilatation in the classical two temperature model
- C_E : specific heat at constant strain
- c_o : longitudinal wave speed
- T : absolute temperature
- T_o : reference temperature
- t : time
- u_i : components of the displacement vector
- $\alpha \geq 0$: two temperature parameter
- α_T : coefficient of linear thermal expansion
- ε : the dimensionless mechanical coupling constant
- θ : thermodynamical temperature
- λ, μ : Lamé's constants

http://dx.doi.org/10.18720/MPM.4412020_8

© 2020, Peter the Great St. Petersburg Polytechnic University

© 2020, Institute of Problems of Mechanical Engineering RAS

ρ : body density

τ_o : relaxation time parameter

β : the fractional-order parameter

Γ : Gamma function

s : a complex parameter related to Laplace transform

K : thermal conductivity

$\theta = T - T_0$: increment such that $\theta / T_0 \ll 1$

I : power intensity

δ : absorption coefficient

Ω : pulse parameter

1. Introduction

In thermoelasticity, the heat conduction in deformable bodies arises from the conductive and thermodynamic temperatures [1-3]. It is seen that in the case of the time-dependent situation, when there is no supply of heat, the two temperatures are the same, whereas, in the case of the time-dependent situation, the two temperatures are different. Some more details of such studies can be found in [4-5]. Indeitsev and Osipova [6] investigated optical excitation of acoustic pulses in conductors through a two-temperature model, where the energy of optical pulses transferred to long-wavelength phonons. It is shown that excited acoustic pulse by laser in conductors can be presented as a convolution of the laser pulse envelope and the transfer function. Shi et al. [7] studied the laser heating and phase change process and inferred that the rise in temperature and the rate of surface melting is proportional to the laser power intensity. Yilbas and Kalyon [8] introduced a closed-form solution for laser evaporative heating process for pulses varying exponentially and introduced an expression for the evaporation front velocity in their analysis. Their analysis gave good results compared with experimental findings limiting the temporal variations of the laser pulse to exponential form. Othman et al. [9-11] studied the behavior of thermoelastic, linear, isotropic material with voids subjected to laser pulse heating in the presence of different parameters in the context of G-N theory of type II-III. They reported that the amplitudes of the field functions depend strongly on the initial stress and rotation.

Youssef established the variational principle and the uniqueness of the initial boundary value problem in generalized thermoelasticity with two temperatures in different cases [12-14].

There is a paradox admitting infinite speeds for propagating signals in the classical two temperatures thermoelasticity theory. Youssef improved the two-temperature generalized thermoelasticity theory based on the conductive and thermodynamic temperature. He considered a hyperbolic form of the two temperatures equation [15].

The concept of derivative and integral have been generalized to a non-integer order and studied by many researchers [16-23]. Various physical processes and models have been implemented through the application of fractional-order derivatives. Applications of the fractional-order theory and many other contributions have been published by many researchers [24-29]. The fractional-order thermoelasticity becomes more realistic when it relies on the fractional-order operator because the presence of the fractional-order derivatives permits the differential equations of the system to take into consideration the effects of the intermediate as well as the previous states to express the present and the next states of the medium.

One of the most famous definitions of fractional order was introduced by Riemann-Liouville and given by [23]:

$${}_{RL}D_t^\beta f(t) = \frac{d^n}{dt^n} \left[\frac{1}{\Gamma(n-\beta)} \int_0^t (t-\tau)^{n-\beta-1} f(\tau) d\tau \right], \quad n-1 < \beta < n. \quad (1)$$

The second definition was presented by [23] and given by:

$${}_cD_t^\beta f(t) = \frac{1}{\Gamma(n-\beta)} \int_0^t (t-\tau)^{n-\beta-1} \frac{d^n f(\tau)}{d\tau^n} d\tau, \quad n-1 < \beta < n. \quad (2)$$

These two definitions are the same if $f(0) = 0$. For more details about the comparison between the two definitions of the fractional-order time derivative introduced by Riemann-Liouville and that of Caputo and various definitions and works of fractional order, derivatives were reported in [25].

Based on the new theory of the hyperbolic two-temperature generalized thermoelasticity by Youssef [15], the present work can be considered as a generalization to the application studied in [15] and more realistic as the present model contains fractional-order derivatives in both equations of motion as well as the heat equation. In the present work we will use the following equation:

$$L_c \{ D_t^\beta f(t) \} = s^{(\beta-n)} L \{ f^n(t) \} \quad n-1 < \beta < n, \quad (3)$$

as in [19] to investigate the behavior of a thermoelastic isotropic and homogeneous half-space in the presence of a short pulse of a laser beam, which is decaying in an exponential manner. In Eq. (3), s denotes the complex parameter related to Laplace transform.

2. One dimensional thermoelastic model

We consider here the following one-dimensional fractional-order system of equations, which is capable of describing the overall behavior of a semi-infinite one-dimensional homogeneous isotropic material occupying the half-space $x \geq 0$ and subjected to laser short-pulse heating exponentially decaying pulse type. The three-dimensional forms of this system can be found in our previous work Bassiouny et al. [25] and Youssef [15]. The medium is subjected to a Gaussian pulse of laser uniformly at the near end. All the field functions are initially set at zero. We also assume that there is no body force applied to the medium. Hence, the generalized thermoelastic one-dimensional coupled system of partial differential equations, in the absence of inner heat sources, body force and free charge assume the following system of equations:

the heat equation:

$$K \left(\frac{\partial^2 \varphi(x,t)}{\partial x^2} \right) = \left(\frac{\partial}{\partial t} + \tau_o \frac{\partial^2}{\partial t^2} \right) (\rho C_E \theta(x,t) + T_o \gamma (1 + \tau^\beta D_t^\beta) e(x,t)) - (1 + \tau_o \frac{\partial}{\partial t}) I_1 \delta e^{-(\Omega t + \delta x)}, \quad (4)$$

the equation of motion:

$$\rho \frac{\partial^2 e(x,t)}{\partial t^2} = (\lambda + 2\mu) (1 + \tau^\beta D_t^\beta) \frac{\partial^2 e(x,t)}{\partial x^2} - \gamma \frac{\partial^2 \theta(x,t)}{\partial x^2}, \quad (5)$$

the constitutive equations can be written in the forms:

$$\sigma(x,t) = (1 + \tau^\beta D_t^\beta) (\lambda + 2\mu) e(x,t) - \gamma \theta(x,t), \quad (6)$$

and

$$e(x,t) = \frac{\partial u(x,t)}{\partial x}. \quad (7)$$

Instead of the classical two temperature relation between the heat conduction φ and the thermodynamical temperature θ given by:

$$\theta = \varphi - \alpha \frac{\partial^2 \varphi}{\partial x^2}, \quad (8)$$

we used the following hyperbolic relation as given in [15]:

$$\frac{\partial^2 \theta}{\partial t^2} = \frac{\partial^2 \varphi}{\partial t^2} - \alpha \frac{\partial^2 \varphi}{\partial x^2}. \quad (9)$$

3. Dimensionless system of equations in Laplace domain

For converting the previous system of Eqs. (4)-(9) into a dimensionless system we used the set of dimensionless variables as in [15] and dropping the primes for convenience, we get the following non-dimensional system of equations:

the non-dimensional heat equation:

$$\frac{\partial^2 \varphi(x,t)}{\partial x^2} = \left(\frac{\partial}{\partial t} + \tau_o \frac{\partial^2}{\partial t^2} \right) (\theta(x,t) + \xi \varepsilon_1 (1 + \tau^\beta D_t^\beta) e(x,t)) - \varepsilon_2 I_1 \delta e^{-(\Omega t + \delta x)}, \quad (10)$$

the non-dimensional equation of motion takes the form:

$$\frac{\partial^2 e(x,t)}{\partial t^2} = (1 + \tau^\beta D_t^\beta) \frac{\partial^2 e(x,t)}{\partial x^2} - \omega \frac{\partial^2 \theta(x,t)}{\partial x^2}, \quad (11)$$

the constitutive equations take the following forms:

$$\sigma(x,t) = (1 + \tau^\beta D_t^\beta) e(x,t) - \omega \theta(x,t), \quad (12)$$

and

$$e(x,t) = \frac{\partial u(x,t)}{\partial x}, \quad (13)$$

the hyperbolic two temperature non-dimensional equation becomes:

$$\frac{\partial^2 \varphi}{\partial t^2} = \frac{\partial^2 \theta}{\partial t^2} - \alpha \frac{\partial^2 \varphi}{\partial x^2}, \quad (14)$$

where $\xi = \gamma / \rho C_E$, $\omega = \gamma T_o / (\lambda + 2\mu)$, $\varepsilon_1 = \gamma^2 K / \rho C_E (\lambda + 2\mu)$ and $\varepsilon_2 = I_1 \delta (1 - \tau_o \Omega) / c_o \eta K$ are non-dimensional constants.

Applying the Laplace transform defined by:

$$L\{f(t)\} = \int_0^\infty e^{-st} f(t) dt \quad (15)$$

together with Caputo's definition (3) to the system of Eqs. (10)-(14) and eliminating $\overline{\theta(x,s)}$, we get the following non-dimensional system of equations in the Laplace domain [9]:

$$\frac{\partial^2 \overline{\varphi(x,s)}}{\partial x^2} = \frac{s \left(\frac{e^{-x\delta} I_1 \varepsilon_2}{s + \Omega} + s(1 + s\tau_o) \left(\varepsilon_1 \xi (1 + s^\beta \tau^\beta) \overline{e(x,s)} + \overline{\varphi(x,s)} \right) \right)}{s + \alpha(1 + s\tau_o)}, \quad (16)$$

$$\frac{\partial^2 \overline{e(x,s)}}{\partial x^2} = \frac{1}{s^2 (1 + s^\beta \tau^\beta)} \left[s^4 \overline{e(x,s)} + \omega (s^2 \frac{\partial^2 \overline{\varphi(x,s)}}{\partial x^2} - \alpha \frac{\partial^4 \overline{\varphi(x,s)}}{\partial x^4}) \right], \quad (17)$$

$$\overline{\sigma(x,s)} = (1 + s^\beta \tau^\beta) \overline{e(x,s)} - \frac{\omega}{s^2} (s^{-2} \overline{\varphi(x,s)} - \alpha \frac{\partial^2 \overline{\varphi(x,s)}}{\partial x^2}), \quad (18)$$

and the relation between the two types of temperature:

$$\overline{\theta(x,s)} = \overline{\varphi(x,s)} - s^{-2} \alpha \frac{\partial^2 \overline{\varphi(x,s)}}{\partial x^2}. \quad (19)$$

Combining Eqs. (17) and (18) gives:

$$\frac{\partial^2 \overline{\sigma(x,s)}}{\partial x^2} = s^2 \overline{e(x,s)}. \quad (20)$$

The system of Eqs. (16)-(20) represents the one-dimensional fractional-order thermoelastic model in the light of generalized fractional-order thermoelasticity with a hyperbolic two-temperature equation.

4. The solution in the Laplace domain

Eliminating $\bar{e}(x, s)$ between the Eqs. (16) and (17), we get the following fourth-order non-homogeneous differential equation:

$$N\overline{\varphi(x, s)} - M \frac{\partial^2 \overline{\varphi(x, s)}}{\partial x^2} + \frac{\partial^4 \overline{\varphi(x, s)}}{\partial x^4} = H e^{-sx}, \quad (21)$$

where:

$$M = \frac{s^2 \left(\alpha + (\tau^\beta s^\beta (s\tau_o + 1) + 1) (\xi\omega\varepsilon_1 + 1) + s(\tau_o (\alpha + \xi\omega\varepsilon_1 + 1) + 1) \right)}{\alpha (\tau^\beta s^\beta + 1) (s\tau_o + 1) (\xi\omega\varepsilon_1 + 1)},$$

$$N = \frac{s^4 (s\tau_o + 1)}{\alpha (\tau^\beta s^\beta + 1) (s\tau_o + 1) (\xi\omega\varepsilon_1 + 1)},$$

and

$$H = - \frac{I_1 s \varepsilon_2 e^{-\delta x} (s^2 - \delta^2 (\tau^\beta s^\beta + 1))}{\alpha (s\tau + 1) (s + \Omega) (\tau^\beta s^\beta + 1) (\xi\omega\varepsilon_1 + 1)}.$$

According to the present formulation of the problem, the most general solution of (21) takes the form:

$$\overline{\varphi(x, s)} = \sum_{i=1}^2 C_i e^{-k_i x} + \psi e^{-x\delta}, \quad (22)$$

where

$\psi = -H / (N - M\delta^2 + \delta^4)$, C_i are coefficients depending on s whose values can be evaluated by using the given boundary conditions and $\pm k_i$ are the roots of the characteristic equations corresponding to the Eq. (21), which is:

$$N - M k^2 + k^4 = 0.$$

After some manipulations to the system of Eqs. (16)-(19) we get the following general solutions of the physical quantities of the present model in the domain of Laplace.

The thermodynamical temperature assumes the form:

$$\overline{\theta(x, s)} = \sum_{i=1}^2 C_i e^{-k_i x} \left(1 - \frac{\alpha k_i^2}{s^2} \right) + e^{-x\delta} \left(1 - \frac{\alpha \delta^2}{s^2} \right). \quad (23)$$

The stress and the strain in the domain of Laplace take the forms:

$$\overline{\sigma(x, s)} = \frac{\sum_{i=1}^2 C_i e^{-k_i x} [-s^2 (1 + s\tau_o) (1 + \varepsilon_1 \xi \omega) + k_i^2 (s + \alpha (1 + s\tau_o) (1 + \varepsilon_1 \xi \omega))] - f_\sigma(s) e^{-x\delta}}{s^2 \varepsilon_1 \xi (1 + s\tau_o) (s + \Omega)}, \quad (24)$$

$$\overline{e(x, s)} = \frac{1}{s^2 \varepsilon_1 \xi (1 + s\tau_o)} \sum_{i=1}^2 C_i e^{-k_i x} [-s(1 + s\tau_o) + k_i^2 (s + \alpha (1 + s\tau_o))] - f_e(s) e^{-x\delta}, \quad (25)$$

where $f_\sigma(s)$ and $f_e(s)$ can be evaluated by using the given boundary conditions.

The Eqs. (22) and (23)-(25) represent the complete solution of the system (16)-(20) in the Laplace transform domain.

5. Determination of the Parameters

To determine the previous parameters, we assume that the medium is initially at rest and has reference temperature T_o so that the initial conditions are given by;

$$\begin{aligned} \varphi(x, 0) = 0, \quad e(x, 0) = 0, \quad \sigma(x, 0) = 0, \\ \partial \varphi(x, 0) / \partial t = 0, \quad \partial e(x, 0) / \partial t = 0, \quad \partial \sigma(x, 0) / \partial t = 0, \end{aligned} \quad (26)$$

we also assume that the medium is subjected to the following boundary conditions at the near end $x = 0$:

$$\varphi(0, t) = 0, \quad \sigma(0, t) = 0, \quad (27)$$

while the boundary conditions $x = \infty$ are given by:

$$\varphi(\infty, t) = 0, \quad \sigma(\infty, t) = 0, \quad 0 < t < \infty. \quad (28)$$

Using the dimensionless variables listed in [9] and applying Laplace transform to the boundary conditions (27)-(28) and dropping the primes we obtain:

$$\bar{\varphi}(0, s) = 0, \quad \bar{\sigma}(0, s) = 0, \quad \bar{\varphi}(\infty, s) = 0, \quad \bar{\sigma}(\infty, s) = 0. \quad (29)$$

Similarly, the dimensionless initial conditions in the domain of Laplace can be obtained. By applying these conditions to the Eqs. (22)-(25), the parameters C_i , $f_e(s)$ and $f_\sigma(s)$ can be obtained as given below:

$$C_i = \frac{I_1 \varepsilon_2 s + (k_i^2 - \delta^2) b}{b(k_1^2 - k_2^2)}, \quad i = 1, 2, \quad (30)$$

$$f_\sigma(s) = \frac{\psi[(1 + s\tau_o)(s^2 - \alpha\delta^2)(1 + \varepsilon_1 \xi \omega) - s\delta^2](s + \Omega)}{s^2 \varepsilon_1 (1 + s\tau_o)(s + \Omega)}, \quad (31)$$

and

$$f_e(s) = \frac{I_1 s \varepsilon_2 + [(1 + s\tau_o)(s^2 + s\delta^2 + \alpha\delta^2)(s + \Omega)\psi]}{s \varepsilon_1 \xi (1 + s\tau_o)(1 + s^\beta \tau^\beta)}, \quad (32)$$

where $b = s + \alpha(1 + s\tau_o)(1 + \varepsilon_1 \xi \omega)$.

After substituting with the parameters given by the Eqs. (30)-(32) into the Eqs. (22)-(25) we obtain the complete solution of the non-dimensional field functions, temperature, stress, and strain in the Laplace domain.

6. Numerical inversion of the Laplace transform

The physical quantities $\varphi(x, t)$, $\theta(x, t)$, $\sigma(x, t)$ and $e(x, t)$ can be obtained by inverted the system of Eqs. (22)-(25) back to the time domain. Therefore, we use a numerical formula based on Fourier expansion. In this technique any function $\bar{f}(s)$ is inverted back to the original function $f(t)$ in the time domain according to the following formula:

$$f(t) = \frac{\exp(ct)}{t_1} \left[\frac{1}{2} \bar{f}(c) + \Re \left(\sum_1^N \bar{f} \left(c + \frac{ik\pi}{t_1} \exp\left(\frac{ik\pi}{t_1}\right) \right) \right) \right], \quad 0 < t_1 < 2t, \quad (33)$$

where \Re is the real part, i is imaginary number unit and N is a sufficiently large integer representing the number of terms in the truncated Fourier series chosen such that:

$$\exp(ct) \Re \left[\bar{f} \left(c + \frac{iN\pi}{t_1} \right) \exp\left(\frac{iN\pi t}{t_1}\right) \right] \leq \epsilon_1, \quad (34)$$

where ϵ_1 is a small positive number that represents the degree of accuracy required. The parameter c is a positive free parameter that must be greater than the real part of all the singularities of $\bar{f}(s)$. The optimal choice of c was obtained according to [31].

7. Numerical Results and Discussion

For numerical computations, we used the physical constants of the Copper material used in [16]. We investigate the distributions of the field functions, that is φ , θ , σ and e for different values of the parameters δ , β and t compare their behavior with the corresponding physical quantities φ^c , σ^c and e^c . The results are presented in three groups of Figures; each group presents the effect of one of the mentioned parameters on the physical quantities.

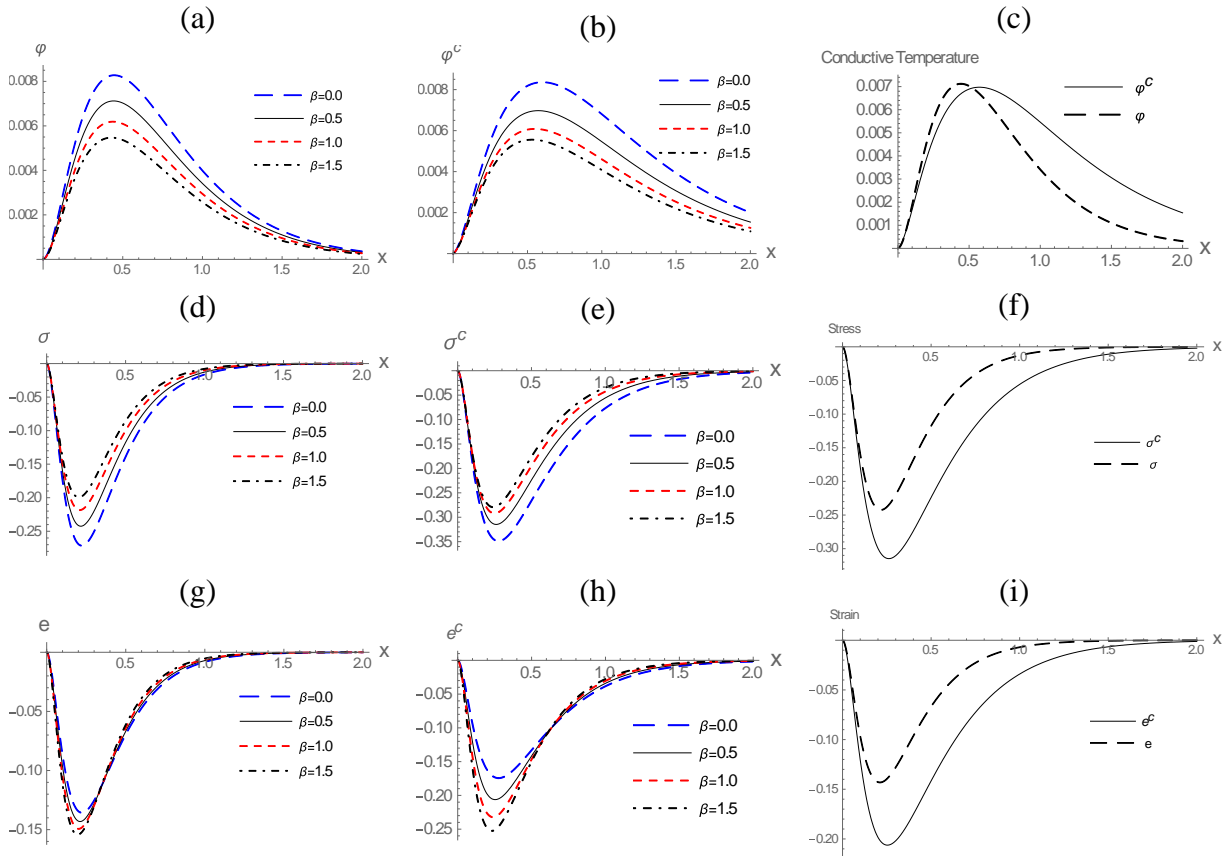


Fig. 1. Effect of fractional order parameter β on φ , σ and e for $\Omega = 6 \times 10^2$, $t = 0.3$, $\tau_o = 0.02$: (a) hyperbolic conductive temperature; (b) parabolic conductive temperature; (c) the hyperbolic and parabolic conductive temperature at $\beta = 0.5$; (d) stress in the hyperbolic case; (e) stress in parabolic case; (f) hyperbolic and parabolic stress at $\beta = 0.5$; (g) strain in hyperbolic case; (h) strain in the parabolic case; (i) hyperbolic and parabolic strain $\beta = 0.5$

Figure 1 illustrates the effects of the fractional-order parameter β on the field functions. In Figures 1 (a) and (b) we noticed that both of the hyperbolic φ , and parabolic conductive temperature φ^c , is inversely proportional to the variation of the fractional-order parameter β , with the peaks occurring at the same point regardless of the value of β , such behavior may be attributed to an increase of the fractionality parameter induces dissipation effects in the medium. Figure 1 (c) shows the comparison between the two types of heat conduction; φ and φ^c . It is also noticed that the hyperbolic heat conduction φ is asymptotically stable, while the heat conduction in a model with classical two temperatures φ^c has local asymptotic stability. Figures 1 (d), (e), and (f) show the effects of fractional order parameter β on the stresses σ and σ^c . Figures 1 (d) and (e) show that the absolute value of the magnitude of the stresses varies inversely with the variation of β , this in accordance with the fact that thermal stress is related to the temperature gradient. In Figure 1 (f), it is seen that the absolute value of the amplitude of the stress σ is less than the stress in the classical two-temperature model σ^c and the stress σ attain its equilibrium state before σ^c .

Figures 1 (g), (h) and (i) illustrate the effects of the fractional-order parameter on the strain. Unlike the effect of β on the stresses, a direct proportion between the absolute value of the amplitude of the strains and the variations of β can be noticed in Fig. 1 (d) and (e).

Figure 2 presents the effects of variations of the pulse intensity Ω on the behavior of the physical quantities φ , σ and e . Figures 2(a), (d) and (g) show that the value of the pulse intensity Ω is directly proportional to the absolute value of the amplitude of the physical quantities φ , σ and e . Figures 2(c), (f) and (i) show significant changes in the amplitude of the field functions φ , σ and e respectively with the two types of heat conduction.

We also noticed a significant change in the absolute value of the amplitude of the field functions φ , σ and e in the two types of heat conduction.

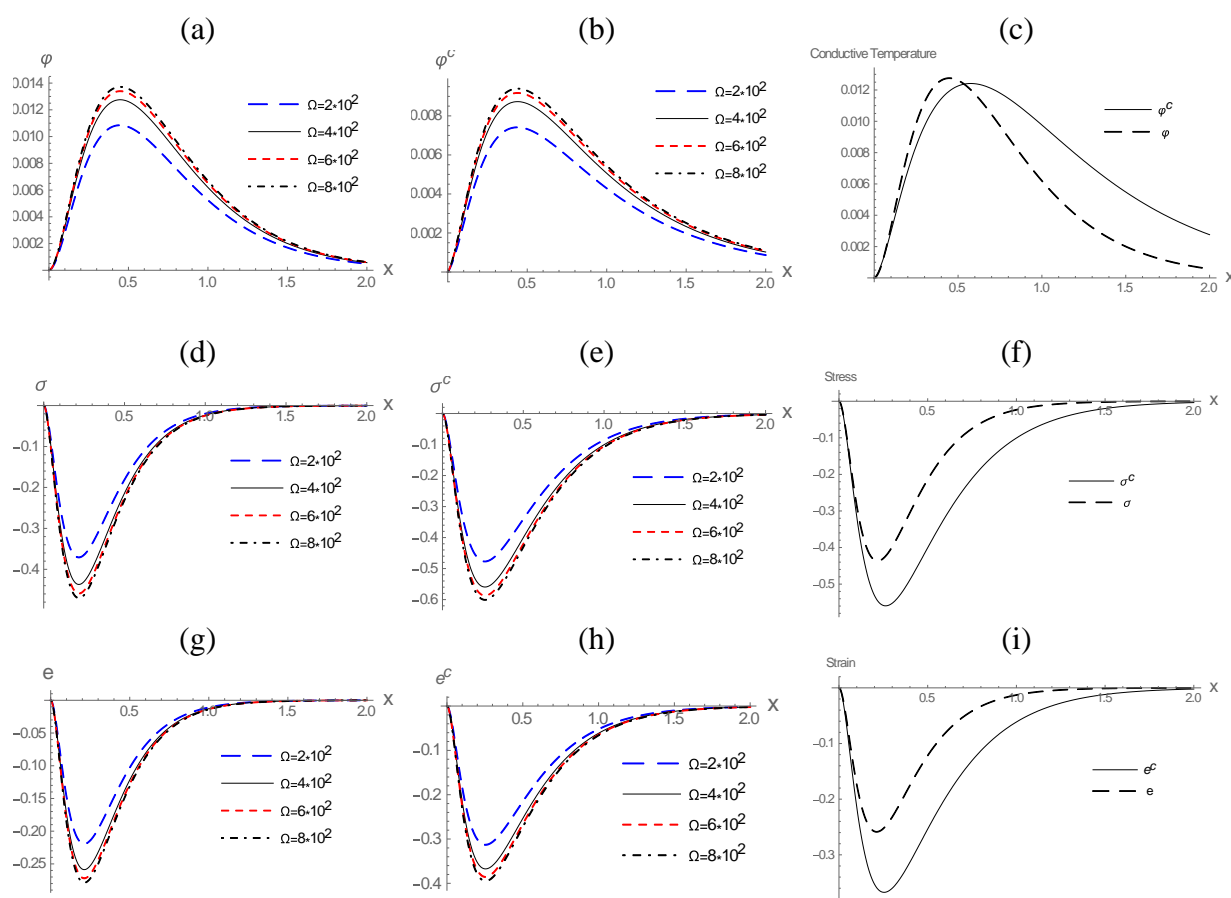


Fig. 2. Effect of pulse parameter Ω on φ , σ and e for $\beta = 0.5$, $t = 0.2$, $\tau_o = 0.02$:

(a) hyperbolic conductive temperature; (b) parabolic conductive temperature;

(c) the hyperbolic and parabolic conductive temperature at $\Omega = 4 \times 10^2$;

(d) stress in the hyperbolic case;

(e) stress in parabolic case; (f) hyperbolic and parabolic stress at $\Omega = 4 \times 10^2$;

(g) strain in hyperbolic case; (h) strain in the parabolic case;

(i) hyperbolic and parabolic strain at $\Omega = 4 \times 10^2$

Figure 3 represent the variations of the field function under the changes of time t . We noticed that the field functions changes significantly with the variation of time t . All the field functions are in direct proportion with the variation of t . Figure 3 (a) and (b) shows that the peaks of the temperatures occur at different points and move away from the near end $x = 0$.

Figures 3 (g), (h) show that the strain resembles the behavior of the stress. Figures 3 (c), (f) and (i) show that the φ , σ and e attain their equilibrium before φ^c , σ^c and e^c , respectively.

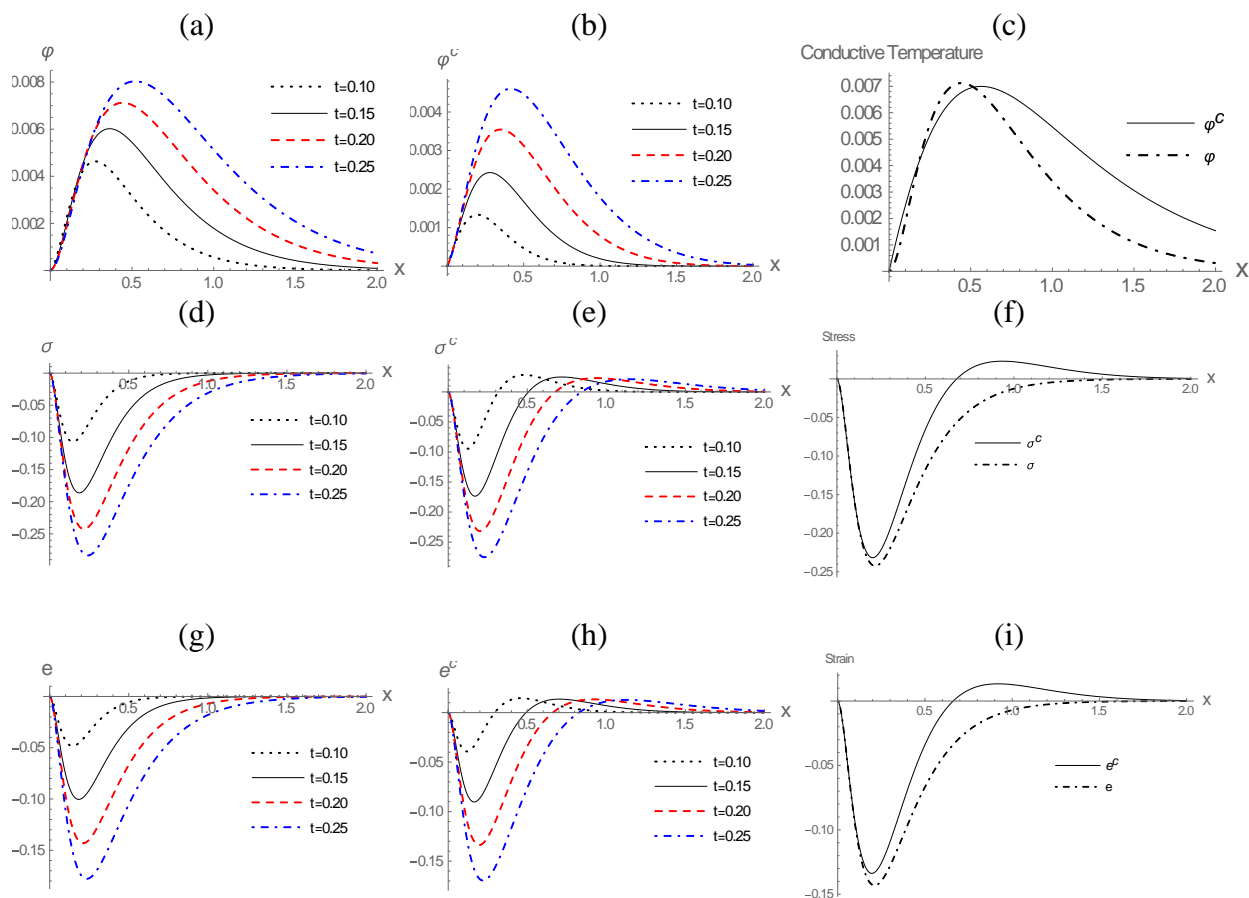


Fig. 3. Effect of time t on φ , σ and e for $\Omega = 10^2$, $\beta = 0.5$, $\tau_o = 0.02$:

- (a) hyperbolic conductive temperature; (b) parabolic conductive temperature;
(c) the hyperbolic and parabolic conductive temperature at $t = 0.2$;
(d) stress in the hyperbolic case;
(e) stress in parabolic case; (f) hyperbolic and parabolic stress at $t = 0.2$;
(g) strain in hyperbolic case; (h) strain in the parabolic case;
(i) hyperbolic and parabolic strain $t = 0.2$

Conclusions

In summary, it is found that the field functions φ , σ and e have asymptotic stability in the hyperbolic case (i.e., in contrast to the classical two-temperature model, where they have local stability). Increasing the strength of the laser pulse leads to an increase in the absolute values of all the field functions magnitudes. The strain resembles the same behavior of the stress with any parameter. Stress and strain tend to equilibrium state rapidly than temperatures. The effect of time on the field functions is more significant than the effects of the other parameters. Increasing the time and the strength of the pulse, pumping more energy into the system, leads to an increase of the absolute values of the amplitude of field functions. Increasing fractional-order parameter, which increases dissipation, results in decreasing the absolute values of the amplitude of φ , σ and e .

Acknowledgements. *The author is grateful to the Deanship of Scientific Research, Prince Sattam Bin Abdulaziz University for extending support and facilities for accomplishing this work.*

References

- [1] Chen PJ, Gurtin ME. On a theory of heat conduction involving two temperatures. *Zeitschrift für angewandte Mathematik und Physik ZAMP*. 1968;19(4): 614-627.
- [2] Chen PJ, Gurtin ME, Williams WO. On the thermodynamics of non-simple elastic materials with two temperatures. *Journal of Applied Mathematics and Physics ZAMP*. 1969;20(1): 107-112.
- [3] Chen PJ, Williams WO. A note on non-simple heat conduction. *Journal of Applied Mathematics and Physics ZAMP*. 1968;19(6): 969-970.
- [4] Boley BA, Tolins IS. Transient coupled thermoelastic boundary value problems in the half-space. *Journal of Applied Mechanics*. 1962;29: 637-646.
- [5] Warren WE, Chen PJ. Wave propagation in the two temperature theory of thermoelasticity. *Acta Mechanica*. 1973;16(1-2): 21-33.
- [6] Indeitsev DA, Osipova EV. A two-temperature model of optical excitation of acoustic waves in conductors. *Doklady Physics*. 2017;62(3): 136-140.
- [7] Shi Y, Zhang Y, Konrad C. Solid-liquid-vapor phase change of a subcooled metal powder particle subjected to nanosecond laser heating. *Nanoscale and Microscale Thermophysical Engineering*. 2007;11(3-4): 301-318.
- [8] Yilbas BS, Kalyon M. Formulation Of Laser Pulse Heating- A Closed Form Solution Including Heating And Cooling Cycles With Pulse Parameter Variation. *Lasers in Engineering*. 2004;14(3): 213-228.
- [9] Othman MI, Zidan ME, Hilal MI. Effect of magnetic field on a rotating thermoelastic medium with voids under thermal loading due to laser pulse with energy dissipation. *Canadian Journal of Physics*. 2014;92(11): 1359-1371.
- [10] Othman MI, Zidan ME, Hilal MI. The effect of initial stress on thermoelastic rotating medium with voids due to laser pulse heating with energy dissipation. *Journal of Thermal Stresses*. 2015;38(8): 835-853.
- [11] Othman MI, Abd-Elaziz EM. The effect of thermal loading due to laser pulse in generalized thermoelastic medium with voids in dual phase lag model. *Journal of Thermal Stresses*. 2015;38(9): 1068-1082.
- [12] Youssef HM. Theory of two-temperature-generalized thermoelasticity. *IMA journal of applied mathematics*. 2006;71(3): 383-390.
- [13] Youssef HM. Theory of two-temperature thermoelasticity without energy dissipation. *Journal of Thermal Stresses*. 2011;34(2): 138-146.
- [14] Youssef HM. Variational principle of two-temperature thermoelasticity without energy dissipation. *Journal of Thermoelasticity*. 2013;1(1): 42-44.
- [15] Youssef HM, El-Bary AA. Theory of Hyperbolic Two-Temperature Generalized Thermoelasticity. *Materials Physics and Mechanics*. 2018;40(2): 158-171.
- [16] Bassiouny E, Abouelnaga Z, Youssef HM. One-dimensional thermoelastic problem of a laser pulse under fractional order equation of motion. *Canadian Journal of Physics*. 2017;95(5): 464-471.
- [17] Miller KS, Ross B. *An Introduction to The Fractional Calculus and Fractional Differential Equations*. John-Wily and Sons Inc, New York; 1993.
- [18] Podlubny I. Geometric and physical interpretation of fractional integration and fractional differentiation. arXiv preprint math/0110241. 2001 Oct 22.
- [19] Caputo M. Linear models of dissipation whose Q is almost frequency independent-II. *Geophysical Journal International*. 1967;13(5): 529-539.

- [20] Caputo M. *Elasticità e dissipazione (Elasticity and anelastic dissipation)*. Zanichelli, Bologna; 1969.
- [21] Caputo M, Mainardi F. Linear models of dissipation in anelastic solids. *La Rivista del Nuovo Cimento*. 1971;1(2): 161-198.
- [22] Caputo M, Mainardi F. A new dissipation model based on memory mechanism. *Pure and Applied Geophysics*. 1971;91(1): 134-147.
- [23] Caputo M. Vibrations of an infinite viscoelastic layer with a dissipative memory. *The Journal of the Acoustical Society of America*. 1974;56(3): 897-904.
- [24] Rudolf H (ed.) *Applications of fractional calculus in physics*. World scientific; 2000.
- [25] Bassiouny E, Youssef HM. Sandwich structure panel subjected to thermal loading using fractional order equation of motion and moving heat source. *Canadian Journal of Physics*. 2018;96(2): 174-182.
- [26] Bassiouny E, Abouelnaga Z and Algelany AM. Thermoelastic Model of Ceramic Materials with Fractional Order Strain and Variable Thermal Conductivity. *International Journal of Engineering Research and Technology*. 2018;11(11): 1795-1810.
- [27] Youssef HM. Theory of generalized thermoelasticity with fractional order strain. *Journal of Vibration and Control*. 2016;22(18): 3840-3857.
- [28] El-Karamany AS, Ezzat MA. On fractional thermoelasticity. *Mathematics and Mechanics of Solids*. 2011;16(3): 334-346.
- [29] Sherief HH, El-Sayed AM, El-Latief AA. Fractional order theory of thermoelasticity. *International Journal of Solids and structures*. 2010;47(2): 269-275.
- [30] Honig Honig G, Hirdes U. A method for the numerical inversion of Laplace transforms. *Journal of Computational and Applied Mathematics*. 1984;10(1): 113-132.
- [31] Sherief HH. State space approach to thermoelasticity with two relaxation times. *International journal of engineering science*. 1993;31(8): 1177-1189.

HYBRID ACOUSTIC PANEL: THE EFFECT OF FIBER VOLUME FRACTION AND PANEL THICKNESS

NPG. Suardana^{1*}, IKG. Sugita¹, IGN. Wardana²

¹Department of Mechanical Engineering, Udayana University, Badung, Bali, Indonesia

²Department of Civil Engineering, Udayana University, Badung, Bali, Indonesia

*e-mail: npgsuardana@unud.ac.id

Abstract. The composite panel test were made of gypsum, pumice powder, and glue with composition of 1:2:1/2 and coconut fiber with volume fraction variation of 10%, 15%, 20%, 25%, and 30% by using Hand lay-up technique. The sound absorption panel was tested for acoustic and mechanical characteristic using test standard with ASTM E1050, ASTM D256, and ASTM D790, respectively. The result of data analysis was presented graphically and the bounding of composite materials was analysed by using SEM photograph. From the data analysis for 10mm thickness of composite with 30% fiber volume fraction gained the highest sound absorption coefficient, the highest impact strength occurred on composite with 25% fiber volume fraction. Meanwhile, the strength and modulus of bending occurred on composite with 15% fiber volume fraction. Sound absorption coefficient for composite with 15mm thickness was higher than 10mm for 10% fiber volume fraction.

Keyword: pumice waste, coconut fiber, gypsum, acoustic and mechanic

1. Introduction

Comfortable and soundproof room is highly needed in the factory, hotel, office or in private room. Soundproof material has an important role to absorb sound so it will decrease the sound resonance intensity to the ears so there will be more comfortable for the user.

The soundproof material is in form of porous material, resonator and panel [1]. Type of the existing soundproof material is a porous material such as foam, glass wool, Rockwool, and resonator. These material usage is relatively expensive and could not be exposed because resulting irritation on skin and respiration.

Development of soundproof with natural material becomes the best choice because it is environmental friendly by improving the usability of wasted material. Some researches on soundproof have been conducted by [1], who develops soundproof from recycled polyester material.

Abundant pumice waste becomes economic consideration to engineer this rock to be more useful material. Pumice has porous structure which is the same with the existing soundproof material. This rock has characteristics of porous structure, light, easy to be gained and cheap but fragile. The abundant pumice waste comes from the result of pumice sieve of unused pumice since the size does not fulfil the criteria of packaging to be marketed (aggregate size of pumice waste less than 10 mm).

Coconut fiber waste is also abundant but it is used for mat, or becomes traditional firing. Coconut fiber is a Lignocellulosic fiber, brittle and possibly modified chemically, non-toxic [2,3] and biodegradable, low density, not abrasive on the tool to work it [3]. Moreover, the coconut fiber waste does not impact the environment. It has holes in the fiber axis [4] so it is

suitable for soundproof material and decrease the density type of the formed material [5]. Research about multi-layer coconut fiber with little latex binder as soundproof shows sound absorption coefficient of 0.7-0.85 for frequency 500-2500Hz which is competitive with the marketed material such as rock wool and other fiber synthetic [6].

This research reviews how pumice hybrid and coconut fiber as amplifier and gypsum as the binder could absorb sound well so it can be applied as acoustic wall.

2. Purpose of the Research

The use of industrial waste is one of the good ways to maximize the existing natural resources so it can be beneficial for human life. The abundant pumice and coconut fiber wastes in Indonesia are highly potential to be developed for composite material of soundproof. This research has specific purposes as follows:

- a. Determining the acoustic characteristic of sound absorption of the pumice-coconut fiber hybrid composite as the effect of coconut fiber volume fraction variation.
- b. Determining mechanical strength of impact load and flexibility of the pumice-coconut fiber hybrid composite as the effect of coconut fiber volume fraction variation.

3. Research Method

The research procedures are firstly the pumice was cleaned by pure water to get clean particles; secondly it was heated with 65°C for 24 hours to get dried pumice. The pumice was sifted to get $\leq 1\text{mm}$ pumice size. The coconut fiber treatment was done by cleaning coconut fiber, boiling the coconut fiber to remove the dirt and then it was dried in 70°C for 24 hours. The fiber was cut off into 10-15mm in length. The fiber was treated by 5% NaOH concentration in 50°C for 2 hours and then cleaned. The fiber was dried in 70°C for 24 hours.

The composite moulding process was done by using hand lay-up method, with 100mm in diameter of mould with 10mm and 15mm thickness. The mould surface was cleaned from any dirt by using tissue and tinner to reduce impurity factor and then covered by glycerine. Afterward, mixed gypsum with glue, and then the pumice was mixed into this mixture. The coconut fiber was poured into this mixture to be hybrid composites in container based on composition of gypsum mixture: pumice: glue 1:2:1/2. Meanwhile, volume fraction of coconut fiber was varied on percentage of 10%, 15%, 20%, 25% and 30%.

Testing of specimen sound absorption coefficient was done by using test machine of impedance tube standing wave method with specification of Measuring Amplifier Brüel & Kjær type 2636, Sine Generator Brüel & Kjær type 1054. The test was done on frequency 120-4000 Hz (ASTM C 423-66). Impact and bending test was done by using Impact (Charpy Type) test and bending test of Tensilon Universal Testing Machine with type RTG 1310. The data analysis was done by using graphic analysis. The final result was in form of data trend which was plotted to be a frequency graphic (Hz)-Coefficient sound absorption (α).

4. Result and Discussion

Based on Figure 1 of relationship diagram of frequency with sound absorption coefficient for composite 10%, 15%, 20%, 25% and 30% coconut fiber with 10mm thickness, there are no trend since the data are random and fluctuating. It is caused by the effect of back cavity depth on sound absorption characteristic of all composite samples. It can be seen that the pick sound absorption happened in some certain frequencies which is possibly caused by back cavity depth, which is similar with the research result of other researchers [7,8]. However, sound absorption coefficient from all specimens had sound absorption coefficient (α) > 0.8 , which means that the sound absorptions are excellent.

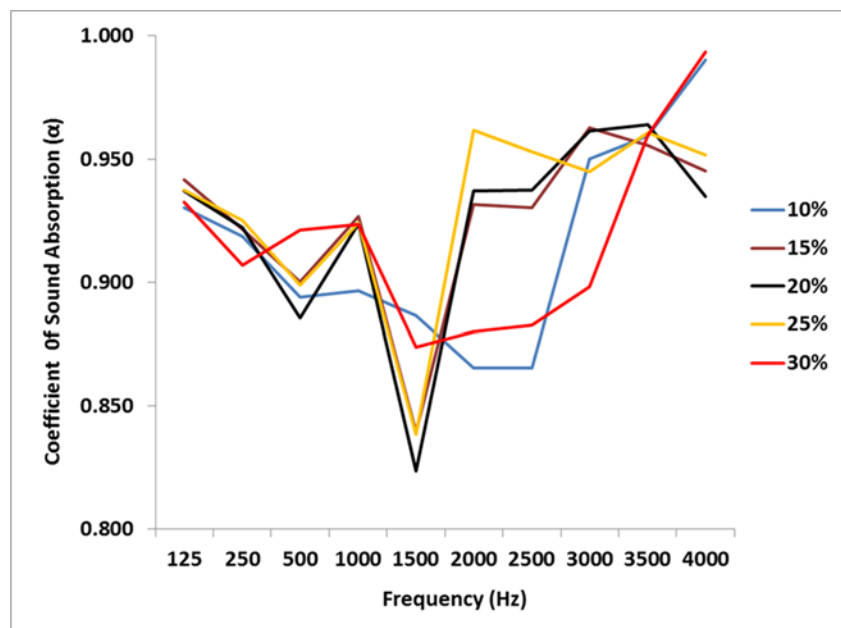


Fig. 1. The effect of frequency on sound absorption coefficient for composites 10%, 15%, 20%, 25% and 30% coconut fiber with 10mm thickness

Coconut fiber addition on the composite improved the sound absorption coefficient. This condition is caused by the absorber characteristic of the fiber and micro pore structure of pumice and gypsum. Besides that, addition of fiber could increase the number of micro empty spaces among the fibers or improving composite porosity so it can improve interaction between sound wave and composite material which causes friction improvement which finally increase the change of sound energy to be lost heat energy [9].

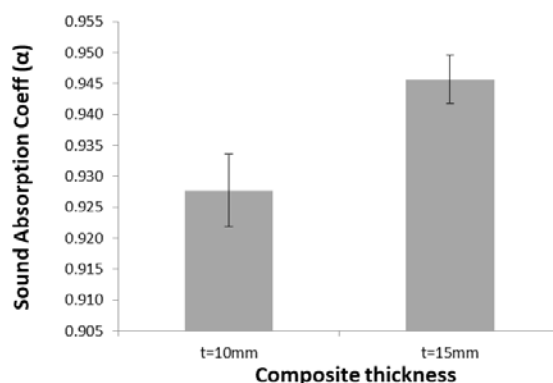


Fig. 2. Comparison diagram of sound absorption coefficient for composite of 10mm and 15mm thickness for 10% fiber volume fraction

Figure 2 shows that thicker composite has bigger sound absorption coefficient than thinner composite. It is because of the thicker of the composite the more spaces or micro spaces owned so the bigger sound energy that could be absorbed. But the addition of thickness will increase the weight of the material and narrow the space. So that future research, how to make thin material with high sound absorption will be done.

Figure 3 shows that the highest impact strength occurred on specimen of 25% volume fraction and then followed by 15% and 20% of fiber volume. It occurred because the matrix binds almost all fiber surface as shown by Figure 4c in which the matrix still fully attaches on the fiber while on the 15% fiber volume fraction the matrix still attaches on the fiber but mostly detached (Fig. 4a), as well as on 20% fiber volume fraction the matrix does not attach

on the fiber well (Fig. 4b). From the data, there is possibility that 25% volume fraction is the highest limit of volume fraction to get the highest specimen impact strength. This explanation is supported by SEM photo of Fig. 4c in which the matrix is still intact binding fibers.

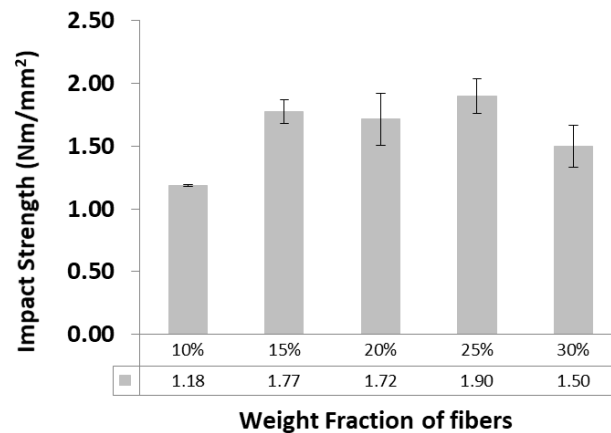


Fig. 3. The effect of coconut fiber volume fraction on composite impact strength

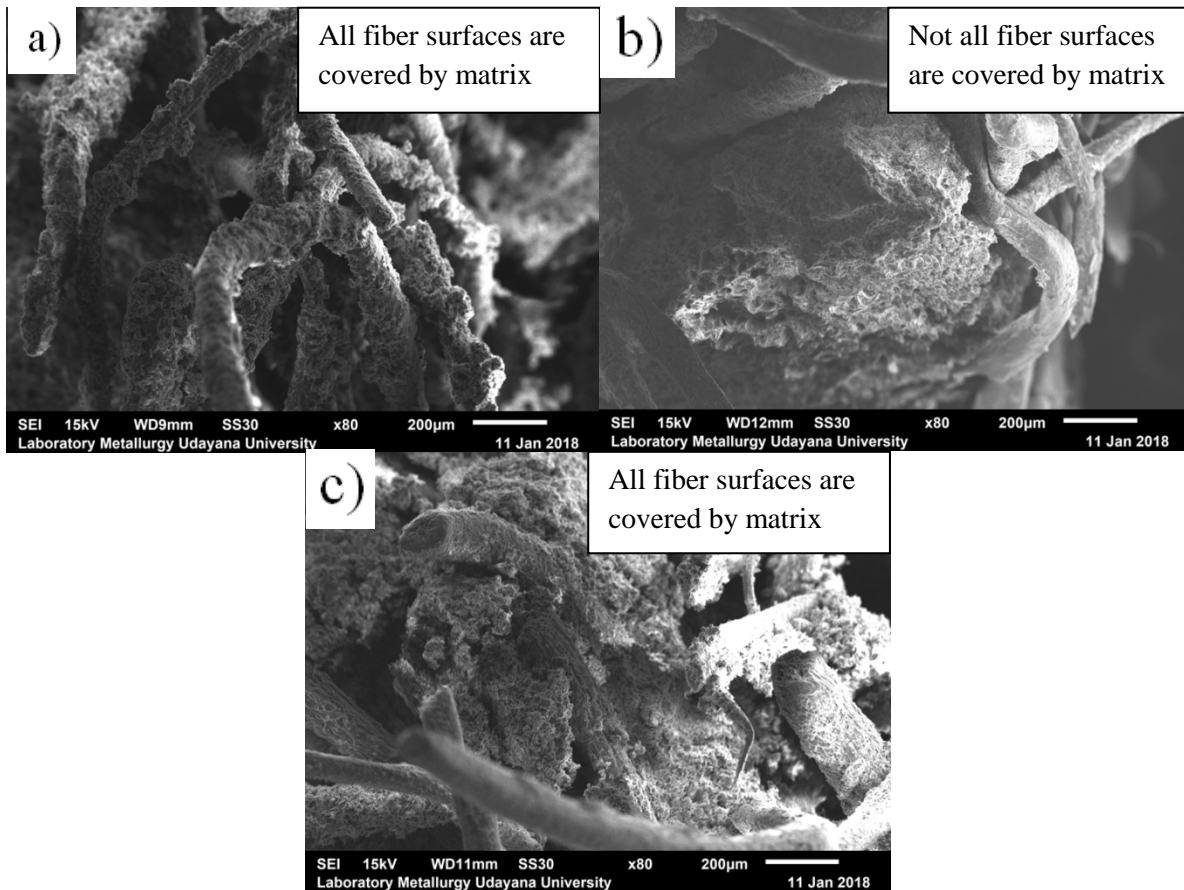


Fig. 4. SEM Photo of composite fraction with fiber volume fraction:
a) 15%, b) 20% and c) 25%

Figure 5 shows that the highest bending strength and modulus bending occurred on specimen of 15% fiber volume fraction and the lowest score gained by 25% volume fraction. It is caused by bending behavior in which in this specimen, the matrix bonding rigidity with pumice takes the most important role which is different with impact in which matrix and pumice are fragile so the fiber takes more roles on it. In other words, bending strength and

modulus bending increases with the decreasing fiber volume fraction of coconut fibers. As a result, the increase of gypsum and pumice stone that has more rigid properties than fiber on the composites were concluded to enhance bending strength and modulus.

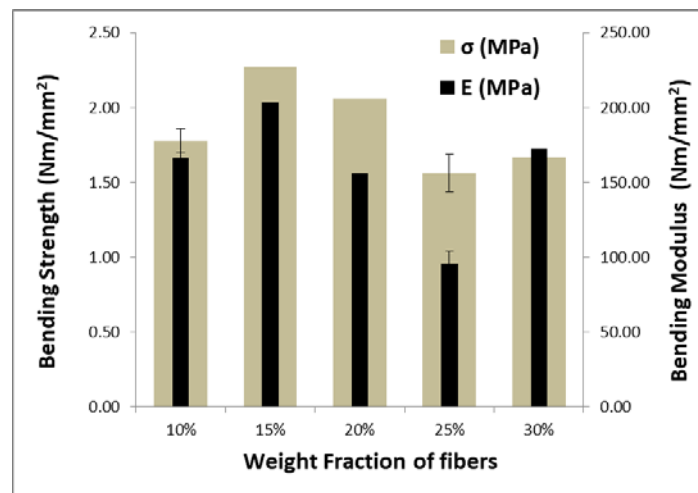


Fig. 5. The effect of coconut fiber volume fraction on composite bending strength

5. Conclusion

This study aimed the investigation of the effect of fiber volume fraction and panel thickness of hybrid acoustic panels which are made of gypsum, pumice powder, and glue with composition of 1:2:1/2 and coconut fiber with volume fraction variation of 10%, 15%, 20%, 25%, and 30% on sound absorption, impact strength and bending strength. According to this study and analysis, that can conclude that the sound absorption coefficient (α) is bigger than 0.8 for all specimen which means that the sound absorption is categorized as excellent, since good material for sound absorption at least $\alpha=0.3$. The thicker the composite, the sound absorption coefficient increases as well. For mechanical properties, the highest impact strength occurred on composite with 25% fiber volume fraction. The highest bending strength and modulus bending specimen occurred on 15% volume fraction. Thus, optimum volume fraction for composite pumice/gypsum/glue to have high sound absorption coefficient, high impact strength and high modulus bending is 15%.

Acknowledgement. This work was supported by the Directorate of Research and Community Services, Directorate General of Research and Development Strengthening, Ministry of Research, Technology, and Higher Education of Republic Indonesia, with agreement letter No. 415.12/UN14.4.A/PL/2017.

References

- [1] Lee Y, Joo C. Sound absorption properties of recycled polyester fibrous assembly absorbers. *AUTEX Research Journal*: 2003;3(2): 78-84.
- [2] Rahman MM, Khan MA. Surface treatment of coir (*Cocos nucifera*) fibers and its influence on the fibers' physico-mechanical properties. *Composite Science Technology*. 2007;67(11-12): 2369-2376.
- [3] Tomczak F, Sydenstricker THD, Satyanarayana KG. Studies on lignocellulosic fibres of Brazil. *Composites Part A: Applied Science and Manufacturing*. 2007;38(7): 1710-1721.
- [4] Brahmakumar M, Pavithran C, Pillai RM. Coconut fiber reinforced polyethylene composites such as effect of natural waxy surface layer of the fiber on fiber or matrix interfacial bonding and strength of composites. *Composite Science and Technology*. 2005;65(3-4): 563-569.

- [5] Wallenberger FT, Weston N. *Natural fibers, plastics and composites*. USA: Kluwer academic publisher; 2004.
- [6] Zulkifli R, Mohd NMJ, Mat TMF, Ismail AR, Nuawi MZ. Acoustic properties of multi-layer coir fibres sound absorption panel. *Journal of Applied Sciences*. 2008;8(20): 3709-3714.
- [7] Jiang S, Xu YY, Zhang HP, White CB, Yan X. Seven-hole hollow polyester fibers as reinforcement in sound absorption chlorinated polyethylene composite. *Applied Acoustics*. 2012;73(3): 243-247.
- [8] Nanting Z, Xueyan G, Mingqi Y, Lan Y, Zhongde S, Yiping Q. Mechanical and sound adsorption properties of cellular poly(lacticacid) matrix composites reinforced with 3D ramie fabrics woven with co-wrapped yarns. *Industrial Crops and Products*. 2014;56: 1-8.
- [9] Seyda C, Dilek K, Habip D. Investigation of pumice stone powder coating of multilayer surfaces in relation to acoustic and thermal insulation. *Journal of Industrial Textiles*. 2015;44(4): 639-661.

STRUCTURAL TRANSFORMATION OF HCP METALLIC NANOWIRE USING CLERI-ROSATO POTENTIAL

M.M. Aish*

Physics Department, Faculty of Science, Menoufia University, 32511 Shebin Elkom, Menofia, Egypt

*e-mail: mohamedeash2@yahoo.com

Abstract. Sub-atomic Dynamic simulations have been carried out on some single-crystal hexagonal metals, HCP nanowires (Cd, Co, Mg, Ti, and Zr) upon application of uniaxial tension with a speed of 20 m/s and to investigate the nature of deformation and fracture. The deformation corresponds to the direction $\langle 0001 \rangle$ plane. A many-body interatomic potential for HCP nanowires within the second-moment approximation of the tight-binding model (the Cleri-Rosato potentials) was employed to carry out three dimensional MD simulations. A computer experiment is performed at a temperature 300K. The stored energy diagrams obtained at various time by the MD simulations of the tensile specimens of these metallic nanowires show a rapid increase in stress up to a maximum followed by a gradual drop to zero when the specimen fails by ductile fracture. The feature of deformation energy can be divided into three regions: quasi-elastic, plastic and failure. The nature of deformation, slipping, twinning and necking were studied. Stress decreased with increasing volume and the breaking position increases. The results showed that breaking position depended on the nanowire length. From this, it appears that Cleri-Rosato potentials make good represent for the deformation behavior of HCP metallic nanowires.

Keywords: molecular dynamics, uniaxial tension, Cleri-Rosato, nanowires, tight-binding and failure

1. Introduction

Physical and mechanical properties of the substances in condensed matter physics depended on size and structure: With decreasing size of the elementary particles that make up the material, increase the strength and feature of plasticity changes were studied in [1]. In the past ten years, special attention has been given to the studied the properties of metallic nanowires and nanofilms and another nano-objects [2]. Nanowires referred to as materials, which are in the cross-section size is not more than 100 nm and significantly extended in length. Other important systems include metallic nanostructured and alloys, which have unique properties, and can be used as structural or functional materials [1]. First of all, this is due to the fact that they have been studied and has accumulated extensive experimental data. Of particular interest in terms of the choice of the object of study are those metals and alloys, in which, first, has the longest period of nanosize. Second, the weak-stable to external influences (temperature, load, doping and so on.). Third, there is a range of structural states near the boundary of stability loss, and these states are in equilibrium or near-equilibrium.

These requirements are responsible, in particular, ordered alloys and intermetallic compounds which contain long periodic structure (LPS). From the normal ordered systems with a simple superstructure, they differ in that the alloys of this class ordered arrangement of atoms periodically or quasi-periodically broken antiphase boundaries (APB). Normally, in ordered alloys and intermetallic compounds APB energetically favorable, however, in

systems with long-period equilibrium nanostructure APB are elements of the structure. Given that the mechanisms of structural-energy transformations at various load conditions, in particular uniaxial strain, help to explain the abnormal strength properties of long-period metal alloys (LPMA), ie the properties of LPMR resist destruction and irreversible change in the shape, the task of studying the mechanisms of structural-energy transformations occurring during high uniaxial strain tension of HCP metallic (Cd, Co, Mg, Ti, and Zr) nanowires, containing LPS. Because of the strong anisotropy of the structure, defects in HCP metals and alloys have a number of features that is of great interest to them and requires detailed consideration. In an ideal HCP – structure each atom is characterized by 6 sets [1|4|2|1] and 6 sets [1|4|2|2]. The ability of metals to form alloys with specific physical and mechanical properties is crucial for the technical application. Because of the strong anisotropy of the structure, defects in HCP metals and alloys have a number of features that is of great interest to them and requires detailed consideration.

Currently, the many-body potentials of the embedded-atom method (EAM) [1,2], Finnis–Sinclair [3] potentials and the second-moment approximation (SMA) of the tight-binding (TB) method [4-9] were studied. According to [4,5], the TB-SMA expression of the total energy of a metallic system is based on a small set of adjustable parameters, which can be determined by adjusting to experimental data [9,10] or ab-initio results [1,10-13]. The author of [12], was studied the features of structural transformations of HCP metallic Ti nanowires using Cleri-Rosato potential at low temperature. In [13-17] the mechanical properties of Ni nanowires were studied in detail. There were other representations [18-20].

Thus, the present work, with the assistance of molecular dynamics simulation (Cleri-Rosato potential), structural-energy transformations in HCP Metallic (Cd, Co, Mg, Ti, and Zr) nanowires, under high-speed deformation of uniaxial tension been processed using mathematical modeling. To the study structural-energy transformations, under high-speed of deformation (10^{10} s^{-1}) were applied on pure metallic nanowire (Cd, Co, Mg, Ti, and Zr). This material has a positive temperature dependence of yield stress. The deformation in such alloys can be a combination of structural and superstructural changes, which entails various effects.

Finally this article discusses the results of Molecular Dynamics simulation to HCP phase in metallic nanowires, obtained using the interatomic potential of strong coupling (tight-binding).

2. MD simulation methodology

MD is a simulation technique where the time evolution of an interacting atoms is followed by integrating their equation of motion. It consists of integrating Newton's second law for each atom present in the system by discretization of time. In general, it is difficult to obtain an analytical solution that precisely describes the atoms' trajectories. Therefore, the equations of motion are solved numerically using a time-discretized finite difference methodology such as the Verlet method or the velocity Verlet method, which incorporate the velocities explicitly into the integration scheme. The initial atomic positions for metallic systems are defined on the crystal lattice of the metal, while the initial velocities are assigned according to the Boltzmann distribution at the given simulation temperature. The validity and accuracy of MD simulation results depend on the accuracy of the interatomic forces used as inputs, which rely on the selection of an efficient underlying interatomic force-field potential. For modeling metallic systems, the most

Modeling considered atomic systems was carried out in the framework of multiparticle tight-binding potential Cleri-Rosato. The repulsive part of this potential is short-range repulsive pair potential Born-Mayer and the attractive part arises from the so-called tight-binding (TB) method second-moment approximation to the electronic density of state in which the ion-ion interaction is described by the band terminology [6]. The uses of these

potentials are well established in a number of studies [7-10]. This potential has been used in several studies of bulk and cluster systems transition and noble metals [1,6-7,13].

Commonly used potential is the semi-empirical embedded atom method (EAM) potential. The parameters of EAM potential are generally obtained by fitting cohesive energy, equilibrium lattice constant, elastic constants, unrelaxed vacancy formation energy, bond length, and diatomic bond strength. Since its introduction, the ability and viability of EAM in modeling metals have been extensively analyzed and tested. The classic EAM method is not suitable for describing systems in which covalent bonds are present, such as carbon (in diamond or graphite structures), because the EAM description does not account for the angular dependence of the interatomic interactions. To account for angular dependence, as in the case of the HCP lattice where it is important, a modified embedded atom method was proposed. The total energy U in a system of N atoms in the EAM framework can be written as:

$$U_s = \sum_i (E_i^R + E_i^B), \quad (1)$$

where

$$E_i^R = \sum_{j \neq i} U_{ij}(r_{ij}) = \sum_j A \cdot \exp[-p(\frac{r_{ij}}{r_0} - 1)], \quad (2)$$

is the two-body term, and

$$E_i^B = -\sqrt{\sum_{j \neq i} \varphi(r_{ij})}, \quad (3)$$

$$\varphi(r_{ij}) = \zeta^2 \cdot \exp[2q(\frac{r_{ij}}{r_0} - 1)], \quad (4)$$

is the many-body term. Where A , p , q , ζ , r_0 - are adjustable parameters governing the interaction between those atoms, r_{ij} - the separation between atoms i and j . The values of Potential parameters Cleri-Rosato were taken from [21]. Table 1 gives the parameters of tight-binding potentials for HCP metals used in this work [21].

Table 1. Parameters of tight-binding potentials for HCP metals [21]

	A (eV)	ζ (eV)	p	q	β
Cd	0.1420	0.8117	10.612	5.206	1.8856
Co	0.0950	1.4980	11.604	2.286	1.6232
Mg	0.0290	0.4992	12.820	2.257	1.6335
Ti	0.1519	1.8112	8.620	2.390	1.587
Zr	0.1934	2.2792	8.250	2.249	1.5925

The model can be used to describe quite well elastic, plastic, defect and mechanical properties of a wide range of FCC- and HCP-metals. Verlet algorithm used to determine the velocities of atomic motion in the simulation were. Cleri-Rosato potentials which were proposed by [21] have already worked well in HCP nanowires studies.

The use of such a cutoff radius ensures that the calculations will not consume large amounts of computational time in evaluating the forces that are near zero. The MD simulations require the solution of $6N$ (N -total number of atoms) simultaneous, coupled, first-order differential equations of motion. This solution is obtained using a fourth-order Runge-Kutta algorithm. Integration accuracy is monitored using back-integration and energy conservation requirements with the velocity reset procedure turned off. The MD simulations were carried out till separation occurs in the tensile specimen.

3. Results and discussion

Since the deformation and fracture of HCP nanowires are of main interest in this work (Table 2). The specimen used for the studied section is a nanowire of $12a_0 \times 12a_0 \times 12c_0$. The total number of atoms used in the simulations equal 1928 according on the crystal structure. The crystal was set-up with a hexagonal orientation and the uniaxial tensile force was applied along the [0001] direction. The feature of deformation, slipping, twinning and necking were studied.

Table 2 gives the measured tensile strength and strain to fracture of the various materials used in this work. As can be expected, Zr exhibits the highest strength (yield strength of =23GPa) while Mg exhibits the lowest strength (yield strength of =4GPa). The strength of Ti was estimated to be=14GPa. The strength of Co was estimated to be =22.5GPa. The strength of Cd was estimated to be =6 GPa. Cadmium showed an earlier fracture while Cobaltshowed the maximum strain before fracture.

Table 2. MD results for calculating of HCP nanowires at 300 K including yielding time, yielding stress and breaking time

HCP Nanowire	Yielding point		Breaking time
	σ (GPa)	T, Ps	t , Ps
Cd	6	10	135
Co	22.5	8	170
Mg	4	8	140
Ti	14	4	150
Zr	23	4	140

Three stages deformation. The experiments were obtained plots of the stored energy of deformation at various times, reflecting the processes in the HCP nanowires during deformation. There are three stages of deformation: the quasi-elastic deformation (I), plastic deformation (II) and the breaking (failure) (III).

For all HCP nanowires, in the first stage there was almost linear increase in stress. The initial stage quasi-elastic area there is only relative displacement of atoms and there are no defects. Therefore, in this region the energy stored varies periodically. This stage is completed at 8 Ps, 8 Ps, 4 Ps, 4 Ps for Mg, Co, Ti and Zr nanowires, respectively. The sharp fall takes place only at the point of transition from the first to second stages of deformation (Fig. 1).

Analysis of the graphs in Fig. 1 shows that the average duration of the first stage of deformation for nanowire, The duration of the plastic deformation step is 210, 160, 165, 115 Ps, for Mg, Co, Ti and Zr nanowires, respectively.

The value of the stored energy at the peak of deformation schedule at the end of the first stage for the reduced nanowires equals 0.05, 0.07, 0.05 and 0.045 eV / atom, respectively. The levels of stored energy at the end of the plastic deformation steps are equals 0.065, 0.145, 0.115, and 0.112 eV / atom, respectively. The neck of the HCP nanowire forms after the slips happened, and the deformations have been carried mainly through the elongation of the neck. Through further analysis, we find that the last stage of plastic deformation of the neck is formed; deformation develops mainly due to the reconstruction and rebuilding of the neck area. Outside this area, the HCP nanowires ordered structure is retained and there are significant changes. Beyond the neck region, atomic structures have no significant changes. The atomic rearrangements in the neck region induce the zigzag increase–decrease in stress as the strain is increased. The atoms, close to the narrowest region of the neck, are highly disordered.

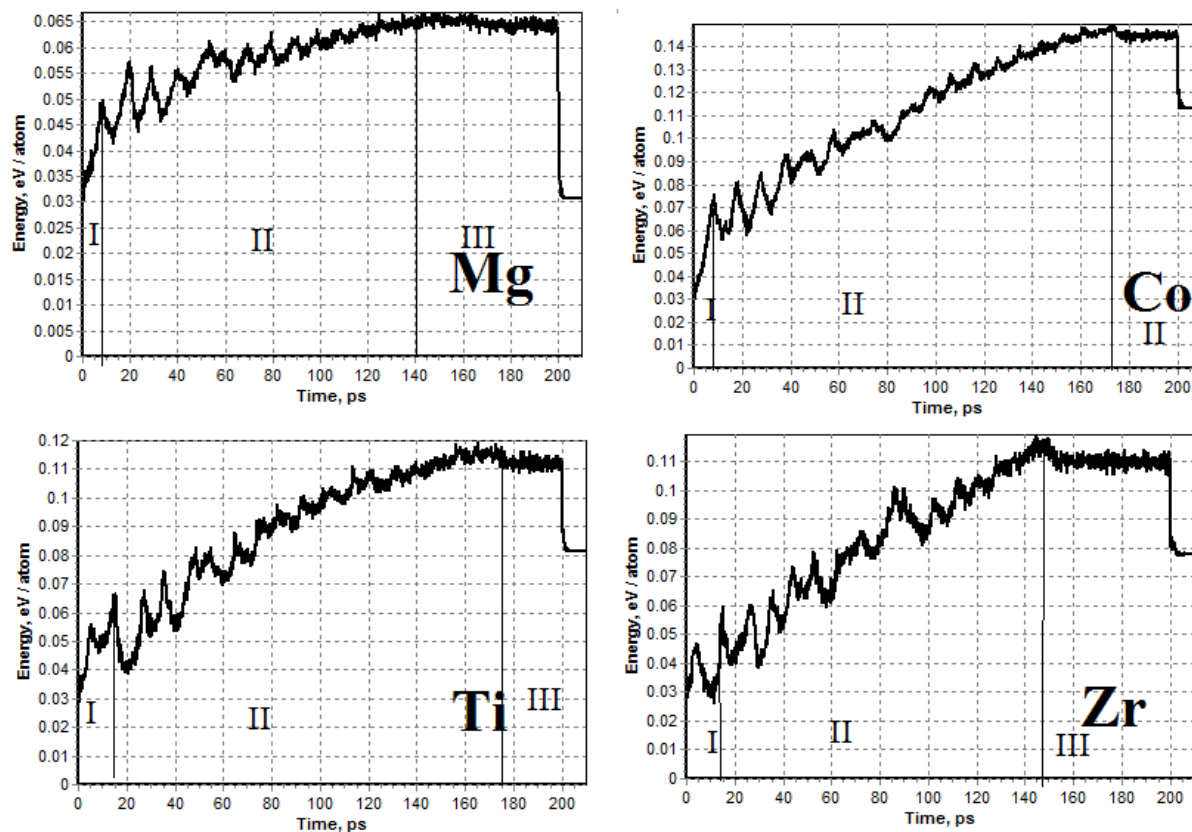


Fig. 1. The dependence of the energy stored by the deformation time of the experiment at 300 K at various time of uniaxial loading for Mg, Co, Ti and Zr nanowires

At the point of breaking, we observe a one-atom thick. With further pulling of the HCP nanowires, the bond between the two atoms lying in the one-atom breaks and then the rupture happens. As can be expected Zirconium exhibits the highest ultimate strength (≈ 26 GPa), while the ultimate strength of Titanium nanowire was estimated to be 18 GPa.

Structure transformation of HCP metallic nanowire. The MD simulation plots of the XOY plane of the tensile specimens at various stages of uniaxial tension are shown in Figs. 2-5 are for the HCP materials, Cd, Co, Mg, Ti and Zr, respectively, It may be noted that the discussion of the results presented here is based not only on the MD simulation plots of the various stages presented here but also on the detailed study of the animation of the process [12].

Figure 6 shows a small compressive bulge of the specimen after the relaxation at time 4 Ps for Zr. A similar situation is found for the other HCP metals investigated, namely, Cd, Co, Mg and Ti. Considerable disorder in the XOY plane of the crystal was observed during the early stages of deformation for all HCP metals (up to 50 Ps as in Figs. 2-5).

As the HCP nanowires was extended, necking area can be seen at times 135 Ps, 170 Ps, 150 Ps, 140 Ps for Cd, Co, Mg and Zr nanowires, respectively, (Figs. 2-5). Since Co is a highly ductile material, the atoms hold together under larger strain before the dislocations formed during the elastic and plastic deformation dislocation and form a ductile fracture. Towards the end of plastic deformation, the neck is elongated almost linearly to a very large strain (Fig. 2). On subsequent pulling, the necked region separates in the failure at 170 Ps.

The radius of the neck was found to increase with increase in the deformation of the nanowire and to decrease with decrease in the ductility. Thus, the radius decreases as we go from Co to Zr to Co to Mg. The region of disordered material as well as the extent of vacancy formation was also found to decrease with decrease in the ductility of the wire.

Initially, dislocations at $\approx 35^\circ$ were observed in the MD data for the case of Zr but due to the high disorder, further dislocation propagation can be observed. Based on the results, as well as the MD simulations at first stage of deformation (Figs. 2-5), the strain to fracture was observed to the HCP nanowires. This can be observed by comparing Figs. 2-5 which shows the variations in the strain to fracture of various nanowires. In the case of HCP nanowires, the work material was disordered from the early stages of necking till the end of the experiment.

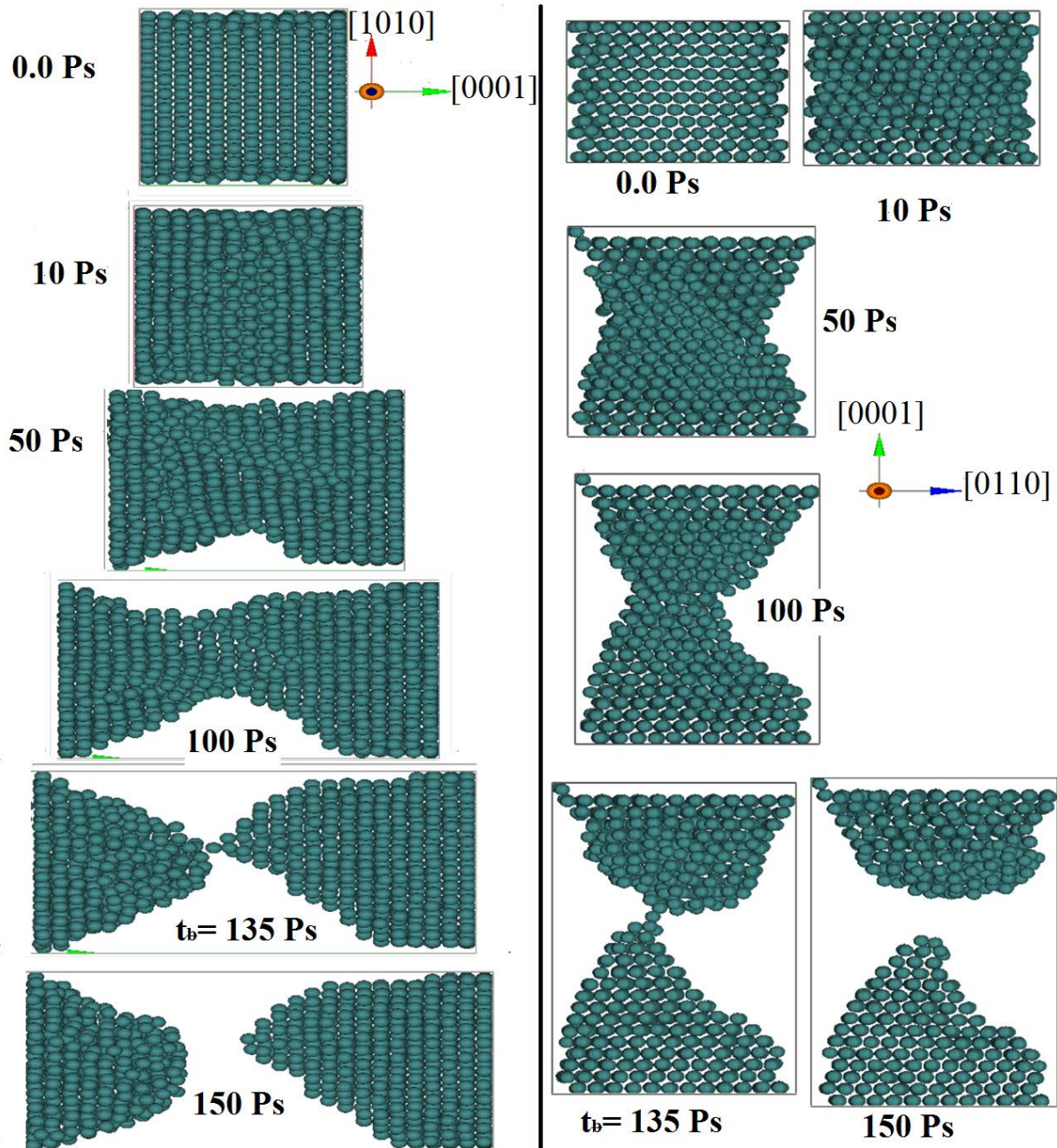


Fig. 2. MD simulation plots of the gage section of a tensile specimen at various time of uniaxial loading for Cd nano-wire in plane [1010] right and in plane [0110] left

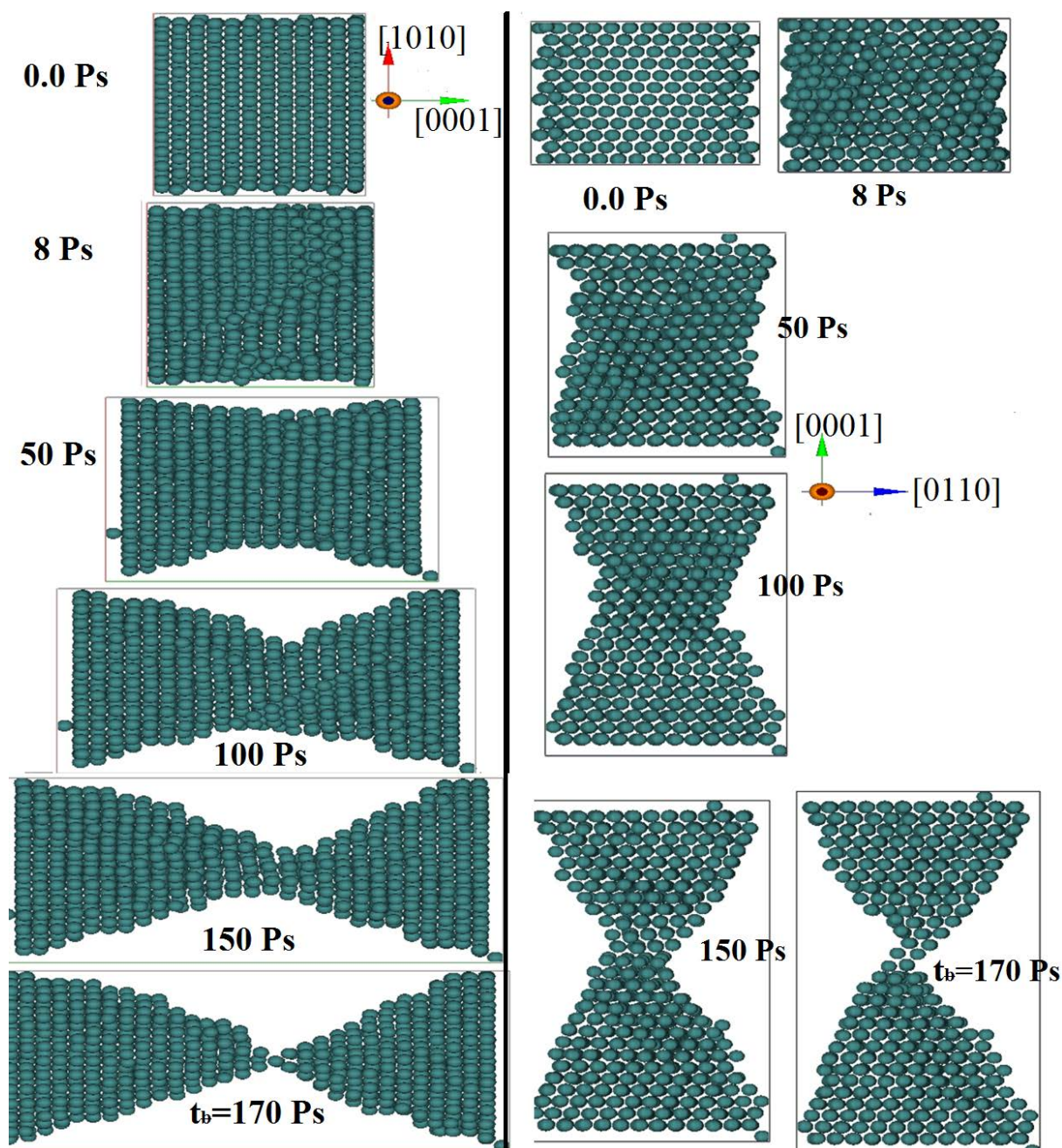


Fig. 3. MD simulation plots of the gage section of a tensile specimen at various time of uniaxial loading for Co nanowire in plane $[1010]$ right and in plane $[0110]$ left

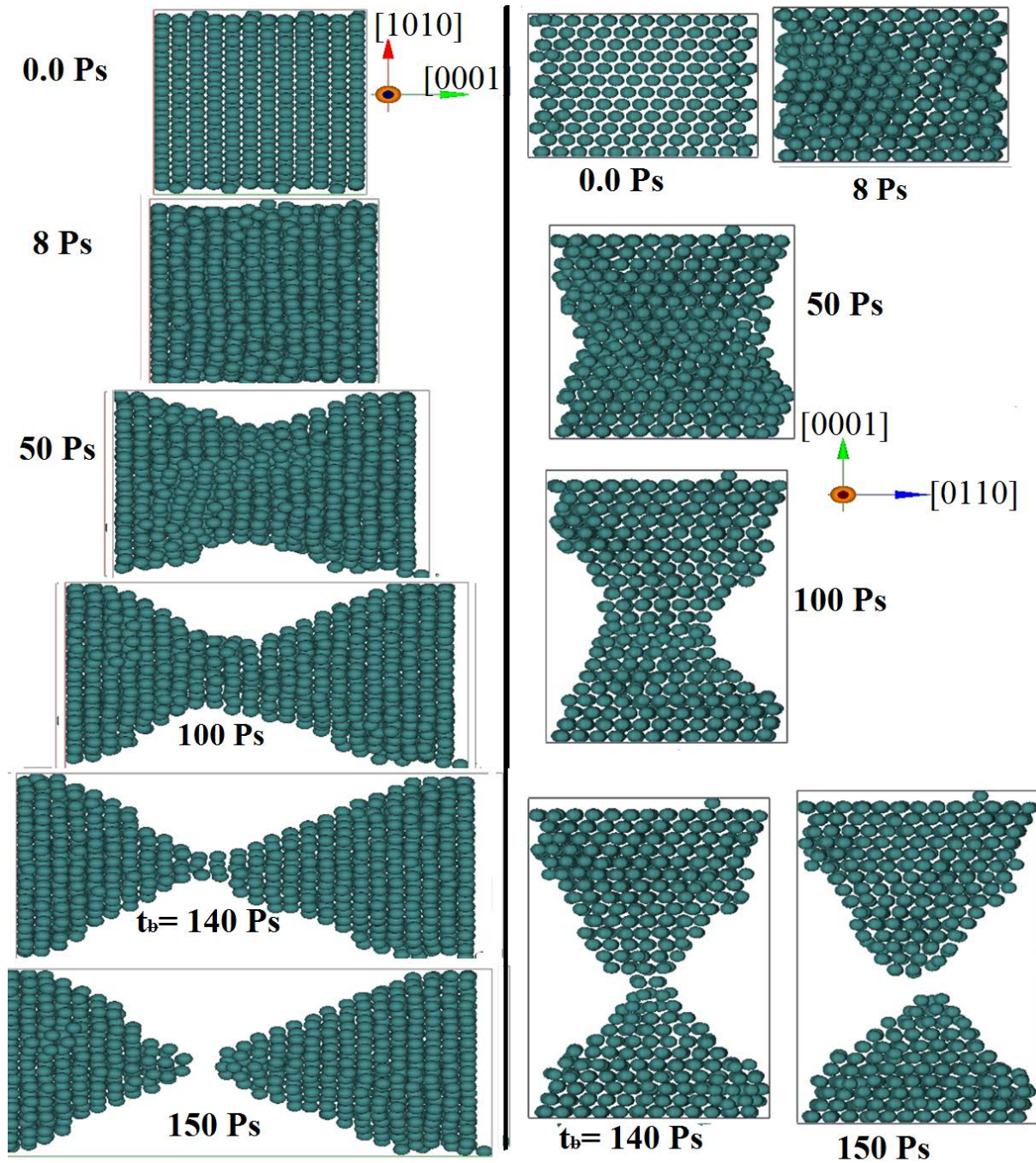


Fig. 4. MD simulation plots of the gage section of a tensile specimen at various time of uniaxial loading for Mg nanowire in plane $[1010]$ right and in plane $[0110]$ left

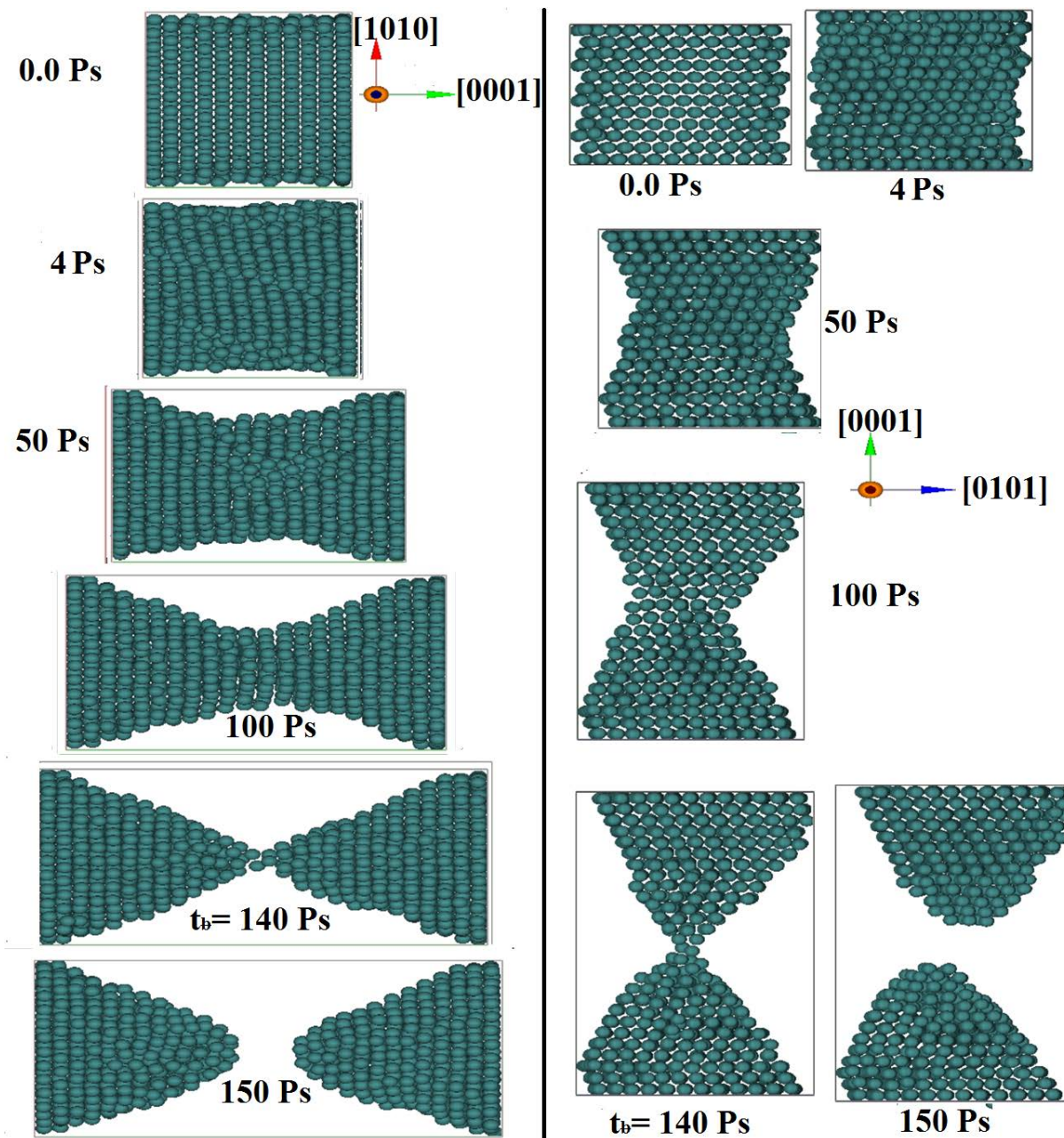


Fig. 5. MD simulation plots of the gage section of a tensile specimen at various time of uniaxial loading for Zr nanowire in plane [1010] right and in plane [0110] left

4. Conclusions

The process of formation of defects in the dynamic deformation of HCP metallic (Cd, Co, Mg, Ti, and Zr) nanowires under uniaxial tension at 300 K have been studied using MD simulation. Structural differences between the structural and energy transformations were as follows: As a result of studies of structural and energy transformations during tensile deformation of HCP metallic (Cd, Co, Mg, Ti, and Zr) nanowires at 300 K, identified three stages of structural and energy transformations: the quasi-elastic, plastic(flow), and fracture.

1. The first stage of structural and energy transformations in the deformation process ends with formation sliding on the substructure of HCP metallic (Cd, Co, Mg, Ti, and Zr) nanowires. At the first stage of deformation, we can see rotation the central portion of nanowire and C-domain formation in the second stage of deformation. The first stage of

structural and energy transformations ends quickly for all of them and peak values 4 Ps for Ti and Zr, 8 Ps for Co and Mg and 10 Ps for Cd. As can be expected the ultimate strength of the HCP nanowires equals 23, 22.5, 14, 6 and 4 for Zr, Co, Ti, Cd and Mg nanowires, respectively,

2. It was found that the features of structural and energy transformations for HCP metallic nanowires in the second stage of deformation affects the orientation of the axis of tension. In the second stage occur collective atomic bias, the formation of dislocations and grain boundaries. As shown in Fig. 2 the period of the plasticity was the largest period of time for Co and Ti and smallest for Zr and Mg.

3. The value of the stored energy at the peak of deformation schedule at the end of the first stage for the reduced nanowires equals 0.07 eV/atom for Co and 0.045 eV/atom for Zr. The levels of stored energy at the end of the plastic deformation steps are equal to 0.065 eV/atom for Mg and 0.112 eV/atom for Zr.

4. The neck area occurs in the third stage of structural and energy transformations. Stored strain energy in that period varies only slightly.

5. The nature of the destruction of blocks corresponds to brittle fracture at 300 K. After fracture of nanowire for all nanowires, found planar defects such as twins and packing defects.

Acknowledgements. No external funding was received for this study.

References

- [1] Liang T, Phillpot SR, Sinnott SB. Parameterization of a reactive many-body potential for Mo–S systems. *Phys. Rev. B.* 2009;79(24): 245110.
- [2] Mishin Y, Farkas D, Mehl MJ, Papaconstantopoulos DA. Interatomic potentials for monoatomic metals from experimental data and ab initio calculations. *Phys. Rev. B.* 1999;59(5): 3393.
- [3] Mishin Y, Mehl MJ, Papaconstantopoulos DA, Voter AF, Kress JD. Structural stability and lattice defects in copper: Ab initio, tight-binding, and embedded-atom calculations. *Phys. Rev. B.* 2001;63(22): 224106.
- [4] Mishin Y, Mehl MJ, Papaconstantopoulos DA. Embedded-atom potential for B₂NiAl. *Phys. Rev. B.* 2002;65(22): 224114.
- [5] Zope RR, Mishin Y. Interatomic potentials for atomistic simulations of the Ti–Al system. *Phys. Rev. B.* 2003;68(2): 024102.
- [6] Elstner M, Porezag D, Jungnickel G, Elsner J, Haugk M, Frauenheim T, Suhai S, Seifert G. Self-consistent-charge density-functional tight-binding method for simulations of complex materials properties. *Phys. Rev. B.* 1998;58(11): 7260.
- [7] Mishin Y, Mehl MJ, Papaconstantopoulos DA. Phase stability in the Fe–Ni system: Investigation by first-principles calculations and atomistic simulations. *Acta Mater.* 2005;53(15): 4029.
- [8] Ghosh G, Delsante S, Borzone G, Asta M, Ferro R. Phase stability and cohesive properties of Ti–Zn intermetallics: First-principles calculations and experimental results. *Acta Mater.* 2006;54(19): 4977–4997.
- [9] Chamati H, Papanicolaou N, Mishin Y, Papaconstantopoulos DA. Embedded-atom potential for Fe and its application to self-diffusion on Fe (100). *Surf. Sci.* 2006;600(9): 1793–1803.
- [10] Robertson IJ, Heine V, Payne MC. Cohesion in aluminum systems: A first-principles assessment of "glue" schemes. *Phys. Rev. Lett.* 1993;70(13): 1944.
- [11] Frederiksen SL, Jacobsen KW, Brown KS, Sethna JP. Bayesian Ensemble Approach to Error Estimation of Interatomic Potentials. *Phys. Rev. Lett.* 2004;93(16): 165501.
- [12] Aish MM, Starostenkov MD. Features of structural transformations of HCP metallic Ti

- nanowires using Cleri-Rosato potential at low temperature. *Letters on Materials*. 2016;6(4): 317-321.
- [13] Starostenkov MD, Aish MM. Feature deformation and breaking of Ni nanowire. *Letters on Materials*. 2014;4(2): 89-92.
- [14] Aish MM, Starostenkov MD. Deformation and Fracture of Metallic Nanowires. *Solid State Phenomena*. 2017;258: 277-280.
- [15] Aish Mohammed, Starostenkov Mikhail. Mechanical properties of metallic nanowires using tight-binding model. *AIP Conf. Proc.* 2016;1698: 040006.
- [16] Aish MM, Starostenkov MD. Characterization of strain-induced structural transformations in CdSe nanowires using molecular dynamics simulation. *Materials Physics and Mechanics*. 2015;24(4): 139-144.
- [17] Starostenkov MD, Aish MM. Molecular dynamic study for ultrathin Nickel nanowires at the same temperature. *Materials Physics and Mechanics*. 2014;21(1): 1-7.
- [18] Starostenkov MD, Aish MM. Effect of length and cross-sectional area on Ni₃Fe alloy plasticity. *Advanced Materials Research*. 2014;1013: 242-248.
- [19] Aish MM, Starostenkov MD. Effect of volume on the mechanical properties of nickel nanowire. *Materials Physics and Mechanics*. 2013;18(1): 53-62.
- [20] Aish MM. The Structural Transformation and Mechanical Strength of Ni, Ti Nanowires and Nitinol Alloys at Various Vacancy Rates: Molecular Dynamic Study Using Cleri-Rosato Potential. *Materials Physics and Mechanics*. 2019;42(2): 211-223.
- [21] Cleri F, Rosato V. Tight-binding potentials for transition metals and alloys. *Phys. Rev. B*. 1993;48(1): 22.

NUMERICAL OPTIMIZATION OF THE CANTILEVER PIEZOELECTRIC GENERATOR

A.N. Soloviev^{1,2}, V.A. Chebanenko^{3*}, I.V. Zhilyaev⁴, A.V. Cherpakov^{1,2}, I.A. Parinov²

¹Don State Technical University, Gagarin sq. 1, Rostov-on-Don, Russia

²Vorovich Mathematics, Mechanics and Computer Science Institute, Southern Federal University,
Milchakova st., 8a, Rostov-on-Don, Russia

³Federal Research Center "Southern Scientific Center of the Russian Academy of Sciences", Chekhova st., 41,
Rostov-on-Don, Russia

⁴University of Applied Sciences and Arts Northwestern Switzerland, Institute of Polymer Engineering,
Bahnhofstrasse, 6, Windisch, Switzerland

*e-mail: valera.chebanenko@yandex.ru

Abstract. In this paper, we consider the adequacy of the use of the straight normal hypothesis in the applied theory for the calculation of a cantilever-type piezoelectric generator that takes into account the incomplete piezo-element coating of the substrate, which was obtained earlier, and a numerical optimization procedure for piezoelectric generator is given, taking into account critical failure stresses.

Keywords: piezoelectric generator, banding, straight normal, semi-analytical method, finite element, numerical optimization

1. Introduction

It is known that piezoelectric materials are widely used as actuators, sensors and generators in the engineering and aerospace field for monitoring the state of structures, shape control, active suppression of parasitic vibrations, noise suppression, etc. Such wide application is achieved due to their good electromechanical properties, flexibility in the design process, ease of production, as well as high energy conversion efficiency in the direct and inverse piezo effect. When using piezoelectric materials as actuators, deformations can be controlled by changing the magnitude of the applied electric potential. In the sensors, deformation measurement is also performed by measuring the induced potential. In the field of energy harvesting by means of piezoelectric materials, the free mechanical energy that is present in the environment is converted into electrical, and then converted into a suitable for low-power device. A detailed survey is given in [1-3]

In recent years, research has been actively developed in the area of piezoelectric transducers of mechanical energy into electrical one. This type of transducers was called piezoelectric generators (PEG). The basic information about PEG, as well as the problems arising at the development stages of energy storage devices, were given in the review papers [3-5], as well as in the fundamental monograph [6].

Typical actuators, sensors and generators, working on bending, are a multi-layered structure consisting of several layers with different mechanical and electrical properties. The traditional design, consisting of two piezoelectric layers, glued to the substrate or to each other is called a bimorph.

Most of the works are devoted to the study of the characteristics of the bimorph cantilever type PEG. There are several ways of modeling PEG: mathematical model with lumped parameters, mathematical model with distributed and finite element (FE) model.

Works [7-9] are devoted to the construction of PEG models on the basis of oscillations of a mechanical system with lumped parameters. The use of such systems is a convenient model approach, since it allows obtaining analytical dependencies between the output parameters of PEG (potential, power, etc.) and electrical, mechanical characteristics and resistance of the external electric circuit.

Simulation using lumped parameters gives an initial idea of the problem, allowing simple expressions to be used to describe the system. However, this simulation method is inaccurate and limited to only one mode of oscillation. In addition, the approach does not take into account important aspects of the related physical system, for example, information on the dynamic form of the oscillation mode and accurate information on the distribution of deformation and its effect on the electrical response of the system.

Another type of simulation is modeling using distributed parameters. Based on the Euler-Bernoulli hypotheses for a beam, analytic solutions of the related problem were obtained in [10,11] for various configurations of the cantilever type PEG. Explicit expressions for the output voltage across the resistor for harmonic oscillations of the cantilever beam were obtained. In addition, the authors studied in detail the behavior of PEG with short-circuited and open-circuit electrical circuits and the effect of the electromechanical coupling coefficient. However, in these studies, the case where the piezoelectric element (PE) does not completely cover the substrate has not been considered.

Works [11-14] are devoted to the FE modeling of cantilever PEGs of various configurations. The case where the PE does not completely cover the substrate is also easily solved by the FE method. Nevertheless, obtaining a numerical-analytical solution for the case of incomplete coating of the substrate by a PE is of some interest.

The above brief analysis of known works has shown that the problem of modeling PEG using analytical methods in full is not yet solved, although it is very relevant.

In previous works, we presented a numerical analytical model based on the Kantorovich method [15], confirmed by FE modeling and a series of experiments [16], and also carried out a FE analysis of the improved model of cantilever PEG [17].

In this paper, we consider the adequacy of the use of the straight normal hypothesis in the applied theory for the calculation of a cantilever-type PEG that takes into account the incomplete PE coating of the substrate, which was obtained earlier in [15], and a numerical optimization procedure for PEG is given, taking into account critical failure stresses.

2. Mathematical modelling of the cantilever PEG

The simplest bimorph design of cantilever PEG is presented in Fig. 1. The cantilever bimorph PEG consists of two PEs (Fig. 1, points 1 and 3) glued to the substrate (Fig. 1, point 2), which is clamped from one end. Electrodes are applied to large sides perpendicular to the x_3 axis. The electrical voltage $v(t)$ is measured on the resistor R .

Piezoelectric elements are polarized in thickness. In this paper, we consider a parallel circuit for connecting PEs to a common electric circuit (see Fig. 1); therefore, it is assumed that the polarization vectors are aligned with the positive direction of the x_3 axis.

The excitation of oscillations in the PEG shown in Fig. 1 occurs through the movement of the clamp relative to a certain plane, so the absolute displacement of the cantilever along the coordinate x_3 will consist of the displacement of the clamp $w_c(t)$ and the relative displacement of the cantilever $w(x_1, t)$.

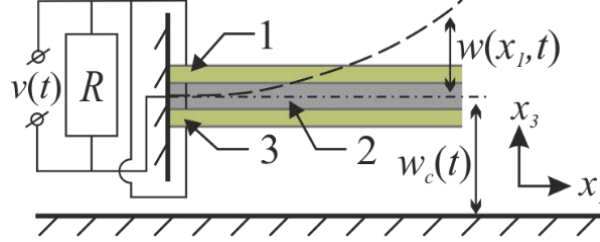


Fig. 1. Bimorph cantilever PEG: 1 and 3 - PEs, 2 - substrate

To analyze the problem of forced oscillations of a cantilever bimorph PEG in [15], we used the Kantorovich method [18]. It is based on the idea of the expansion of the displacement of the beam in a row:

$$w(x_1, t) = \sum_{i=1}^N \eta_i(t) \phi_i(x_1), \quad (1)$$

where N is the number of vibration modes to be considered, $\eta_i(t)$ is unknown generalized coordinates, $\phi_i(x_1)$ are known test functions that satisfy the boundary conditions.

Earlier, in [15], applied numerical theories were constructed to simulate the performance characteristics of a cantilever type PEG. Simulation took place on the basis of the Hamilton principle within the framework of the Euler-Bernoulli hypotheses:

$$\begin{aligned} \mathbf{M}\ddot{\boldsymbol{\eta}}(t) + \mathbf{D}\dot{\boldsymbol{\eta}}(t) + \mathbf{K}\boldsymbol{\eta}(t) - \boldsymbol{\Theta}v(t) &= \mathbf{p}, \\ C_p \dot{v}(t) + \boldsymbol{\Theta}^T \dot{\boldsymbol{\eta}}(t) + \frac{v(t)}{R} &= 0, \end{aligned} \quad (2)$$

where $\mathbf{D} = \mu\mathbf{M} + \gamma\mathbf{K}$ is the Rayleigh-type damping matrix, and the remaining coefficients are:

$$\begin{aligned} C_p &= \frac{b_p L_p}{h_p} \vartheta_{33}^{S*}, & K_{ij} &= \int_0^L EI \phi_i''(x_1) \phi_j''(x_1) dx_1, & \theta_i &= \int_0^L J_p \phi_i''(x_1) dx_1, \\ M_{ij} &= \int_0^L m \phi_i(x_1) \phi_j(x_1) dx_1, & p_i &= -\ddot{w}_c(t) \left[\int_0^L m \phi_i(x_1) dx_1 \right], \end{aligned} \quad (3)$$

where M_{ij} is the elements of the mass matrix, K_{ij} is the elements of the stiffness matrix, $v(t)$ is the voltage across the resistor R , C_p is the electrical capacitance, θ_i is the elements of the electromechanical coupling vector, p_i is elements of the effective mechanical load vector.

Next we will consider PEG, the substrate of which has the following characteristics: geometric dimensions $L \times b \times h$, $108 \times 10 \times 1$ mm³, density ρ_s 1650 kg/m³, elastic modulus c_s 15 GPa. PEs have the following characteristics: geometric dimensions $L_p \times b_p \times h_p$, $56 \times 6 \times 0.5$ mm³, density ρ_p 8000 kg/m³, elastic modulus c_p 7.5 GPa, relative permittivity $\varepsilon_{33}^S / \varepsilon_0$ 5000, piezoelectric modulus d_{31} 350 pC/N. The excitation in the system is given by the harmonic displacement of the base $w_c = \tilde{w}_c e^{i\omega t}$, whose amplitude is $\tilde{w}_c = 0.1$ mm.

The damping coefficients μ and γ for the natural frequencies ω_i and ω_j are found from the solution of the following equation [19]:

$$\frac{1}{2} \begin{bmatrix} 1/\omega_i & \omega_i \\ 1/\omega_j & \omega_j \end{bmatrix} \begin{Bmatrix} \mu \\ \gamma \end{Bmatrix} = \begin{Bmatrix} \xi_1 \\ \xi_2 \end{Bmatrix}, \quad (4)$$

where ξ_1 and ξ_2 are the modal damping coefficients, which are selected for reasons of agreement with the experimental data. In this work, the modal damping coefficients for the first two modes were set equal to $\xi_1 = \xi_2 = 0.02$ in accordance with the results of earlier experimental studies of cantilever PEGs [16].

3. Adequacy of the hypothesis of a straight normal

The Euler-Bernoulli hypotheses assume that the beam is uniform in thickness. In our case, we have a three-layer beam (Fig. 2). Moreover, the modulus of elasticity of the substrate (inner layer) is 3.8 times smaller than the elastic modulus of the PEs (outer layers). This fact may indicate a break in the normal when the beam is bent. This in turn can lead to inaccurate results when using the theory based on the Euler-Bernoulli hypotheses in the calculation of such a construction. With the help of the FE calculation, we analyze the deformations in the cross section of the beam and compare them with theory.

For the analysis, a model of cantilever bimorph PEG, shown in Fig. 2, was chosen.

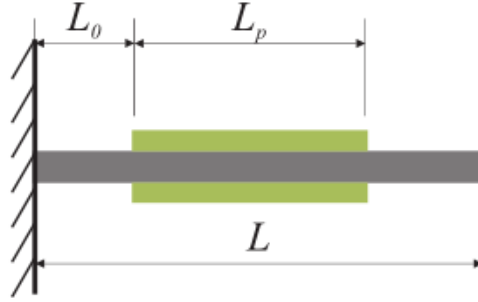


Fig. 2. Cantilever type PEG

In order to take into account the incomplete covering of the piezoelectric substrate by the generator shown in Fig. 2, the function $\phi_i(x_1)$ should be specified as follows:

$$\phi_i(x_1) = \begin{cases} \phi_i^{(1)}(x_1), & x_1 \leq L_0 \\ \phi_i^{(2)}(x_1), & L_0 < x_1 \leq L_0 + L_p \\ \phi_i^{(3)}(x_1), & x_1 > L_0 + L_p \end{cases} \quad (5)$$

In this case, the specific mass m , for the cross section shown in Fig. 2, is calculated as follows:

$$m = \rho_s S_s + 2\rho_p S_p, \quad (6)$$

where ρ_s is the density of the substrate, ρ_p is the piezoceramic density, $S_s = hb$ is the cross-sectional area of the substrate, and $S_p = h_p b_p$ is the cross-sectional area of the PE.

The flexural rigidity EI for this construction is calculated as follows:

$$EI = c_p \left[\iint_{S_{pup}} x_3^2 dS + \iint_{S_{plow}} x_3^2 dS \right] + c_s \iint_{S_s} x_3^2 dS, \quad (7)$$

where c_p and c_s are the moduli of elasticity of piezoceramics and substrates, respectively, and S_{pup} and S_{plow} are the cross-sectional areas along which integration is performed for the lower and upper PEs, respectively.

The function J_p in the electromechanical coupling vector is:

$$J_p = \frac{e_{31}^*}{h_p} \left(\iint_{S_{pup}} x_3 dS + \iint_{S_{plow}} x_3 dS \right). \quad (8)$$

The boundary conditions and the conjugation conditions necessary for finding the functions $\phi_i(x_1)$ for a given construction will be as follows:

$$\begin{aligned}
\phi_i^{(1)}(0) &= 0, & \phi_i^{(2)'''}(L_0 + L_p) &= \frac{EI^{(1)}}{EI^{(2)}} \phi_i^{(3)'''}(L_0 + L_p), \\
\phi_i^{(1)'}(0) &= 0, & \phi_i^{(2)''''}(L_0 + L_p) &= \frac{EI^{(1)}}{EI^{(2)}} \phi_i^{(3)''''}(L_0 + L_p), \\
\phi_i^{(1)}(L_0) &= \phi_i^{(2)}(L_0), & \phi_i^{(2)}(L_0 + L_p) &= \phi_i^{(3)}(L_0 + L_p), \\
\phi_i^{(1)'}(L_0) &= \phi_i^{(2)'}(L_0), & \phi_i^{(2)'}(L_0 + L_p) &= \phi_i^{(3)'}(L_0 + L_p), \\
\phi_i^{(1)''}(L_0) &= \frac{EI^{(2)}}{EI^{(1)}} \phi_i^{(2)''}(L_0), & \phi_i^{(3)''}(L) &= 0, \\
\phi_i^{(1)'''}(L_0) &= \frac{EI^{(2)}}{EI^{(1)}} \phi_i^{(2)'''}(L_0), & \phi_i^{(3)'''}(L) &= 0,
\end{aligned} \tag{9}$$

where $EI^{(1)}$ is the bending stiffness of the segment without a PE, and $EI^{(2)}$ with a PE.

A similar problem was modeled in the ACELAN FE package. With a certain indentation to the right at three points near the left edge of the PE, the longitudinal strain distributions along the thickness were obtained (see Fig. 3).

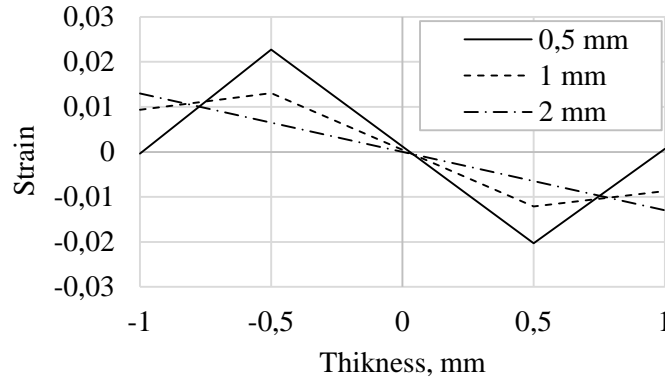


Fig. 3. Strain distribution along the thickness in the vicinity of the left edge of PE

The FE calculation showed that, in the vicinity of the first resonance frequency, the deflected mode of the three-layer structure is well described by the hypothesis of a single normal, with the exception of the edges of the PE, and the size of this region does not exceed the thickness of the packet. Thus, in Fig. 3, the plots of the longitudinal strain distribution along the beam thickness for distances from the left edge of the PE 0.5, 1 and 2 mm are shown for the model shown in Fig. 2. A similar distribution is also found at the right edge of the PE. Considering that the PE length in calculation is 56 mm, the applied theory of oscillations of a three-layer beam is described with a high degree of accuracy on the basis of the hypothesis of a single normal.

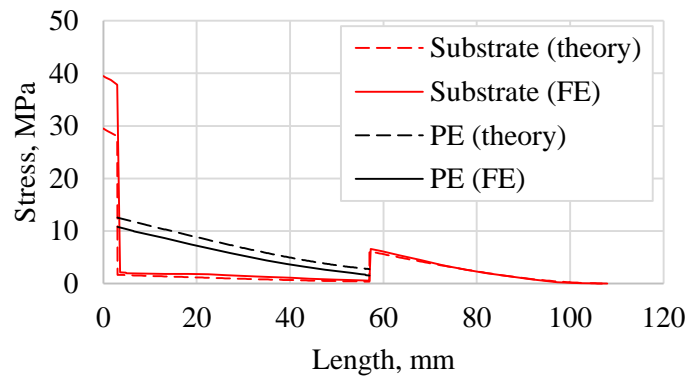


Fig 4. Stress distribution in the cantilever transducer along the length of transducer on the upper surfaces of layers

Comparison of the results of the calculation of the stress-strain and electric state of cantilever transducer according to the applied theory and the FE model in the framework of the deflected mode with the condition of an open circuit at a frequency in the neighborhood of the first resonance shows a good qualitative coincidence of the characteristics (Fig. 4 and 5). In quantitative terms, with a relative deflection difference of 9%, the relative difference in maximum stresses at the free boundaries of the PE in their middle part along the length did not exceed 10%. In addition, a comparison was made with the known FE model, built in the ANSYS package, according to which the relative error in determining the resonant frequencies and the output electric voltage was 6%.

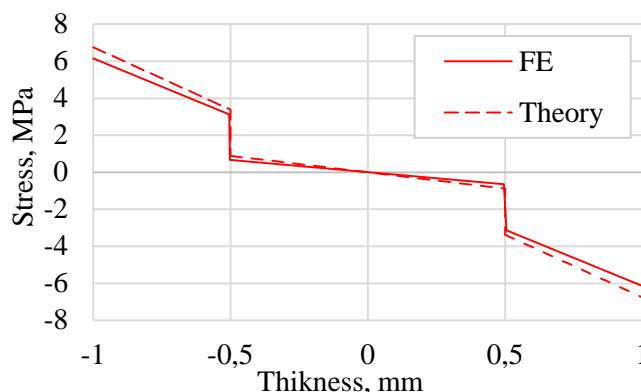


Fig 5. Stress distribution in the cantilever transducer along the thickness in the middle point of PE

4. Numerical optimization

Of particular interest is the study of the influence of geometric parameters on the output characteristics of PEG, taking into account the critical stresses for each material. We introduce the strength limit in the following form

$$\sigma_m = k\sigma_c, \quad (10)$$

here, σ_m is the maximum permissible value of the mechanical stress, k is the safety factor, and σ_c is the critical value of the mechanical stress at which the material is broken.

For substrate and PE materials [20], let us take the critical values of σ_c for the case of tension equal to 150 and 66 MPa, respectively. Safety factor is $k = 0.5$.

For optimization, a bimorph cantilever PEG model with an attached mass, which is located at some margin on the free end of the beam, was selected (see Fig. 6.).

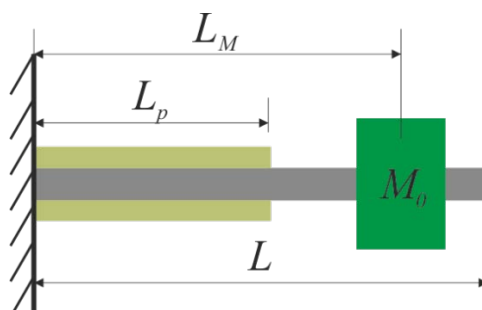


Fig. 6. Cantilever type PEG with proof mass

In order to take into account the incomplete covering of the piezoelectric substrate by the generator shown in Fig. 6, the function $\phi_i(x_1)$ should be given as follows:

$$\phi_i(x_1) = \begin{cases} \phi_i^{(1)}(x_1), & x_1 \leq L_p \\ \phi_i^{(2)}(x_1), & L_p < x_1 \leq L_M \\ \phi_i^{(3)}(x_1), & x_1 > L_M \end{cases} \quad (11)$$

Adding an attached mass to the design requires consideration of its influence in the system of differential equations, since it is an additional inertial load that affects the kinetic energy. Taking into account the attached mass, the expressions for the components M_{ij} and p_i vary as follows:

$$M_{ij} = \int_0^L m\phi_i(x_1)\phi_j(x_1)dx_1 + M_0\phi_i(L_M)\phi_j(L_M), \quad (12)$$

$$p_i = -\ddot{w}_c(t) \int_0^L m\phi_i(x_1)dx_1 + M_0\dot{\phi}_i(L_M),$$

where L_M is the position coordinate of the attached mass. In this case it is the free end of the beam.

The boundary conditions and the conjugation conditions for finding $\phi_i(x_1)$ will be as follows:

$$\begin{aligned} \phi_i^{(1)}(0) &= 0, & \phi_i^{(2)''}(L_M) &= \phi_i^{(3)''}(L_M), \\ \phi_i^{(1)'}(0) &= 0, & \phi_i^{(2)'''}(L_M) &= \phi_i^{(3)'''}(L_M) - \alpha\beta^4\phi_i^{(2)}(L_M), \\ \phi_i^{(1)}(L_p) &= \phi_i^{(2)}(L_p), & \phi_i^{(2)}(L_M) &= \phi_i^{(3)}(L_M), \\ \phi_i^{(1)'}(L_p) &= \phi_i^{(2)'}(L_p), & \phi_i^{(2)'}(L_M) &= \phi_i^{(3)'}(L_M), \\ \phi_i^{(1)''}(L_p) &= \frac{EI^{(2)}}{EI^{(1)}}\phi_i^{(2)''}(L_p), & \phi_i^{(3)''}(L) &= 0, \\ \phi_i^{(1)'''}(L_p) &= \frac{EI^{(2)}}{EI^{(1)}}\phi_i^{(2)'''}(L_p), & \phi_i^{(3)'''}(L) &= 0, \end{aligned} \quad (13)$$

where $\alpha = M / mL$, β is an eigenvalue, $EI^{(1)}$ is the bending stiffness of a segment covered by a PE, and $EI^{(2)}$ is without a PE.

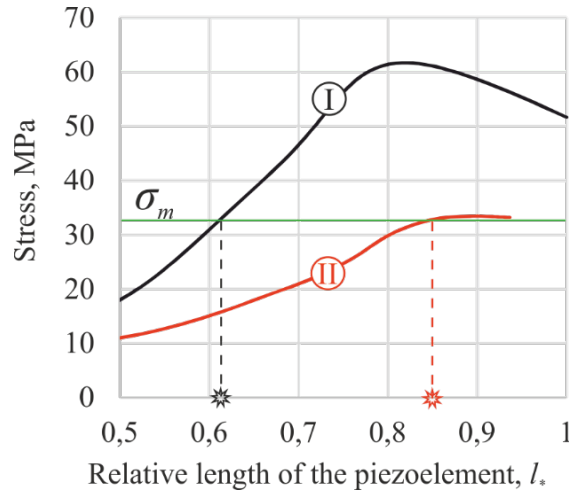


Fig 7. Dependences of the maximum mechanical stresses arising in the clamp of PEG on the relative length l_* of PE for two configurations

Investigations of the efficiency of various types of structures from geometric parameters with allowance for the critical tensile stresses for a piezoceramic layer and a substrate are carried out. Thus, for the model shown in Fig. 6, the dependence of the output parameters on the PE's length was compared in the presence of (I) and the absence (II) of the attached mass M_0 .

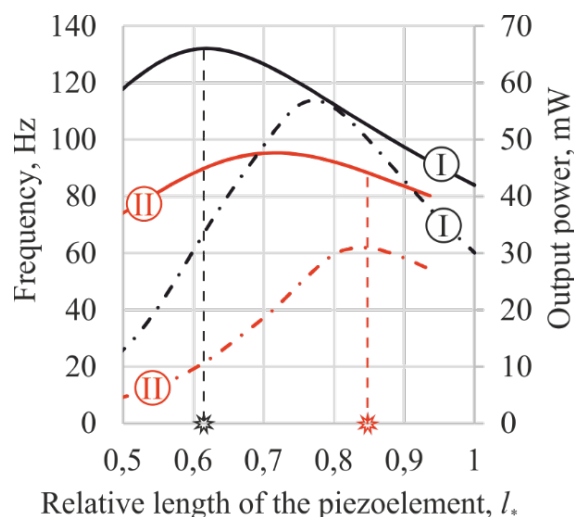


Fig. 8. Dependences of the output parameters of PEG on the relative length l_* of PE for two configurations: resonance frequencies (solid lines) and maximum output power (dot-dash lines)

The results of the research showed that, in the presence and absence of M_0 , mechanical stresses begin to exceed the permissible stress limits σ_m beginning with a certain value of the PE's length (see Fig. 7). It turned out that there is an interval of frequencies (82-94 Hz) where the first resonance frequencies in the case of the presence (I) and absence (II) of the attached mass coincide. The maximum power that can be obtained in the presence of M_0 (I) was about 31 mW at a frequency of 88 Hz with the relative length of PE $l_* = L_p / L_0$ equal to 0.85 (see Fig. 8). The same output power can be obtained in the absence of M_0 (II) at a frequency of 131 Hz for a length $l_* = 0.63$.

5. Conclusions

It is shown that the developed applied theory based on the single normal hypothesis satisfactorily describes the deflected mode in the internal part of the PEs. An exception to this is the small vicinity of the ends of piezoelectric layers, but the effect of this feature on the integral characteristics of piezoelectric is not significant.

An example of optimization of a cantilever-type PEG is shown taking into account the critical mechanical stresses for PEG materials. The optimization results showed that there is a frequency interval where the first resonant frequencies of the PEG with the attached mass and without coincide, but the PEG model without the presence of mass can not work in this interval, since the threshold of critical stresses is exceeded.

Acknowledgements. The publication was prepared in the framework of RFBR grant № 18-38-00912 mol_a.

References

- [1] Gaudenzi P. *Smart structures: physical behavior, mathematical modeling and applications*. New York: Wiley; 2009.
- [2] Chopra I. Review of state of art of smart structures and integrated systems. *AIAA Journal*. 2002;40(11): 2145-2187.
- [3] Chebanenko VA, Akopyan VA, Parinov IA. Piezoelectric generators and energy harvesters: modern state of the art. In: Parinov IA (ed.) *Piezoelectrics and Nanomaterials: Fundamentals, Developments and Applications*. New York: Nova Science Publishers; 2015. p.243-277.

- [4] Liu Y, Tian G, Wang Y, Lin J, Zhang Q, Hofmann HF. Active piezoelectric energy harvesting: general principle and experimental demonstration. *Journal of Intelligent Material Systems and Structures*. 2009;20(5): 575-586.
- [5] Liao Y, Sodano HA. Structural effects and energy conversion efficiency of power harvesting. *Journal of Intelligent Material Systems and Structures*. 2009;20(5): 505-515.
- [6] Erturk A, Daniel JI. *Piezoelectric energy harvesting*. New York: John Wiley & Sons; 2011.
- [7] Dutoit NE, Brian LW, Kim SG. Design considerations for MEMS-scale piezoelectric mechanical vibration energy harvesters. *Integrated Ferroelectrics*. 2005;71(1): 121-160.
- [8] Adhikari S, Friswell MI, Inman DJ. Piezoelectric energy harvesting from broadband random vibrations. *Smart Materials and Structures*. 2009;18(11): 115005.
- [9] Shu YC, Lien IC. Analysis of power output for piezoelectric energy harvesting systems. *Smart materials and structures*. 2006;15(6): 1499.
- [10] Erturk A, Inman DJ. On mechanical modeling of cantilevered piezoelectric vibration energy harvesters. *Journal of Intelligent Material Systems and Structures*. 2008;19(11): 1311-1325.
- [11] Stanton SC, McGehee CC, Mann BP. Nonlinear dynamics for broadband energy harvesting: Investigation of a bistable piezoelectric inertial generator. *Physica D: Nonlinear Phenomena*. 2010;239(10): 640-53.
- [12] Nechibvute A, Chawanda A, Luhanga P. Finite element modeling of a piezoelectric composite beam and comparative performance study of piezoelectric materials for voltage generation. *ISRN Materials Science*. 2012;2012: 1-11.
- [13] Solovyev AN, Duong LV. Optimization for the harvesting structure of the piezoelectric bimorph energy harvesters circular plate by reduced order finite element analysis. *International Journal of Applied Mechanics*. 2016;8(3): 1650029.
- [14] Junior CD, Erturk A, Inman DJ. An electromechanical finite element model for piezoelectric energy harvester plates. *Journal of Sound and Vibration*. 2009;327(1-2): 9-25.
- [15] Soloviev AN, Chebanenko VA, Parinov IA. Mathematical modelling of piezoelectric generators on the base of the Kantorovich method. In: *Analysis and Modelling of Advanced Structures and Smart Systems*. Singapore: Springer; 2018. p.227-258.
- [16] Shevtsov SN, Soloviev AN, Parinov IA, Cherpakov AV, Chebanenko VA. *Piezoelectric Actuators and Generators for Energy Harvesting*. Heidelberg: Springer; 2018.
- [17] Soloviev AN, Parinov IA, Cherpakov AV, Chebanenko VA, Rozhkov EV. Analyzing the output characteristics of a double-console PEG based on numerical simulation. *Materials Physics and Mechanics*. 2018;37(2): 168-175.
- [18] Wait R, Mitchell AR. *Finite element analysis and applications*. New York: John Wiley & Sons Inc; 1985.
- [19] Chopra AK. *Dynamics of structures. Theory and Applications to Earthquake Engineering*. New Jersey: Prentice Hall; 2017.
- [20] Zatsarinniy VP. *Strength of piezoceramics*. Rostov-on-Don: Publishing house of Rostov State University; 1978. (In Russian)

SINGLE-WALLED CARBON NANOTUBE AS A NANOSCALE QUANTUM SYSTEM

M.V. Krasinkova*

Ioffe Institute, Politekhnikeskaya 26, St. Petersburg, 194021, Russia

*e-mail: marinak@mail.ioffe.ru

Abstract. It is shown that a single-walled carbon nanotube based on a carbon monolayer (graphene) rolled up into a cylinder is a nanoscale quantum system characterized by the presence of electron crystals, like graphene. In contrast to the extremely unstable graphene quantum system, the nanotube quantum system is stable at a certain curvature of the carbon skeleton. The curvature causes the redistribution of π electrons between internal and external electron crystals accompanied by the formation of additional one-dimensional or quasi-one-dimensional crystals of pairs of π^* electrons excited into a higher $3s2p_z$ energy state and located on the nanotube external side. The stability of the nanotube quantum system and its unusual physical properties are due to these crystals of π^* electron pairs.

Keywords: carbon nanotubes, electron crystals, nanoscale quantum systems, ballistic conductivity

1. Introduction

The interest to single-walled carbon nanotubes is caused by a number of properties that promise their widespread use in electronics based on quantum systems, including the systems based on carbon and its compounds. Of practical interest are the following properties of carbon nanotubes: the tendency to form bundles from individual tubes [1,2], an almost complete absence of defects [2], high emission currents at a relatively low voltage accompanied by light emission in the red and near infrared regions [3,4], ballistic conductivity at room temperature and achievement of intrinsic contact resistance close to a half of the quantum limit ($h/4e^2$) at low temperature [5,6,7], high Josephson supercurrents [8], and also induced and intrinsic superconductivity [9]. The natures of all these phenomena are still unknown. It is not clear even why electrical properties of tubes, such as armchair and zigzag ones, differ from each other, though the only difference between them is in the hexagon orientation relative to the tube axis [7]. The nature of high Schottky barriers at contacts with metals [10] and the nature of the inhomogeneities of electron and light emissions from the tube surface [3,4] also remain unclear.

Since attempts to explain the above phenomena in the approximation of weakly interacting particles were unsuccessful, an attempt will be made to explain them in the approximation of strongly interacting electrons, i.e., in the approximation used earlier for graphene [11]. It was shown in [11] that a strong exchange interaction (resonant π binding) and strong Coulomb interaction between π electrons at neighboring atoms in graphene led to the localization of π electrons on carbon atoms and their strongly correlated state which manifested itself in the formation of two spin-polarized π electron crystals located on opposite sides of the carbon skeleton.

Since the nanotube is a carbon monolayer rolled up into a cylinder and resonant π binding and Coulomb interaction between π electrons are preserved, the formation of electron crystals should be also expected in it. The only difference is that both electron crystals (external and internal with respect to the carbon skeleton) must also have a cylindrical shape. However, it was also noted in [11] that a slightest disturbance in the carbon monolayer flatness (for example, a displacement of a π electron at polarization) causes significant changes in the monolayer quantum system. It is evident that monolayer rolling up must also lead to changes in the nanotube quantum system.

The goals of our study were, first, to consider the features of quantum systems of the armchair and zigzag nanotubes and, second, to show how the unusual properties of these nanotubes can be understood in the approximation of strongly interacting electrons.

It is known that carbon nanotubes are divided into single-walled and multi-walled ones. We consider only single-walled ones, since π electron interactions between neighboring tubes should be taken into account in multi-walled tubes along with interactions between π -electrons in each tube (like in graphite). Therefore, the properties of multi-walled and single-walled tubes can differ considerably.

It is also known that single-walled nanotubes differ in the orientation of carbon hexagons relative to the tube axis (chirality). For the sake of brevity, we consider only two cases of hexagon orientation, which corresponds to two types of tubes, i.e., zigzag and armchair ones.

2. On preferred diameter of single-walled nanotubes

In order to carry out a comparative analysis of two types of nanotubes (armchair and zigzag), we consider the tubes with the same number of hexagon rows parallel to the nanotube axis and determine their diameters. Then we cut out rings five hexagons wide each and draw a projection of these rings on a plane. Fig. 1 (a, b) shows the projections of such tube rings containing 12 rows of hexagons each.

The choice of tubes with 12 hexagon rows is not random. As will be shown below, it is dictated by the conditions of stability of this carbon modification. The diameter of the selected nanotubes is easily calculated if we know the C – C bond length. As the first approximation, we can assume that all bonds in the hexagon are similar and their lengths are equal to the bond length in graphene (1.41 Å). Under these assumptions, the tube diameter with 12 hexagon rows is in the range 8-9 Å (or, more precisely, 8.08 Å and 9.33 Å for the armchair and zigzag tubes, respectively). Note that these diameters are close to those obtained experimentally in [12], where the highest peak in the distribution of single-walled nanotubes in diameter was observed for a diameter of 10.5 Å and a lower peak was observed for a diameter of 8.5 Å.

It is clearly seen from the projection of the armchair tube that the number of rows in these tubes can be only even, since every next row of hexagons is shifted with respect to the preceding row. Further consideration will show that the even number of hexagon rows is also important for zigzag tubes. There is another limitation on the number of rows common to both types of tubes. It is a consequence of the multiplicity of bonds in graphene equal to 1.33 ($1\sigma + 0.33\pi$) corresponding to the maximum binding energy in it. To achieve such a multiplicity of coupling, it must be possible drawing of 9 resonance structures of the Kekule type.

Let us explain this statement. Since only two double bonds out of six are possible in each hexagon of any resonant structure of a carbon monolayer, a multiplicity of π bond equal to 0.33 can be achieved when each bond is a double one in three resonant structures. Hence, the number of structures must be 9. This pattern of 9 resonant structures for both types of tubes is possible if the number of hexagon rows is a multiple of three. If we take into account

the even number of rows noted above, the number of rows in the tubes must be a multiple of 6. The tubes with 12 hexagon rows satisfy this condition.

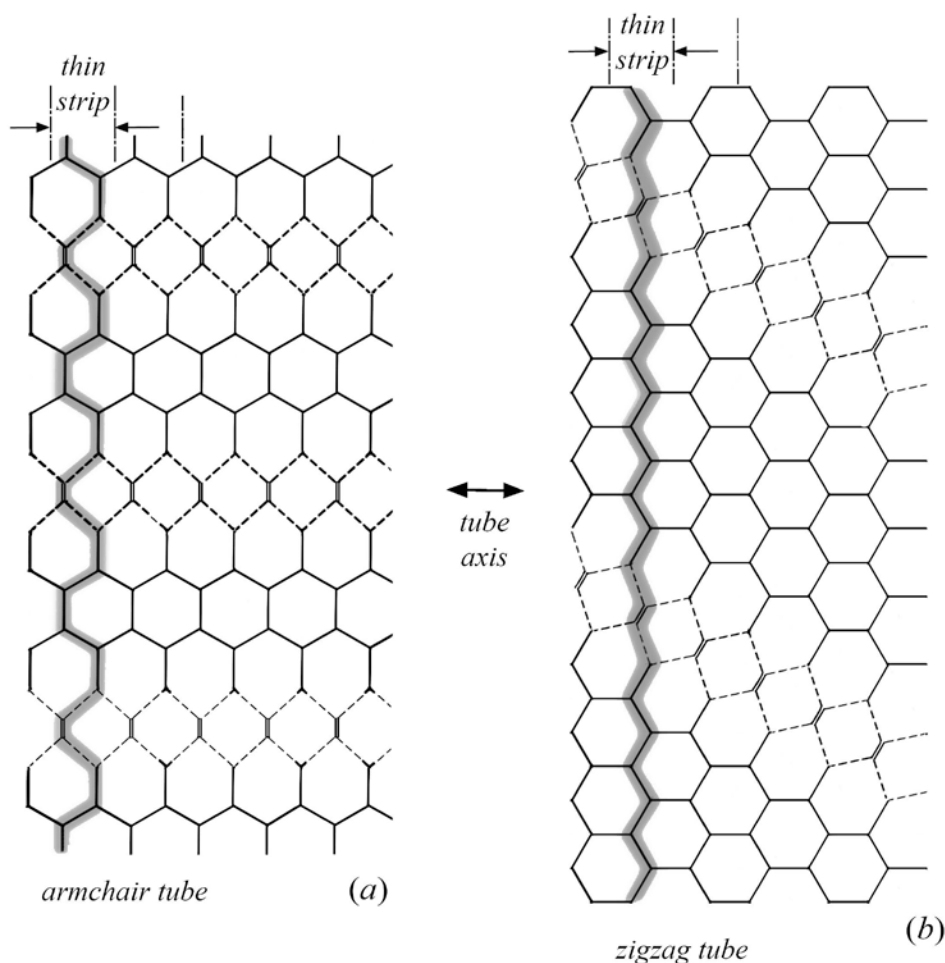


Fig. 1. Projections of nanotube rings containing 5 hexagons in width and 12 hexagon rows in perimeter of a circle for the armchair (a) and zigzag type tubes (b). Resonant π bonds are shown by the thin lines, stationary π^* bonds are shown by the double lines and the single bonds are shown by the dash lines. The dot-and-dash lines with two arrows show the thin strips containing one carbon atom chain highlighted by shading. Three 1D crystals of π^* electron pairs are shown in (a) and two quasi-1D crystals are shown in (b). The line with two arrows on the ends shows the tube axis direction

The tube diameter calculated above is the carbon skeleton diameter. However, to characterize the tube, the diameters of the external and internal π electron crystals, which are at a distance equal to the carbon atomic radius (0.91 \AA) from the carbon skeleton, are also important. The diameters of the electron crystals calculated with due account for the atomic radius turned out to be 9.90 \AA and 11.15 \AA (external) and 6.26 \AA and 7.51 \AA (internal) for the armchair and zigzag tubes, respectively. Note that electron diffraction studies of the nanotube diameter (for example, by transmission electron microscopy) give the diameter of the external electron crystal with which the electron beam interacts rather than the carbon skeleton diameter. Therefore, the experimental data should be compared with the diameter of the external electron crystal. Note that the calculated average (for both types of nanotubes) diameter of the external electron crystal (10.5 \AA) is in good agreement with the experimental data [12].

A comparison of two types of tubes with the same number of hexagon rows shows that the diameter of the carbon skeleton of the armchair tube is noticeably smaller than the zigzag tube diameter (8.08 versus 9.33 Å). This means that the curvatures of the carbon tube skeleton estimated as $1/r$, where r is the skeleton radius, are different. The curvature of the armchair tube is greater than that of the zigzag tube (0.24 versus 0.21).

3. Curvature of carbon skeleton and number of excited π electrons

Let us consider the effect of curvature of the nanotube carbon skeleton on the π electron state in them. The rolling up of a carbon monolayer into a tube leads to an expansion of the external electron crystal and a compression of the internal one. Such changes should be accompanied by changes in the exchange interaction between π electrons, an increase in the Coulomb interaction in the internal electron crystal and its weakening in the external one.

However, to provide stability of a quantum nanotube system, it is important to maintain the equality of electron densities of the external and internal electron crystals, since only when these densities are equal all Coulomb interactions between π electrons are balanced inside and between electron crystals.

Apparently, the condition in the quantum nanotube system can be satisfied due to the transition of a part of π electrons from the internal electron crystal to the external side of the nanotube, i.e., transition of a π electron from the lower lobe of its $2p_z$ state to the upper one. However, such a transition will encounter a strong Coulomb repulsion from the external electron crystal. The result of such repulsion, as shown in [11] for graphene polarization, can be a change in the hybrid state of the carbon atom to which this π electron belongs from $sp^2 + 2p_z$ to $sp^2 + 3s2p_z$ state and excitation of the π electron from the $2p_z$ state into one of two $3s2p_z$ hybrid states located on the external side of the nanotube. To distinguish such a excited electron from a π electron in the $2p_z$ state, we denote it as π^* electron.

A change in the hybrid state of carbon atom will be accompanied by a loss of its resonant π binding with three nearest neighboring atoms. Three resonant π bonds will be replaced by two single bonds with two neighboring atoms and one stationary (non-resonant) π^* bond with the third neighboring atom which is closer to the excited atom than the other two (Fig. 2).

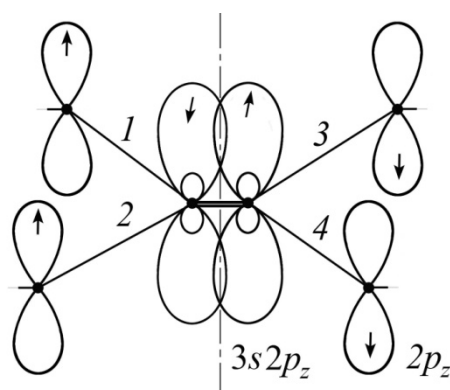


Fig. 2. Formation of four single bonds (1-4) and a stationary π^* bond by a pair of π^* electrons excited into the $3s2p_z$ state. The dot-and-dash line shows the tube axis direction

This point requires some explanation. A monolayer rolling up can be accompanied by a decrease in the distance and the bond length between carbon atoms. This decrease will depend on the bond orientation relative to the tube axis. So, if the length of the bond parallel to the tube axis remains unchanged at a monolayer rolling up, the length of the bond located at an angle to the axis decreases, and the length of the bond perpendicular to the axis also

decreases, but in a greater degree. Therefore, the hexagons are deformed, and the distances between atoms in the hexagon become different (Fig. 1).

The bonds perpendicular to the tube axis are present only in the armchair tubes, and the bonds parallel to the axis are present only in the zigzag ones. Therefore, the π^* electron excited into the $3s2p_z$ state in the armchair nanotube does not have an alternative when choosing an atom with a π electron of which it can be paired. It will be the π electron of the carbon atom closest to the excited atom because its π electron is redundant in the system of two π electron crystals (it does not have a pair in the internal electron crystal after the excited electron leaves it). Since the number of electrons in the quantum system in the internal and external electron crystals should be the same, the extra electron will also be pushed out of the external electron crystal and excited into the $3s2p_z$ state, but of its own atom. As a result, two adjacent closely spaced carbon atoms will be in the same hybrid $3s2p_z$ state, and their π^* electrons can be paired, thus forming a stationary π^* bond (Fig. 2). Such pairing is energetically favorable for a quantum nanotube system, since it partially compensates for the energy loss of two resonant π bonds of three ones.

To evaluate the number of π electrons migrating to the external side of the tube and the type of their ordering, we separate the projections of both tube rings into separate very narrow strips with a width equal to one carbon chain (Fig. 1 a, b). Each such strip in a nanotube corresponds to a thin ring containing only one carbon atom chain. Obviously, such a chain will be a sequence of atoms located in an armchair array for an armchair-type nanotube, and it will be a zigzag array for a zigzag-type nanotube.

The number of π electrons migrating to the external side of such a thin ring can be calculated from the condition of electron density equality on the external and internal sides of the nanotube. This equality suggests that the ratio between the numbers of electrons on two sides of a thin ring is inversely proportional to the ratio between curvatures of the π electron crystals.

The calculations showed that only three π electrons (from 24 π electrons) migrate to the external side of the ring in each thin ring of the armchair tube, while only two π electrons migrate to the external side in the thin ring of the zigzag tube. This is because the curvature of the zigzag carbon skeleton is less than the curvature of the armchair carbon skeleton. Thus, the difference between the number of π electrons on the external and internal sides of the thin ring containing one carbon chain will be six electrons for the armchair tube and four for the zigzag tube, or three and two π^* electron pairs, respectively (Fig. 1).

As a result, when a monolayer rolls up into an armchair tube, one fourth of π electrons change their state from the $2p_z$ to the $3s2p_z$ one, while only one sixth of π electrons change their state in the zigzag tube. Then the concentration of π electrons in the $2p_z$ state in the armchair tube decreases from 4×10^{15} to 3×10^{15} electrons per cm^2 , and it decreases to 3.3×10^{15} electrons per cm^2 in zigzag tubes. The average concentration of π^* electron pairs in the armchair tubes is estimated to be 5×10^{14} , and it is 3.5×10^{14} electron per cm^2 in zigzag tubes.

However, the concentration of the electron pairs is not so important for the conductivity of nanotubes, as the type of their ordering on the nanotube surface.

First, we consider the ordering of electron pairs of π^* bonds in one thin ring. Owing to the Coulomb repulsion between pairs, they are apparently distributed in the ring at equal distances from each other, i.e., the thin ring perimeter is divided into three equal parts for the armchair tube and two parts for the zigzag tube.

Let us consider ordering of π^* electron pairs between neighboring thin rings. π^* electron pairs in a quantum system with π electron crystals can be regarded as defects. Since defects in any crystalline structure tend to ordering, which reduces the system free energy, we can assume that they are ordered in nanotubes as well. As the π^* electron concentration is low, ordering is possible only in the form of 1D or quasi-1D crystals.

Since only three π^* electron pairs are formed in each thin ring of the armchair tube, there must also be three 1D crystals of π^* electron pairs. They will be located at equal distances from each other equal to three hexagon rows. The crystals will be oriented along the tube axis, since the shortest bonds in the armchair tubes perpendicular to the tube axis are located along it (Fig. 1a).

Only two quasi-1D crystals of pairs can be formed in a zigzag tube. They will also be located parallel to each other, but already at the distance determined by five hexagon rows. (It becomes clear why the zigzag tube should have an even number of rows). Since the shortest bonds in these tubes are oriented at an angle to the tube axis, the quasi-1D crystals will be located at the same angle to the tube axis and will embrace the tube in a spiral. Since the shortest bonds in each hexagon in the zigzag tubes are neighbors with an angle of about 120° between them, the spiral direction can be either clockwise or counterclockwise (Fig. 1b).

It can be seen from the above that, when a quantum system of graphene is rolled up into a nanotube, two spin-polarized electron crystals of $2p_z$ electrons are preserved, but with a loss of some of π electrons. In this case, 1D or quasi-1D crystals of pairs of π^* electrons excited into the $3s2p_z$ state arise in the nanotube quantum system. The number of 1D crystals in the armchair and zigzag tubes is different due to different curvatures of their carbon skeletons. The orientations of these crystals relative to the tube axis are also different, but due to different orientations of stationary π^* bonds.

4. Effect of 1D electron pair crystals on nanotube properties

The presence of 1D crystals of excited π^* electron pairs on the tube external side must lower the ionization potential of the nanotube and decrease the electric field threshold at which electron emission begins. In addition, the electron emission may be accompanied by the emission of electron pairs, pair breaking, and the release of π^* binding energy. The π^* binding energy is unknown. Only the energy of a π bond in carbon compounds is known. It is about 1.5 eV. The π^* bond energy should be slightly higher, since the $3s2p_z$ state is characterized by a volume larger than the $2p_z$ state, and the lateral overlapping of electron states can be a little larger. An energy of 1.5 eV and slightly higher correspond to radiation in the red and near infrared. The radiation emission accompanying the electron emission precisely in this range was obtained experimentally [3,4], where a very narrow emission band (0.022 eV) with a maximum of about 1.85 eV was observed. Perhaps, this energy corresponds to the π^* binding energy.

Since emission from nanotubes is associated with 1D crystals, it can be expected that it will be strongly inhomogeneous over the nanotube surface, which was also observed experimentally.

As for the conductivity of armchair nanotubes, it can be assumed that it occurs through tunneling of 1D crystals of pairs as a whole through gaps between adjacent π^* bonds. The geometric gap between the pairs is about 2.5 \AA , but if we take into account the volume of two $3s2p_z$ states, it proves to be less than 1 \AA . (Note that direct overlapping of these states is impossible because of their occupation by electron pairs). Since such tunneling occurs without resistance, it can be regarded as a mechanism of ballistic conductivity accomplished by electron pairs.

Tunneling of quasi-1D crystals of pairs is impossible in zigzag tubes, since the field applied along the tube axis cannot provide a spiral motion.

Note also that in the case of conductivity by pairs, the problem of contacts with metals, where there are no pairs, arises. An ideal contact for this case would be a superconductor. Perhaps, the absence of electron pairs in metals is responsible for the high Schottky barrier observed experimentally [10].

The 1D crystals of pairs create a strong inhomogeneity of the electric field on the nanotube surface in the form of negative charge strips protruding from the nanotube surface. Therefore, when the tubes approach each other, the Coulomb interaction can arise between them. As a result, they will be ordered relative to each other. Perhaps, the tendency to form bundles is explained by this Coulomb interaction.

5. Conclusions

It is shown that when a carbon monolayer (graphene) rolls up into a single-walled nanotube, the graphene-based system retains its quantum character, but with significant changes in it. In addition to the conservation of the system of π electrons in the $2p_z$ state forming two spin-polarized electron crystals strongly coupled to the carbon skeleton and providing resonant π binding between atoms, a second system of π^* electrons arises. It is a set of 1D or quasi-1D crystals of pairs of π^* electrons excited into the $3s2p_z$ state and forming stationary π^* bonds between excited carbon atoms. It has been shown that it is these 1D or quasi-1D crystals of π^* electron pairs that ensure the cylindrical nanotube shape stability and are responsible for the nanotube unusual physical properties.

Acknowledgements. No external funding was received for this study.

References

- [1] Charlier JC, Gonze X, Michenand JP. First Principles Study of Carbon Nanotube Solid-state Packing. *Europhys.Lett.* 1995;29: 43-48.
- [2] Thess A, Lee R, Nikolaev P, Dai H, Petit P, Robert J, Xu C, Lee YH, Kim SG, Rinzler AG, Colbert DT, Escuseria G, Tomanek D. Crystalline Ropes of Metallic Carbon Nanotubes. *Science.* 1996;273: 483-487.
- [3] Bonard JM, Stockli T, Maier F, De Heer WA, Chatelain A, Salvétat JP, Forro L. Field-Emission-Induced Luminescence from Carbon Nanotube. *Phys.Rev.Lett.* 1998;8: 1441-1444.
- [4] Zhu W, Bower C, Zhou O. Large current density from carbon nanotube field emitters. *Appl.Phys.Lett.* 1999;75: 873.
- [5] White CT, Todorov TN. Carbon nanotubes as long ballistic conductors. *Nature.* 1998;393: 240-242.
- [6] Kong J, Yenilmez E, Tomblor TW, Kim W, Dai H, Lauphlin RB, Liu L, Jayanthi CS, Wu SY. Quantum interference and ballistic transmission in nanotube electron wave guides. *Phys.Rev.Lett.* 2001;87: 106801.
- [7] Yao Z, Dekker C, Avouris Ph. Electrical Transport Through Single-Wall Carbon Nanotubes. In: Dresellhaus MS, Dresellhaus G, Avouris Ph (eds.) *Carbon Nanotubes. Synthesis, Structure, Properties, and Application. Topics in Applied Physics*; 2001.
- [8] Kasumov AYu, Deblock R, Kociak M, Reulet B, Bouchiat H, Khodos II, Gorbatov YuB, Volkov VT, Burhard M. Supercurrents Through Single-Walled Carbon Nanotubes. *Science.* 1999;284: 1508-1511.
- [9] Ferrier M, Kasumov A, Deblock R, Gueron S, Bouchiat H. Induced and intrinsic superconductivity in carbon nanotubes. *J.Phys.D: Appl.Phys.* 2010;43: 374003.
- [10] Heinze S, Tersoff J, Martel R, Derys V, Appenzeller J, Avouris Ph. Carbon Nanotubes as Schottky Barrier Transistors. *Phys.Rev.Lett.* 2002;89: 106801.
- [11] Krasinkova MV. Atomically flat carbon monolayer as an extremely unstable quasi-2D mesoscopic quantum system. *Materials Physics and Mechanics.* 2016;29(1): 93-100.
- [12] Iijima S, Ichihashi T. Single-shell carbon nanotubes of 1-nm diameter. *Nature (London).* 1993;363: 603-605.

STRUCTURE AND PROPERTIES OF NANOPOROUS OXIDE DIELECTRICS MODIFIED BY CARBON

Yu.V. Sakharov*

Tomsk State University of Control Systems and Radioelectronics (TUSUR),

40, Lenin Str., Tomsk, Russian Federation

*e-mail: iurii.v.sakharov@tusur.ru

Abstract. A physical method of receiving nanoporous films of the silicon dioxide (SiO_2) and tantalum pentoxide (Ta_2O_5) in vacuum conditions is brought forward in this work. The structure and properties of nanoporous films received as a result of self-organization at magnetron sputtering of a compound target are researched in it. Correlations of the quantity and size of pores, the structure and properties of nanoporous films are determined, as well. The self-organization process proves to form spatially sputtered pores, to change electrophysical properties of dielectric films and it enlarges their functions.

Keywords: nanoporous oxide films, carbon, self-organization process, magnetron sputtering

1. Introduction

The study of nanoporous dielectric films has been set a new impulse of late as a result of substantially enlarged sphere of their practical use. Such films can be used both in microelectronics as insulating stuff with low dielectric permittivity, and they can be used in photonics as anti-reflection coating in optoelectronic devices [1,2]. The nanoporous dielectric films can be also used as basic material for receiving nanomembranes and selective gas-sensing, sensor devices [3,4]. A number of methods of receiving nanoporous dielectric structure were worked out – anodizing, zol-gel method, matrix template synthesis are among them [2,5,6]. All the enumerated methods are chemical which makes it difficult to use them when producing micro – and nanoelectronics devices.

The purpose of the given research is to work out the integral schemes of the formation methods of nanoporous films of the silicon dioxide (SiO_2) and tantalum pentoxide (Ta_2O_5) basing on the technological modes of forming films with their structural and electrophysical properties.

2. Experiment and measurement methods

The basis of the suggested method is the self-organization principle proceeding in the plasma glow discharge which is formed by DC magnetron sputtering source, compound sputtering targets Si:C (graphite) or Ta:C (graphite) being its cathode [7]. The graphite area on the compound sputtering target expressed in percentage - S_c varied in such a case, which resulted in changing the pore quantity and size. Sputtering was done in the oxygen atmosphere with the pressure in an evacuated vessel equal to 4×10^{-1} Pa. Such are the conditions under which dielectric films of the silicon dioxide (SiO_2) and tantalum pentoxide (Ta_2O_5) are received, and injecting carbon is to make a sound nanoporous structure. The given method was patented earlier and it was used for receiving the films SiO_2 with low dielectric permittivity [8]. This method, however, is supposed to be applied to other oxide films used in micro – and

nanoelectronics, in Ta_2O_5 in particular. The pore formation in this process is explained by gaseous compounds CO or CO_2 which on educing, make the film friable forming in it open pores and gas inclusions.

The thickness of the dielectric films which were researched in the electrophysical operations was 100 nm. The films Al, about 100 nm thick, were used as electrodes at electrical measurements. These films were made by means of thermal evaporation in vacuum. Condensing structures Al-SiO₂-Al and Al-Ta₂O₅-Al were formed like matrixes with the active area of 1x1 mm on the ceramized substrates of 60×48×0.6 mm in size.

The determination of the pore quantity and size was done by means of electrochemical copper jumping. The width of the Tauc gap (E_t) was defined by the extrapolation $(\alpha E)^{1/2}$ dependence on the photon energy E in the range of the wave lengths of 200-1100 nm [9]. The spectral dependence of the film absorption index (α) was defined by transmission and reflection spectrums with the help of spectrometer USB2000. The determination of the thickness and dielectric film refraction index was stated by means of a spectral ellipsometric complex. The microanalysis was done with the help of the Bruker Quantax 50 EDX microanalyzer as a part of an electron microscope Hitachi TM-1000. The spectral analysis of the researched films was done by using an IR –spectrometer in the range of the frequencies of 500 – 5000 sm^{-1} .

3. Experiment results and analysis

Electric properties. The research of the electric capacity of the structures Al-SiO₂-Al and Al-Ta₂O₅-Al has revealed the general tendency of dielectric permittivity changing and that of angle tangent of dielectric losses with the increase percentage of graphite content on the compound target when $S_c < 40\%$, however, at great values of S_c the qualitative type of dependences differed. At the same time the dependence of electric strength on S_c was similar, and it decreased gradually for the both structures (Fig. 1, Fig. 2)

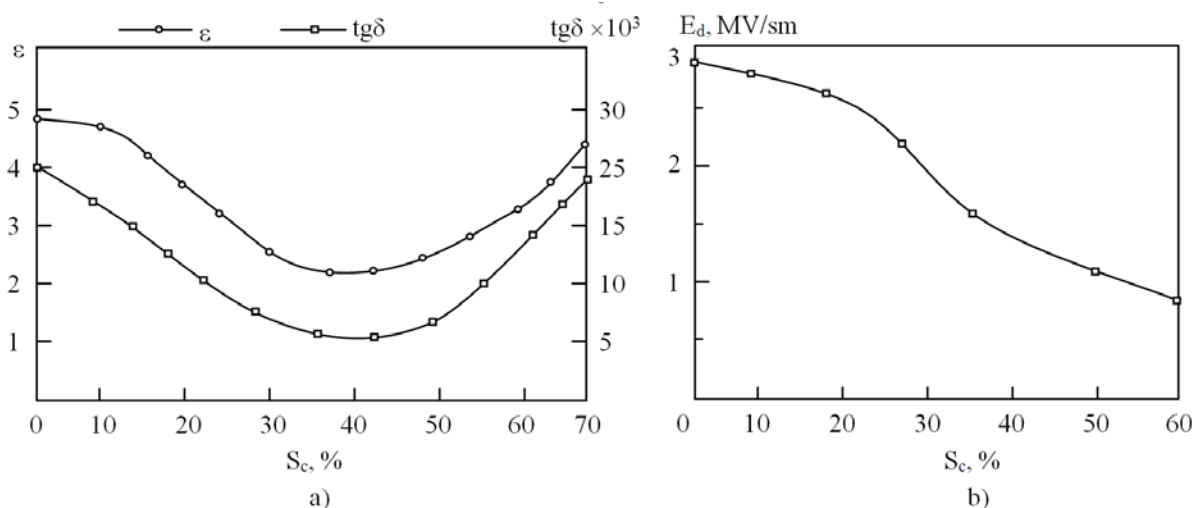


Fig. 1. Dependence of dielectric permittivity ϵ , tangent losses $tg\delta$ (a) and electric strength E_d on S_c (b) for the structure Al-SiO₂-Al

It is evident that the reduction of dielectric permittivity for films SiO₂ can be explained only by the formation of gas inclusions, because all the other possible ways (the formation of chemical bonds of silicon with carbon, the formation of carbon injections) would lead to an opposite result. The tangent reduction of the dielectric loss angle is supposedly connected both with the gas inclusions, having a considerably smaller tangent of loss angle, and also with the reduced film defect because of the chemical reactions which are supposed to be more

intensive in the places of defect localization. The growth of these values at $S_c > 40\%$ is caused by the oxygen deficit and formation of films SiO_x , in which x proceeds to 1 which can result in the formation of local regions containing underoxidized silicon and, hence, can enlarge tangent of dielectric loss angle. This is verified by the microanalysis, Auger electron spectroscopy (AES) and IR-spectroscopy data. Electric strength reduction is quite characteristic of nanoporous films that have heterogeneous structure, and probably, it is connected with penetration of the material of the upper electrode into the dielectric film [10].

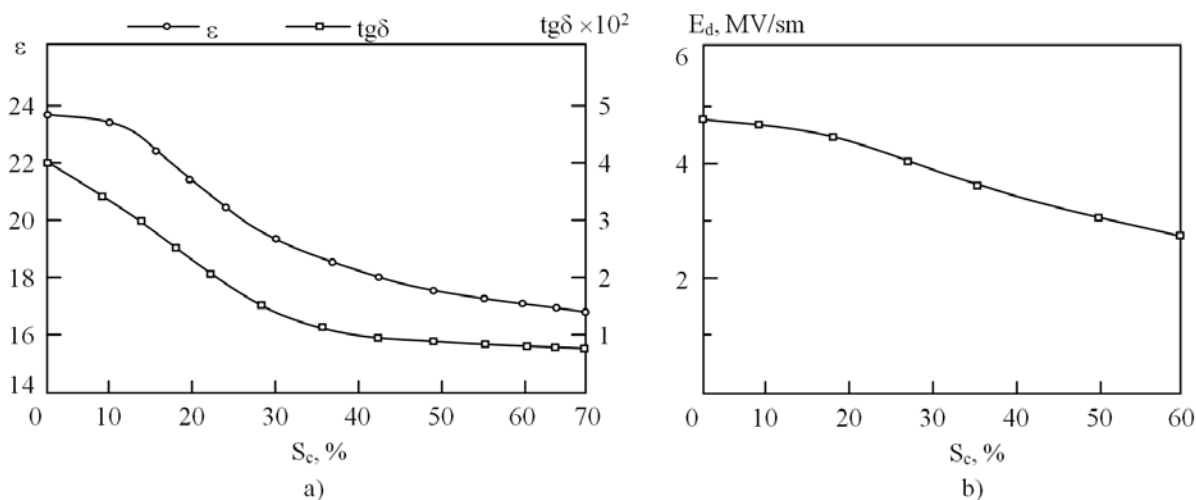


Fig. 2. Dependence of dielectric permittivity ϵ , tangent losses $\text{tg}\delta$ (a) and electric strength E_d on S_c (b) for the structure Al-Ta₂O₅-Al

On the analogy of the previous account, the same changes are supposed to occur in the films Ta₂O₅, however, the dependence type in them is somewhat different, which can be explained by the chemical properties of Ta, itself.

Optical properties. The research of physical properties of dielectric films SiO₂ and Ta₂O₅ has revealed the change of the refraction index n and the width of the optical gap E_t (Fig. 3).

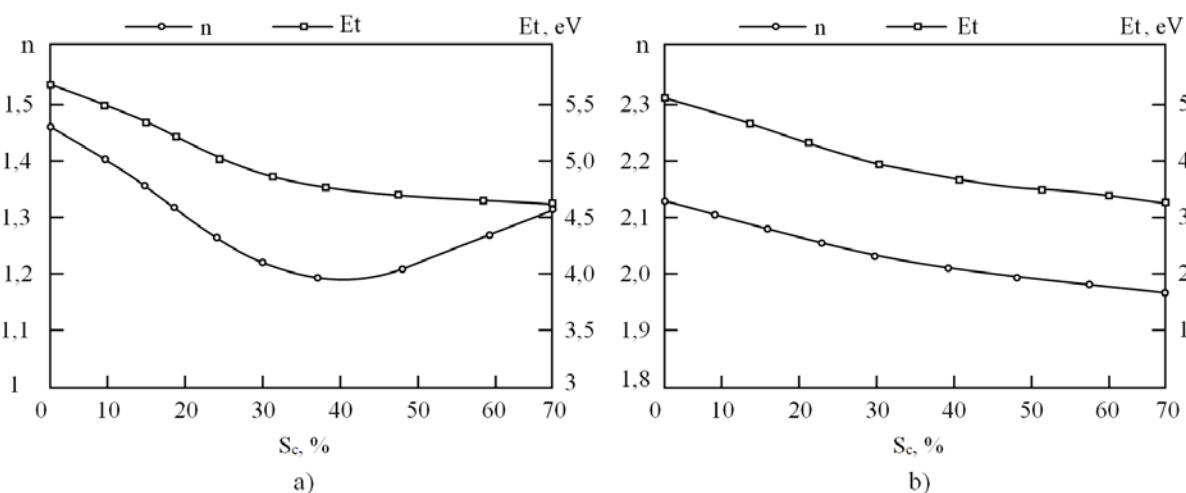


Fig. 3. Refraction index dependence n (at the wavelength $\lambda=632$ nm) and that of the width of the optical gap E_t on S_c for the structure Al-SiO₂-Al (a) and Al-Ta₂O₅-Al (b)

The behaviour of the refraction index correlates with the change of dielectric permittivity, which is quite conformable to the theory. Reduction of the width of the optical

gap can be connected both with the electronic structure change of dielectric films, themselves, and the presence of gas in the pores.

Structure of surface. The research of the dielectric film porosity illustrated quite even distribution of the pores over the dielectric area. Small mesopores with the diameter of less than 10 nm and larger ones with the diameter of more than 50 nm can be visually distinguished [11]. The porosity of the film SiO_2 considerably rises with the value growth of S_c reaching its peak at $S_c \sim 50\%$, then the growth is replaced by the saturation area (Fig. 4). The qualitative dependence type for the films SiO_2 and Ta_2O_5 is equal, at that. Porosity was determined by capacitance method [12]. The structure of the surface also undergoes considerable changes (Fig. 5).

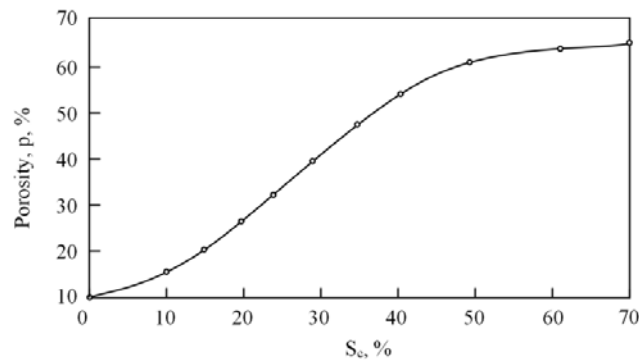


Fig. 4. Relationship between porosity of dielectric film SiO_2 and S_c

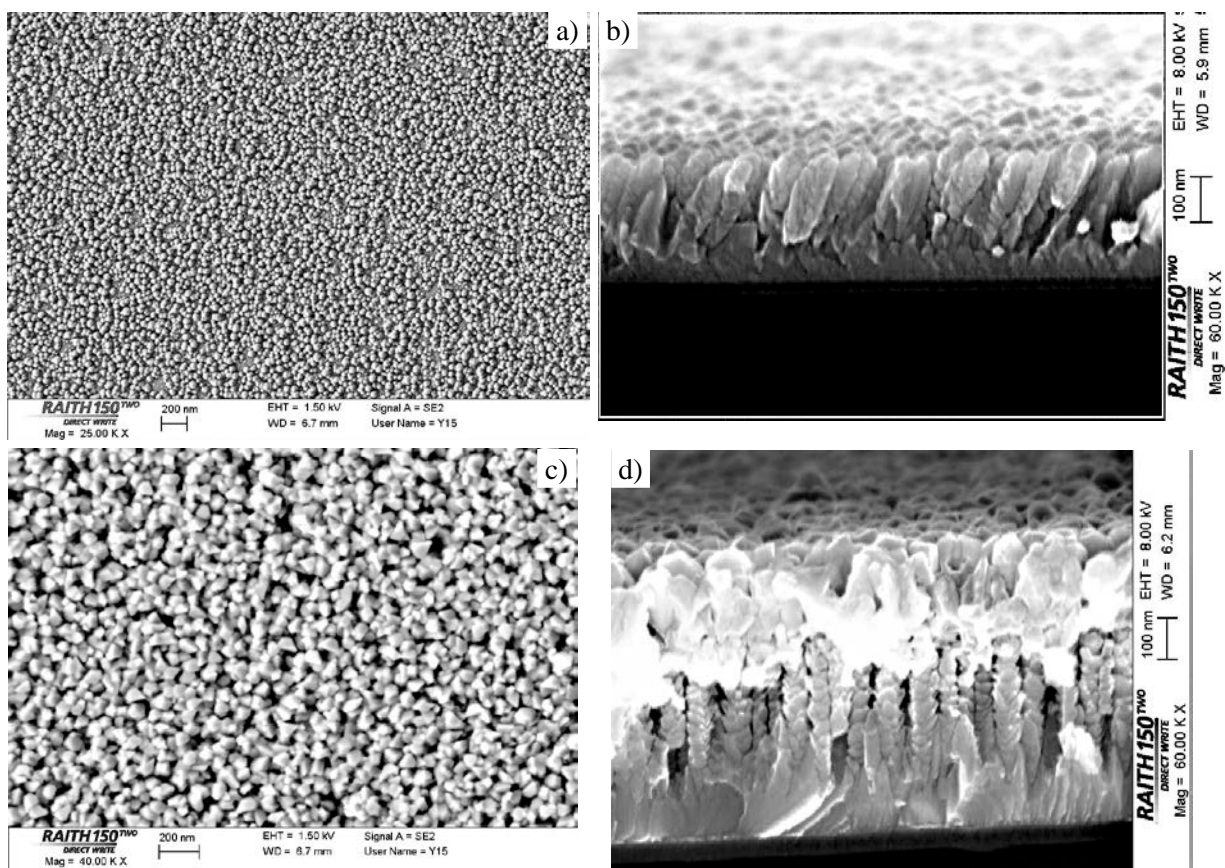


Fig. 5. The surface of the nanoporous dielectric SiO_2 ($S_c = 60\%$) received with the help of the probe microscope: a – surface of the plate, b – chip in the edge of the plate, c – surface of the plate (with an upper aluminium electrode with a thickness of 200 nm) d – chip in the edge of the plate (with an upper aluminium electrode with a thickness of 200 nm)

Spectral analysis. The analysis of the structure of the researched films SiO_2 done by a microanalyzer revealed some rise of oxygen content with the growth of Sc, the same concerned the films Ta_2O_5 . Moreover, IR spectrums of the researched films proved a sharp growth of absorption at the wavelength $\nu=2350 \text{ cm}^{-1}$ corresponding to oscillations of bonds C–O. There are also changes in the area: $\nu_1 = 3000 \text{ cm}^{-1}$, $\nu_2 = 3400 \text{ cm}^{-1}$, $\nu_3 = 3600 \text{ cm}^{-1}$, and also some changes of peak $\nu_4 = 935\text{-}940 \text{ cm}^{-1}$. Peaks ν_1 , ν_2 , ν_3 are usually referred to as OH – groups and H_2O molecules, peak ν_4 refers to Si-O-Si bond (valency oscillations) [13].

Supposedly, it can be explained by the presence of water in the pores owing to the capillary effect, and also to the reaction products – gases CO or CO_2 . It can occur, as well, owing to the adsorption of gases CO or CO_2 from the atmosphere [14]. The given peak amplitude rises with the growth of Sc, which can be connected with the occurrence of oxygen vacancies in the silicon and negative charge. The occurrence of the effective negative charge on the silicon atom adds to a better adsorption capacity. Thus this resulted in the stimulated adsorption. The preliminary experiments have already proved the selectivity of hydrocarbons and gas CO adsorption, and also of organic compounds with different functional groups.

4. Conclusions

1. The experiments proved that the carbon injection into the process of the formation of the films SiO_2 and Ta_2O_5 leads to the formation of self-organized nanoporous structure. The size and density of the pores is determined by the quantity of the injected carbon.

2. Electrical and optical parameters of the films SiO_2 and Ta_2O_5 are largely defined by the porosity and they have similar tendencies in some intervals, however, the general dependence type is stated by the chemical properties of the spattered material, itself.

3. Common tendencies in the change of electrophysical properties and in the surface structure of the films SiO_2 and Ta_2O_5 with the carbon injected into them, make it possible to assume that analogous changes will be developed in other oxide dielectrics which are formed in the plasma of the glow discharge, though the qualitative dependence type will be different.

4. The formation of the nanoporous structure contributes to the rise of the selective adsorption capacity of the researched dielectrics, mainly, owing to capillary condensation in mesapores and also stimulated adsorption, which can serve the basis of creating gas-sensing sensor devices [15].

Acknowledgements. *The work was carried out within the framework of the scientific project "Theoretical and experimental studies of ultra-wideband optoelectronic devices of fiber-optic information transmission systems and radio photonics based on photonic integrated circuits of its own design" carried out by the team of the LIOR scientific laboratory with the financial support of the Ministry of Science and Higher Education of Russia (project number FEWM-2020-0040). The experimental results were obtained using the equipment of Impulse CCP (registration number 200568)..*

References

- [1] Gidley DW, Peng H, Vallery R. Positron Annihilation Spectroscopy. In: Baklanov M, Maex K, Green M (eds.) *Dielectric Films for Advanced Micr-oelectronics*. Chichester: Wiley; 2007. p.86-100.
- [2] Sadykov AI, Kushnir SE, Roslyakov IV, Baranchikov AE, Napolskii KS. Selenic acid anodizing of aluminium for preparation of 1D photonic crystals. *Electrochem. Commun.* 2019;100: 104-107.
- [3] Sakharov Y, Troyan P, Zhidik Y. Energy efficient sensors based on carbon-modified silica films. In: *Proc. 2019 International Siberian Conference on Control and Communications (SIBCON)*. IEEE; 2019. p. 18739807.

- [4] Zhang H, Wang Y, Zhu X, Li Y, Cai W. Bilayer Au nanoparticle-decorated WO₃ porous thin films: On-chip fabrication and enhanced NO₂ gas sensing performances with high selectivity. *Sens. Actuators, B*. 2019;280: 192-200.
- [5] Zhang C, Shi Y, Fu Z. A facile method for the fabrication of SiO₂ and SiO₂/TiO₂ hollow particles using Na₂SO₄ particles as templates. *J. Sol-Gel Sci. Technol.* 2019;91(3): 431-440.
- [6] Ma S, Wang Y, Liu C, Xu Q, Min Z. Preparation and characterization of nanoporous polyimide membrane by the template method as low-k dielectric material. *Polym. Adv. Technol.* 2016;27(3): 414-418.
- [7] Sakharov YV, Troyan PE. Technology of porous silicon dioxide films synthesis and their electrical properties. In: *24th International Crimean Conference Microwave and Telecommunication Technology, CriMiCo*; 2014. p.682-683.
- [8] Sakharov YV, Usov SP, Troyan PE. *The method of obtaining porous silicon dioxide*. RU2439743 (Patent), 2012.
- [9] Tumuluri A, Lakshun NK, Raju JK. Band gap determination using Tauc's plot for LiNbO₃ thin films. *Int. J. of ChemTech Res.* 2014;6: 3353-3356.
- [10] Vanstreels K, Ciofi I, Barbarin Y, Baklanov M. Influence of porosity on dielectric breakdown of ultralow-k dielectrics. *J. Vac. Sci. Technol. B*. 2013;31(5): 050604.
- [11] Troyan PE, Sakharov YuV, Zhigal'skii AA, Makrushin AS. An electron-microscopic study of SiO₂ films with a carbon impurity. *Russ. Phys. J.* 2006;49(2): 219-220.
- [12] Adamyan A, Adamian Z, Aroutiounian V. Capacitance method for determination of basic parameters of porous silicon. *Phys. Status Solidi C*. 2007;4(6): 1976-1980.
- [13] Grill A, Neumayer DA. Structure of low dielectric constant to extreme low dielectric constant SiCOH films: Fourier transform infrared spectroscopy characterization. *J. of App. Phys.* 2003;94(10): 6697-6707.
- [14] Cui S, Yu S, Lin B, Shen X, Zhang X, Gu D. Preparation of amine-modified SiO₂ aerogel from rice husk ash for CO₂ adsorption. *J. Porous Mater.* 2017;24(2): 455-461.
- [15] Usov SP, Sakharov YV, Troyan PE. *The Sensitive Element of the Sensor Hydrocarbons*. RU101197 (Patent), 2011.

PAIR INTERACTION OF COAXIAL CIRCULAR PRISMATIC DISLOCATION LOOPS IN ELASTIC SOLIDS WITH SPHERICAL SURFACES

S.A. Krasnitckii¹⁻³, A.M. Smirnov^{1*}, M.Yu. Gutkin¹⁻³

¹ITMO University, Kronverkskii pr. 49, St. Petersburg, 197101, Russia

²Peter the Great St. Petersburg Polytechnic University, Polytekhnicheskaya 29, St. Petersburg, 195251, Russia

³Institute of Problems in Mechanical Engineering, Russian Academy of Sciences, Bolshoi 61, Vasil. Ostrov,
St. Petersburg, 199178, Russia

*e-mail: smirnov.mech@gmail.com

Abstract. In the present work, the pair interaction of coaxial circular prismatic dislocation loops (PDLs) arbitrary placed in elastic solids with free spherical surfaces is considered. The analytical solutions for the pair interaction energies of PDLs in an elastic sphere, an elastic medium with a spherical pore and a spherical layer are given in the form of double power series and illustrated by energy maps built in the space of the normalized PDL radii and axial positions. The results can be used for analyzing the theoretical models of stress relaxation processes in bulk and hollow core-shell nanoparticles and pentagonal particles, which occur through the formation of dislocation ensembles.

Keywords: prismatic dislocation loops, dislocation ensembles, stress relaxation

1. Introduction

Dislocation loops are typical defects in solids, which play a significant role in the physics and micromechanics of crystalline materials [1,2]. In particular, the formation of prismatic dislocation loops (PDLs) is one of the main mechanisms of elastic strain and stress relaxation in solid-state structures containing inhomogeneities and pores. For instance, the ensembles of concentric PDLs lying in the same plane and encircling the highly compressed precipitates in gadolinium gallium garnet crystals were examined by optical microscopy in [3,4]. Subsequently, this mechanism was theoretically described in [5] for the case of generation of a single PDL encircled spherical inclusion. The generation of a misfit PDL at the interface of the dilatational spherical inclusion was theoretically investigated in [6]. Another relaxation mechanism is the punching of ensembles of coaxial PDLs by the inclusion to the matrix. It was observed experimentally in [7-9] and then studied by analytical calculations [10] and dislocation dynamics computer simulations [11]. The generation of satellite PDLs as the effective relaxation mechanism in GaAs films containing As-Sb clusters subjected to one-dimensional dilatation eigenstrain was experimentally [12,13] and theoretically [14,15] investigated.

To analyze the critical conditions of PDL formation, the authors of the aforementioned theoretical models [5,6,10,14,15] used the well-known solution for the strain energy of a PDL in an infinite homogeneous elastic medium, given by Dundurs and Salamon [16], in which case the image force effects on the relaxation processes were neglected. This limitation could

be overcome by using strict analytical solutions of relevant boundary-value problems in the theory of elasticity for PDLs in solids with spherical surfaces/interfaces.

By now, some strict analytical solutions describing the elastic fields and energies of circular PDLs in an infinite medium [16-18], near a flat free surface [19] and a planar interface [16,20], in thin plates [21,22], in homogeneous [23-25] and heterogenous core-shell [26] cylinders as well as in solids with spherical boundaries [27-31] have been fairly well discussed. The displacement field of a circular PDL in an elastic sphere was first presented in [27]. The elastic fields and energy of a circular PDL coaxial to the spherical pore in an infinite medium were obtained in [28] that allowed to analyze a critical condition for punching of a single PDL by the bubbles (pores under pressure) and verified these results with experimental observations of PDL ensembles in irradiated materials containing helium [32,33] or hydrogen [34] in bubbles. Recently, similar solution has been suggested to use in dislocation dynamics computer simulations [31]. The case of dislocation emission induced by the spherical pore under remote loading was also studied by molecular dynamics simulations [35,36].

The displacement field of a circular dislocation loop occupying an arbitrary position inside an elastically inhomogeneous core-shell spherical particle was found in [29]. The solution was given in the form of double series of vector functions with unknown coefficients which have to be determined by solving an infinite system of algebraic equations. The authors of [29] demonstrated their analytical results with a numerical calculation of the image force acting on a PDL symmetrically placed in the core that seems difficult to use in physical applications.

A more applicable solution, from our point of view, is presented in [30] where the stress field of a circular PDL is obtained in terms of the Legendre polynomials series for the following cases: an elastic sphere, an infinite elastic medium with a spherical pore, and an elastic spherical layer with free surfaces. The corresponding solutions have been applied for analyzing the initial stages of stress relaxation processes through the formation of individual PDLs in bulk [37] and hollow [38] core-shell nanoparticles, in icosahedral [39] and decahedral [40,41] small particles (see also a brief review [42]). These theoretical models give results which are in good agreement with experimental data [43,44].

Thus, the aforementioned strict analytical solutions have been used for analyzing the critical conditions of stress relaxation through generation of individual PDLs. However, both the experimental examinations and computer simulations show that, in many real structures, a number of similar PDLs can nucleate and behave in tight interaction with each other, which requires the development of suitable mathematical means for studying these situations. One of such means is the energy of pair interactions between PDLs.

In the present work, we consider the interaction of two coaxial circular PDLs arbitrary placed in different elastic bodies with free spherical surfaces such as an elastic sphere, an elastic medium with a spherical pore, and a spherical layer. Using the strict analytical solution of the boundary-value problem for a circular PDL in an elastic sphere [30], we find an analytical form for the interaction energy and illustrate this result by energy maps built in the space of the normalized PDL radii and axial positions. In our further work, we are going to use these results in analyzing theoretical models of stress relaxation processes in core-shell nanoparticles and pentagonal particles, which occur through the formation of various dislocation ensembles.

2. Model

Consider an elastically isotropic spherical layer with inner and outer radii a_p and a , respectively, containing a pair of interstitials (for definiteness) circular PDLs which are characterized by the following plastic distortion component [45]:

$$\beta_{zz}^{(k)} = b_k H(1 - r/c_k) \delta(z - z_k), \quad k = 1, 2, \quad (1)$$

where b_k is the Burgers vector magnitude of the PDL- k , $H(t)$ is the Heaviside function, $\delta(z - z_k)$ is the Dirac delta function, c_k is the radius of the PDL- k , and z_k is its coordinate (see Fig. 1).

The interaction energy W_{int}^{1-2} between PDL-1 and PDL-2 in the spherical layer can be determined as the work spent to create the PDL-1 in the stress field $\sigma_{zz}^{(2)}$ of the PDL-2:

$$W_{int}^{1-2} = \int_V \beta_{zz}^{(1)} \sigma_{zz}^{(2)} dV = b_1 \int_V H(1 - r/c_1) \delta(z - z_1) \sigma_{zz}^{(2)} dV = b_1 \int_{S_1} \sigma_{zz}^{(2)} \Big|_{z=z_1} dS = 2\pi b_1 \int_{\xi}^{c_1} \sigma_{zz}^{(2)} r dr, \quad (2)$$

where r is the polar radius; $\xi = 0$ in the case when the PDL-1 plane does not intersect the inner spherical surface, i.e. when $z_1 \geq a_p$, and $\xi = \sqrt{a_p^2 - z_1^2}$ in the case when the PDL-1 plane intersects the inner spherical surface, i.e. when $z_1 < a_p$.

According to [30], the axial stress $\sigma_{zz}^{(2)}$ of PDL-2 in the elastic layer can be presented as a sum of the axial stress ${}^{\infty}\sigma_{zz}^{(2)}$ of PDL-2 in an infinite elastic medium and an additional term ${}^*\sigma_{zz}^{(2)}$ which provides the fulfillment of the boundary conditions on the free spherical surfaces:

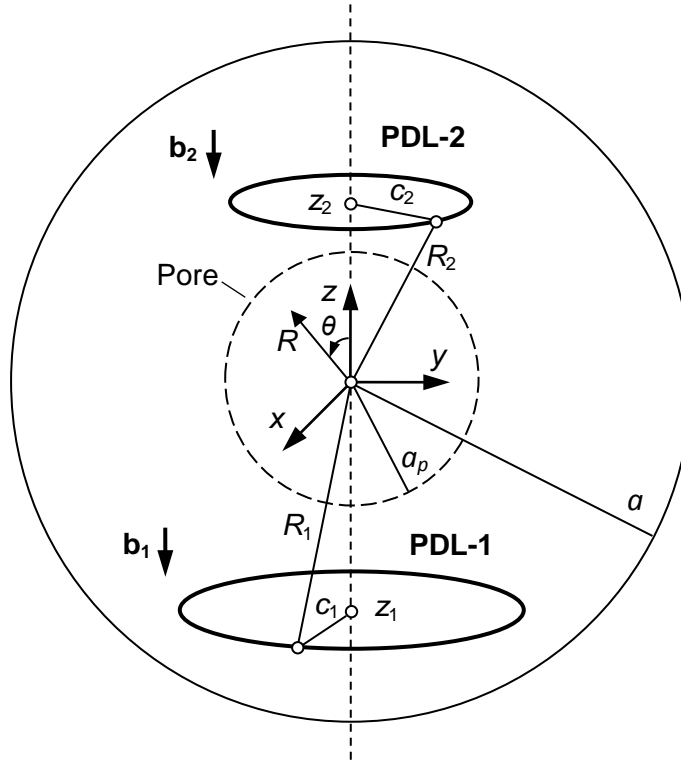


Fig. 1. A pair of interstitial circular PDLs in a spherical layer. The corresponding coordinate system is located in the center of spherical surfaces

$$\sigma_{zz}^{(2)} = {}^{\infty}\sigma_{zz}^{(2)} + {}^*\sigma_{zz}^{(2)}, \quad (3a)$$

$${}^{\infty}\sigma_{zz}^{(2)} = -\frac{Gb_2}{2(1-\nu)} \left[\frac{1}{c_2} J(1,0;1) + \frac{|z - z_2|}{c_2^2} J(1,0;2) \right], \quad (3b)$$

$${}^*\sigma_{zz}^{(2)} = \sigma_{RR} \cos^2 \theta + \sigma_{\theta\theta} \sin^2 \theta - \sigma_{R\theta} \sin 2\theta, \quad (3c)$$

$$\begin{aligned}
{}^* \sigma_{RR}^{(2)} = 2G \sum_{n=0}^{+\infty} & \left[-A_n^{(2)}(n+1)(n^2 - k - 2 - 2\nu)R^n - B_n^{(2)}n(n-1)R^{n-2} + \right. \\
& \left. + \frac{C_n^{(2)}n}{R^{n+1}}(n^2 + 3n - 2\nu) - \frac{D_n^{(2)}}{R^{n+3}}(n+1)(n+2) \right] P_n(\cos \theta), \quad (3d)
\end{aligned}$$

$$\begin{aligned}
{}^* \sigma_{R\theta}^{(2)} = 2G \sum_{n=1}^{+\infty} & \left[-A_n^{(2)}(n^2 + 2n - 1 + 2\nu)R^k - B_k^{(2)}(n-1)R^{n-2} - \right. \\
& \left. - \frac{C_n^{(2)}}{R^{n+1}}(n^2 - 2 + 2\nu) + \frac{D_n^{(2)}}{R^{n+3}}(n+2) \right] \frac{dP_n(\cos \theta)}{d\theta}, \quad (3e)
\end{aligned}$$

$$\begin{aligned}
{}^* \sigma_{\theta\theta}^{(2)} = 2G \sum_{k=0}^{+\infty} & \left\{ \left[-A_n^{(2)}(n+1)(n^2 + 4n + 2 + 2\nu)R^n - B_n^{(2)}n^2R^{n-2} + \right. \right. \\
& \left. \left. + \frac{C_n^{(2)}n}{R^{n+1}}(n^2 - 2n - 1 + 2\nu) - \frac{D_n^{(2)}(n+1)^2}{R^{n+3}} \right] P_n(\cos \theta) - \right. \\
& \left. - \left[A_n^{(2)}(n+5 - 4\nu)R^n + B_n^{(2)}R^{n-2} + \frac{C_n^{(2)}}{R^{n+1}}(-n+4 - 4\nu) + \frac{D_n^{(2)}}{R^{n+3}} \right] \frac{dP_n(\cos \theta)}{d\theta} \cot \theta, \quad (3f)
\end{aligned}$$

where G is the shear modulus, ν is the Poisson ratio, $J(m, n; p)$ are the Lipchitz-Hankel integrals defined as $J(m, n; p) = \int_0^\infty J_m(\kappa) J_n(\kappa r / c_2) \exp[-\kappa |z - z_2| / c_2] \kappa^p d\kappa$, $J_m(\kappa)$ and $J_n(\kappa r / c_2)$ are the Bessel functions, $A_n^{(2)}$, $B_n^{(2)}$, $C_n^{(2)}$, and $D_n^{(2)}$ are the coefficients determined in [30] from the boundary conditions on the free inner and outer spherical surfaces, and $P_n(t)$ are the Legendre polynomials determined by the following explicit formula

$$P_n(t) = \frac{1}{2^n} \sum_{s=0}^{[n/2]} (-1)^s \binom{n}{s} \binom{2n-2s}{n} t^{n-2s}. \quad (4)$$

Here $t = \cos \theta$, $[n/2]$ gives the greatest integer less than or equal to $n/2$, and $\binom{n}{s}$ are the binomial coefficients.

Substituting (3a) to (2), we obtain after integration

$${}^\infty W^{1-2} = \frac{\pi G b_1 b_2}{(1-\nu)} \left[r J(1, 1; 0) + \frac{|z - z_2|}{c_2} r J(1, 1; 1) \right]_{r = \xi}^{r = c_1} \Big|_{z = z_1}. \quad (5)$$

Then one can simplify equations (3c-f) for ${}^* \sigma_{zz}^{(2)}$ by using the following recurrence relations for the Legendre polynomials [30]:

$$t^2 P_n(t) = \frac{(n+1)(n+2)}{(2n+1)(2n+3)} P_{n+2}(t) + \frac{2n^2 + 2n - 1}{(2n-1)(2n+3)} P_n(t) + \frac{n(n-1)}{(2n-1)(2n+1)} P_{n-2}(t), \quad (6a)$$

$$t \sqrt{1-t^2} P_n^1(t) = \frac{n(n+1)(n+2)}{(2n+1)(2n+3)} P_{n+2}^1(t) - \frac{n(n+1)}{(2n-1)(2n+3)} P_n^1(t) - \frac{(n-1)n(n+1)}{(2n-1)(2n+1)} P_{n-2}^1(t), \quad (6b)$$

where $P_n^1(t) = -\sqrt{1-t^2} dP_n(t) / dt$.

Substituting recurrence relations (6) to (3c), after some algebra we finally find

$$\begin{aligned}
{}^* \sigma_{zz}^{(2)} = \frac{Gb}{1-\nu} \sum_{n=0}^{+\infty} & \left[A_n^{(2)} \frac{2(n+1)(1+\nu - 2n\nu - 2n^2)}{2n-1} R^n + B_{n+2}^{(2)}(n+1)(n+2)R^n \right. \\
& \left. + A_{n+2}^{(2)} \frac{(n+2)(n+3)(2n^2 + 9n + 7)}{2n+3} R^{n+2} - \frac{2n(1-3\nu + 2n(2-\nu) + 2n^2)}{2n+3} \frac{C_n^{(2)}}{R^{n+1}} + \right.
\end{aligned}$$

$$+(n-1)n \frac{D_{n-2}^{(2)}}{R^{n+1}} - \frac{(n-2)n(2n^2-7n+5)}{2n-1} \frac{C_{n-2}^{(2)}}{R^{n-1}} \Big] P_n(\cos \theta), \quad (7)$$

where $C_{-2}^{(2)} = D_{-2}^{(2)} = C_{-1}^{(2)} = D_{-1}^{(2)} = 0$.

With Eq. (7) and taking into account that, for $z = z_1$, the relations $\cos \theta = z_1 / R$ and $r dr = R dR$ hold, integral (2) gives

$$\begin{aligned} {}^*W^{1-2} = & \frac{\pi G b_1 b_2}{1-\nu} \sum_{n=0}^{+\infty} \left[A_n^{(2)} \frac{2(n+1)(1+\nu-2n\nu-2n^2)}{2n-1} Q_{n,1} + B_{n+2}^{(2)} (n+1)(n+2) Q_{n,1} \right. \\ & + A_{n+2}^{(2)} \frac{(n+2)(n+3)(2n^2+9n+7)}{2n+3} Q_{n,2} - C_n^{(2)} \frac{2n(1-3\nu+2n(2-\nu)+2n^2)}{2n+3} T_{n,1} + \\ & \left. + D_{n-2}^{(2)} (n-1)n T_{n,3} - C_{n-2}^{(2)} \frac{(n-2)n(2n^2-7n+5)}{2n-1} T_{n,3} \right], \quad (8) \end{aligned}$$

where $Q_{n,l}$ and $T_{n,l}$ are polynomials determined by equations

$$Q_{n,l} = \sum_{s=0}^{\lfloor n/2 \rfloor} \frac{(-1)^s}{2^n (s+l)} \binom{n}{s} \binom{2n-2s}{n} z_1^{n-2s} (R_1^{2(s+l)} - \zeta^{2(s+l)}), \quad (9a)$$

$$T_{n,l} = \sum_{s=0}^{\lfloor n/2 \rfloor} \frac{(-1)^s}{2^n (-2k+2s+l)} \binom{n}{s} \binom{2n-2s}{n} z_1^{n-2s} (R_1^{-2k+2s+l} - \zeta^{-2k+2s+l}). \quad (9b)$$

Here $\zeta = z_1$ if $z_1 \geq a_p$, and $\zeta = a_p$ if $z_1 < a_p$.

Thus, the interaction energy W_{int}^{1-2} for PDL-1 and PDL-2 in the spherical layer is given by

$$W_{int}^{1-2} = {}^\infty W^{1-2} + {}^*W^{1-2}, \quad (10)$$

where ${}^\infty W^{1-2}$ is determined by Eq. (5) and ${}^*W^{1-2}$ by Eqs. (8) and (9).

3. Results

To illustrate the results obtained, consider an example of the pair interaction between PDL-1, which has arbitrary radius c_1 and axial position z_1 , and PDL-2 with fixed radius $c_2 = 100b_2$ and axial position $z_2 = 0$. Figures 2a-d show the maps of the interaction energy W_{int}^{1-2} in normalized coordinates of radius c_1/c_2 and axial position z_1/c_2 of PDL-1 in (a) an infinite medium, (b) an elastic sphere of radius $a = 1.5c_2$, (c) an infinite medium with a spherical pore of radius $a_p = 0.5c_2$, and (d) a spherical layer of radii $a_p = 0.5c_2$ and $a = 1.5c_2$. As is seen, the interaction energy of PDLs strongly depends on their radii and positions in the elastic body. Moreover, it is highly sensitive to the presence of the inner and outer free surface in the case when at least one of the PDLs is localized near the surface. It is worth noting that, in this case, the outer free surface makes a greater effect on the interaction energy than the inner free surface. The most evident and interesting manifestation of the outer surface effect is the region of negative values of the interaction energy near the equator and the outer free surface (at the right bottom corner of the maps in Figs. 2(b,d)). It means that PDL-1 of radius $0.9a < c_1 < a$ is attracted to immobilized PDL-2 in this region, while in all the remaining area of the body, where the interaction energy is positive, PDL-1 is repulsed of PDL-2. In contrast, the inner free surface does not give such effect.

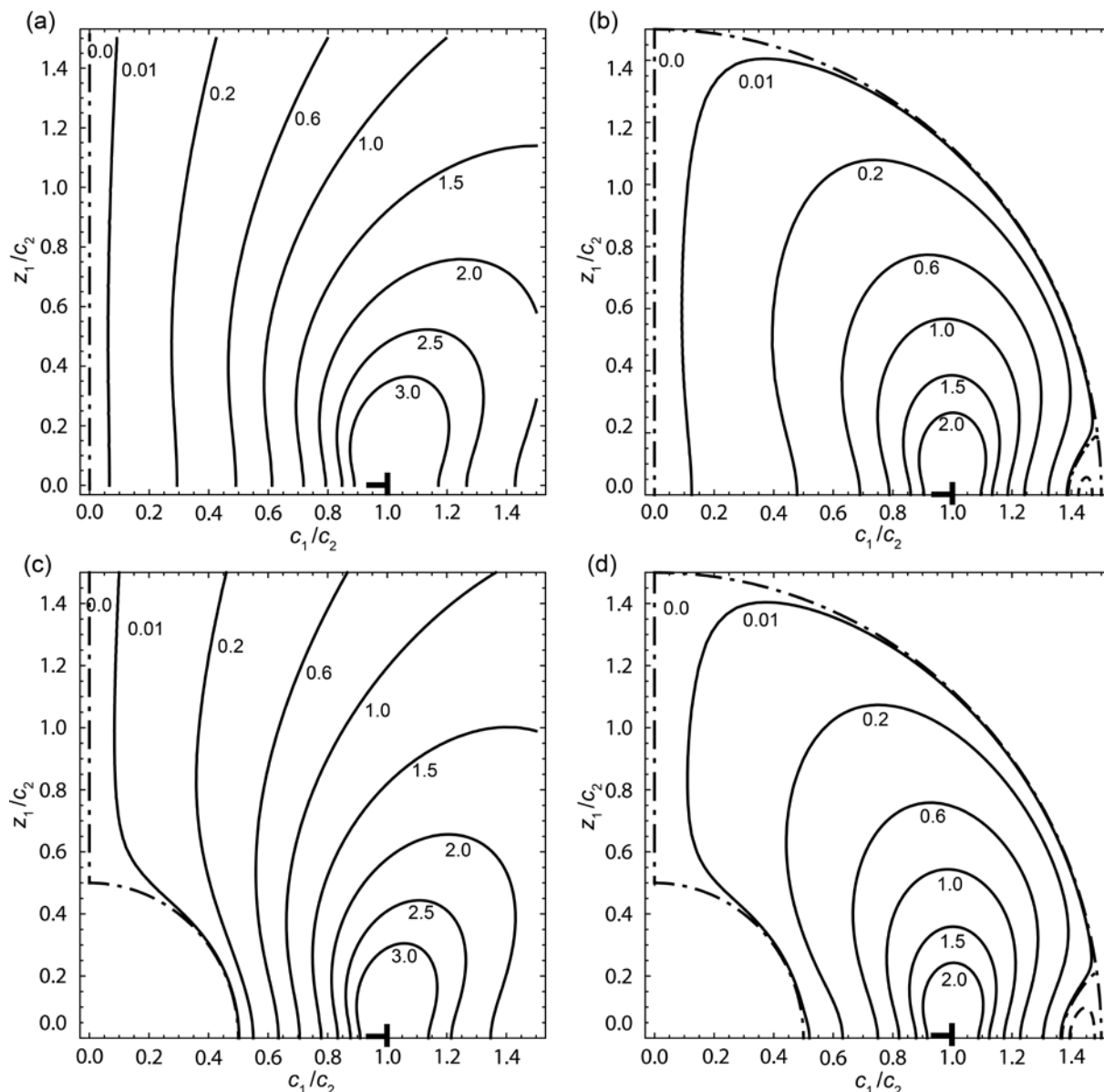


Fig. 2. The maps of pair interaction energy W_{int}^{1-2} for PDL-1 with arbitrary radius c_1 and position z_1 and PDL-2 of radius $c_2 = 100b_2$, placed in plane $z_2 = 0$ in (a) an infinite medium, (b) an elastic sphere of radius $a = 1.5c_2$, (c) an infinite medium with a spherical pore of radius $a_p = 0.5c_2$, and (d) a spherical layer of radii $a_p = 0.5c_2$ and $a = 1.5c_2$. The energy is given in units $Gb_1b_2c_2$

4. Conclusions

The phenomenon of pair interaction of circular PDLs in solids with spherical boundaries such as an elastic sphere, an infinite medium with a spherical pore, and a spherical layer with free surfaces is studied in detail. An explicit formula for interaction energy of two coaxial circular PDLs is obtained in the form of double power series. This result is illustrated by maps of the interaction energy in the space of PDL radii and axial positions. It is shown that the interaction energy of PDLs is strongly screened by free spherical surfaces when at least one of the PDLs is localized near the surface. The outer free surface makes a greater effect on the interaction energy than the inner free surface. In particular, there is a region near the equator and the outer free surface, where the interaction energy changes its sign. The inner free surface does not give such effect. Our results give an opportunity to analyze stress relaxation

processes through the generation of PDL ensembles in porous materials as well as bulk and hollow core-shell nanoparticles and pentagonal particles.

Acknowledgments. SAK is thankful to the Russian Foundation for Basic Research (project No. 18-33-00725) for support of this work.

References

- [1] Hirth JP, Lothe J. *Theory of Dislocations*. New York: Wiley; 1982.
- [2] De Wit R. The continuum theory of stationary dislocations. *Solid State Physics*. 1960;10: 249-292.
- [3] Matthews JW, Klokholm E, Sadagopan V, Plaskett TS, Mendel E. Dislocations in gadolinium gallium garnet ($Gd_3Ga_5O_{12}$) – I. Dislocations at inclusions. *Acta Metallurgica*. 1973;21(3): 203-211.
- [4] Westmacott KH, Barnes RS, Hull D, Smallman RE. Vacancy trapping in quenched aluminium alloys. *Philosophical Magazine*. 1961;6(67): 929-935.
- [5] Matthews JW. Generation of large prismatic dislocation loops at inclusions in crystals. *Physica status solidi (a)*. 1973;15(2): 607-612.
- [6] Kolesnikova AL, Romanov AE. Misfit dislocation loop nucleation at a quantum dot. *Technical Physics Letters*. 2004;30(2): 126-128.
- [7] Barnes RS, Mazey DJ. Stress-generated prismatic dislocation loops in quenched copper. *Acta Metallurgica*. 1963;11(4): 281-286.
- [8] Makenas BJ, Birnbaum HK. Phase changes in the niobium-hydrogen system I: Accommodation effects during hydride precipitation. *Acta Metallurgica*. 1980;28(7): 979-988.
- [9] Calhoun RB, Mortensen A. Equilibrium shape of prismatic dislocation loops under uniform stress. *Acta Materialia*. 1999;47(8): 2357-2365.
- [10] Johnson WC, Lee JK. A dislocation model for the plastic relaxation of the transformation strain energy of a misfitting spherical particle. *Acta Metallurgica*. 1983;31(7): 1033-1045.
- [11] Geslin PA, Appolaire B, Finel A. Investigation of coherency loss by prismatic punching with a nonlinear elastic model. *Acta Materialia*. 2014;71: 80-88.
- [12] Chaldyshev VV, Bert NA, Romanov AE, Suvorova AA, Kolesnikova AL, Preobrazhenskii VV, Werner P, Zakharov ND, Claverie A. Local stresses induced by nanoscale As-Sb clusters in GaAs matrix. *Applied Physics Letters*. 2002;80(3): 377-379.
- [13] Bert NA, Chaldyshev VV, Suvorova AA, Preobrazhenskii VV, Putyato MA., Semyagin BR, Werner P. Enhanced precipitation of excess As on antimony delta layers in low-temperature-grown GaAs. *Applied Physics Letters*. 1999;74(11): 1588-1590.
- [14] Kolesnikova AL, Romanov AE, Chaldyshev VV. Elastic-energy relaxation in heterostructures with strained nano-inclusions. *Physics of the Solid State*. 2007;49(4): 667-674.
- [15] Bert NA, Kolesnikova AL, Romanov AE, Chaldyshev VV. Elastic behavior of a spherical inclusion with a given uniaxial dilatation. *Physics of the Solid State*. 2002;44(12): 2240-2250.
- [16] Dundurs J, Salamon NJ. Circular prismatic dislocation loop in a two-phase material. *Physica status solidi (b)*. 1972;50(1): 125-133.
- [17] Kroupa F. Circular edge dislocation loop. *Czechoslovak Journal of Physics B*. 1960;10: 284-293.
- [18] Bullough R, Newman RC. The spacing of prismatic dislocation loops. *Philosophical Magazine*. 1960;5: 921-926.
- [19] Baštecká J. Interaction of dislocation loop with free surface. *Czechoslovak Journal of Physics B*. 1964;14(6): 430-442.
- [20] Salamon NJ, Comninou M. The circular prismatic dislocation loop in an interface. *Philosophical Magazine A*. 1979;39: 685-691.

- [21] Chou YT. The energy of circular dislocation loops in thin plates. *Acta Metallurgica*. 1963;11: 829-834.
- [22] Kolesnikova AL, Romanov AE. Virtual circular dislocation-disclination loop technique in boundary-value problems in the theory of defects. *Journal of Applied Mechanics*. 2004;71: 409-417.
- [23] Ovid'ko IA, Sheinerman AG. Misfit dislocation loops in composite nanowires. *Philosophical Magazine*. 2004;84(20): 2103-2118.
- [24] Aifantis KE, Kolesnikova AL, Romanov AE. Nucleation of misfit dislocations and plastic deformation in core/shell nanowires. *Philosophical Magazine*. 2007;87(30): 4731-4757.
- [25] Cai W, Weinberger CR. Energy of a prismatic dislocation loop in an elastic cylinder. *Mathematics and Mechanics of Solids*. 2009;14: 192-206.
- [26] Colin J. Prismatic dislocation loops in strained core-shell nanowire heterostructures. *Physical Review B*. 2010;82: 054118.
- [27] Willis JR, Bullough B, Stoneham AM. The effects of dislocation loop on the lattice parameter, determined by X-ray diffraction. *Philosophical Magazine*. 1983;48(1): 95-107.
- [28] Wolfer WG, Drugan WJ. Elastic interaction energy between a prismatic dislocation loop and a spherical cavity. *Philosophical Magazine A*. 1988;57(6): 923-937.
- [29] Bondarenko VP, Litoshenko NV. Stress-strain state of a spherical layer with circular dislocation loop. *International Applied Mechanics*. 1997;33: 525-531.
- [30] Kolesnikova AL, Gutkin MYu, Krasnitckii SA, Romanov AE. Circular prismatic dislocation loops in elastic bodies with spherical free surfaces. *International Journal of Solids Structures*. 2013;50(10): 1839-1857.
- [31] Wang Y, Zhang X, Cai W. Spherical harmonics method for computing the image stress due to a spherical void. *Journal of the Mechanics and Physics of Solids*. 2019;126: 151-167.
- [32] Evans JH, Van Veen A, Caspers LM. In-situ TEM observations of loop punching from helium platelet cavities in molybdenum. *Scripta Metallurgica*. 1983;17(4): 549-553.
- [33] Donnelly SE. The density and pressure of helium in bubbles in implanted metals: a critical review. *Radiation Effects and Defects in Solids*. 1985;90(1-2): 1-47.
- [34] Condon JB, Schober T. Hydrogen bubbles in metals. *Journal of Nuclear Materials*. 1993;207: 1-24.
- [35] Chang HJ, Segurado J, de la Fuente OR, Pabón BM, Lorca J. Molecular dynamics modeling and simulation of void growth in two dimensions. *Modelling and Simulation in Materials Science and Engineering*. 2013;21(7): 075010.
- [36] Wang HY, Li XS, Zhu WJ, Deng XL, Song ZF, Chen XR. Atomistic modelling of the plastic deformation of helium bubbles and voids in aluminium under shock compression. *Radiation Effects and Defects in Solids*. 2014;169 (2): 109-116.
- [37] Gutkin MY, Kolesnikova AL, Krasnitsky SA, Romanov AE. Misfit dislocation loops in composite core-shell nanoparticles. *Physics of the Solid State*. 2014;56(4): 723-730.
- [38] Gutkin MYu, Kolesnikova AL, Krasnitckii SA, Romanov AE, Shalkovskii AG. Misfit dislocation loops in hollow core-shell nanoparticles. *Scripta Materialia*. 2014;83: 1-4.
- [39] Gutkin MYu, Kolesnikova AL, Krasnitckii SA, Dorogin LM, Serebryakova VS, Vikarchuk AA, Romanov AE. Stress relaxation in icosahedral small particles via generation of circular prismatic dislocation loops. *Scripta Materialia*. 2015;105: 10-13.
- [40] Krauchanka MY, Krasnitckii SA, Gutkin MYu, Kolesnikova AL, Romanov AE. Generation of circular prismatic dislocation loops in decahedral small particles. *Scripta Materialia*. 2018;146: 77-81.
- [41] Krauchanka MY, Krasnitckii SA, Gutkin MYu, Kolesnikova AL, Romanov AE. Circular loops of misfit dislocations in decahedral core-shell nanoparticles. *Scripta Materialia*. 2019;167: 81-85.

- [42] Gutkin MYu, Kolesnikova AL, Romanov AE. Nanomechanics of stress relaxation in composite low-dimensional structures. In: Altenbach H, Öchsner A (eds.), *Encyclopedia of Continuum Mechanics*. Springer, Berlin, Heidelberg; 2020. p. 1778-1799.
- [43] Ding Y, Sun X, Wang ZL, Sun S. Misfit dislocations in multimetallic core-shelled nanoparticles. *Applied Physics Letters*. 2012;100(11): 111603.
- [44] Khanal S, Casillas G, Bhattarai N, Velázquez-Salazar JJ, Santiago U, Ponce A, Mejía-Rosales S, José-Yacamán M. CuS₂-passivated Au-core, Au₃Cu-shell nanoparticles analyzed by atomistic-resolution Cs-corrected STEM. *Langmuir*. 2013;29(29): 9231-9239.
- [45] Mura T. *Micromechanics of Defects in Solids*. Netherland: Martinus Nijhoff Publishers; 1987.

CRYSTALLOGRAPHIC ORIENTATION, DELAY TIME AND MECHANICAL CONSTANTS INFLUENCE ON THERMAL FATIGUE STRENGTH OF SINGLE - CRYSTAL NICKEL SUPERALLOYS

A.V. Savikovskii^{1*}, A.S. Semenov¹, L.B. Getsov²

¹Peter the Great St. Petersburg Polytechnic University, Polytechnicheskaya 29, St. Petersburg, 195251, Russia

²Joint-Stock Company "I.I. Polzunov Scientific and Development Association on Research and Design of Power Equipment", Polytechnicheskaya 24, St. Petersburg, 194021, Russia

*e-mail: savikovskii.artem@yandex.ru

Abstract. The influence of a delay time at the maximum temperature on the number of cycles for the macrocrack initiation for two thermal loading programs was investigated for two single-crystal nickel-based superalloys VIN3 and ZhS32. An analytic approximation of a delay time influence was proposed. Comparison of computational results and analytic formula on the base of constitutive equations with the experimental data was performed for considered single-crystal superalloys and showed a good accuracy. Influence of several mechanical constants of nickel alloy on thermal fatigue strength is presented and discussed. The influence of crystallographic orientation of the corset sample on the thermal fatigue durability with delay times for various thermal loading programs and different single-crystal nickel superalloys was investigated.

Keywords: thermal fatigue, single-crystal nickel-based superalloy, deformation criterion, corset sample, crystallographic orientation, finite element modeling, analytic approximation

1. Introduction

Single-crystal nickel-based superalloys [1] are used for production of gas turbine engines (GTE) [2]. These materials have a pronounced anisotropy and temperature dependence of properties. Cracking in the turbine blades is caused often by thermal fatigue [3,4]. For investigation of thermal fatigue durability under a wide range of temperatures with and without delay times the experiments are carried out on different types of samples, including corset (plane) specimen [3] on the installation developed in NPO CKTI [5] (see Fig. 1). Fixed in axial direction by means of two bolts with a massive foundation the corset sample (see Fig. 2) is heated periodically by passing electric current through it. The fixing of sample under heating leads to the high stress level and inelastic strain appearance. The FE simulation is required for the computation of inhomogeneous stress and inelastic strain fields.

The aims of the study are: (I) to study numerically a stress-strain state of the sample during cyclic heating and cooling due to its clamping, (II) to study systematically the effect of delay at maximum temperature on the thermal fatigue durability on the base of the four-term deformation criterion [6-8] of thermal-fatigue failure for single crystal superalloys using the results of finite element (FE) simulation of full-scale experiments and results of analytical formulae and (III) to study systematically the effect of crystallographic orientation on the thermal fatigue durability. The results of simulation and their verification are obtained for different single-crystal nickel-based superalloys: VIN3 and ZhS32.



Fig. 1. Testing setup for thermal fatigue experiments

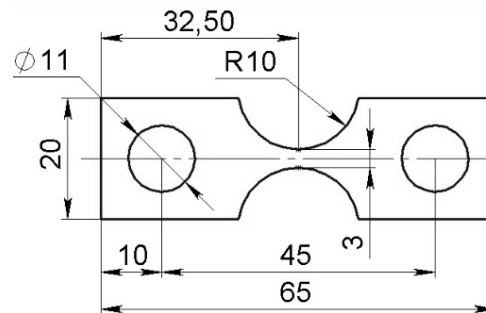


Fig. 2. Geometrical parameters of the corset sample

2. Results of thermo-elasto-visco-plastic analysis

The axial fixing of the corset specimen under heating leads to the high axial stress and inelastic strain appearance. The numerical simulation is required for the computation of inhomogeneous stress and inelastic strain fields in sample. Modeling and simulation of inelastic cyclic deformation of corset samples has been performed by means of the FE programs ANSYS and PANTOCRATOR [9], which allows to apply the micromechanical (microstructural, crystallographic, physical) models of plasticity and creep for single crystals [10-14]. The micromechanical plasticity model accounting 12 octahedral slip systems with lateral and nonlinear kinematic hardening [10,15] is used in the FE computation for the simulation of single crystal superalloy behavior under cyclic loading. The Norton power-type law is used to describe creep properties.

Modeling of inelastic deformation in the corset samples has been performed with taking into account of the temperature dependence of all material properties, anisotropy of mechanical properties of single-crystal sample, inhomogeneous nonstationary temperature field, mechanical contacts between bolt and the specimen, between specimen and foundation, friction between the contact surfaces, temperature expansion in the specimen. The viscous properties are taken into account because of high temperature despite of a quick time of heating and cooling of the corset samples.

The two FE formulations for the thermo-mechanical problem have been considered:

- FE model with taking into account equipment;
- FE model without taking into account equipment (simplified formulation [16] for the sample only).

Using of the second formulation provides significant saving computational time due to reduction in the number of degrees of freedom and refusal to solve a contact problem. It is very actual for the numerous multivariant computations for different regimes of loading and the crystallographic orientations. The validity of the simplified formulation is based on the comparison with the results of full-scale formulation (with taking into account equipment), as

well as on the comparison with the relative displacements of two markers measured in experiments.

In the general case there is no symmetry in the problem (Fig. 3a) due to anisotropy of mechanical properties of single crystal sample. However in the important for practice case of [001] crystallographic orientation of sample the symmetry in respect to planes xz and yz (see Fig. 3a) can be introduced. Equipment and bolts are modeled by linear elastic material (steel), and for the sample elasto-visco-plastic model of material is used. The problem is solved in a three-dimensional quasi-static formulation. As boundary conditions the symmetry conditions are set: zero displacements on the y -axis on the xz plane and zero displacements on the x -axis on the yz plane. On the lower side of the equipment zero displacements along the x and z axes are set. On the bolt cap the pressure of 100 MPa has been applied that is equivalent to the tightening force of the bolt. The temperature boundary conditions are set from the experimental data at maximum and minimum temperature with linear interpolation in time. The results of finite element heat conduction simulations [17] consistent with experimental temperature field distributions. The mechanical properties for the alloy VIN3 are taken from the paper [18] and for the alloy ZHS32 from [19] are summarized in Tables 1 and 2. The mechanical properties of bolts are taken for pearlitic steel [20].

Table 1. Mechanical properties of VIN3 used in simulations [18]

T	$^{\circ}C$	20	500	700	900	1000	1050
E_{001}	MPa	126000	110000	104000	89000	80000	75000
ν	-	0.39	0.41	0.42	0.42	0.425	0.428
α	1/K	$1.21 \cdot 10^{-5}$	$1.33 \cdot 10^{-5}$	$1.4 \cdot 10^{-5}$	$1.5 \cdot 10^{-5}$	$1.57 \cdot 10^{-5}$	$1.6 \cdot 10^{-5}$
σ_y^{001}	MPa	555	800	930	910	645	540
n	-	3	3	3	3	3	3
A	$\text{MPa}^{-n} \text{s}^{-1}$	$1 \cdot 10^{-27}$	$8 \cdot 10^{-17}$	$2.3 \cdot 10^{-15}$	$6.5 \cdot 10^{-14}$	$3.5 \cdot 10^{-13}$	$8 \cdot 10^{-13}$

Table 2. Mechanical properties of ZHS32 used in simulations [19]

T	$^{\circ}C$	20	500	700	900	1000	1050
E_{001}	MPa	137000	110000	105000	99800	94800	92300
ν	-	0.395	0.4248	0.4284	0.4317	0.4347	0.4361
α	1/K	$1.24 \cdot 10^{-5}$	$1.6 \cdot 10^{-5}$	$1.7 \cdot 10^{-5}$	$1.81 \cdot 10^{-5}$	$2.22 \cdot 10^{-5}$	$2.42 \cdot 10^{-5}$
σ_y^{001}	MPa	919	904	901	895	670	580
n	-	8	8	8	8	8	8
A	$\text{MPa}^{-n} \text{s}^{-1}$	$1 \cdot 10^{-42}$	$2.5 \cdot 10^{-31}$	$8.5 \cdot 10^{-30}$	$2 \cdot 10^{-28}$	$6 \cdot 10^{-27}$	$7 \cdot 10^{-26}$

In simplified formulation of the problem (see Fig. 3b) we consider only the sample without equipment, in which zero displacements on the symmetry planes xz and yz are set, the outer face of the sample parallel to the symmetry plane xz was fixed in the direction of the axis x . To exclude solid body motions, a number of points on this face are also fixed in the direction of the y and z axes.

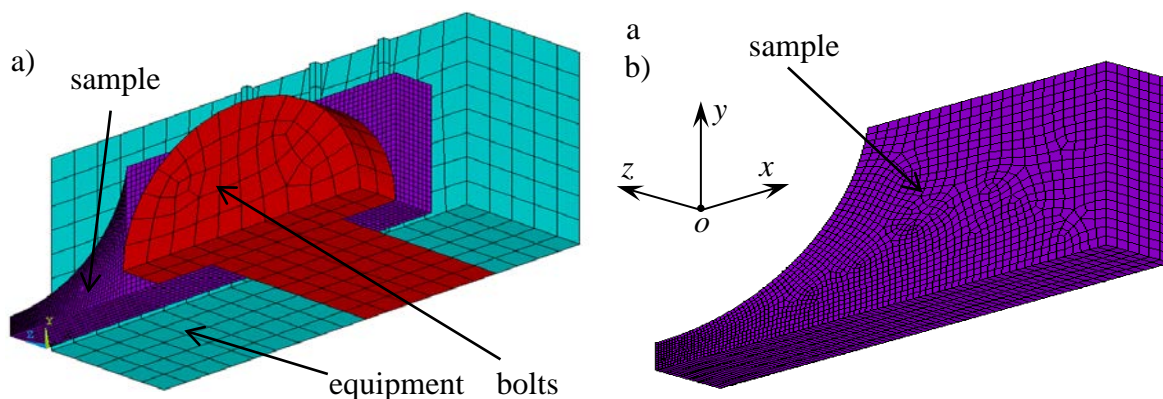


Fig. 3. FE models of the corset sample for thermo-elasto-visco-plastic problem solution:
 a) model ($1/4$ due to symmetry) with taking into account of equipment,
 b) simplified model ($1/4$ due to symmetry) without taking into account of equipment

Figure 4 shows distributions of plastic strain intensity field for two nickel superalloys and three different temperature modes after 7 cycles (for VIN3 the effective length of the sample is 42 mm, for ZHS32 is 50 mm) [17] obtained with using the FE model ($1/4$ due to symmetry) without taking into account equipment (Fig. 3b).

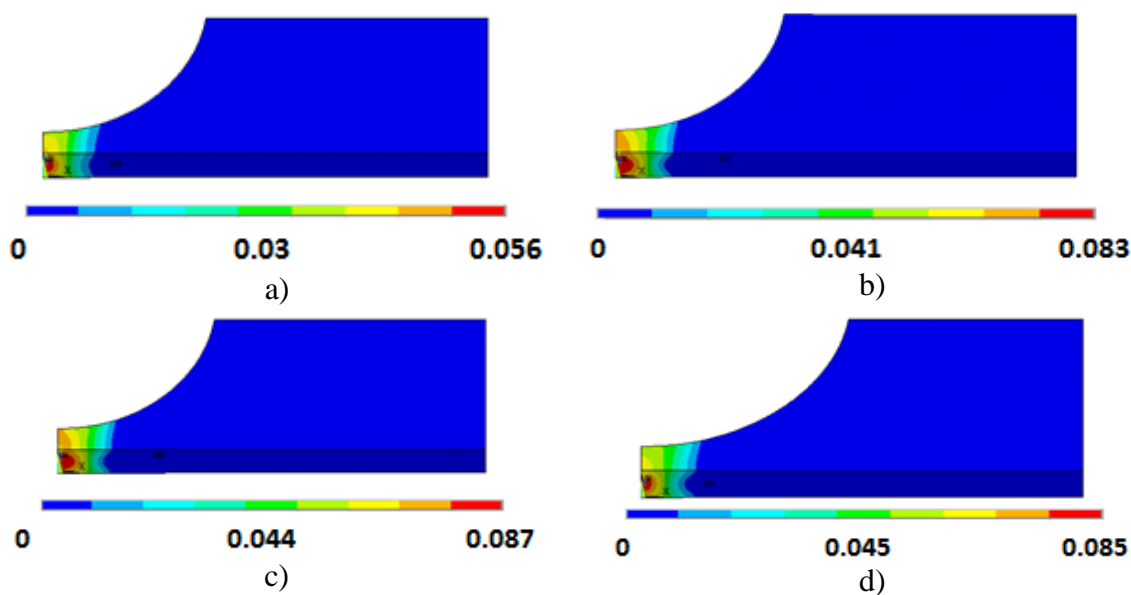


Fig. 4. Plastic strain intensity field distributions in the corset sample after 7 cycles for:
 a) superalloy ZhS32, loading regime $150\div 900^{\circ}\text{C}$;
 b) superalloy ZhS32, loading regime $500\div 1050^{\circ}\text{C}$;
 c) superalloy ZhS32, loading regime $700\div 1050^{\circ}\text{C}$;
 d) superalloy VIN3, loading regime $500\div 1050^{\circ}\text{C}$

Table 3 shows the equivalent (effective) length of the sample for the simplified formulation for different alloys, which has been found by the comparison with full model using the condition of equality of the inelastic strain ranges. In the FE simulations with acceptable engineering accuracy can be used the value 40 mm. Effective length takes into account the compliance of equipment and its variation in considered range has no appreciable on the results.

Table 3. The equivalent length of the corset sample for different alloys

VIN3	ZhS32
38 – 46 mm	40 – 52 mm

3. Influence of the delay on the thermal fatigue durability

FE computations are carried out for a part of a corset sample (simplified FE model with effective length of sample equal 40 mm, see Fig. 3b). The temperature fields are set from the experimental data at maximum and minimum temperature cycle phase with using linear interpolation in time.

The influence of the delay at maximum temperature on the number of cycles to the formation of macrocrack is analyzed in the range from 1 min to 1 hour for the cyclic loading regimes with:

- maximum temperature of 1050°C and minimum temperature of 700°C;
- maximum temperature of 1050°C and minimum temperature of 500°C;
- maximum temperature of 1000°C and minimum temperature of 500°C;
- maximum temperature of 900°C and minimum temperature of 150°C.

The heating time in the cycle is 10s, the cooling time is 16s for VIN3. The heating times in the cycle are 15s, 15s, 10s, 25s, the cooling times are 15s, 15s, 14s, 75s for ZhS32. The mechanical properties for the alloy VIN3 were taken from the paper [18] and for the alloy ZhS32 from [19] (see also Tables 1 and 2).

The problem is solved in a quasi-static 3-dimensional formulation. The FE model is shown in Fig. 3b. The boundary conditions are zero displacements in the direction of the x -axis on two side faces of the sample with the normal along the x -axis. To exclude rigid body motions, a number of points on these faces in the direction of the y and z axes are also fixed.

Temperature evolutions in central point of sample with and without delay for loading regimes 700÷1050°C, 500÷1050°C, 250÷1000°C and 150÷900°C are presented schematically in Fig. 5.

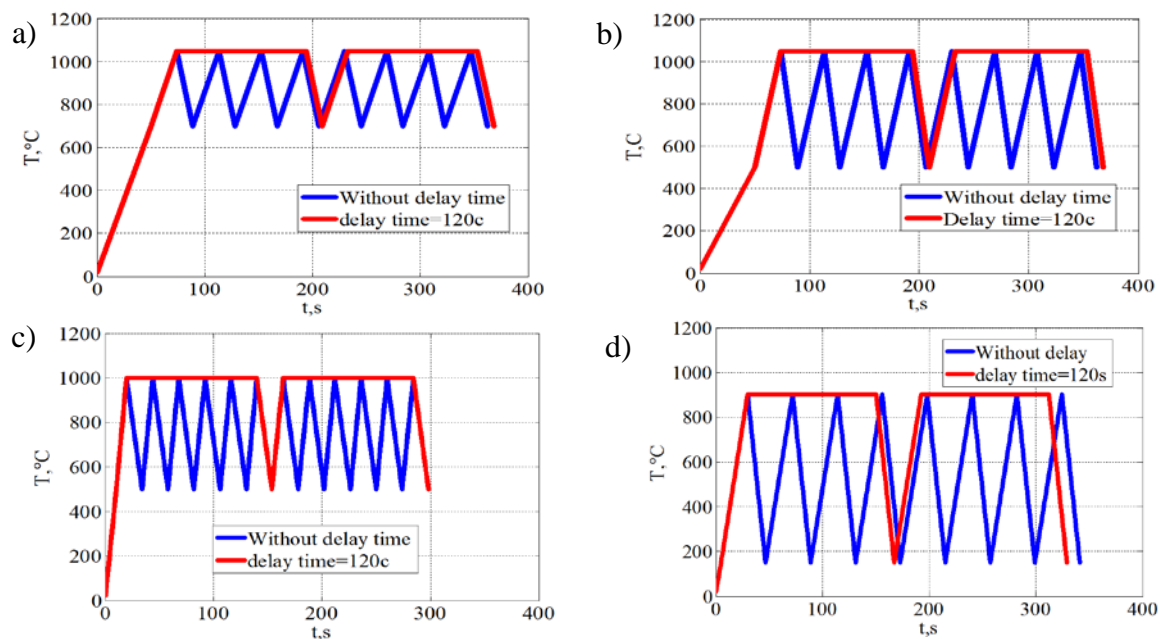


Fig. 5. Schematic presentations of temperature evolutions in central point of sample for loading regimes with and without delay time:

a) 700÷1050°C; b) 500÷1050°C; c) 500÷1000°C and d) 150÷900°C

Damage calculation and estimation of the number of cycles for the macrocrack initiation are made on the basis of four-term deformation criterion [6-8,14]:

$$D = \sum_{i=1}^N \frac{(\Delta \varepsilon_{eqi}^p)^k}{C_1(T)} + \sum_{i=1}^N \frac{(\Delta \varepsilon_{eqi}^c)^m}{C_2(T)} + \max_{0 \leq t \leq t_{\max}} \frac{\varepsilon_{eq}^p}{\varepsilon_r^p(T)} + \max_{0 \leq t \leq t_{\max}} \frac{\varepsilon_{eq}^c}{\varepsilon_r^c(T)}, \quad (1)$$

where the first term takes into account the range of plastic strain within the cycle, the second term deals with the range of creep strain within the cycle, the third term is unilaterally accumulated plastic strain (ratcheting), the fourth term is unilaterally accumulated creep strain. The number of cycles to initiate macrocrack N is determined from the condition $D = 1$. The equivalent strain for single crystal is defined by maximum shear strain in the slip system with normal to the slip plane $\mathbf{n}_{\{111\}}$ and the slip direction $\mathbf{l}_{\langle 011 \rangle}$:

$$\varepsilon_{eq} = \mathbf{n}_{\{111\}} \cdot \boldsymbol{\varepsilon} \cdot \mathbf{l}_{\langle 011 \rangle}. \quad (2)$$

Usually it takes in (1) the values of constants: $k=2$, $m=\frac{5}{4}$, $C_1 = (\varepsilon_r^p)^k$, $C_2 = (\frac{3}{4} \varepsilon_r^c)^m$,

where ε_r^p and ε_r^c are ultimate strains of plasticity and creep under uniaxial tension. In the FE computations the values of ultimate strains $\varepsilon_r^p = \varepsilon_r^c = 18\%$ are used the same for all considered alloys. Improvement of the prediction accuracy of the delay time influence on durability can be achieved by the refinement of the constant strains ε_r^p on the basis of data without delay.

Analytic approximation [21] is offered to enter for describing of delay time influence on thermal fatigue durability. The additive strain decomposition [22] is used for the small strain case under uniaxial relaxation at constant temperature and total strain:

$$\varepsilon = \varepsilon_e + \varepsilon_p + \varepsilon_c + \varepsilon_t = \varepsilon_0, \quad (3)$$

where ε is the total strain, $\varepsilon_e = \frac{\sigma}{E}$ is the elastic strain, ε_p is the plastic strain, ε_c is the creep strain and ε_t is the thermal strain, ε_0 is constant. Differentiating (3) and using $\dot{\varepsilon}_p = \frac{\dot{\sigma}}{H}$

(where H is the hardening modulus), Norton law $\dot{\varepsilon}_c = A\sigma^n$ with taking into account notation $E_T = (E^{-1} + H^{-1})^{-1}$ for the tangent modulus it can be obtained equation:

$$\sigma^{-n} \dot{\sigma} = -AE_T. \quad (4)$$

Using result of integration of differential equation (4) from t_0 to t for $\sigma(t)$ in the relation $\dot{\varepsilon}_c = A\sigma^n$ allow us to introduce differential equation for creep strain:

$$\dot{\varepsilon}_c = A \left[\sigma_0^{1-n} + (n-1)AE_T(t-t_0) \right]^{\frac{n}{1-n}}. \quad (5)$$

Result of integration of (5) from t_0 to t has the form:

$$\Delta \varepsilon_c = -\frac{1}{E_T} \left\{ \frac{1}{\left[\sigma_0^{1-n} + (n-1)AE_T(t-t_0) \right]^{\frac{1}{1-n}}} - \frac{1}{(\sigma_0^{1-n})^{\frac{1}{1-n}}} \right\}, \quad (6)$$

which can be rewritten as following:

$$\Delta \varepsilon_c = \frac{\sigma_0}{E_T} \left\{ 1 - \left[1 + \frac{(n-1)E_T}{\sigma_0} A \sigma_0^{n-1} (t-t_0) \right]^{\frac{1}{1-n}} \right\}. \quad (7)$$

Using simplified two-term deformation criterion with taking into account creep strain terms:

$$\frac{\varepsilon_{accumul}^c}{\varepsilon_r} + N \left(\frac{\Delta \varepsilon_c}{\varepsilon_r} \right)^m = 1, \quad (8)$$

where ε_r is the ultimate strain of creep under uniaxial tension, N is the number of cycles of macrocrack initiation we obtain:

$$N = \left(\frac{\varepsilon_r}{\frac{\sigma_0}{E_T} \left\{ 1 - \left[1 + \frac{(n-1)E_T}{\sigma_0} A \sigma_0^{n-1} t_{delay} \right]^{\frac{1}{1-n}} \right\}} \right)^m \cdot \left(1 - \frac{\varepsilon_{accumul}^c}{\varepsilon_r} \right). \quad (9)$$

In the simulations we use: $\sigma_0 = (\alpha_{20-T_{max}} \cdot T_{max} - \alpha_{20-T_{min}} \cdot T_{min}) \cdot E_T \cdot 0.9$, $\alpha_{20-T_{max}}$ and $\alpha_{20-T_{min}}$ are the coefficients of linear thermal expansion, $E_T = 9.48 \cdot 10^4 / 9.98 \cdot 10^4$ MPa, $A = 2 \cdot 10^{-28} / 6 \cdot 10^{-27}$ MPa⁻ⁿs⁻¹, $\varepsilon_r = 0.18$ for alloy ZhS32, $A = 8 \cdot 10^{-13}$ MPa⁻ⁿs⁻¹, $\varepsilon_r = 0.18$ for alloy VIN3. Multiplier $1 - \frac{\varepsilon_{accumul}^c}{\varepsilon_r}$ is picking up to correlate one point with experiment.

Comparison of results of FE simulations, experiments and analytical approximation (9) concerning the effect of the delay time at the maximum temperature on the thermal fatigue durability for single-crystal superalloys VIN3 and ZhS32 for four temperature modes is given in Fig. 6.

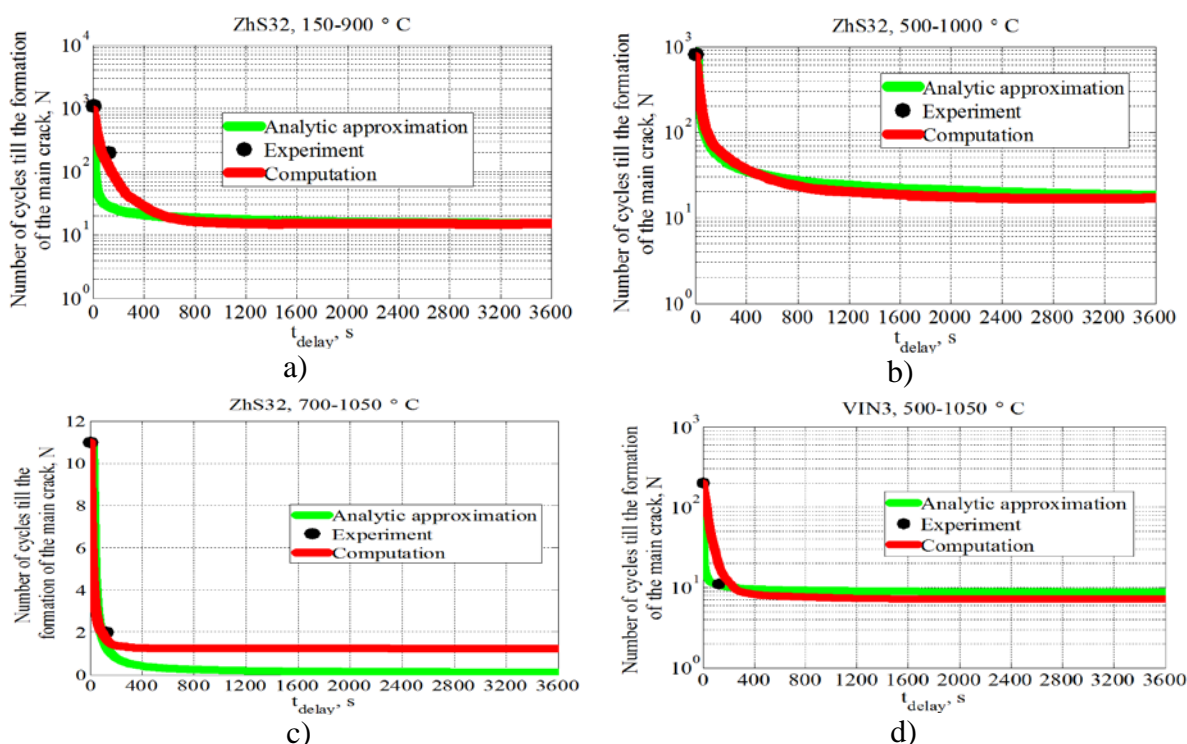


Fig. 6. Comparison of results of FE simulations, analytical approximation and experimental data for alloys: a) ZhS32, loading regime 150÷900°C, heating time is 25 s, cooling time is 75 s; b) ZhS32, loading regime 500÷1000°C, heating time is 10 s, cooling time is 14 s; c) ZhS32, loading regime 700÷1050°C, heating time is 15 s, cooling time is 15 s; d) VIN3, loading regime 500÷1050°C, heating time is 10 s, cooling time is 16 s

Figure 7 shows creep strain intensity field distributions for nickel superalloys ZhS32 and VIN3 in case without delay time and with delay time 5 minutes after 10 cycles.

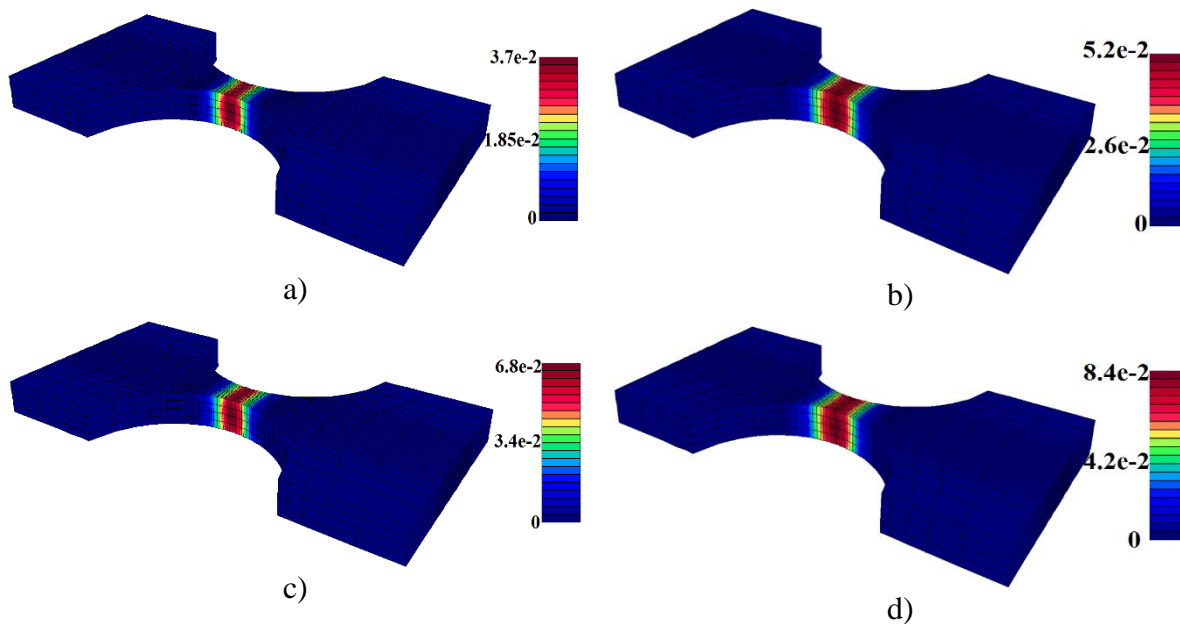


Fig. 7. Creep strain distributions:

- a) ZhS32, loading regime 150÷900°C, without delay time; b) VIN3, loading regime 500÷1050°C, without delay time; c) ZhS32, loading regime 150÷900°C, with delay time 5 minutes; d) VIN3, loading regime 150÷900°C, with delay time 5 minutes

Several material parameters appearing in the analytic formula (9) and calculations such as A , n and ε_r are more complicated to obtain and to find in open sources. Influence of these constants on thermal fatigue durability for nickel alloys ZhS32 and VIN3 and two temperature loading regimes is investigated. The results of parametrical analysis are presented in Fig. 8 with varied values of A , n and ε_r .

Numerical simulations show that parameters n and ε_r influence stronger, then parameter A on thermal fatigue durability.

In gas turbine blades direction of mechanical, thermal and other loadings may not the same as crystallographic orientation (CGO) of single-crystal blade. CGO of gas turbine blades and the samples have an effect on creep rate and thermal fatigue durability. Influence of CGO on thermal fatigue strength is important to predict behavior and damage of single-crystal alloys. Influence of crystallographic orientation (CGO) on thermal fatigue strength for superalloys ZhS32 and VIN3 for four temperature modes is presented in Fig. 9.

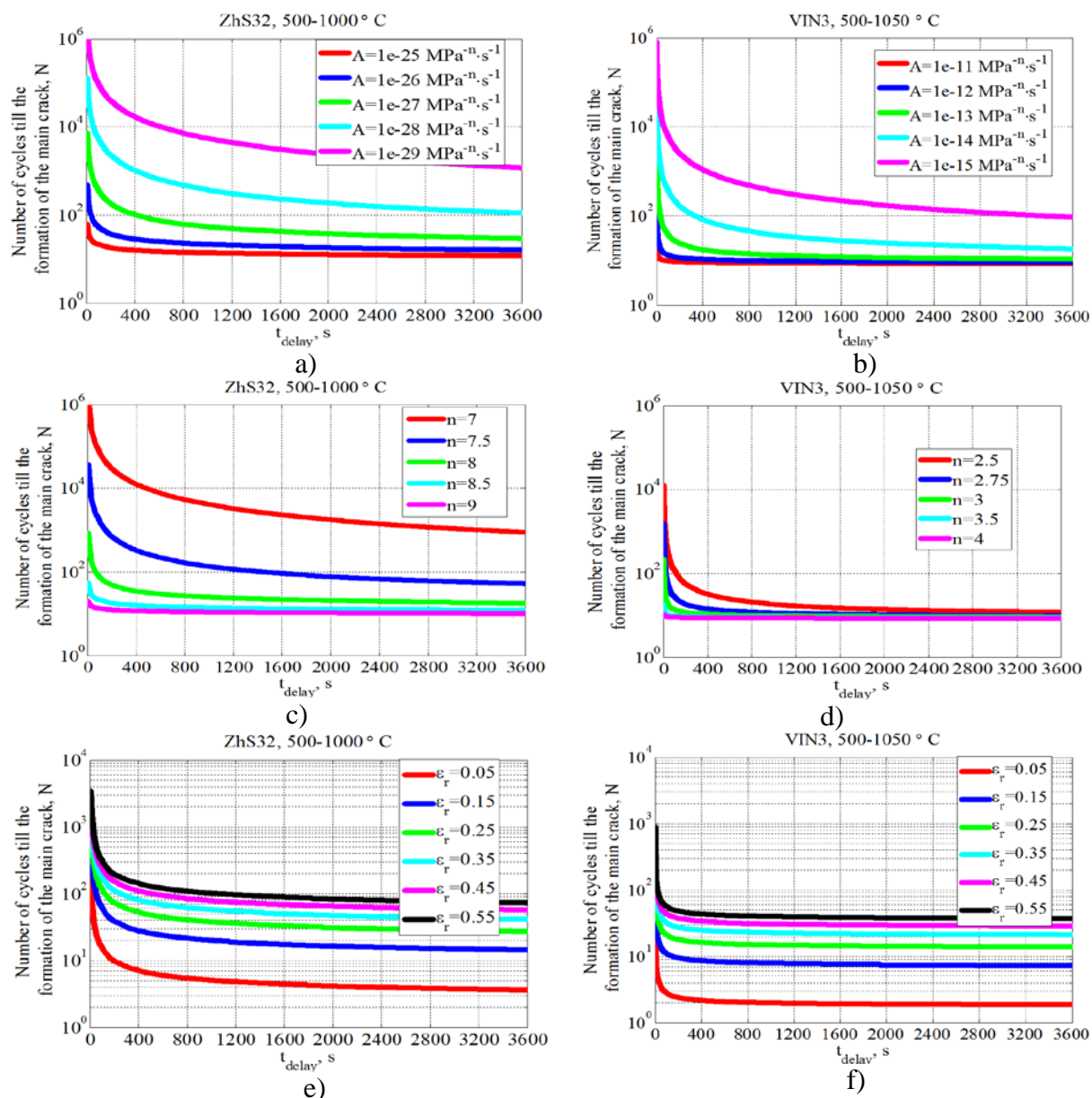


Fig. 8. Influence of material parameters of nickel-based alloys on thermal fatigue durability:

a) Influence of parameter A , ZhS32, loading regime 500÷1000°C, $\varepsilon_r = 0.18$, $n = 8$;

b) Influence of parameter A , VIN3, loading regime 500÷1050°C, $\varepsilon_r = 0.18$, $n = 3$;

c) Influence of parameter n , ZhS32, loading regime 500÷1050°C, $\varepsilon_r = 0.18$, $A = 6 \cdot 10^{-27} \text{ MPa}^{-n} \text{ s}^{-1}$

d) Influence of parameter n , VIN3, loading regime 500÷1050,

$$\varepsilon_r = 0.18, A = 8 \cdot 10^{-13} \text{ MPa}^{-n} \text{ s}^{-1};$$

e) Influence of parameter ε_r , ZhS32, loading regime 500÷1050°C, $n = 8$,

$$A = 6 \cdot 10^{-27} \text{ MPa}^{-n} \text{ s}^{-1};$$

f) Influence of parameter ε_r , VIN3, loading regime 500÷1050°C, $n = 3$, $A = 8 \cdot 10^{-13} \text{ MPa}^{-n} \text{ s}^{-1}$

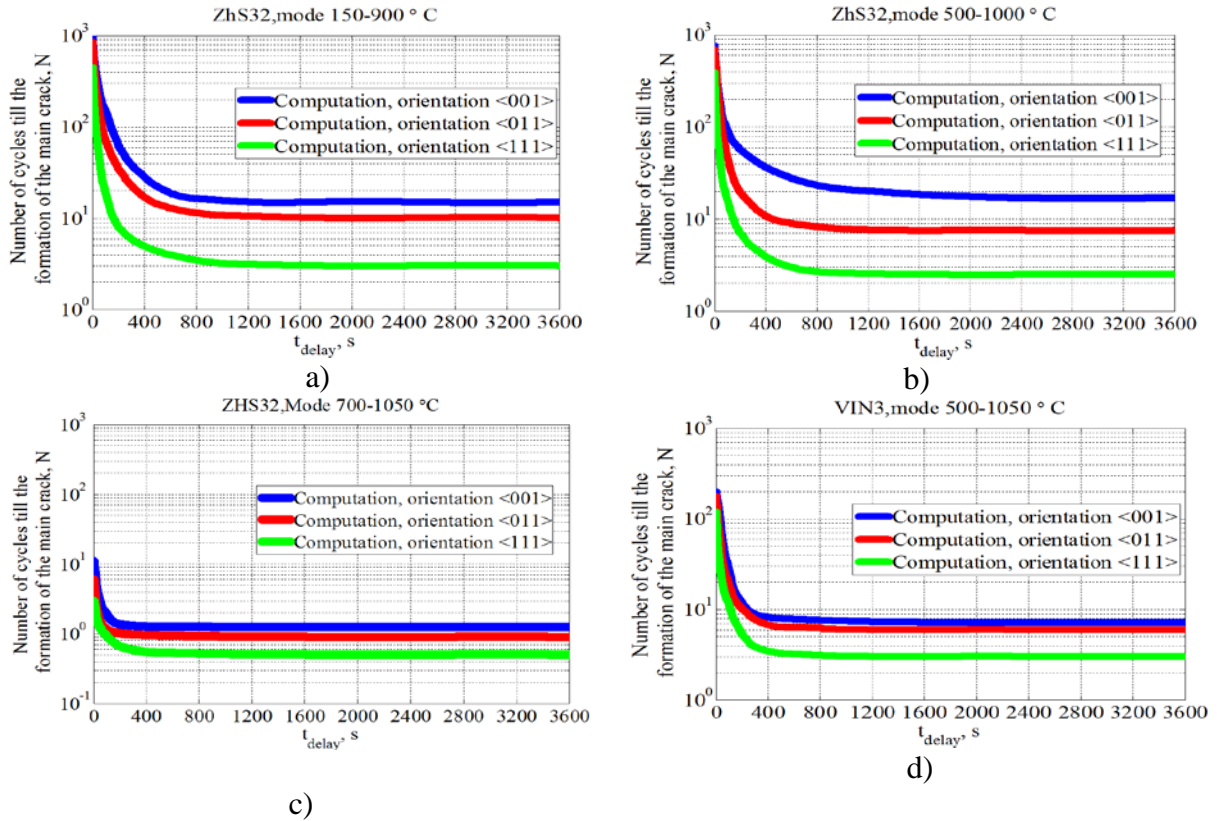


Fig. 9. Influence of crystallographic orientation on thermal fatigue durability for single-crystal nickel-based superalloys:

- a) ZhS32, $T = 150 \div 900^\circ\text{C}$, heating time is 25s, cooling time is 75s, $\varepsilon_r = 0.18$;
- b) ZhS32, $T = 500 \div 1000^\circ\text{C}$, heating time is 10s, cooling time is 14s, $\varepsilon_r = 0.18$;
- c) ZhS32, $T = 700 \div 1050^\circ\text{C}$, heating time is 15s, cooling time is 15s, $\varepsilon_r = 0.18$;
- d) VIN3, $T = 500 \div 1050^\circ\text{C}$, heating time is 10s, cooling time is 16s, $\varepsilon_r = 0.18$

The reason of the superiority of thermal fatigue durability for samples with CGO <001> over CGO <011> and <111> is associated with lower values of Young's modulus for CGO <001> ($E_{\langle 111 \rangle} / E_{\langle 001 \rangle} = 2.4$, $E_{\langle 111 \rangle} / E_{\langle 011 \rangle} = 1.4$ at 1000°C).

4. Conclusions

Computational results of thermal fatigue durability showed a good agreement with the experiments, which suggests that finite-element modeling and analytical approximation (9) in combination with deformation criterion (1) can be used to predict thermal-fatigue strength of single-crystal nickel-based superalloys.

Investigation of material parameters influence show that creep exponent n and tensile rupture strain ε_r affect more stronger that creep parameter A on thermal fatigue durability of single-crystal nickel based superalloys. Constants n and ε_r should be more accurately obtained from experimental data.

The thermal fatigue durability of corset samples from superalloys ZhS32 and VIN3 with CGO <001> exceeds the thermal fatigue durabilities of CGO <011> and <111> (Fig. 9) for all considered loading programs and alloys.

Comparison analysis of superalloys ZhS32 and VIN3 showed that superalloy ZhS32 has thermal fatigue strength higher than superalloy VIN3 for the same considered loading program.

Acknowledgments. The reported study was supported by RFBR according to the research project №19-08-01252.

References

- [1] Shalin RE, Svetlov IL, Kachanov EB, Toloraiya VN, Gavrilin OS. *Single crystals of nickel heat-resistant alloys*. M.: Mashinostroenie; 1997.
- [2] Kablov EN, Golubovsky ER. *Heat resistance of nickel-based alloys*. M.: Mashinostroenie; 1998.
- [3] Dulnev RA, Kotov PI. *Thermal fatigue*. M.: Mashinostroenie; 1980.
- [4] Getsov LB, Dobina NI, Rybnikov AI, Semenov AS, Staroselskii A, Tumanov NV. Thermal fatigue resistance of a monocrystalline alloy. *Strength of materials*. 2008;40(5): 538-551.
- [5] Getsov LB. *Materials and strength of gas turbine parts*. Rybinsk: Gazoturbinnye Tekhnologii; 2010.
- [6] Getsov LB, Semenov AS. Criteria of fracture of polycrystalline and single crystal materials under thermal cyclic loading. *Proceedings of CKTI*. 2009;296: 83-91.
- [7] Semenov AS, Getsov LB. Thermal fatigue fracture criteria of single crystal heat-resistant alloys and methods for identification of their parameters. *Strength of Materials*. 2014;46(1): 38-48.
- [8] Getsov LB, Semenov AS, Staroselsky A. A failure criterion for single-crystal superalloys during thermocyclic loading. *Materials and technology*. 2008;42: 3-12.
- [9] Semenov AS. PANTOCRATOR – finite-element program specialized on the solution of non-linear problems of solid body mechanics. *Proc. of the V-th International. Conf. "Scientific and engineering problems of reliability and service life of structures and methods of their decision"*. SPb.: Izd-vo SPbGPU; 2003: 466-480.
- [10] Cailletaud GA. Micromechanical approach to inelastic behaviour of metals. *Int. J. Plast.* 1991;8: 55-73.
- [11] Asaro RJ. Crystal plasticity. *Journal of Applied Mechanics*. 1983;50(4b): 921-934.
- [12] Trusov PV, Volegov PS, Kondratyev NS. *The physical theory of plasticity*. Perm; 2013. (In Russian)
- [13] Semenov AS. Identification of anisotropy parameters of phenomenological plasticity criterion for single crystals on the basis of micromechanical model. Scientific and technical sheets SPbGPU. *Physical and mathematical Sciences*. 2014;2(194): 15-29.
- [14] Semenov AS, Grishchenko AI, Kolotnikov ME, Getsov LB. Finite-element analysis of thermal fatigue of gas turbine blades. *Vestnik UGATU (scientific journal of Ufa State Aviation Technical University)*, 2019;23(1): 70-81.
- [15] Melnikov BE, Semenov AS, Semenov SG. Multimodel analysis of elastoplastic deformation of materials and structures. Current state. *Trudi CNII im. Acad. A. N. Krylova*. 2010;(53): 85-92.
- [16] May S, Semenov AS. Modeling of inelastic cyclic deformation of monocrystalline specimens. *Proc. of the XXXIX week of science of SPbPU*. 2010;5: 73-74.
- [17] Savikovskii AV, Semenov AS, Getsov LB. Coupled thermo-electro-mechanical modeling of thermal fatigue of single-crystal corset samples. *Materials Physics and Mechanics*. 2019;3(42): 296-310.
- [18] Semenov SG, Getsov LB, Semenov AS, Petrushin NV, Ospennikova OG, Zhivushkin AA. The issue of enhancing resource capabilities of nozzle blades of gas turbine engines through the use of new single crystal alloy. *Journal of Machinery Manufacture and Reliability*. 2016;4: 30-38.

- [19] Getsov LB, Semenov AS, Tikhomirova EA, Rybnikov AI. Thermocyclic and static failure criteria for single crystal superalloys of gas turbine blades. *Materials and technology*. 2014;2: 255-260.
- [20] Maslenkov SB, Maslenkova EA. *Steels and alloys for high temperatures*. Moscow: Metallurgia; 1991.
- [21] Savikovskii A, Semenov A, Getsov L. Analysis of crystallographic orientation influence on thermal fatigue with delay of the single-crystal corset sample by means of thermo-elasto-visco-plastic finite-element modeling. *Matec Web of Conferences*. 2018;245.
- [22] Palmov VA, Stain E. Decomposition of final elastic-plastic deformation into elastic and plastic components. *Bulletin of Perm national research Polytechnic University*. 2001;9: 110-126.

УПРУГИЕ СВОЙСТВА, ПОВЕРХНОСТЬ НАГРУЖЕНИЯ И КРИТЕРИЙ ТЕЧЕНИЯ НАНОПОРОШКОВЫХ КОМПАКТОВ

Г.Ш. Болгачев*, Е.А. Чингина, Н.Б. Волков, К.Е. Лукьяшин

Институт электрофизики УрО РАН, Амундсена 106, Екатеринбург, Россия

*e-mail: grey@iep.uran.ru

Аннотация. Методом гранулярной динамики исследуются различные процессы компактирования наноразмерной гранулированной системы, которая соответствует нанопорошку на основе оксида алюминия. Для всех процессов: рассчитаны кривые уплотнения «плотность – давление» порошкового компакта, из суммарной деформации выделены упругий и пластичный вклады, в приближении изотропного материала определены упругие модули тела. Установлена недостаточность приближения изотропности. В пространстве инвариантов тензора напряжений построена поверхность нагружения наноразмерного порошка. Выявлена неприменимость традиционного ассоциированного закона к описанию процессов деформирования оксидных нанопорошков, и предложено альтернативное правило пластического течения.

Ключевые слова: нанопорошок, поверхность нагружения, ассоциированный закон

1. Введение

В сфере производства новых материалов с уникальными свойствами заманчивыми перспективами обладают оксидные керамические материалы на основе таких соединений, как оксид алюминия [1-8], оксид иттрия [7,9,10], и т.д. Оксид алюминия, в частности, обладает высокой теплопроводностью и прозрачностью, что делает его перспективным кандидатом в качестве рабочей среды для твердотельных лазеров [4], высокими прочностными характеристиками, химической и жаропрочностью, что обуславливает его востребованность как конструкционного материала [1,2]. Повышение прочностных свойств, как и улучшение прозрачности, требует уменьшения среднего размера зерен в изготавливаемой керамике вплоть до величин порядка 10 нм [3,6]. В связи с этим в последнее время большие усилия направлены на развитие нанотехнологий, и в частности, производство наноструктурированных керамик методами порошковой металлургии [6-15]. Одним из часто используемых этапов данных методов является холодное прессование наноразмерных порошков. В отличие от порошков микронного и более крупных размеров нанопорошки обладают рядом неожиданных свойств [11,16-18], влияющих на их прессование и последующее спекание. В первую очередь, это ярко выраженный размерный эффект: чем меньше размер частиц порошка, тем труднее его прессовать. Достижение необходимых плотностей оксидного нанопорошка на стадии холодного прессования подчас требует давлений в несколько ГПа [11,15-18]. Помимо этого, как было недавно обнаружено [16-18], нанопорошки оксидных материалов слабо чувствительны к схеме прессования – различия по плотности в процессах всестороннего сжатия и одноосного компактирования не превышают 1%. Таким образом, наноразмерные порошки по своим механическим свойствам принципиально отличаются от обычных порошковых тел.

http://dx.doi.org/10.18720/MPM.4412020_16

© 2020, Peter the Great St. Petersburg Polytechnic University

© 2020, Institute of Problems of Mechanical Engineering RAS

Бурное развитие экспериментальных методик и дальнейший успех в производстве наноструктурированной оксидной керамики требуют соответствующего развития теоретических представлений о механических свойствах нанопорошкового компакта. В пространстве инвариантов тензора напряжений поверхность нагружения нанопорошков имеет выпуклую форму эллиптического типа [12-19], что предполагает в качестве континуального подхода для описания свойств нанопорошка использование модифицированных вариантов теории пластичности [12-15,19,20]. При этом, конечно, ряд положений и терминология теории приобретают довольно условный характер: в частности, пластичность порошкового тела связана не с деформацией отдельных частиц, а с процессами взаимного проскальзывания, переупаковкой. Особенности нанопорошкового тела требуют серьезной ревизии основных положений теории и верификации ее результатов относительно свойств описываемого объекта. Натурный эксперимент не может дать всестороннюю информацию о характеристиках порошковой системы и изменении ее свойств в процессах компактирования. Гораздо более подробную информацию можно получить в рамках реализованного в данном исследовании микроскопического рассмотрения, т.е. компьютерного моделирования порошка методом гранулярной динамики [16-18,21-25].

В качестве объекта исследования выступает монодисперсная (диаметр частиц $d_g = 10$ нм) модельная система, соответствующая нанопорошку оксида алюминия с сильной склонностью к агломерированию. Реальные порошки такого типа производятся в ИЭФ УрО РАН (Екатеринбург) методами электрического взрыва проводников [26] и лазерного испарения мишеней [9,27]. Отдельные частицы характеризуются сферической формой и высокими прочностными характеристиками. Сферичность частиц и их высокая прочность, неподверженность пластическому смятию, делают метод гранулярной динамики особенно перспективным и адекватным инструментом теоретического анализа.

2. Описание численных экспериментов

Модельная ячейка имеет форму прямоугольного параллелепипеда с размерами x_{cell} , y_{cell} и z_{cell} . Для генерации начальных засыпок используется алгоритм, описанный в [16], который позволяет создавать изотропные и однородные структуры в виде связанного 3D-периодического кластера. Количество частиц $N_p = 4000$, начальная плотность $\rho_0 = 0.24$. Под плотностью ρ подразумевается относительный объем твердой фазы, т.е. $\rho = (\pi/6)N_p d_g^3 / V_{cell}$, где d_g – диаметр частиц, V_{cell} – объем модельной ячейки. На всех сторонах ячейки используются периодические граничные условия. Деформирование системы осуществляется одновременным изменением выбранных размеров модельной ячейки и пропорциональным перемасштабированием соответствующих координат всех частиц. После каждого акта деформирования определяется новое равновесное положение частиц. Данная процедура соответствует воздействию на порошок в квазистатических условиях. Тензор полных деформаций модельной системы в декартовых координатах диагонален. Приращение его компонент на каждом шаге деформирования были связаны друг с другом соотношениями: $\Delta \varepsilon_{xx} = \kappa_x \Delta \varepsilon_{zz}$, $\Delta \varepsilon_{yy} = \kappa_y \Delta \varepsilon_{zz}$. Вертикальная ось Oz всегда соответствовала максимальному сжатию. Шаг деформации вдоль данной оси для всех процессов был установлен равным $\Delta \varepsilon_{zz} = \Delta z_{cell} / z_{cell} = -0.0005$, а различия между процессами, т.е. специфика уплотнения, определялись значениями коэффициентов κ_x и κ_y .

Усредненный по модельной ячейке тензор напряжений σ_{ij} рассчитывался по известной формуле Лава [21-23,28]

$$\sigma_{ij} = \frac{-1}{V_{cell}} \sum_{k < l} f_i^{(k,l)} r_j^{(k,l)}, \quad (1)$$

где суммирование проводится по всем парам взаимодействующих частиц k и l ; $f^{(k,l)}$ – полная сила, воздействующая на частицу k со стороны частицы l ; $r^{(k,l)}$ – вектор, соединяющий центры рассматриваемых частиц. Как правило, предполагается [12-15], что напряженное состояние пластично деформируемого тела, достаточно характеризовать первыми двумя инвариантами тензора напряжений, или однозначно связанными с этими инвариантами средним (гидростатическим) напряжением p и интенсивностью τ девиатора напряжений ($\tau_{ij} = \sigma_{ij} - p\delta_{ij}$, где δ_{ij} – единичный тензор):

$$p = \frac{-1}{3} \text{Sp}(\sigma_{ij}), \quad \tau^2 = \sum_{i,j=1}^3 \tau_{ij} \tau_{ji}. \quad (2)$$

В дальнейшем также введем обозначения для осевых давлений: $p_x = -\sigma_{xx}$, $p_y = -\sigma_{yy}$ и $p_z = -\sigma_{zz}$. Силовые характеристики межчастичных взаимодействий описывались соотношениями [16-18]:

$$f_a(r) = \frac{\pi^2}{3} \frac{(nd_0^3)\varepsilon d_g^6}{(r + \alpha d_0)^3 [(r + \alpha d_0)^2 - d_g^2]^2}, \quad (3)$$

$$\frac{f_e(r)}{Ed_g^2} = \frac{(h/d_g)^{3/2}}{3(1-\nu)^2} - \frac{\pi}{4} \frac{(1-\nu)}{(1-2\nu)(1+\nu)} \left[\frac{h}{d_g} + \ln \left(1 - \frac{h}{d_g} \right) \right], \quad h = d_g - r, \quad (4)$$

$$f_t(\delta) = \min \left\{ \frac{4Ea\delta}{(2-\nu)(1+\nu)}; \mu f_e; \pi a^2 \sigma_b \right\}, \quad a = \sqrt{hd_g} / 2, \quad (5)$$

$$M_p(\theta_p) = \min \left\{ \frac{8Ea^3\theta_p}{3(1+\nu)}; \mu M(a); \frac{\pi}{2} a^3 \sigma_b \right\}, \quad M(a) = -2\pi \int_0^a \sigma_n(r) r^2 dr, \quad (6)$$

$$M_r(\theta_r) = \min \left\{ \frac{4}{3} \frac{Ea^3\theta_r}{1-\nu^2}; \frac{1}{3} a f_e \right\}. \quad (7)$$

Здесь: модифицированная формула Гамакера (3) определяет силу дисперсионных притяжений f_a [29,30]; модифицированный закон Герца (4) – силу f_e упругого отталкивания частиц [31]; линеаризованный закон Катанео-Миндлина (5) – тангенциальное взаимодействие прижатых частиц (силы «трения») [32-34]; линеаризованный закон Егера (6) (или закон Рейснера-Сагоси [35,36]) – момент M_p поверхностных сил, возникающий при взаимном вращении прижатых частиц вокруг контактной оси на угол θ_p ; закон Лурье (7) – момент M_r поверхностных сил, возникающий при изгибе контактной оси на угол θ_r (при появлении прочного сцепления между частицами; см. [37], стр. 272, ур. (4.5)). В представленных соотношениях: r – расстояние между центрами взаимодействующих частиц, ε и d_0 – энергетический и размерный параметры межмолекулярных сил; α – коэффициент, определяющий минимальный зазор между соприкасающимися частицами ($r = d_g$), и устанавливающий максимальную силу адгезионного сцепления ($f_{a,\max} = f_a(d_g)$); E и ν – модуль Юнга и коэффициент Пуассона частиц; δ – тангенциальное смещение контактной площадки; a – радиус контактной площадки; μ – коэффициент трения; σ_b – критическое напряжение сдвига, которое характеризует сдвиговую прочность материала; σ_n – нормальные напряжения на контактной поверхности.

Появление/разрушение прочной связи между частицами описывается с помощью параметра Δr_{ch} , который характеризует необходимое прижатие частиц [16]. Принимается, что уменьшение расстояния r между центрами частиц до значения $r_{min} \leq \Delta r_{ch}$ инициирует образование прочного сцепления. После образования прочной связи между частицами дальнейшее сжатие (при уменьшении r) продолжает соответствовать упругому взаимодействию (4), а при растяжении (увеличение r) имеем линейную взаимосвязь силы f_e и расстояния r вплоть до значения $r' = r_{min} + \Delta r_{ch}$. При $r > r'$ вводится частичное разрушение контакта, которое описывается увеличением параметра r_{min} , так чтобы разность $r - r_{min}$ оставалась равна своему максимальному значению Δr_{ch} . Полное разрушение контакта между частицами происходит при растяжении до значения $r = d_g$. С появлением прочного сцепления между частицами ограничения в соотношениях (5) и (6), связанные с коэффициентом трения μ , снимаются.

В качестве материала частиц подразумевается оксид алюминия в α -фазе, для которого принято [16]: $E = 382$ ГПа, $\nu = 0.25$, $nd_0^3 = \sqrt{2}$, $\alpha d_0 = 0.1$ нм; $\varepsilon = 1224k_B$, $\sigma_b = 0.02E$. Размер частиц $d_g = 10$ нм, коэффициент межчастичного трения $\mu = 0.1$, параметр $\Delta r_{ch} = 0.01d_g$. Таким образом моделируемая система близка по своим параметрам к модельной системе II работы [16], т.е. соответствует сильно агломерированному нанопорошку оксида алюминия работы [38].

Для идентификации различных промоделированных процессов уплотнения в дальнейшем используются значения коэффициентов κ_x и κ_y , и процесс обозначается парой « $\kappa_x; \kappa_y$ ». Компьютерные эксперименты были выполнены для следующих процессов:

1. «1;1» – всестороннее однородное сжатие. Тензоры приращения деформаций $\Delta \varepsilon_{ij}$ и напряжений σ_{ij} являются шаровыми, т.е. $\Delta \varepsilon_{ij} = (\varepsilon/3)\delta_{ij}$, $\sigma_{ij} = -p\delta_{ij}$, где $\varepsilon = \text{Sp}(\Delta \varepsilon_{ij})$.
2. «0.9;1»: интенсивность девиатора тензора приращений деформаций $\gamma_{ij} = \Delta \varepsilon_{ij} - (\varepsilon/3)\delta_{ij}$ равна $\gamma = |\varepsilon| \sqrt{6}/87$.
3. «0.75;1»: $\gamma = |\varepsilon| \sqrt{6}/33$.
4. «0.5;1»: $\gamma = |\varepsilon| \sqrt{6}/15$.
5. «0.25;1»: $\gamma = |\varepsilon| \sqrt{6}/9$.
6. «0;1» – сжатие вдоль осей Oy и Oz : $\gamma = |\varepsilon| \sqrt{1/6}$.
7. «0;0.5»: $\gamma = |\varepsilon| \sqrt{2}/3$.
8. «0;0» – одноосное сжатие вдоль оси Oz : $\gamma = |\varepsilon| \sqrt{2/3}$.
9. «0;-0.1», т.е. сжатие по оси Oz с одновременным незначительным растяжением по оси Oy : $\gamma = |\varepsilon| \sqrt{74}/9$.
10. «0;-0.2»: $\gamma = |\varepsilon| \sqrt{31/24}$.
11. «0;-0.3»: $\gamma = |\varepsilon| \sqrt{278/147}$.

В дополнение были промоделированы три процесса вида « κ_n, κ_n » со значениями

$$\kappa_1 = \frac{1}{4}; \quad \kappa_2 = \frac{\sqrt{3}-1}{\sqrt{3}+2} \cong 0.196; \quad \kappa_3 = \frac{-1\sqrt{31}-4}{2\sqrt{31}+2} \cong -0.103, \quad (8)$$

которые по величине отношения γ/ε являются аналогами, соответственно, процессов «0;1», «0;0.5» и «0;-0.2».

3. Кривые уплотнения

Во всех перечисленных в предыдущем разделе процессах уплотнение модельной ячейки проводилось до заданного уровня $p_{\max} = 5$ ГПа внешней нагрузки вдоль оси Oz , т.е. до выполнения условия $p_z = p_{\max}$. Затем осуществлялась разгрузка модельной ячейки, в ходе которой ячейка деформировалась по всем направлениям с такими же относительными скоростями, что и при уплотнении, но противоположного знака. Кривые уплотнения и разгрузки $p_z(\rho)$ пяти процессов показаны на Рис. 1. Отметим, что для построения каждой кривой проводилось несколько (от 6 до 10) статистически независимых расчетов, после чего проводилось усреднение расчетных данных. Стадия разгрузки, или «упругой» разгрузки [17,19,24], характеризуется изменением плотности $\Delta\rho_u$. Однако сброс давления помимо чисто упругой разгрузки межчастичных контактов сопровождается также необратимыми процессами относительного перемещения частиц. Поэтому название этих стадий «упругими» достаточно условно, и предполагает лишь то, что упругие процессы здесь, скорее всего, преобладают.

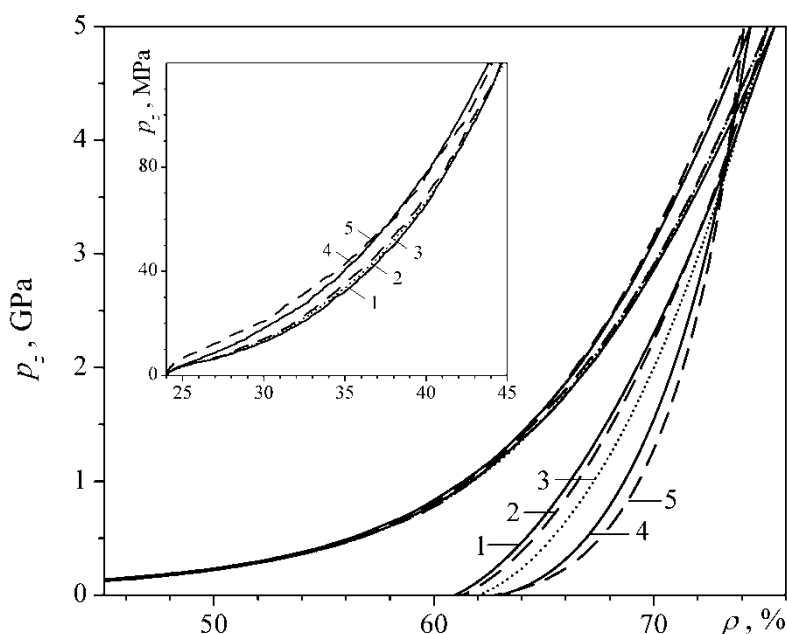


Рис. 1. Кривые уплотнения в координатах «плотность – давление p_z » для процессов «1;1» (сплошная линия 1), «0.5;1» (штриховая линия 2), «0;1» (пунктирная линия 3), «0;0» (сплошная линия 4) и «0;–0.3» (штриховая линия 5). На вставке в увеличенном масштабе показан начальный участок уплотнения

Рисунок 1 показывает, что на стадии нагружения кривые уплотнения нанопорошка «плотность – максимальное давление» очень близки друг к другу. Процессы «1;1», «0.5;1» и «0;1» совпадают в пределах погрешности расчета (порядка 0.3%), а отклонение от них процесса «0;0» (одноосное сжатие) по плотности составляет около 1%. Нечувствительность уплотняемости нанопорошка к схеме нагружения отмечалась ранее в работах [16-18]. Причина такой нечувствительности, по-видимому, состоит во взаимной компенсации двух противоположных эффектов. С одной стороны, переход к несимметричному нагружению (от всестороннего сжатия «1;1» к двухосному «0;1» и далее к одноосному «0;0») приводит при заданном уровне внешнего (максимального) давления (p_z) к снижению среднего давления в порошке, что должно снижать плотность компакта. Так, для одноосного процесса «0;0» при $p_z = 5$ ГПа расчетное гидростатическое давление составляет всего $p = 3.9$ ГПа. С другой стороны,

рост сдвиговых деформаций и напряжений, характеризуемых интенсивностями девиаторов деформаций (γ) и напряжений (τ), способствует достижению более высоких плотностей. Если для всестороннего сжатия $\gamma, \tau \equiv 0$, то для одноосного процесса $\gamma = 0.816$, а величина τ при максимальном давлении, как показывают численные оценки, достигает 1.3 ГПа.

На стадиях «упругой» разгрузки различие по плотности между промоделированными процессами становится более заметным, и составляет при полном сбросе внешнего давления около 2% между одноосным и всесторонним процессами. Причем, если при нагружении одноосный процесс характеризовался меньшими значениями плотности, то после «упругой» разгрузки меньшая плотность соответствует уже процессу всестороннего сжатия-растяжения. Изменения плотности на стадиях разгрузки $\Delta\rho_u$ для процессов «1;1» и «0;0» составляют, соответственно, 14.5% и 11.3%.

Отдельно был исследован вопрос о значимости третьих инвариантов тензоров деформаций и напряжений для описания порошкового тела. Как отмечается в [12], для широкого класса изотропных материалов, например, классические упругие и вязкие тела, скалярные механические свойства определяются лишь первыми двумя инвариантами этих тензоров. Данное приближение вполне оправдывает себя и при описании порошков микронного и более крупных размеров [12,19,20]. Однако для наноразмерных порошков данное приближение до сих пор не проверялось. С целью выполнения такой проверки нами были проанализированы процессы «0;1», «0;0.5» и «0;-0.2» в сравнении с их аналогами – процессами « κ_n, κ_n » (8), см. Рис. 2. Несмотря на равенство отношений γ/ε , анализируемые пары процессов характеризуются различными значениями третьего инварианта тензора деформаций.

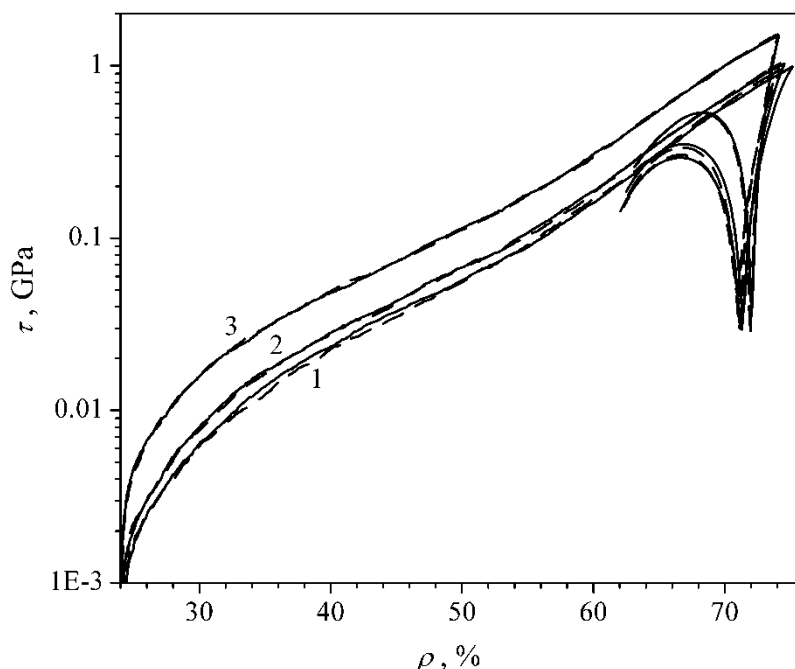


Рис. 2. Интенсивность девиатора напряжений в зависимости от плотности компакта для процессов: «0;1», «0;0.5» и «0;-0.2» (сплошные линии 1, 2 и 3, соответственно); « κ_1, κ_1 », « κ_2, κ_2 » и « κ_3, κ_3 » (штриховые линии 1, 2 и 3, соответственно)

Если в качестве дополнительной характеристики использовать величину $I_3 = \|\gamma_{ij}\|^{1/3} / \varepsilon$ (где $\|\gamma_{ij}\| = \gamma_{xx}\gamma_{yy}\gamma_{zz}$ – определитель девиатора деформаций), то для пары процессов «0;1» и « κ_1, κ_1 » имеем $I_3 = -0.21$ и $+0.21$, соответственно; для пары «0;0.5» и « κ_2, κ_2 » – 0 и 0.24; для пары «0;-0.2» и « κ_3, κ_3 » – 0.56 и 0.58. Как следствие, данные пары характеризуются различными значениями отдельных компонент тензора напряжений и аналогичного третьего инварианта девиатора напряжений. Так, для пары «0;0.5» – « κ_2, κ_2 » при давлении $p_z = 5$ ГПа плотность компакта достигает $\rho \cong 74.5\%$, и «боковые» давления в процессе «0;0.5» составляют $p_x \cong 3.6$ ГПа и $p_y \cong 4.3$ ГПа, а в процессе « κ_2, κ_2 » – $p_x \cong p_y \cong 3.8$ ГПа. Тем не менее, несмотря на явное различие в напряженном состоянии, реализуемом в данных процессах, кривые их уплотнения в инвариантных переменных $p(\rho)$ и $\tau(\rho)$ совпадают в пределах погрешности расчета. Зависимости интенсивности девиатора напряжений от плотности компакта всех шести анализируемых процессов представлены на Рис. 2. Видно, что кривые $\tau(\rho)$ каждой пары удовлетворительно согласуются как на стадии нагружения, так и на стадиях разгрузки. Аналогичное согласие демонстрируют и кривые $p(\rho)$. Таким образом, совпадение кривых $p(\rho)$ и $\tau(\rho)$ для процессов с различными значениями третьих инвариантов тензоров деформаций и напряжений подтверждает традиционно используемую в теории пластичности гипотезу о достаточности первых двух инвариантов данных тензоров для описания наноразмерных порошковых систем.

4. Выделение «упруго-обратимого» вклада

В работах [17,18] упругий вклад $\Delta\rho_e$ в суммарном изменении плотности компакта на стадии уплотнения был отождествлен со значением $\Delta\rho_u$ – изменением плотности, фиксируемым на стадии сброса внешнего давления. Однако такое отождествление не является строгим, поскольку на стадии сброса давления в порошковой системе одновременно с процессами упругой разгрузки межчастичных контактов неизбежно происходят процессы относительного (тангенциального) проскальзывания частиц, соответствующие с макроскопической точки зрения процессу пластического течения материала. По этой же причине оценку модуля всестороннего сжатия

$$K_p = \rho \left. \frac{dp}{d\rho} \right|_{ela}, \quad (9)$$

произведенную в работе [39] по наклону кривой $p_z(\rho)$ на начальном участке сброса давления, можно считать лишь «оценкой снизу». Стоит также отметить высокую трудозатратность такой оценки упругих свойств. Анализ их изменения с ростом плотности компакта требует моделирования большого количества ветвей упругой разгрузки [17,39].

В связи со сказанным в настоящей работе был реализован принципиально иной способ оценки упругих свойств компакта. Упругое приращение напряжений $\Delta\sigma_{ij}$ в моделируемой системе, соответствующее малому приращению плотности $\Delta\rho$, «замерялось» на каждом шаге деформации модельной ячейки сразу же после изменения ее размеров и пропорционального приращения соответствующих координат всех частиц. Только после этого измерения «включался» механизм релаксации, т.е. начиналось перемещение частиц к новым положениям равновесия. Таким образом, процессы взаимного проскальзывания оказываются отделены от чисто упругой деформации. Стоит отметить, что относительные перемещения частиц,

пропорциональные деформированию модельной ячейки, соответствуют известному приближению Фойгта для поля деформаций в сплошной среде [28].

Принимая в качестве предположения изотропность порошкового компакта, можем использовать для описания его упругих свойств закон Гука в виде [40,41]

$$\Delta\sigma_{ij} = K_p \varepsilon + 2\mu_e \left(\Delta\varepsilon_{ij} - \frac{\varepsilon}{3} \delta_{ij} \right), \quad 2\mu_e = 3K_p \frac{1-2\nu_p}{1+\nu_p}, \quad (10)$$

что позволяет определить упругие модули порошкового тела K_p и ν_p . Выражение для модуля всестороннего сжатия записано выше, см. ур. (9), а коэффициент Пуассона ν_p для моделируемых процессов может быть определен по отношению приращений различных компонент тензора напряжений, например,

$$\langle\langle 0.5;1 \rangle\rangle: \left. \frac{\Delta p_x}{\Delta p_z} \right|_{ela} = \frac{1+3\nu_p}{2+\nu_p}; \quad \langle\langle 0;1 \rangle\rangle: \left. \frac{\Delta p_x}{\Delta p_z} \right|_{ela} = 2\nu_p; \quad \langle\langle 0;0 \rangle\rangle: \left. \frac{\Delta p_x}{\Delta p_z} \right|_{ela} = \frac{\nu_p}{1-\nu_p}. \quad (11-a)$$

Отметим, что для процесса «1;1» (всестороннее однородное сжатие) коэффициент Пуассона определить невозможно, а для процессов с тремя различными диагональными компонентами тензора деформаций, например, процесс «0;0.5», коэффициент Пуассона можно определить, используя различные пары компонент тензора напряжений:

$$\langle\langle 0;0.5 \rangle\rangle: \left. \frac{\Delta p_x}{\Delta p_z} \right|_{ela} = \frac{3\nu_{p,x}}{2-\nu_{p,x}}; \quad \left. \frac{\Delta p_y}{\Delta p_z} \right|_{ela} = \frac{1+\nu_{p,y}}{2-\nu_{p,y}}. \quad (11-b)$$

В случае справедливости приближения изотропности значения $\nu_{p,x}$ и $\nu_{p,y}$, конечно же, должны совпадать. Полученные с использованием выражений (9)–(11) упругие модули представлены на Рис. 3 и 4.

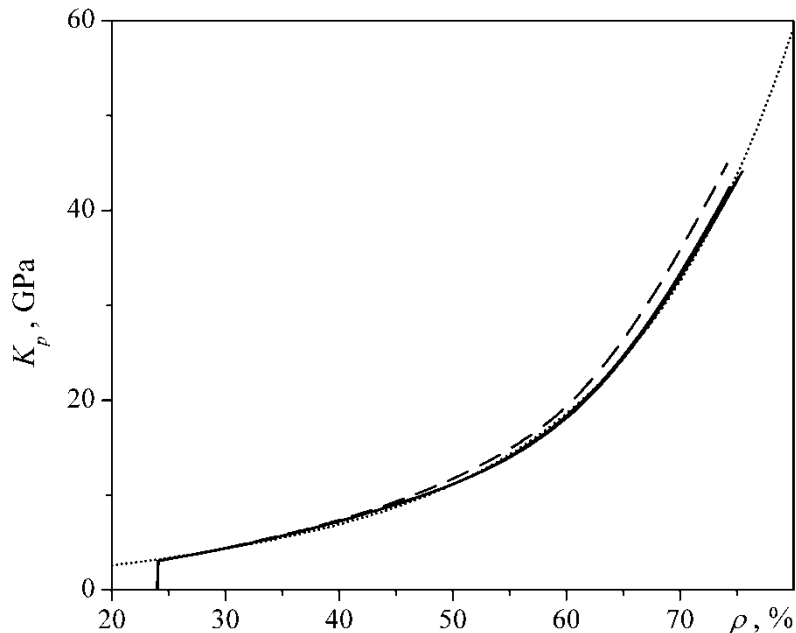


Рис. 3. Модуль всестороннего сжатия, рассчитанный по ур. (9), для процессов «1;1», «0;1», «0;0» (сплошные линии снизу вверх, почти неразрешимы) и «0;–0.3» (штриховая линия). Пунктирная линия – аппроксимация по ур. (12)

Рисунок 4 показывает, что коэффициент Пуассона не может рассматриваться как однозначная функция плотности компакта - мы наблюдаем различные зависимости $\nu_p(\rho)$ для различных процессов, а также несовпадение значений $\nu_{p,x}$ и $\nu_{p,y}$ для

процесса «0;0.5». Это свидетельствует о том, что упругие свойства моделируемой системы не могут описываться законом (10) с двумя упругими модулями, т.е. приближение изотропности материала для уплотняемого порошка не выполняется. Расчетные данные показывают, что распределение направлений межчастичных контактов в порошковой системе изотропно в пределах погрешности расчета во всех промоделированных процессах, однако распределение контактных сил имеет заметную угловую зависимость (см., например, Рис. 14 в [16]). Последнее, видимо, в совокупности с нелинейным законом упругого взаимодействия частиц (4) приводит к существенной анизотропии упругих свойств компакта, наведенной условиями внешнего нагружения.

Несмотря на отмеченную выше наведенную анизотропию определяемый первыми инвариантами тензоров деформации и напряжений модуль всестороннего сжатия K_p , представленный на Рис. 3, определяется для большинства промоделированных процессов вполне однозначно, и удовлетворительно аппроксимируется общим выражением

$$K(\rho) = k_1\rho + k_2\rho \exp(k_3\rho), \quad (12)$$

с коэффициентами $k_1 = 10.987$ ГПа, $k_2 = 0.638$ ГПа, $k_3 = 5.744$. Исключение составляют лишь процессы с растяжением вдоль оси Oy . Здесь, по-видимому, проявляется близость к поверхности разрушения порошкового тела, которая согласно исследованиям [17,25] располагается на плоскости « p - τ » несколько левее кривой $\tau(p)$ процесса одноосного сжатия «0;0».

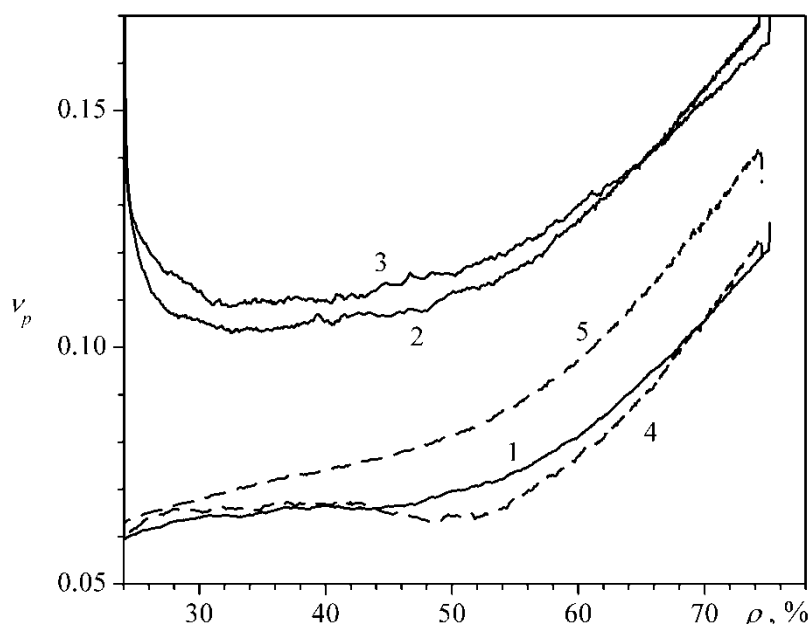


Рис. 4. Коэффициент Пуассона, рассчитанный по ур. (11), для процессов «0.5;1», «0;1» и «0;0» (сплошные линии 1, 2 и 3, соответственно), а также коэффициенты $v_{p,x}$ (штриховая линия 4) и $v_{p,y}$ (штриховая линия 5) для процесса «0;0.5»

При известной зависимости $K_p(\rho)$ упругую составляющую приращения плотности $\Delta\rho_{ela}$, накапливаемую в процессе нагружения, можно рассчитать по уравнению:

$$\Delta\rho_{ela} = \int_0^p \frac{\rho}{K_p(\rho)} dp. \quad (13)$$

Вычисляя численно записанный интеграл вдоль кривой нагружения $p(\rho)$, получаем взаимосвязь $\Delta\rho_{ela}$ с параметрами, которые определяют состояние порошкового компакта (ρ , p , p_{max} и др.). Полученные таким образом зависимости $\Delta\rho_{ela}(p)$ представлены на Рис. 5. Заметное различие в кривых $\Delta\rho_{ela}(p)$ для процессов с практически совпадающими зависимостями $K_p(\rho)$ обусловлено различием в кривых уплотнения $p(\rho)$, которые неявно входят в подинтегральное выражение ур. (13).

Кривые $\Delta\rho_{ela}(p_{max})$ имеют такой же нелинейный характер, что и кривые на Рис. 5, и качественно соответствуют аналогичным зависимостям, представленным в работе [17]. В количественном плане, полученные значения упругой деформации $\Delta\rho_{ela}$ несколько ниже значений, соответствующих близкой по параметрам модельной системе II в работе [17], где упругая часть приращения плотности отождествлялась с величиной $\Delta\rho_u$. Так, при давлении $p_{max} = 5$ ГПа для процесса всестороннего сжатия системы II в [17] получено $\Delta\rho_{ela} = 14.65\%$, в то время как сейчас для процесса «1;1» мы имеем $\Delta\rho_{ela} = 12.68\%$. Снижение расчетных значений упругой деформации связано с исключением в алгоритме расчета упругих свойств, используемым в настоящей работе, вклада процессов пластического характера (взаимное проскальзывание частиц).

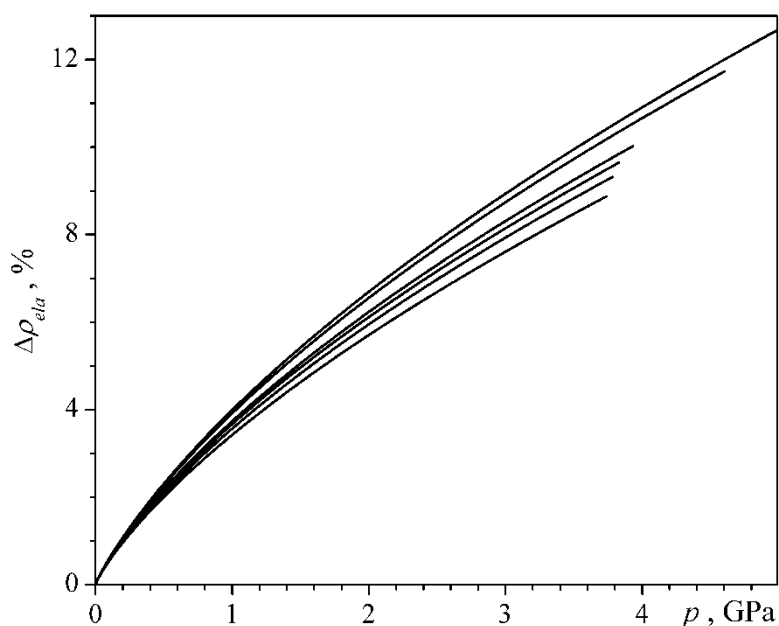


Рис. 5. Упругая часть приращения плотности компакта, вычисленная по расчетным кривым уплотнения и ур. (9), (13), в зависимости от гидростатического давления p для процессов (линии сверху вниз): «1;1», «0;1», «0;0», «0;-0.1», «0;-0.2» и «0;-0.3»

Полученные зависимости $\Delta\rho_{ela}(p)$ позволяют выделить из общей деформации модельной ячейки $\rho(p)$ необратимую (пластическую) составляющую $\rho_{plast} = \rho - \Delta\rho_{ela}$. Зависимость величины ρ_{plast} от внешнего давления представлена на Рис. 6. Там же для сравнения представлены исходные кривые уплотнения $\rho(p_{max})$, содержащие упругий вклад $\Delta\rho_{ela}$. Зависимости $\rho_{plast}(p_{max})$, также как и исходные зависимости, соответствующие различным процессам, достаточно близки друг к другу. Интересно отметить, что при относительно низких давлениях ($p_{max} \leq 100$ МПа) наибольшие

значения достигаемой плотности (как ρ , так и ρ_{plast}) реализуются в процессе всестороннего сжатия «1;1», а в области высоких давлений ($p_{max} > 1$ ГПа) ввиду высоких значений упругого вклада $\Delta\rho_{ela}$ этот процесс характеризуется уже наименьшими значениями пластической составляющей ρ_{plast} . Различие значений ρ_{plast} между процессами одноосного и всестороннего сжатия достигает 1.5% при $p_{max} = 5$ ГПа. В гипотетическом пределе неограниченно высоких давлений ($p_{max} \rightarrow \infty$) зависимости $\rho_{plast}(p_{max})$ близки к степенному виду $\rho_{plast} = \rho_{\infty} - k_p / p_{max}^{1/2}$, что позволяет оценить максимально возможную плотность компактов ρ_{∞} . Для исследованных процессов, как показывает вставка на Рис. 6, она лежит в диапазоне от 67% (всестороннее сжатие «1;1») до 72% (процесс «0;-0.3»).

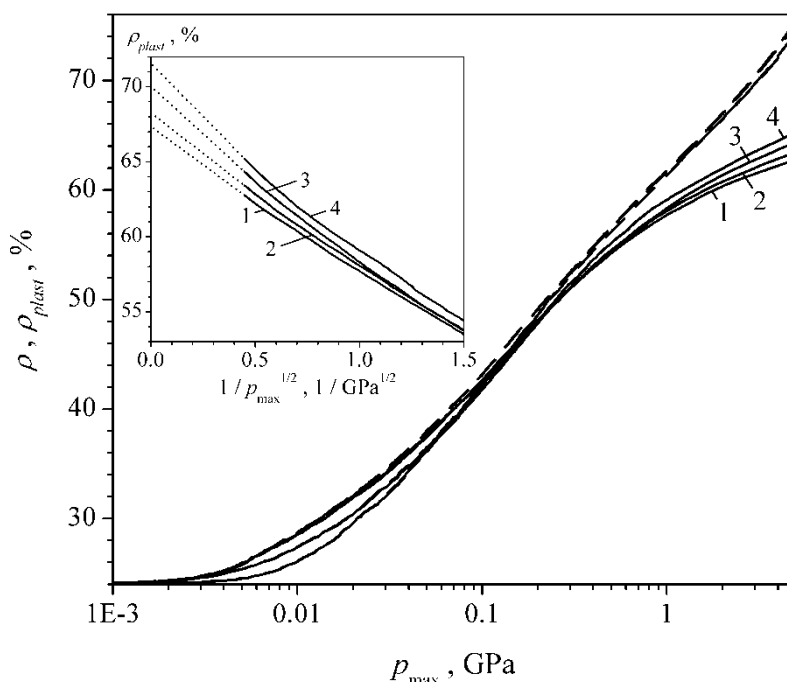


Рис. 6. Плотность компакта ρ (штриховые линии) и пластично-необратимый вклад ρ_{plast} (сплошные линии) в зависимости от максимального внешнего давления (p_{z_0} вдоль оси Oz) для процессов «1;1», «0;1», «0;0» и «0;-0.3» (линии 1, 2, 3 и 4, соответственно). На вставке: величины ρ_{plast} в области высоких давлений и аппроксимация к пределу $p_{max} \rightarrow \infty$ (пунктирные линии)

5. Поверхность нагружения

Ключевым параметром деформируемого тела при описании его механических свойств в рамках феноменологии теорий пластичности [12-15,19,20] является поверхность нагружения, которая в пространстве компонент тензора напряжений определяет границу между областью упругих деформаций и областью пластичного течения. В отличие от пластически несжимаемых материалов, в частности, компактных металлов, поверхность нагружения порошка должна зависеть не только от интенсивности девиатора напряжений (τ), но и от значения первого инварианта тензора напряжений (p), а также в качестве параметра - от текущей плотности, переходя в пределе беспористого состояния в условие текучести сплошного материала. Под плотностью при этом в соответствии с принятой аналогией необходимо понимать величину ρ_{plast} , т.е. накопленные «пластические» деформации без учета упругого вклада.

Для описания поведения пористых тел, реакцией которых на изменение знака нагрузки можно пренебречь, многие исследователи используют аппроксимацию уравнения поверхности нагружения в виде эллипса в координатах « $p - \tau$ » [12-15,19]. К нанопорошковым компактам, как отмечено в предшествующих работах [17,18], эллиптическая поверхность неприменима. Если спеченное пористое тело характеризуется наличием сформированных контактов между частицами, в силу чего способно практически одинаково сопротивляться растягивающим и сжимающим деформациям, то порошок оказывает относительно слабое сопротивление растягивающим деформациям. Следствием этого является существенное искажение эллипса текучести и заметный общий сдвиг в сторону положительных значений гидростатического давления [17,18].

Другой отмеченной в [17,25] особенностью порошкового тела является наличие поверхности разрушения (fracture surface) в области процессов с растягивающими напряжениями. В пространстве инвариантов « $p - \tau$ » поверхность разрушения располагается несколько левее кривой $\tau(p)$, соответствующей одноосному сжатию «0;0». В связи с этим, в настоящей работе мы использовали процессы лишь с относительно небольшим растяжением («0;-0.1», «0;-0.2» и «0;-0.3»), располагающиеся на плоскости « $p - \tau$ » вблизи кривой одноосного сжатия. При этом, в основном, анализу подвергается область сжимающих деформаций, в диапазоне от одноосного до всестороннего уплотнения, которая отвечает за т.н. «консолидирующую» часть поверхности нагружения (the consolidation locus of yield surface [19]).

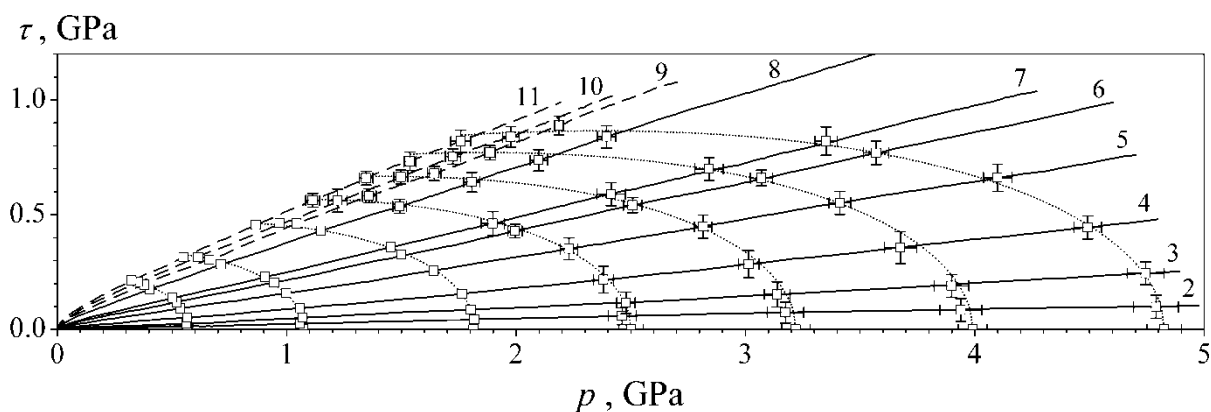


Рис. 7. Зависимости интенсивности девиатора напряжений от гидростатического давления для промоделированных процессов (номера линий соответствуют номерам процессов в разделе 2). Точками отмечены состояния, соответствующие значениям $\rho_{plast} = 0.55, 0.58, 0.60, 0.61, 0.617, 0.622$ и 0.627 . Пунктирные линии показывают положения поверхности нагружения по ур. (14) для этих значений ρ_{plast}

Кривые уплотнения промоделированных процессов в пространстве инвариантов « $p - \tau$ », а также точки (p, τ) на этих кривых, соответствующие заданным значениям плотности ρ_{plast} , представлены на Рис. 7. Для 4-х больших значений ρ_{plast} (0.61, 0.617, 0.622 и 0.627) показаны также погрешности статистического усреднения расчетных данных. При меньших плотностях диапазон погрешностей становится сопоставим, или даже меньше, размера точек на рисунке. Кривая всестороннего сжатия «1;1» (линия 1) в этих координатах располагается вдоль оси абсцисс. В пределах статистического разброса все расчетные точки, представленные на Рис. 7, удовлетворительно аппроксимируются общей зависимостью $\tau(p)$ для поверхности нагружения в виде:

$$\frac{\tau}{p_a} = \left[\tau_1 + \tau_2 \left(\frac{p}{p_a} \right) \right] \sqrt{1 - \frac{p}{p_a}}, \quad (14)$$

где p_a – величина p , соответствующая заданному значению плотности ρ_{plast} при всестороннем сжатии (процесс «1;1»), т.е. координата пересечения поверхности нагружения с осью гидростатического давления; а коэффициенты τ_1 и τ_2 зависят от плотности следующим образом: $\tau_1 = 2.40 - 3.62 \rho_{plast}$, $\tau_2 = 0.51 - 0.42 \rho_{plast}$. Определяемые ур. (14) изолинии показаны на Рис. 7 пунктиром. Видно, что расположение и форма уровней поверхности нагружения, соответствующих заданным значениям плотности ρ_{plast} , в целом, подтверждает выпуклость и гладкость (без угловых точек) поверхности нагружения порошкового компакта в виде сдвинутого и деформированного эллипса.

6. Критерий течения оксидных нанопорошков

Расчитанные кривые уплотнения и построенное семейство изолиний ($\rho_{plast} = \text{const}$) поверхности нагружения, представленные на Рис. 7, позволяют провести детальный анализ характера течения порошкового тела. В рамках феноменологии пластичного тела широко используется гипотеза «ассоциированного закона» [12-14,19,20], согласно которой приращение деформаций при его течении должно быть ортогонально поверхности нагружения в пространстве компонент тензора напряжений. При этом под деформациями необходимо понимать именно пластические части полных деформаций.

Приращение полных деформаций в промоделированных процессах определяется характером деформирования модельной ячейки. Разбивая их на упругие и пластические деформации, т.е. $\Delta \varepsilon_{ij} = \Delta \varepsilon_{ij}^{(e)} + \Delta \varepsilon_{ij}^{(p)}$, определим упругие части соотношениями:

$$\Delta \varepsilon_{xx}^{(e)} = -\frac{\Delta p_x}{3K_p}, \quad \Delta \varepsilon_{yy}^{(e)} = -\frac{\Delta p_y}{3K_p}, \quad \Delta \varepsilon_{zz}^{(e)} = -\frac{\Delta p_z}{3K_p}, \quad (15)$$

которые, как нетрудно убедиться, соответствуют выражению (9) для упругого модуля всестороннего сжатия. Вычитая определяемые уравнениями (15) упругие части из полных деформаций получаем пластические деформации $\Delta \varepsilon_{ij}^{(p)}$, которые могут быть использованы для верификации феноменологической теории пластичного тела, и в частности, ассоциированного закона.

Одним из следствий ассоциированного закона является соосность девиаторов тензоров напряжений и приращения деформаций, т.е. $\tau_{ij} \propto \gamma_{ij}^{(p)}$. В случае трехосного нагружения с заданными значениями диагональных компонент тензора приращений деформаций указанная соосность устанавливает соотношение между диагональными значениями тензора напряжений, которую можно использовать для оценки, например, компоненты p_y по известным значениям p_x и p_z :

$$p_y^{(ass)} = \frac{\Delta \varepsilon_{zz}^{(p)} - \Delta \varepsilon_{yy}^{(p)}}{\Delta \varepsilon_{zz}^{(p)} - \Delta \varepsilon_{xx}^{(p)}} p_x + \frac{\Delta \varepsilon_{yy}^{(p)} - \Delta \varepsilon_{xx}^{(p)}}{\Delta \varepsilon_{zz}^{(p)} - \Delta \varepsilon_{xx}^{(p)}} p_z. \quad (16)$$

Как видно из представленного соотношения, при равенстве двух диагональных компонент тензора деформаций, соответствующие диагональные компоненты тензора напряжений также совпадают. Таким образом, для большинства из промоделированных процессов выполнимость соосности гарантирована условиями симметрии: равенство напряжений по направлениям с одинаковой скоростью деформации.

Все три диагональных компонента тензора деформаций различаются в процессах «0;0.5», «0;-0.1», «0;-0.2» и «0;-0.3». Сопоставление расчетных величин давления p_y и величин $p_y^{(ass)}$, определяемых соотношением (16), представлено для этих процессов на

Рис. 8. Рисунок показывает достаточно хорошее совпадение величин p_y и $p_y^{(ass)}$, т.е. в пределах расчетной погрешности можно констатировать выполнение соосности девиаторов деформаций и напряжений.

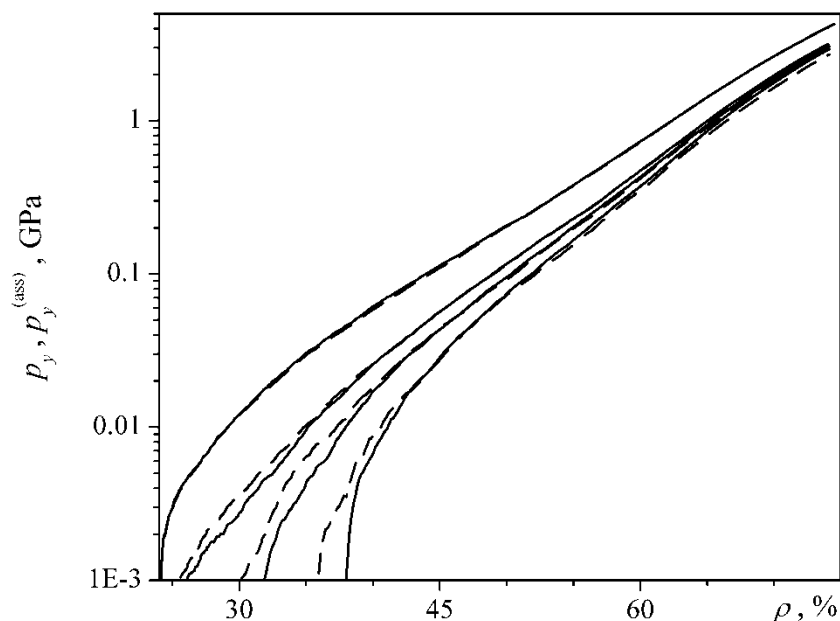


Рис. 8. Зависимость давления по оси Oy от плотности компакта для процессов (сверху вниз) «0;0.5», «0;-0.1», «0;-0.2», «0;-0.3». Сплошные линии – расчетные кривые, штриховые линии – кривые $p_y^{(ass)}$, рассчитанные по ур. (16)

Применительно к инвариантам тензоров деформаций и напряжений другим интересным следствием ассоциированного закона для порошковых тел является соотношение

$$(\varepsilon^{(p)}, \gamma^{(p)}) = \lambda_1' \nabla \Phi, \quad (17)$$

где в качестве потенциала Φ выступает либо диссипативный потенциал деформируемого тела, либо его функция нагружения, изоуровни которой совпадают с уровнями поверхности нагружения (14), представленными на Рис. 7. Как было показано в [18], выбор в качестве потенциала Φ функции нагружения предпочтителен, поскольку последняя является более наглядной, однозначной и надежной характеристикой порошкового тела. В частности, установлено, что поверхность нагружения практически не зависит от промежуточных разгрузок в процессе уплотнения и, как следствие, - от начального состояния, определяемого начальной плотностью ρ_0 , пресуемого порошка.

Соотношение (17) требует [14], чтобы направление вектора пластических деформаций $(\varepsilon^{(p)}, \gamma^{(p)})$ было ортогонально изоуровням поверхности нагружения, показанным на Рис. 7. На Рис. 9 представлены направления векторов $(\varepsilon^{(p)}, \gamma^{(p)})$ и векторов $\nabla \Phi$ для двух изолиний, при $\rho_{plast} = 0.60$ и 0.627 . Видим, что выполнение ассоциированного закона (17), т.е. коллинеарность векторов $(\varepsilon^{(p)}, \gamma^{(p)})$ и $\nabla \Phi$, наблюдается только в тривиальном случае всестороннего сжатия. Малейшее отклонение от всесторонних условий, уже для процесса «0.9;1», демонстрирует заметное нарушение коллинеарности (17). При этом вектор деформирования $(\varepsilon^{(p)}, \gamma^{(p)})$ для всех процессов отклоняется от $\nabla \Phi$ в сторону кривой уплотнения $\tau(\rho)$, направление которой можно определить вектором $(\Delta \rho, \Delta \tau)$.

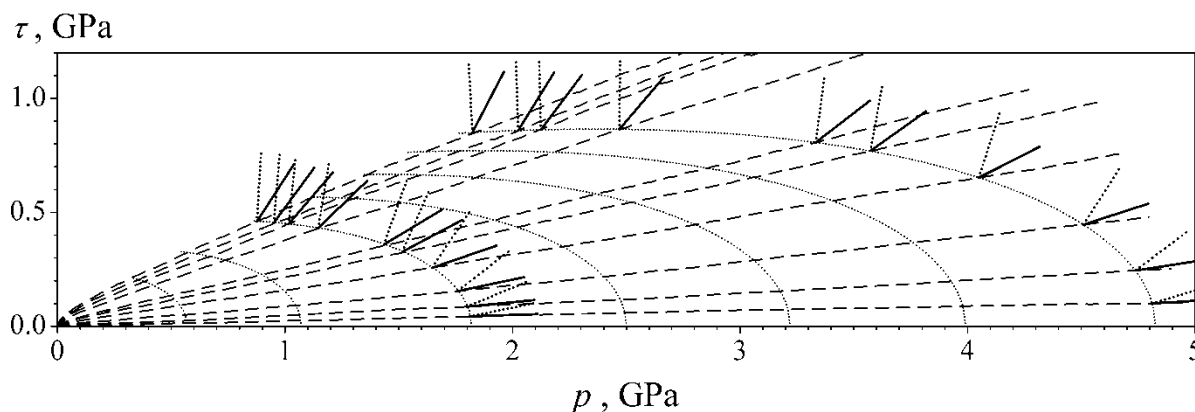


Рис. 9. Кривые уплотнения и изолинии поверхности нагружения (линии те же, что и на Рис. 7). Стрелки на пересечениях кривых уплотнения и изолиний для значений $\rho_{plast} = 0.60$ и 0.627 показывают направление вектора $\nabla\Phi$, т.е. нормали к поверхности нагружения, (верхние пунктирные стрелки) и направление вектора $(\varepsilon^{(p)}, \gamma^{(p)})$, определяющего характер деформирования, (нижние сплошные стрелки)

Отмеченная особенность позволяет сформулировать альтернативный критерий течения оксидных нанопорошков в виде [18]:

$$(\varepsilon^{(p)}, \gamma^{(p)}) = (1 - \omega) \lambda_1' \nabla\Phi + \omega \lambda_2 (\Delta p, \Delta \tau), \quad (18)$$

где ω – весовой коэффициент, определяющий влияние осуществляемого процесса на «направление» деформаций, инициируемых в порошковой системе; λ_2 – размерный коэффициент, определяемый следующим образом,

$$\lambda_2 = \lambda_1' \frac{|\nabla\Phi|}{|(\Delta p, \Delta \tau)|} = \lambda_1' \sqrt{\left[\left(\frac{\partial\Phi}{\partial p} \right)_\tau^2 + \left(\frac{\partial\Phi}{\partial \tau} \right)_p^2 \right]} / [\Delta p^2 + \Delta \tau^2]. \quad (19)$$

Переходя от соотношения для инвариантов (18) к тензорам деформаций и напряжений, получим общую форму записи правила течения нанопорошкового тела в виде

$$\Delta \varepsilon_{\alpha\beta} = (1 - \omega) \lambda_1' \cdot \frac{\partial\Phi}{\partial p^{\alpha\beta}} + \omega \lambda_2 \left(\Delta p \frac{\partial p}{\partial p^{\alpha\beta}} + \Delta \tau \frac{\partial \tau}{\partial p^{\alpha\beta}} \right), \quad (20)$$

где

$$\frac{\partial\Phi}{\partial p^{\alpha\beta}} = \left(\frac{\partial\Phi}{\partial p} \right)_\tau \frac{\partial p}{\partial p^{\alpha\beta}} + \left(\frac{\partial\Phi}{\partial \tau} \right)_p \frac{\partial \tau}{\partial p^{\alpha\beta}}, \quad \frac{\partial p}{\partial p^{\alpha\beta}} = \frac{\delta_{\alpha\beta}}{3}, \quad \frac{\partial \tau}{\partial p^{\alpha\beta}} = \frac{1}{\tau} (p_{\alpha\beta} - p \cdot \delta_{\alpha\beta}),$$

$\delta_{\alpha\beta}$ – символ Кронекера. Первое слагаемое справа в соотношении (20) соответствует ассоциированному закону, а второе слагаемое определяет влияние осуществляемого процесса. Рис. 9 показывает, что весовой коэффициент этого влияния ω не является постоянным. С приближением к процессу всестороннего сжатия вектор деформирования $(\varepsilon^{(p)}, \gamma^{(p)})$ становится гораздо ближе к вектору $(\Delta p, \Delta \tau)$, т.е. весовой коэффициент становится близок к единице.

Можно предположить, что величина ω является функцией производной $\tau_p = d\tau / dp$ вдоль кривой $\tau(p)$, определяющей процесс компактирования. Вводя единичные векторы

$$v = \frac{(e, \gamma)}{|(e, \gamma)|}, \quad n = \frac{\nabla\Phi}{|\nabla\Phi|}, \quad t = \frac{(1, \tau_p)}{|(1, \tau_p)|},$$

и требуя обращения в ноль векторного произведения векторов v и $(1 - \omega)n + \omega t$, получим для расчета величины ω соотношение:

$$\omega = \frac{v_1 n_2 - v_2 n_1}{v_1(n_2 - t_2) - v_2(n_1 - t_1)}. \quad (21)$$

Значения коэффициента ω в зависимости от отношения τ_p , рассчитанные по этому соотношению, для пересечений кривых уплотнения всех исследованных процессов с 7-ю изолиниями, показанными на Рис. 7 и 9, представлены на Рис. 10. Анализ полученных данных показывает, что функция $\omega(\tau_p)$ не зависит от величины ρ_{plast} , т.е. является общей для всех изолиний, и удовлетворительно аппроксимируется выражением:

$$\omega = \omega_1 - \omega_2 \tau_p, \quad (22)$$

с коэффициентами $\omega_1 = 0.9$ и $\omega_2 = 1.0$. Полученное выражение (22) замыкает систему предшествующих соотношений, определяющих изменение компонент тензора деформаций порошкового компакта при заданном внешнем воздействии, т.е. при заданном приращении компонент тензора напряжений.

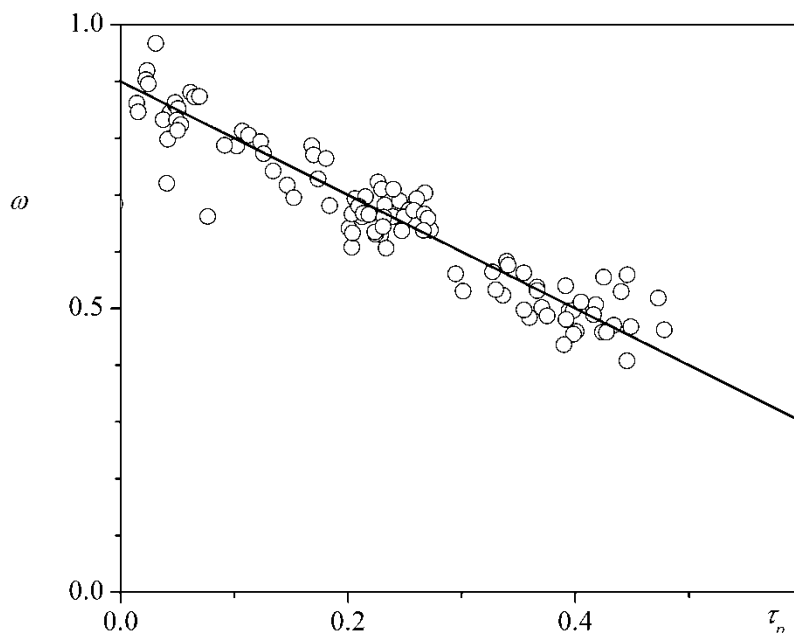


Рис. 10. Параметр ω , определяющий в соответствии с ур. (18)–(20) направление вектора пластических деформации, в зависимости от отношения скорости изменения инвариантов тензора напряжений

7. Заключение

Для модельной системы, которая соответствует наноразмерному порошку оксида алюминия, рассчитаны кривые уплотнения при компактировании в различных условиях. Рассмотрены процессы всестороннего однородного сжатия, двух- и одноосного прессования, а также ряд процессов всестороннего неоднородного сжатия, т.е. с различной скоростью сжатия вдоль различных направлений. Исследованы упругие свойства порошковых компактов. Обнаружена инвариантность модуля всестороннего сжатия и непостоянство коэффициента Пуассона, что говорит о неприменимости приближения изотропного тела к порошковому компакту и, как следствие, недостаточности двух упругих модулей для описания его упругих свойств. Тем не менее, надежно устанавливаемое значение модуля всестороннего сжатия

позволяет определить упругие и пластические части приращения плотности и тензора деформаций.

Выполнена верификация теории пластично уплотняемого пористого тела [12-15], традиционно применяемой для описания порошковых компактов. Установлена нечувствительность механических свойств порошкового тела от значений третьих инвариантов тензоров деформаций и напряжений, а также соосность девиаторов деформаций и напряжений, что полностью согласуется с традиционными теоретическими представлениями. Однако, в целом, следует признать, что известное ассоциированное правило пластического течения неприменимо к наноразмерным оксидным порошкам, поскольку в пространстве инвариантов тензора напряжений вектор инвариантов тензора приращений пластических деформаций оказывается неортогонален изоуровням поверхности нагружения. Вместо традиционного ассоциированного закона предложен другой критерий, который позволяет предсказать характер деформационных процессов в системе. Согласно предложенному критерию, вид тензора приращений деформаций определяется не только направлением вектора-градиента функции нагружения (ассоциированный закон), но и направлением «вектора», который определяет изменение компонент тензора напряжений при реализуемом процессе компактирования. Соотношение вкладов от этих двух векторов задается весовым коэффициентом ω . Сформулирована полная система соотношений, однозначно определяющая изменение компонент тензора деформаций в исследуемых системах при заданном внешнем воздействии. Помимо критерия течения данная система содержит аппроксимацию изоуровней поверхности нагружения и зависимость весового коэффициента ω от инвариантов тензора напряжений.

Благодарности. Работа выполнена при частичной финансовой поддержке РФФИ (проект 16-08-00277).

Литература

- [1] Pickens JR. Review: Aluminium powder metallurgy technology for high-strength applications. *J. Mater. Sci.* 1981;16(6): 1437-1457.
- [2] Bengisu M, Inal OT. Densification and mechanical properties of shock-treated alumina and its composites. *J. Mater. Sci.* 1994;29(18): 4824-4833.
- [3] Pecharroman C, Mata-Osoro G, Diaz LA, Torrecillas R, Moya JS. On the transparency of nanostructured alumina: Rayleigh-Gans model for anisotropic spheres. *Opt. Express.* 2009;17(8): 6899-6912.
- [4] Roussel N, Lallemand L, Chane-Ching JY, Guillemet-Fristch S, Durand B, Garnier V, Bonnefont G, Fantozzi G, Bonneau L, Trombert S, Garcia-Gutierrez D. Highly Dense, Transparent α -Al₂O₃ Ceramics From Ultrafine Nanoparticles Via a Standard SPS Sintering. *J. Am. Ceram. Soc.* 2013;96(4): 1039-1042.
- [5] Shen L, Hu C, Zhou S, Mukherjee A, Huang Q. Phase-dependent photoluminescence behavior of Cr-doped alumina phosphors. *Opt. Mater.* 2013;35(6): 1268-1272.
- [6] Penilla EH, Kodaera Y, Garay JE. Blue-Green Emission in Terbium-Doped Alumina (Tb:Al₂O₃) Transparent Ceramics. *Adv. Funct. Mater.* 2013;23(48): 6036-6043.
- [7] Luo J, Xu J. Y₂O₃-doped Al₂O₃ transparent ceramics prepared by low temperature microwave sintering. In: *Proceedings of the 5th International Conference on Advanced Design and Manufacturing Engineering (ICADME 2015)*. Shenzhen: Atlantis Press; 2015. p.99-103.
- [8] Zhou C, Jiang B, Fan J, Mao X, Pan L, Jiang Y, Zhang L, Fang Y. Translucent Al₂O₃ ceramics produced by anaqueous tape casting method. *Ceram. Int.* 2016;42(1): 1648-1652.
- [9] Kaygorodov AS, Ivanov VV, Khrustov VR, Kotov YA, Medvedev AI, Osipov VV, Ivanov MG, Orlov AN, Murzakaev AM. Fabrication of Nd:Y₂O₃ transparent ceramics by

- pulsed compaction and sintering of weakly agglomerated nanopowders. *J. Eur. Ceram. Soc.* 2007;27(2-3): 1165-1169.
- [10] Bagayev SN, Osipov VV, Shitov VA, Pestryakov EV, Kijko VS, Maksimov RN, Lukyashin KE, Orlov AN, Polyakov KV, Petrov VV. Fabrication and optical properties of Y_2O_3 -based ceramics with broad emission bandwidth. *J. Eur. Ceram. Soc.* 2012;32(16): 4257-4262.
- [11] Филоненко ВП, Хвостанцев ЛГ, Баграмов РХ, Трусов ЛИ, Новиков ВИ. Компактирование порошков вольфрама различной дисперсности гидростатическим давлением до 5 ГПа. *Порошковая металлургия.* 1992;4: 16-20.
- [12] Штерн МБ, Сердюк ГГ, Максименко ЛА, Трухан ЮВ, Шуляков ЮМ. *Феноменологические теории прессования порошков.* Киев: Наук. думка; 1982.
- [13] Олевский ЕА, Штерн МБ. Реологические основы процессов консолидации порошков и концепция «среднеквадратичных». *Порошковая металлургия.* 2004;7-8: 35-45.
- [14] Maximenko AL, Olevsky EA, Shtern MB. Plastic behavior of agglomerated powder. *Comput. Mater. Sci.* 2008;43(4): 704-709.
- [15] Boltachev GS, Nagayev KA, Paranin SN, Spirin AV, Volkov NB. Theory of the magnetic pulsed compaction of nanosized powders. In: Cabral V, Silva R. (eds.) *Nanomaterials: Properties, Preparation and Processes.* New York: Nova Science Publishers, Inc.; 2010. p.1-58.
- [16] Boltachev GS, Lukyashin KE, Shitov VA, Volkov NB. Three-dimensional simulations of nanopowder compaction processes by granular dynamics method. *Phys. Rev. E.* 2013;88(1): 012209.
- [17] Boltachev GS, Volkov NB, Kochurin EA, Maximenko AL, Shtern MB, Kirkova EG. Simulation of the macromechanical behavior of oxide nanopowders during compaction processes. *Granul. Mater.* 2015;17(3): 345-358.
- [18] Boltachev GS, Lukyashin KE, Maximenko AL, Maksimov RN, Shitov VA, Shtern MB. Compaction and flow rule of oxide nanopowders. *Optical materials.* 2017;71: 145-150.
- [19] Schwedes J. Cohesive Granular Materials. *Powder Technology.* 1975;11(1): 59-67.
- [20] Nott PR. Classical and Cosserat plasticity and viscoplasticity models for slow granular flow. *Acta Mechanica.* 2009;205(1-4): 151-160.
- [21] Agnolin I, Roux JN. Internal states of model isotropic granular packings. I. Assembling process, geometry, and contact networks. *Phys. Rev. E.* 2007;76(6): 061302.
- [22] Gilabert FA, Roux JN, Castellanos A. Computer simulation of model cohesive powders: Influence of assembling procedure and contact laws on low consolidation states. *Phys. Rev. E.* 2007;75(1): 011303.
- [23] Gilabert FA, Roux JN, Castellanos A. Computer simulation of model cohesive powders: Plastic consolidation, structural changes, and elasticity under isotropic loads. *Phys. Rev. E.* 2008;78(3): 031305.
- [24] Salot C, Gotteland P, Villard P. Influence of relative density on granular materials behavior: DEM simulations of triaxial tests. *Granular Matter.* 2009;11(4): 221-236.
- [25] Pizette P, Martin CL, Delette G, Sornay P, Sans F. Compaction of aggregated ceramic powders: From contact laws to fracture and yield surfaces. *Powder Technology.* 2010;198(2): 240-250.
- [26] Kotov YA. Electric Explosion of Wires as a Method for Preparation of Nanopowders. *J. Nanopart. Res.* 2003;5(5-6): 539-550.
- [27] Котов ЮА, Осипов ВВ, Иванов МГ, Саматов ОМ, Платонов ВВ, Азаркевич ЕИ, Мурзакаев АМ, Медведев АИ. Исследование характеристик оксидных нанопорошков, получаемых при испарении мишени импульсно-периодическим CO_2 лазером. *ЖТФ.* 2002;72(11): 76-82.

- [28] Nicot F, Darve F. A multi-scale approach to granular materials. *Mechanics of Materials*. 2005;37(9): 980-1006.
- [29] Hamaker HC. The London – van der Waals attraction between spherical particles. *Physica*. 1937;4(10): 1058-1072.
- [30] Болтачев ГШ, Волков НБ. Моделирование процесса компактирования нанопорошков в рамках гранулярной динамики. *ЖТФ*. 2011;81(7): 18-29.
- [31] Boltachev GS, Volkov NB, Zubarev NM. Tangential interaction of elastic spherical particles in contact. *Int. J. Solids Struct*. 2012;49(15-16): 2107-2114.
- [32] Cattaneo C. Sul contatto di due Corpi Elastici. *Accademia dei Lincei, Rendiconti, Series 6*. 1938;27: 342-478.
- [33] Mindlin RD. Compliance of Elastic Bodies in Contact. *J. Appl. Mech. (Trans ASME)*. 1949;16: 259-268.
- [34] Mindlin RD, Deresiewicz H. Elastic Spheres in Contact Under Varying Oblique Forces. *J. Appl. Mech. (Trans ASME)*. 1953;20: 327-344.
- [35] Reissner E, Sagoci HF. Forced Torsional Oscillations of an Elastic Half-Space. *J. Appl. Phys*. 1944;15(9): 652-654.
- [36] Jäger J. Axisymmetric bodies of equal material in contact under torsion or shift. *Archive of Applied Mechanics*. 1995;65(7): 478-487.
- [37] Лурье АИ. *Пространственные задачи теории упругости*. Москва: Государственное издательство технико-теоретической литературы; 1955.
- [38] Болтачев ГШ, Волков НБ, Кайгородов АС, Лознухо ВП. Особенности одноосного квазистатического компактирования оксидных нанопорошков. *Российские нанотехнологии*. 2011;6(9-10): 125-130.
- [39] Болтачев ГШ, Волков НБ, Двилис ЭС, Хасанов ОЛ. Компактирование и упругая разгрузка нанопорошков в рамках метода гранулярной динамики. *ЖТФ*. 2015;85(2): 94-101.
- [40] Ландау ЛД, Лифшиц ЕМ. *Теория упругости*. Москва: Наука; 1987.
- [41] Седов ЛИ. *Механика сплошной среды, т. 2*. Москва: Наука; 1976.

ELASTIC PROPERTIES, YIELD SURFACE AND FLOW RULE OF NANOPOWDER COMPACTS

G.Sh. Boltachev*, E.A. Chingina, N.B. Volkov, K.E. Lukyashin

Institute of Electrophysics, Ural Branch of RAS, Amundsen str. 106, Ekaterinburg, Russia

*e-mail: grey@iep.uran.ru

Abstract. Different compaction processes of the nanosized granular system, which is a prototype of an alumina nanopowder, are studied by the granular dynamics method. For all processes: compaction curves “density vs. pressure” of the powder compact are calculated, the elastic and the plastic parts are extracted from the total deformation, the body elastic moduli are determined within the isotropic solid approximation. The inadequacy of the isotropy approximation is established. The nanopowder yield surface is constructed in the space of stress tensor invariants. The inapplicability of the traditional associated flow rule for description of oxide nanopowders compaction processes is revealed. An alternative flow rule is suggested.

Keywords: nanopowder, yield surface, associated flow rule

Acknowledgements. The work was carried out with partial financial support of the RFBR (project 16-08-00277).

References

- [1] Pickens JR. Review: Aluminium powder metallurgy technology for high-strength applications. *J. Mater. Sci.* 1981;16(6): 1437-1457.
- [2] Bengisu M, Inal OT. Densification and mechanical properties of shock-treated alumina and its composites. *J. Mater. Sci.* 1994;29(18): 4824-4833.
- [3] Pecharroman C, Mata-Osoro G, Diaz LA, Torrecillas R, Moya JS. On the transparency of nanostructured alumina: Rayleigh-Gans model for anisotropic spheres. *Opt. Express.* 2009;17(8): 6899-6912.
- [4] Roussel N, Lallemand L, Chane-Ching JY, Guillemet-Fristch S, Durand B, Garnier V, Bonnefont G, Fantozzi G, Bonneau L, Trombert S, Garcia-Gutierrez D. Highly Dense, Transparent α -Al₂O₃ Ceramics From Ultrafine Nanoparticles Via a Standard SPS Sintering. *J. Am. Ceram. Soc.* 2013;96(4): 1039-1042.
- [5] Shen L, Hu C, Zhou S, Mukherjee A, Huang Q. Phase-dependent photoluminescence behavior of Cr-doped alumina phosphors. *Opt. Mater.* 2013;35(6): 1268-1272.
- [6] Penilla EH, Kodera Y, Garay JE. Blue-Green Emission in Terbium-Doped Alumina (Tb:Al₂O₃) Transparent Ceramics. *Adv. Funct. Mater.* 2013;23(48): 6036-6043.
- [7] Luo J, Xu J. Y₂O₃-doped Al₂O₃ transparent ceramics prepared by low temperature microwave sintering. In: *Proceedings of the 5th International Conference on Advanced Design and Manufacturing Engineering (ICADME 2015)*. Shenzhen: Atlantis Press; 2015. p.99-103.
- [8] Zhou C, Jiang B, Fan J, Mao X, Pan L, Jiang Y, Zhang L, Fang Y. Translucent Al₂O₃ ceramics produced by aqueous tape casting method. *Ceram. Int.* 2016;42(1): 1648-1652.
- [9] Kaygorodov AS, Ivanov VV, Khrustov VR, Kotov YA, Medvedev AI, Osipov VV, Ivanov MG, Orlov AN, Murzakaev AM. Fabrication of Nd:Y₂O₃ transparent ceramics by

pulsed compaction and sintering of weakly agglomerated nanopowders. *J. Eur. Ceram. Soc.* 2007;27(2-3): 1165-1169.

[10] Bagayev SN, Osipov VV, Shitov VA, Pestryakov EV, Kijko VS, Maksimov RN, Lukyashin KE, Orlov AN, Polyakov KV, Petrov VV. Fabrication and optical properties of Y_2O_3 -based ceramics with broad emission bandwidth. *J. Eur. Ceram. Soc.* 2012;32(16): 4257-4262.

[11] Filonenko VP, Khvostantsev LG, Bagramov RK, Trusov LI, Novikov VI. Compacting tungsten powders with varying particle size using hydrostatic pressure up to 5 GPa. *Powder Metall. Met. Ceram.* 1992;31(4): 296-299.

[12] Shtern MB, Serdyuk GG, Maksimenko LA, Truhan YV, Shulyakov YM. *Phenomenological Theories of Powder Pressing*. Kiev: Naukova Dumka; 1982. (In Russian)

[13] Olevskii EA, Shtern MB. Rheological Foundations of Powder Consolidation Processes and the "Mean-Square" Concept. *Powder Metall. Met. Ceram.* 2004;43(7-8): 355-363.

[14] Maximenko AL, Olevsky EA, Shtern MB. Plastic behavior of agglomerated powder. *Comput. Mater. Sci.* 2008;43(4): 704-709.

[15] Boltachev GS, Nagayev KA, Paranin SN, Spirin AV, Volkov NB. Theory of the magnetic pulsed compaction of nanosized powders. In: Cabral V, Silva R. (eds.) *Nanomaterials: Properties, Preparation and Processes*. New York: Nova Science Publishers, Inc.; 2010. p.1-58.

[16] Boltachev GS, Lukyashin KE, Shitov VA, Volkov NB. Three-dimensional simulations of nanopowder compaction processes by granular dynamics method. *Phys. Rev. E.* 2013;88(1): 012209.

[17] Boltachev GS, Volkov NB, Kochurin EA, Maximenko AL, Shtern MB, Kirkova EG. Simulation of the macromechanical behavior of oxide nanopowders during compaction processes. *Granul. Mater.* 2015;17(3): 345-358.

[18] Boltachev GS, Lukyashin KE, Maximenko AL, Maksimov RN, Shitov VA, Shtern MB. Compaction and flow rule of oxide nanopowders. *Optical materials.* 2017;71: 145-150.

[19] Schwedes J. Cohesive Granular Materials. *Powder Technology.* 1975;11(1): 59-67.

[20] Nott PR. Classical and Cosserat plasticity and viscoplasticity models for slow granular flow. *Acta Mechanica.* 2009;205(1-4): 151-160.

[21] Agnolin I, Roux JN. Internal states of model isotropic granular packings. I. Assembling process, geometry, and contact networks. *Phys. Rev. E.* 2007;76(6): 061302.

[22] Gilabert FA, Roux JN, Castellanos A. Computer simulation of model cohesive powders: Influence of assembling procedure and contact laws on low consolidation states. *Phys. Rev. E.* 2007;75(1): 011303.

[23] Gilabert FA, Roux JN, Castellanos A. Computer simulation of model cohesive powders: Plastic consolidation, structural changes, and elasticity under isotropic loads. *Phys. Rev. E.* 2008;78(3): 031305.

[24] Salot C, Gotteland P, Villard P. Influence of relative density on granular materials behavior: DEM simulations of triaxial tests. *Granular Matter.* 2009;11(4): 221-236.

[25] Pizette P, Martin CL, Delette G, Sornay P, Sans F. Compaction of aggregated ceramic powders: From contact laws to fracture and yield surfaces. *Powder Technology.* 2010;198(2): 240-250.

[26] Kotov YA. Electric Explosion of Wires as a Method for Preparation of Nanopowders. *J. Nanopart. Res.* 2003;5(5-6): 539-550.

[27] Kotov YA, Osipov VV, Ivanov MG, Samatov OM, Platonov VV, Azarkevich EI, Murzakaev AM, Medvedev AI. Properties of Oxide Nanopowders Prepared by Target Evaporation with a Pulse-Periodic CO_2 Laser. *Technical Physics.* 2002;47(11): 1420-1426.

- [28] Nicot F, Darve F. A multi-scale approach to granular materials. *Mechanics of Materials*. 2005;37(9): 980-1006.
- [29] Hamaker HC. The London – van der Waals attraction between spherical particles. *Physica*. 1937;4(10): 1058-1072.
- [30] Boltachev GS, Volkov NB. Simulation of Nanopowder Compaction in Terms of Granular Dynamics. *Technical Physics*. 2011;56(7): 919-930.
- [31] Boltachev GS, Volkov NB, Zubarev NM. Tangential interaction of elastic spherical particles in contact. *Int. J. Solids Struct*. 2012;49(15-16): 2107-2114.
- [32] Cattaneo C. Sul contatto di due Corpi Elastici. *Accademia dei Lincei, Rendiconti, Series 6*. 1938;27: 342-478.
- [33] Mindlin RD. Compliance of Elastic Bodies in Contact. *J. Appl. Mech. (Trans ASME)*. 1949;16: 259-268.
- [34] Mindlin RD, Deresiewicz H. Elastic Spheres in Contact Under Varying Oblique Forces. *J. Appl. Mech. (Trans ASME)*. 1953;20: 327-344.
- [35] Reissner E, Sagoci HF. Forced Torsional Oscillations of an Elastic Half-Space. *J. Appl. Phys*. 1944;15(9): 652-654.
- [36] Jäger J. Axisymmetric bodies of equal material in contact under torsion or shift. *Archive of Applied Mechanics*. 1995;65(7): 478-487.
- [37] Lur'e AI. *Three-Dimensional Problems of the Theory of Elasticity*. NY: Interscience Publishers; 1964.
- [38] Boltachev GS, Volkov NB, Kaygorodov AS, Loznukho VP. The Peculiarities of Uniaxial Quasistatic Compaction of Oxide Nanopowders. *Nanotechnologies in Russia*. 2011;6(9-10): 639-646.
- [39] Boltachev GS, Volkov NB, Dvilis ES, Khasanov OL. Compaction and Elastic Unloading of Nanopowders in Terms of Granular Dynamics. *Technical Physics*. 2015;60(2): 252-259.
- [40] Landau LD, Lifshitz EM. *Theory of Elasticity*. Oxford: Pergamon Press; 1993.
- [41] Sedov LI. *Mechanics of Continuous Media, vol. 2*. Singapore: World Scientific; 1997.

Submission of papers:

Manuscript should be submitted (**both MS Word and PDF**) by e-mail to: **mpmjournal@spbstu.ru**

After a confirmation of the paper acceptance, the authors should send the signed hard copy of the "Transfer of Copyright Agreement" form (available at <http://www.mpm.spbstu.ru> section "Authors") by regular post to "Materials Physics and Mechanics" editorial office:

Periodicals Editorial Office, Institute of Advanced Manufacturing Technologies, Peter the Great St.Petersburg Polytechnic University, Polytechnicheskaya, 29, St.Petersburg 195251, Russia.

The scanned copy of the signed "Transfer of Copyright Agreement" should be send by e-mail to: **mpmjournal@spbstu.ru**.

Filetype:

Authors are invited to send their manuscripts **as MS Word file with PDF format copy**.

MS Word file should be prepared according to the general instructions bellow; we are kindly asking the authors to look through the detail instruction at: <http://www.mpm.spbstu.ru>.

Length:

Papers should be limited to 30 typewritten pages (including Tables and Figures placed in the proper positions in the text).

Structure of the manuscript:

PAPER TITLE: CENTERED,

TIMES NEW ROMAN 14 BOLD, CAPITAL LETTERS

A.B. Firstauthor¹, C.D. Secondauthor^{2*} -Times New Roman 12, bold, centered

¹Affiliation, address, country - Times New Roman 10, centered

*e-mail: e-mail of the corresponding author - Times New Roman 10, centered

Abstract. Times New Roman 12 font, single line spacing. Abstract should not exceed 12 lines.

Keywords: please, specify paper keywords right after the abstract.

Paper organization. Use Times New Roman 12 font with single line spacing. Use *Italic* font in order to stress something; if possible, please, use **bold** for headlines only.

Page numbering. Please, do not use page numbering.

Tables, Figures, Equations. Please, see the sample file at <http://www.mpm.spbstu.ru> for more details.

References

References should be subsequently numbered by Arabic numerals in square brackets, e.g. [1,3,5-9], following the sample style below:

[1] Koch CC, Ovid'ko IA, Seal S, Veprek S. *Structural Nanocrystalline Materials: Fundamentals and Applications*. Cambridge: Cambridge University Press; 2007.

[2] Hull D, Bacon DJ. *Introduction to Dislocations*. 5nd ed. Amsterdam: Butterworth-Heinemann; 2011 Available from: <https://www.sciencedirect.com/science/book/9780080966724?via%3Dihub> [Accessed 19th June 2018].

[3] Romanov AE, Vladimirov VI. Disclinations in crystalline solids. In: Nabarro FRN (ed.) *Dislocations in Solids*. Amsterdam: North Holland; 1992;9. p.191-402.

[4] Mukherjee AK. An examination of the constitutive equation for elevated temperature plasticity. *Materials Science and Engineering: A*. 2002;322(1-2): 1-22.

- [5] Soer WA, De Hosson JTM, Minor AM, Morris JW, Stach EA. Effects of solute Mg on grain boundary and dislocation dynamics during nanoindentation of Al–Mg thin films. *Acta Materialia*. 2004;52(20): 5783-5790.
- [6] Matzen ME, Bischoff M. A weighted point-based formulation for isogeometric contact. *Computer Methods in Applied Mechanics and Engineering*. 2016;308: 73-95. Available from: doi.org/10.1016/j.cma.2016.04.010.
- [7] Joseph S, Lindley TC, Dye D. Dislocation interactions and crack nucleation in a fatigued near-alpha titanium alloy. To be published in *International Journal of Plasticity*. *Arxiv*. [Preprint] 2018. Available from: <https://arxiv.org/abs/1806.06367> [Accessed 19th June 2018].
- [8] Pollak W, Blecha M, Specht G. *Process for the production of molded bodies from silicon-infiltrated, reaction-bonded silicon carbide*. US4572848A (Patent) 1983.
- [9] Brogan C. *Experts build pulsed air rig to test 3D printed parts for low carbon engines*. Available from: <http://www.imperial.ac.uk/news/186572/experts-build-pulsed-test-3d-printed/> [Accessed 19th June 2018].

Правила подготовки статей:

Рукопись (**английский язык, MS Word и копия PDF**) должна быть направлена в редакцию журнала по электронной почте: **mpmjournal@spbstu.ru**.

После подтверждения принятия статьи в печать, авторы должны отправить подписанные:

1. Соглашение о передаче авторских прав (<http://www.mpm.spbstu.ru>, раздел «Авторам»);
2. Экспертные заключения о том, что материалы статьи не содержат сведений, составляющих государственную тайну, и информацию, подлежащую экспортному контролю; по адресу:

Россия, 195251, Санкт-Петербург, Политехническая, д. 29, Санкт-Петербургский политехнический университет Петра Великого, Институт передовых производственных технологий, Редакция периодических изданий.

Скан-копии подписанных документов просим направить по электронной почте: **mpmjournal@spbstu.ru**

Тип файла:

Редакция принимает **файлы MS Word с копией в формате PDF**. Статья должна быть подготовлена в соответствии с настоящей инструкцией, мы просим авторов также следовать более подробным инструкциям на сайте журнала <http://www.mpm.spbstu.ru> в разделе «Авторам».

Длина статьи:

Статья не должна превышать 30 страниц формата А4, включая Таблицы и Рисунки, размещенные непосредственно в соответствующих местах.

Общие правила оформления статьи:

НАЗВАНИЕ СТАТЬИ: ВЫРОВНЯТЬ ПО ЦЕНТРУ,

ШРИФТ, TIMES NEW ROMAN 14 BOLD, ЗАГЛАВНЫЕ БУКВЫ

Автор(ы): **А.Б. Первыйавтор¹, В.Г. Автор^{2*}** - шрифт Times New Roman 12, bold, по центру

¹Наименование организации, адрес, страна - шрифт Times New Roman 10, по центру

* e-mail автора, представившего статью - шрифт Times New Roman 10, по центру

Аннотация. Аннотация статьи составляет не более 12 строк. Используйте шрифт Times New Roman 12, одинарный межстрочный интервал.

Ключевые слова: укажите ключевые слова после аннотации.

Как организовать текст статьи. Используйте шрифт Times New Roman 12, одинарный межстрочный интервал. При необходимости выделить какую-либо информацию используйте *курсив*. Используйте **полужирный** шрифт только для заголовков и подзаголовков.

Номера страниц. Пожалуйста, не используйте нумерацию страниц

Таблицы, Рисунки, Уравнения. Подробные правила оформления данных элементов статьи приведены в инструкции на сайте журнала <http://www.mpm.spbstu.ru>

Литература

Ссылки приводятся в тексте в квадратных скобках [1,3,5-9]. Стиль оформления ссылок:

[1] Koch CC, Ovid'ko IA, Seal S, Veprck S. *Structural Nanocrystalline Materials: Fundamentals and Applications*. Cambridge: Cambridge University Press; 2007.

[2] Hull D, Bacon DJ. *Introduction to Dislocations*. 5nd ed. Amsterdam: Butterworth-Heinemann; 2011 Available from: <https://www.sciencedirect.com/science/book/9780080966724?via%3Dihub> [Accessed 19th June 2018].

[3] Romanov AE, Vladimirov VI. Disclinations in crystalline solids. In: Nabarro FRN (ed.) *Dislocations in Solids*. Amsterdam: North Holland; 1992;9. p.191-402.

[4] Mukherjee AK. An examination of the constitutive equation for elevated temperature plasticity. *Materials Science and Engineering: A*. 2002;322(1-2): 1-22.

- [5] Soer WA, De Hosson JTM, Minor AM, Morris JW, Stach EA. Effects of solute Mg on grain boundary and dislocation dynamics during nanoindentation of Al–Mg thin films. *Acta Materialia*. 2004;52(20): 5783-5790.
- [6] Matzen ME, Bischoff M. A weighted point-based formulation for isogeometric contact. *Computer Methods in Applied Mechanics and Engineering*. 2016;308: 73-95. Available from: doi.org/10.1016/j.cma.2016.04.010.
- [7] Joseph S, Lindley TC, Dye D. Dislocation interactions and crack nucleation in a fatigued near-alpha titanium alloy. To be published in *International Journal of Plasticity*. *Arxiv*. [Preprint] 2018. Available from: <https://arxiv.org/abs/1806.06367> [Accessed 19th June 2018].
- [8] Pollak W, Blecha M, Specht G. *Process for the production of molded bodies from silicon-infiltrated, reaction-bonded silicon carbide*. US4572848A (Patent) 1983.
- [9] Brogan C. *Experts build pulsed air rig to test 3D printed parts for low carbon engines*. Available from: <http://www.imperial.ac.uk/news/186572/experts-build-pulsed-test-3d-printed/> [Accessed 19th June 2018].

МЕХАНИКА И ФИЗИКА МАТЕРИАЛОВ

44 (1) 2020

Учредители: Санкт-Петербургский политехнический университет Петра Великого,

Институт проблем Машиноведения Российской академии наук

Издание зарегистрировано федеральной службой по надзору в сфере связи,
информационных технологий и массовых коммуникаций (РОСКОМНАДЗОР),

свидетельство ПИ №ФС77-69287 от 06.04.2017 г.

Редакция журнала

Профессор, д.т.н., академик РАН, А.И. Рудской – главный редактор

Профессор, д.ф.-м.н., член-корр. РАН, Д.А. Индейцев – главный редактор

Профессор, д.ф.-м.н. И.А. Овидько (1961 - 2017) – основатель и почетный редактор

Профессор, д.ф.-м.н. А.Л. Колесникова – ответственный редактор

Доцент, к.т.н. А.С. Немов – ответственный редактор

А.Ю. Ромашкина, к.т.н. – выпускающий редактор

Л.И. Гузилова – редактор, корректор

Телефон редакции

+7(812)552 77 78, доб. 224

E-mail: mpmjournal@spbstu.ru

Компьютерная верстка А.Ю. Ромашкина

Подписано в печать 15.03.2020 г. Формат 60x84/8. Печать цифровая
Усл. печ. л. 10,0. Тираж 100. Заказ ____.

Отпечатано с готового оригинал-макета, предоставленного автором
в Издательско-полиграфическом центре Политехнического университета Петра
Великого. 195251, Санкт-Петербург, Политехническая ул., 29.
Тел.: +7(812)552 77 78, доб. 224.

On cracking in thick GaN layers grown on sapphire substrates	1-7
M.G. Mynbaeva, A.A. Sitnikova, A.N. Smirnov, K.D. Mynbaev, H. Lipsanen, A.V. Kremleva, D.A. Bauman, V.E. Bougrov, A.E. Romanov	
Two scale homogenization in ternary locally resonant metamaterials	8-18
C. Comi, M. Moscatelli, J-J. Marigo	
Probing of polycrystalline magnesium at ultrasonic frequencies by mechanical spectroscopy	19-25
V.V. Kaminskii, Y.V. Lyubimova, A.E. Romanov	
Interaction of impurity atoms of light elements with vacancies and vacancy clusters in fcc metals	26-33
G.M. Poletaev, I.V. Zorya, R.Y. Rakitin, M.A. Iliina, M.D. Starostenkov	
Deposition kinetics and boundary layer theory in the chemical vapor deposition of β-SiC on the surface of C/C composite	34-47
H. Aghajani, N. Hosseini, B. Mirzakhani	
Strain-hardening effect on critical strain assessment of pipe plastic bending at buckling	48-60
M. Zheng, Z.M. Li	
Homogeneous horizontal and vertical seismic barriers: mathematical foundations and dimensional analysis	61-65
V.A. Bratov, A.V. Ilyashenko, S.V. Kuznetsov, T.-K. Lin, N.F. Morozov	
Hyperbolic two temperature fractional order one dimensional thermoelastic model heated by a pulse of laser	66-76
E. Bassiouny	
Hybrid acoustic panel: the effect of fiber volume fraction and panel thickness	77-82
NPG. Suardana, IKG. Sugita, IGN. Wardana	
Structural transformation of HCP metallic nanowire using cleri-rosato potential	83-93
M.M. Aish	
Numerical optimization of the cantilever piezoelectric generator	94-102
A.N. Soloviev, V.A. Chebanenko, I.V. Zhilyaev, A.V. Cherpakov, I.A. Parinov	
Single-walled carbon nanotube as a nanoscale quantum system	103-109
M.V. Krasinkova	
Structure and properties of nanoporous oxide dielectrics modified by carbon	110-115
Yu.V. Sakharov	
Pair interaction of coaxial circular prismatic dislocation loops in elastic solids with spherical surfaces	116-124
S.A. Krasnitckii, A.M. Smirnov, M.Yu. Gutkin	
Crystallographic orientation, delay time and mechanical constants influence on thermal fatigue strength of single - crystal nickel superalloys	125-136
A.V. Savikovskii, A.S. Semenov, L.B. Getsov	
Упругие свойства, поверхность нагружения и критерий течения нанопорошковых компактов	137-158
Г.Ш. Болтачев, Е.А. Чингина, Н.Б. Волков, К.Е. Лукьяшин	